RÉPUBLIQUE FRANÇAISE
Liberté Égalité Fraternité

Université de Toulouse

Doctorat de l'Université de Toulouse

préparé à Toulouse INP

Modélisation et simulation de flammes d'aluminium

Thèse présentée et soutenue, le 30 octobre 2024 par

Jean VILLARD

École doctorale
MEGEP - Mécanique, Energétique, Génie civil, Procédés

Spécialité
Energétique et transferts

Unité de recherche
CERFACS

Thèse dirigée par
Jean-Christophe JOUHAUD

Composition du jury
M. Fabien HALTER, Rapporteur, Université Orléans - ICARE/CNRS
M. Aymeric VIé, Rapporteur, EM2C
Mme Bénédicte CUENOT, Examinatrice, SAFRAN
M. Christian HASSE, Examinateur, TU Darmstadt
M. Xiao Cheng MI, Examinateur, Eindhoven University of Technology
M. Jean-Christophe JOUHAUD, Directeur de thèse, CERFACS

Membres invités
Mme Eleonore Riber, CERFACS

Abstract

As society is moving away from hydrocarbons, there is a need for a clean way to store and transport energy over the globe. For this need, metal fuels are very attractive and excellent candidates as alternative carbon-free and renewable fuels. Due to their high energy density, availability, stability and low cost, metals and especially aluminum could replace hydrocarbons in many applications. In addition, metal oxides are solid and may be easily collected and recycled (J.M. Bergthorson et al., Applied Energy, 2015). Aluminum is already well known as a fuel, used for many years in space propulsion. However, the detailed understanding of the combustion of aluminum particles remains a challenge which requires to combine sophisticated experiments with numerical simulation. The modeling of aluminum combustion then must take into account all existing phenomena, from melting and evaporation of the metal particles to gaseous and heterogeneous oxidation and finally condensation and solidification into metal oxide particles. In this work, a complete model for burning aluminum particles has been developed and implemented in the massively parallel Navier-Stokes compressible solver AVBP in order to compute a stabilized laminar flame. The model includes the dual composition of the aluminum particles with an alumina cap, heterogeneous surface reactions and condensation of the combustion products, and nucleation of products into particles following Finke et al. (J. Finke., Combustion and flame, 2023). The Lagrangian tracking of these product particles is an original feature of the model, with regards to the literature where an Eulerian formulation is mostly reported. It offers the possibility to give more details about the formed metal oxide particles, in particular their size. Results and analysis of 1D and 2D stabilized aluminum laminar flames obtained with this model confirm the validity of the approach.

Résumé

Afin de limiter l'utilisation d'hydrocarbures, il est nécessaire de trouver un moyen propre de stocker et transporter l'énergie sur de grandes distances. Les combustibles métalliques constituent d'excellents candidats en tant que combustibles alternatifs, renouvelables et sans émissions de carbone. En effet, ils présentent une haute densité énergétique, sont disponibles à bas coût et sont faciles à stocker et transporter sous forme de poudre. De plus, les produits de combustion sont des oxydes métalliques solides qui pourraient être collectés et recyclés (J.M. Bergthorson et al., Applied Energy, 2015). L'aluminium est utilisé depuis de nombreuses années comme combustible, notamment en tant que carburant pour la propulsion spatiale et militaire. Cependant, la compréhension détaillée de la combustion des particules d'aluminium reste un enjeu majeur nécessitant de combiner résultats expérimentaux et simulations numériques avancées. La modélisation de ce type de combustion implique de prendre en compte tous les phénomènes impliqués. Ces phénomènes complexes sont nombreux, de la fusion et l'évaporation des particules d'aluminium à l'oxydation gazeuse et de surface, jusqu'à la condensation et la solidification en particules d'oxyde métallique des produits de combustion. Durant cette thèse, un modèle complet pour la combustion des particules d'aluminium a été implémenté dans le code massivement parallèle AVBP afin de stabiliser numériquement des flammes d'aluminium. Le modèle prend en compte la présence du lobe d'alumine sur les particules d'aluminium, les réactions hétérogènes de surface et la condensation détaillée des produits de combustion en utilisant le modèle proposé par Finke et al. (J. Finke., Combustion and Flame, 2023). Ce modèle permet de suivre les produits de combustion liquides de façon Lagrangienne contrairement aux travaux présents dans la littérature qui utilisent une formulation Eulérienne. Ce dernier point permet d'étudier l'évolution de la morphologie des particules d'alumine, ce qui constitue un enjeu clef dans le but de les collecter et de les recycler. Ce modèle a été utilisé pour simuler la combustion de particules d'aluminium isolées, des flammes 1D ainsi que des flammes 2D pouvant être comparées aux résultats expérimentaux présents dans la littérature.

Remerciements

I want to first thank the members of my jury for taking the time out of their very busy schedules to make this PhD defense possible, from taking the time to read and review this manuscript to traveling to Toulouse. The review reports were very thorough, and the conversation during the defense was extremely interesting.

La thèse est un travail de longue haleine impliquant une lourde charge mentale. Heureusement, grâce à de nombreuses personnes, cette charge m'a semblé bien plus facile à porter.

Merci à mes encadrants de m'avoir donné l'opportunité de faire cette thèse au Cerfacs. Les conversations scientifiques enrichissantes ont bien sûr été essentielles à l'aboutissement de ce travail de thèse. Mais c'est surtout leur gentillesse qui a constitué un soutien unique pour moi. Nous partageons une certaine ~~obstination~~ détermination qui fut essentielle pour ce travail particulier et malgré laquelle ce fut toujours un plaisir de travailler avec vous.

Je tiens à remercier l'équipe CSG pour sa rapidité d'intervention et sa patience face à de nombreuses questions plus ou moins intelligentes. Un autre soutien essentiel fut l'équipe administrative, notamment Chantal, qui a elle aussi toujours été là pour s'occuper de problématiques parfois plus obscures que ce qui peut être trouvé dans ce manuscrit. Ces deux équipes m'ont permis de pleinement me concentrer sur mon travail de thèse, ce qui est une chance pour laquelle je suis très reconnaissant.

J'ai pu rencontrer des gens formidables au Cerfacs qui ont grandement contribué à mon bonheur pendant ces années de thèse. Je tiens bien sûr à remercier mes coburreaux du J24, Thomas qui m'a accueilli et énormément aidé pendant mon stage et le début de ma thèse. Il me tarde que tu reviennes, j'ai progressé sur Fifa, Pas Sûr que tu Gagnes maintenant. Alexandre pour tous les délires, bruits et autres singeries qui améliorent grandement le moral. Eloise pour sa gentillesse et ses compétences surdéveloppées en informatique, je ne comprends toujours pas pourquoi tu essaies de faire tourner un code dans lequel les solutions ne sont même pas alignées sur le maillage alors que tu pourrais être chez Google. Dans le même genre, il y a bien sûr Guillaume qui connaît aussi bien les calculateurs que les calculs qu'il fait tourner dessus. Tu as bientôt fini, ce fut un plaisir de t'accueillir dans ce bureau pour ta fin de thèse. Louis venu du nord, ton bref passage fut aussi un plaisir. Dix fois merci de m'avoir supporté moi et mon humour différent, ridicule amenant parfois des divergences de concentration difficiles à digérer. Merci aux thésards de ma génération. Yann et Clément pour les séances d'escalade et aussi un peu de tennis. Thomas Naess, on aura commencé et finis ensemble, ce fut un plaisir de ~~subir~~ vivre ce voyage dans des conditions similaires. Avec ton nouveau casque, tu vas pouvoir impressionner toute ta box avec encore plus que tes performances sportives, qui seront bien sûr décuplées. Mooooonnnnnnnnnnssssssiiiiieeeeeeeeuuuuuuurrrrr Vanbersel, ton seul défaut est ton niveau sur Mario Kart, contrairement à Suzie qui n'a aucun défaut. Ca-

mille, tu as trouvé avec cet homme chaussure parfaite à ton pied. Jean-Jacques qui est tellement gentil et avenant que l'on dirait qu'il vient d'un pays imaginaire, c'est un truc de Tarnais ! Chlotilde qui fleurit son quotidien, et le nôtre. Merci à Lukas de m'avoir appris des principes culturelles germaniques importants tel que la sainte trinité des ingrédients dans la bière ou l'art de mettre des chaussettes blanches dans des claquettes en plastique. Merci à Raphael et Mehdi qui, en plus de faire avancer la science, finiront peut-être par résoudre la vitale question de l'importance de la texture des desserts Newrest, une étude paramétrique est en cours. Jessica encore plus adorable que son homme, c'est une performance. Merci à Nathanael pour la diffusion de la culture bretonne au labo. Merci à mes compagnons de voyages de Nancy, Hector et Felicia, ce fut un plaisir de partager ce voyage à Nancy. Je conseille particulièrement l'hôtel de l'académie. Félicia a adoré et si vous voulez savoir où c'est, n'hésitez pas à lui demander sa carte de France, c'est quelque chose. Thomas Gianoli pour me rappeler que j'ai beaucoup de marge de progression à l'escalade, j'espère qu'ils ouvriront bientôt des 10f+ pour que t'arrêtes de t'ennuyer. Bon courage à Anne-Laure et toi, vous allez assurer. Francis, toujours là pour aider avec le sourire, merci pour tes connaissances dans la navigation des mondes obscures de N2F et de la publication scientifique. Merci à Arthur pour toutes les conversations au bar, toujours très agréable de discuter avec toi. Susanne pour me rappeler que je n'ai pas de mémoire, sinon j'oublie. Je crois que ton français est désormais tellement bon qu'on va enfin pouvoir parler anglais. Alexandre, promis au prochain spectacle de notre leader suprême, je viendrais les yeux ouverts. Merci à Etienne et Lucien de m'avoir mis le pied à l'étrier lors de mon arrivée aux Cerfacs. Merci à la super team du I16 (si vous visitez ce bureau, faites attention aux éruptions Pestriennes), Thomas et Antoine. Toujours là pour prendre le temps de m'écouter sur des problématiques différentes et me conseiller judicieusement. Ils sont aussi soutenus par Anthony pour leurs performances de course, il a l'avantage de ne jamais tomber à court de batterie. Merci au bureau du I8, je conseille d'y faire un tour. Avec tous les objets qui y sont exposés c'est désormais plus un musée ... ou un zoo, vous pourrez notamment y trouver le lion le plus musicalement talentueux du monde. Merci à Balázs et Eric pour les séances d'escalade. Mouze pour sa bonne humeur, parfois bruyante mais toujours contagieuse. Rémi pour ses anecdotes scientifiques sur l'aérodynamisme d'un corps ovale ainsi que l'écoulement d'éthanol à travers un conduit sphérique, je ne suis pas certain que le machine learning était nécessaire. David pour sa bonne humeur incroyable et très contagieuse, 30 ans de carrière j'ai jamais vu ça. Alexis, un personnage si riche dont je n'ai toujours pas réussi à en faire le tour. Victor, on m'a dit que t'as récemment changé de bureau, j'espère qu'il est bien. Merci Quentin et Jonathan qui m'ont fait découvrir les arcanes de la chimie en étant toujours disponible pour m'aider. Merci à la génération de thésard m'ayant précédé. Minh, Christopher, Jonathan, T. Lafarge, Nicolas, Florian, Adèle, Thomas Astoul et Willca. J'en oublie forcement, mais vous avez tous contribué à embellir mon arrivée au Cerfacs. Merci et surtout bon courage à ceux des générations suivantes. Pierre-Antoine, Emile, Justin, Etienne, Loic, Lakshmanan, Solene et tous ceux que j'oublie. Vous allez voir, à un moment c'est fini, si si, je vous assure. Même moi je n'en reviens pas.

Merci à toute l'équipe aluminium de l'IMFT. Jimmy et Antoine, qui sont un peu les seuls en France à pouvoir vraiment me comprendre (voir page ix de la thèse d'Antoine pour plus de précisions). Jimmy pour ton aide précieuse en début de thèse. Antoine pour toutes les discussions enrichissantes durant cette thèse mais aussi ta gentillesse naturelle, amuse-

toi bien à la campagne. Ilan, je sais que tu es allé voir la page ix de la thèse d'Antoine mais ne t'inquiète pas, ça va bien se passer, le sujet est aussi capricieux qu'intéressant.

Je tiens à remercier mes amis qui m'ont soutenu aussi bien pendant qu'avant cette thèse. Marine et David qui m'ont accompagné pendant toutes les études, il me tarde sincèrement que vous reveniez à Toulouse. Mon quotidien est clairement moins agréable depuis que vous êtes partis. En parlant de faire l'erreur de quitter la ville rose, Marco, je suis très heureux que Marseille t'ait repoussé à Toulouse. Ton soutien et les moments passés ensemble ont vraiment facilité cette thèse. Baptiste, qui m'aide à maintenir la Terre en orbite au moins une fois par semaine. Le Wiesbaden VfL va atteindre des sommets encore plus hauts que ceux que tu aimes skier. Merci à tout l'équipage du Titanic pour entretenir mon alcoolisme. J'ai une pensée émue pour Lucille et Pauline qui sont venues me voir pour l'amour des maths. Le passage de la découverte du théorème de Pythagore à une soutenance de thèse de 2h en combustion a dû être plutôt agréable. J'espère que le roi de Belgique ne nous en voudra pas trop d'avoir visité sa demeure en n'étant pas totalement sobre. On avait précédemment le lion le plus musicalement talentueux de France, il ne faudrait pas oublier son égal, le renard. Merci à Florent, j'ai enfin trouvé quelqu'un qui sur-réfléchit plus que moi, je ne sais pas si c'est toujours une bonne chose pour la santé mentale des gens qui nous entourent ... ni la nôtre d'ailleurs. Antho même si tu nies apprécier mon humour, je sais que c'est pour toi une véritable passion, nan mais si, vraiment. Nicolas, qui fait plus de kilomètres en courant que moi en voiture chaque semaine. En plus d'être sportif, tu m'as montré toute la grandeur de tes talents de musicien avec la recomposition de nombreux thèmes de film pendant les quelques mois de coloc. Victor, je sais que même 20 ans après mon doctorat, je n'aurais pas le savoir nécessaire pour expliquer réellement ta folie, ne change rien. Merci à Charles et Amir pour tous les bons moments depuis le lycée. Céline, la seule viking qui consomme plus de litres de crème solaire que de bière, je vais essayer de lire les panneaux de limitation de vitesse (j'allais ajouter «, promis » mais c'est un peu ambitieux).

Je souhaite remercier mon père pour son soutien indéfectible ainsi que sa générosité tout au long de ma vie dans des conditions parfois très difficiles. Sans ce soutien, cette thèse n'aurait certainement jamais vu le jour. Je suis conscient de la chance inouïe que j'ai de t'avoir comme père. Merci à François, malgré le fait que « les maths, ça ne sert à rien » comme tu disais à tes profs, tu as fait la moitié de la France pour me voir déblatérer des sottises pendant 2 heures, ce qui me touche beaucoup. Merci Marine d'être avec mon frère, je crois sincèrement qu'il n'aurait pas pu trouver meilleure personne pour l'accompagner. Bienvenue à toi Basile, au moment où j'écris ces lignes ton âge se compte en heures. Le monde va te paraître grand et mystérieux dans un premier temps mais tu seras toujours bien accompagné pour le parcourir. En parlant d'être bien accompagné, merci à toi Pierre pour ton soutien et le temps passé ensemble, toujours très agréable. Merci à toi Lise pour ta gentillesse et ta bienveillance hors norme. Léon et Adèle, mes neveu et nièce d'amour. Vous allez désormais devoir partager ce titre, mais vous pourrez toujours compter sur moi. Merci à Hubert et Annie d'avoir été des oncle et tante super chouettes mais aussi d'avoir pondu mes deux cousins que je remercie tout autant. Merci à Pépère que je n'ai pas beaucoup connu et dont le souvenir principal que j'ai de toi est ta gentillesse.

Enfin, il est parfois tentant devant la brutalité et l'imperfection de ce monde de ne plus vouloir se battre, de laisser l'obscurité gagner. Malheureusement pour le diable, il existe des êtres d'une générosité et d'une force exceptionnelle, qui constituent à eux seuls

une raison de se battre, et ce, quel que soit l'adversité. Émilienne, si l'humanité partageait tes qualités, le paradis où tu es maintenant serait bien fade en comparaison du monde que tu as quitté, je te dédie ce manuscrit.

Contents

Introduction

Global warming is expected to be one of the top challenges humanity will have to face in the years to come. Indeed, according to the latest IPCC report [78], its effects are going to have a major impact on peak temperatures, soil moisture and annual precipitation. That will induce huge consequences for humanity in terms of water and food availability, health, infrastructures and ecosystems. This rise in temperature is directly linked to carbon emitted by human activities and it is therefore crucial to curb these emissions.

To do so, new behavioral, but also technological changes must rapidly occur to prevent a drop in living standards as well as many deaths. It is important to note that over 94 % of CO2 emissions are the result of the production and consumption of gas, oil and coal [77]. Furthermore, according to the IEA [60], the peaks in demand for all these hydrocarbons are in sight and replacements for such fuels must be quickly developed.

Several potential candidates exist to replace hydrocarbon fuels. The key characteristics of a fuel are availability, cost, ease of use, ease of storage and storage density. For example, oil is, or at least was, easy to extract with not much cost and requires only a combustion engine with a non-pressurized tank and therefore no loss of stored energy over time. Meaning that it can be easily extracted, shipped around the globe and stored by anyone with a compact and easy-to-use technology. All of this at an increasing but still fairly low cost. None of the alternatives fuels proposed today present all of these characteristics but they could complement each other for different applications.

One of the simpler alternative is the use of batteries to store and use electricity. This present mainly two advantages. First electrical engines are well known and easy to use and maintain. Second, the storage efficiency of battery is fairly high. However, producing 800 million vehicles with a 15 kWh Li-ion battery would consume 30 % of the world's lithium reserves [2, 82]. Knowing that a standard small electric car requires a 50 kWh battery (52kWh for a Renault Zoe for example) and that there is an estimated 1.474 billion vehicles in the world today [61] , one can easily understand that Li-ion battery won't be able to replace classic fuels. Furthermore, these batteries only have a specific energy of around 260 wh/kg vs 12.5 kWh/kg for diesel. Finally stored diesel does not lose energy over time while the storage timescale for batteries is counted in days for Li-ion batteries [108]. These two last facts mean that a Li-ion battery powered vehicle will be sensibly heavier than an oil powered vehicle for the same autonomy and that Li-ion batteries cannot be used to ship electricity over long distances.

A more conventional candidate to replace hydrocarbons would be bio-fuels due to its compatibility with hydrocarbons engines. But because of the low productivity of photosynthesis [12, 13], the land area required to replace current energy vectors would be too high. Therefore, the use of these bio-fuels should be limited to the replacement of hydrocarbons when alternatives are unusable or limited. One example is the use of SAF in aeronautic.

Another fuel receiving a lot of attention is hydrogen, and rightly so. It has a high specific energy and could be burned in a gaseous form in modified classical engines. However, it is not easy to store, requiring high pressure in its gaseous form and a temperature of -253°C in its liquid form. Furthermore, any leakage could have catastrophic consequences due to its very large flammability limits [23].

As can be seen on figure 1, most of the metal fuels have a much higher energy density compared to diesel or gasoline, while presenting good values of specific energy. Moreover, metal fuels generate solid combustion products that could be retrieved and turned back into fuel using a clean primary source of energy [63].

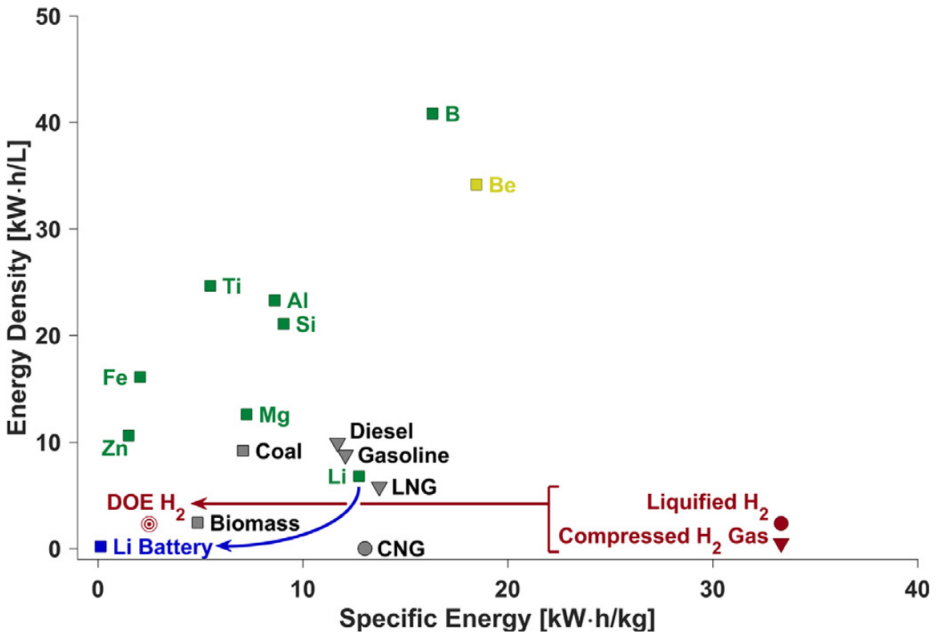

Figure 1 – Energy density and specific energy of various metal fuels compared to hydrocarbons, hydrogen and batteries. Figure extracted from [12]

However, burning capacities as well as availability at a reasonable price leave only three metals as interesting candidates for being used as fuel. Indeed, as explained by Lomba in his PhD thesis [82], while beryllium has the best energy density, it suffers from a high ignition temperature and toxicity issues. Bore is hard to ignite with high combustion time, making it difficult to stabilize a flame for O2 concentrations lower than 70 %. Titanium also has a relatively high combustion time. Lithium reacts violently with water and presents safety and toxicity issues. Finally, silicon has a slow reaction rate, making it difficult to obtain a stable flame from it. The remaining three candidates are aluminum,

iron and magnesium. The latter suffers from low reserves, eliminating it for large-scale use [108]. The two remaining candidates are aluminum and iron, presenting a high energy density, low price and availability.

The reason why these fuels are not currently used as clean energy carriers is that the technology maturity required to burn metals as an energy source while retrieving and recycling the combustion products does not exist yet. This is because metal combustion is hard to stabilize and our understanding of its complex combustion phenomenology is still at an early stage.

At the end, no alternative fuel presents as many advantages as hydrocarbons. This is why none of them can be used as a single replacement for all hydrocarbons. They all have pros and cons and therefore their own potential applications, as summarized in figure 2.

	-	+	Potential applications
Hydrocarbons	-Reject carbon -Not renewable, reserves are getting low	-Ease of storage -Ease of use -Low cost -High specific energy and energy density	All the current ones
Biofuels	-Require a lot of farming area -Low efficiency -Expensive	-Same as hydrocarbons, except for the cost	When a fuel with similar properties with gasoline is the only option
Hydrogen	-Safety issues -Hard to store and distribute -Low energy density	-High specific energy -Ease of use: Adapted existing gas burner	To replace natural gas but with higher security restrictions.
Li-ion battery	-Lack of availability of lithium -Low energy density -Low specific energy	-Ease of use -Ease of storage for short distances or periods of time -Safe to store	To easily store and use energy when weight or volume are not an issue
Metal fuels (Fe, Al)	-Low understanding of the phenomenology -Technology at a very low stage -Hard to use	-Ease of storage and distribution: Same as coal -High specific energy and energy density -Safe to use	To easily store and move large quantities of energy around the globe Safe to use

Figure 2 – Comparison of several promising fuels against hydrocarbons

Metal fuels could clearly play a key-role in the future mix of energy vectors needed to replace all the applications of hydrocarbons. While they are technologically difficult to use as an energy vector, they present superior energy density and specific energies while being easier to safely store and transport over long distances. None other alternative fuels present such advantages. However, technological difficulties stem from the complex phenomenology of metal combustion that is not well understood yet.

This is why it has been chosen to study the combustion of aluminum in the current work to improve our understanding of one of the most promising fuel of tomorrow.

In this manuscript, the unique phenomenology of aluminum combustion is first introduced in chapter 1 using experimental and numerical results from the literature. Then, the general equations already present in AVBP are presented in chapter 2 for both the Eulerian and Lagrangian solvers. Next, in chapter 3, the details of each of the phenomenon involved in aluminum combustion are detailed alongside the model implemented in the current work. Finally, this model is used to compute increasingly complex configurations. From the combustion of an isolated aluminum particle in chapter 4 to the simulation of 1D flames in chapter 5, and finally 2D dust aluminum-air dust flames in 6. Comparisons with experimental and numerical results from the literature are presented in these 3 chapters.

The work presented in this manuscript has been performed in the frame of the European Union's Horizon 2020 research and innovation program under the Center of Excellence in Combustion (CoEC) project, grant agreement no. 952181.

Chapter 1

Introduction to the phenomenology of aluminum combustion

Aluminum combustion presents its own complicated phenomenology and the goal of this first chapter is to introduce it. To do so, experimental and numerical works from the literature are presented and the main results are discussed. This is first done for the combustion of an isolated aluminum particle and then for dust flames. After having introduced the state of the art of aluminum combustion, the details of each phenomena involved are discussed together with their implementation in chapter 3.

Overview

1.1 Combustion of an isolated aluminum particle

Before considering the combustion of an aluminum dust flame, it is interesting to study how a single aluminum particle burns. This has been studied for several decades in the arms and space industry. Indeed, the solid propellant of Ariane 5 boosters is composed of 18 % of aluminum [35]. The combustion of these particles brings a high energy supply. This energy surplus increases the flame temperature by 1000 K and plays a major role regarding engine stability [74].

According to Karasev et al. [68], solid propellant follows the strong agglomeration scenario. Meaning that the melting and ignition of aluminum particles occur mostly at the burning surface. Therefore, the aluminum particles in the the propellant agglomerate to form burning liquid droplets with a diameter of 100-500 μm that are ejected from the surface. This phenomenon can be seen in figure 1.1.

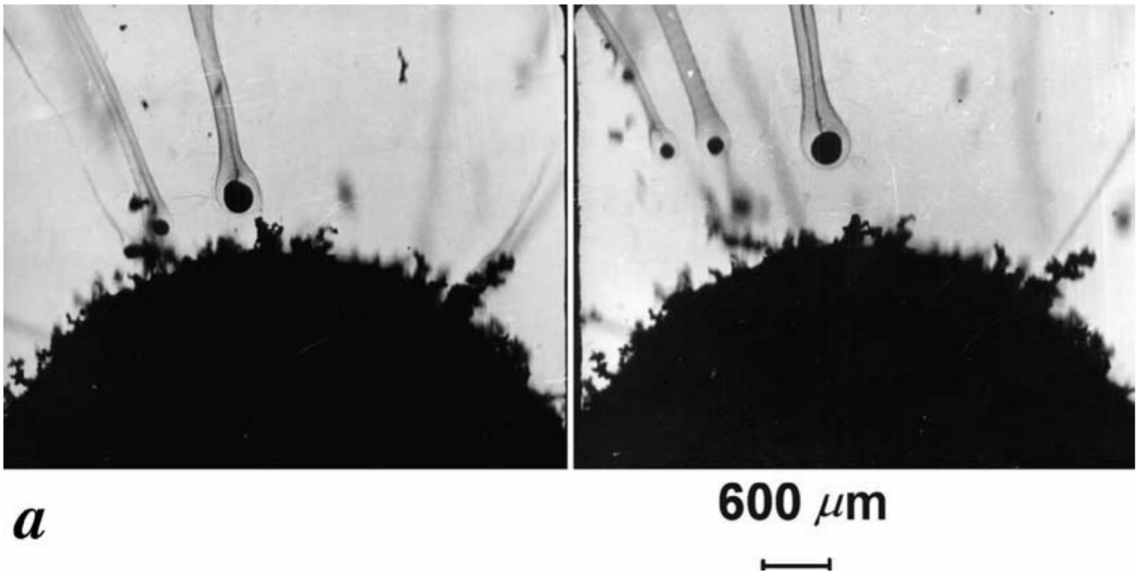

Figure 1.1 – High-speed photographic data of two consecutive shadow images illustrating the generation of agglomerates by the propellant burning surface. Figure extracted from [68].

This is why the experimental study of particles with a diameter higher than 10 μm has first been studied. All the work performed through the years gives a great understanding about the combustion of an isolated aluminum particle.

1.1.1 Experimental studies of the combustion of an isolated aluminum particle

The combustion of isolated particles has been experimentally studied multiple times. The main objective of all these studies is generally twofold. First, to improve our understanding of the many complex mechanisms involved in the combustion of aluminum. And second, to determine a combustion law capable of predicting the characteristic combustion time of a burning aluminum particle in function of the diameter and the gas phase species

concentrations. Indeed, because the mechanisms involved are not yet well understood, and thus hard to take into account in modelization, it is important to have these simpler laws. These empirical laws can then be used as a simpler way of modelizing aluminum combustion without having to account to the full phenomenology. For example, Lacassagne et. al [74] derived from these empirical laws a model for the burning of aluminum particles in a rocket engine. Moreover, they give empirical data that can be used to validate models involving more complex aspects of aluminum combustion. A good example of this is how Zhang et al.[114] used such empirical laws to validate the combustion time of their model.

Let us now study some of these experimental works and their main conclusions.

Sarou-Kanian et al. [96] obtained good pictures illustrating the ignition, and then burning of an isolated aluminum particle. The images captured in this work show how an aluminum particle burns. The ignition process can be seen in figure 1.2

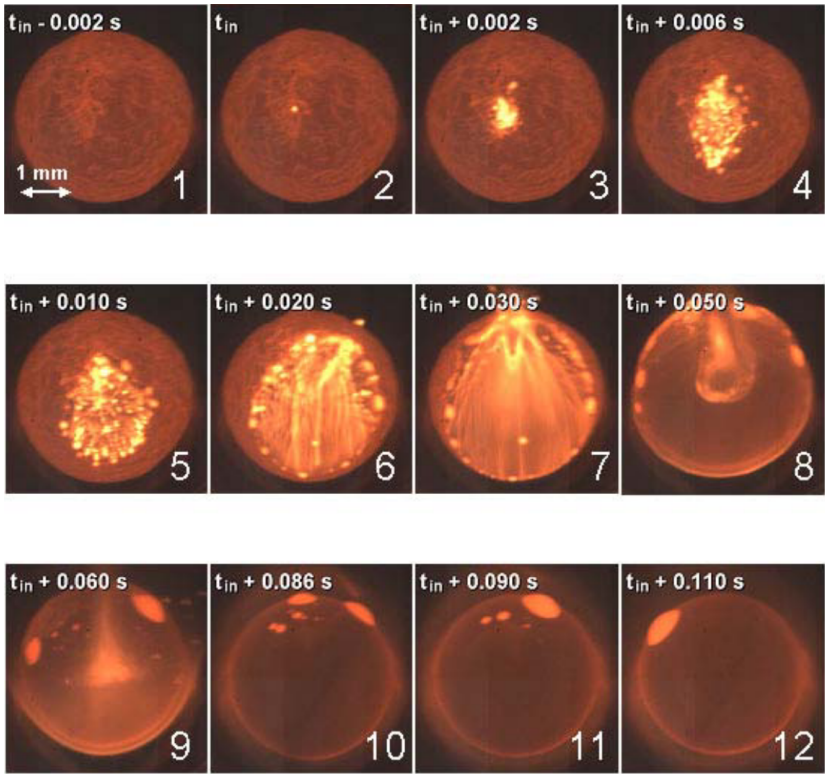

Figure 1.2 – Experimental images capturing the ignition process of an aluminum particle using a CO_2 laser. Figure extracted from [96].

The ignition process observed in figure 1.2 is obtained by heating up a levitating aluminum particle using a CO_2 laser. The particle has a diameter of approximately 3 mm which is much bigger than the micrometric particles considered in the current work. By having a greater mass, the particle takes longer to heat up and the ignition is therefore slower. Using this technique allows to better capture this ignition process that is similar to the ignition of a micrometric particle.

On the first frame, a rough surface can be observed, this is the external layer composed of alumina (Al_2O_3). This external layer prevents any chemical reactions between

the aluminum and the oxidizer in the air. Once the temperature of the particle reaches 933 K, the fusion temperature of aluminum, the aluminum core starts melting but cannot react yet because it is still trapped within the alumina layer. The fusion temperature of alumina is 2350 K, but the ignition occurs at lower temperatures. Indeed, as the aluminum core melts, its volume increases by 6.26 % [105, 110], exerting pressure on the external layer. The external layer will start to break under this pressure which can be seen on the frames 2 to 7. As the core get exposed, the chemical surface reactions start and are visible as a light emission, increasing even more the particle temperature. As the particle reaches 2350 K, the external layer melts and forms droplets on the particle surface. The formed droplets then accumulate into a lobe and the particle is now a burning aluminum particles. This last process of the ignition phase is visible on the frames 8 to 12.

Once the particle has ignited, it is formed by a an aluminum core and an alumina lobe. Since the diameter of the particle is here around 3 mm, there is no surface reactions during the combustion process (see part 3.4). Therefore the particle keeps evaporating gaseous aluminum that burns with the gaseous oxidiser. This is very similar to what happens for classical hydrocarbons droplet and can be seen in figure 1.3.

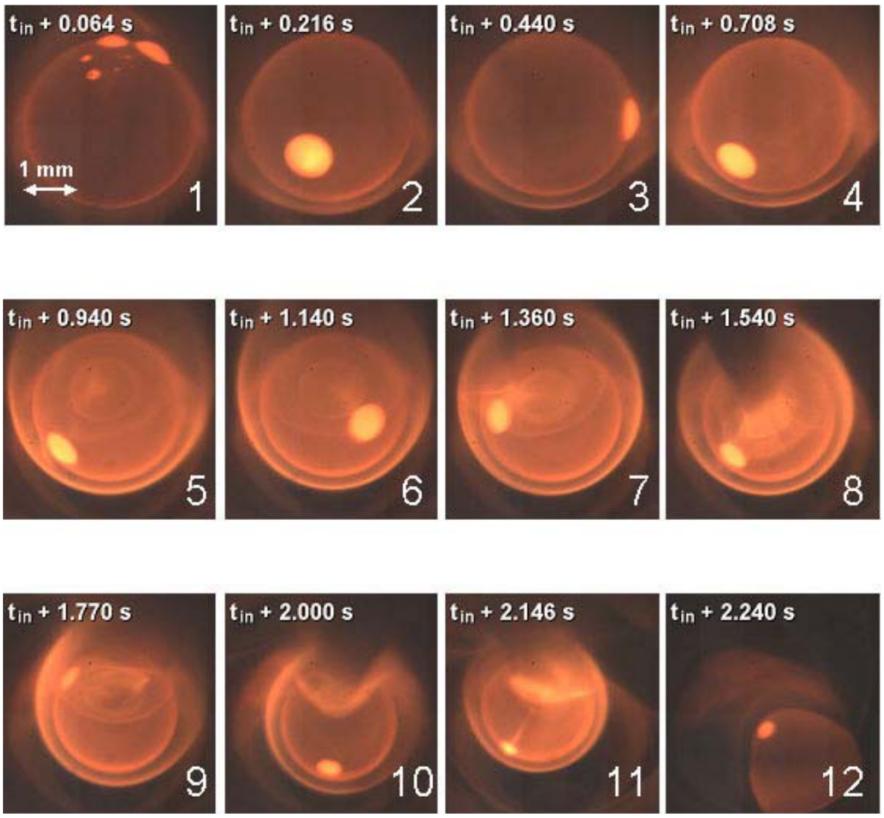

Figure 1.3 – Experimental images capturing the burning process of an aluminum particle. Figure extracted from [96].

The presence of a lobe on the particle surface limits the evaporation rate and therefore reduces combustion speed.

This experimental work gives a great insight on how an aluminum particle is ignited

and burns. As previously explained, another major key reason for studying experimental combustion of isolated aluminum particles is to obtain a burning time. This allows to later fit a burning-rate law. Many authors have done this type of work and a good compilation of the results for particles with diameters ranging from 10 to 1000 μm was proposed by Beckstead et. al [9] in figure 1.4.

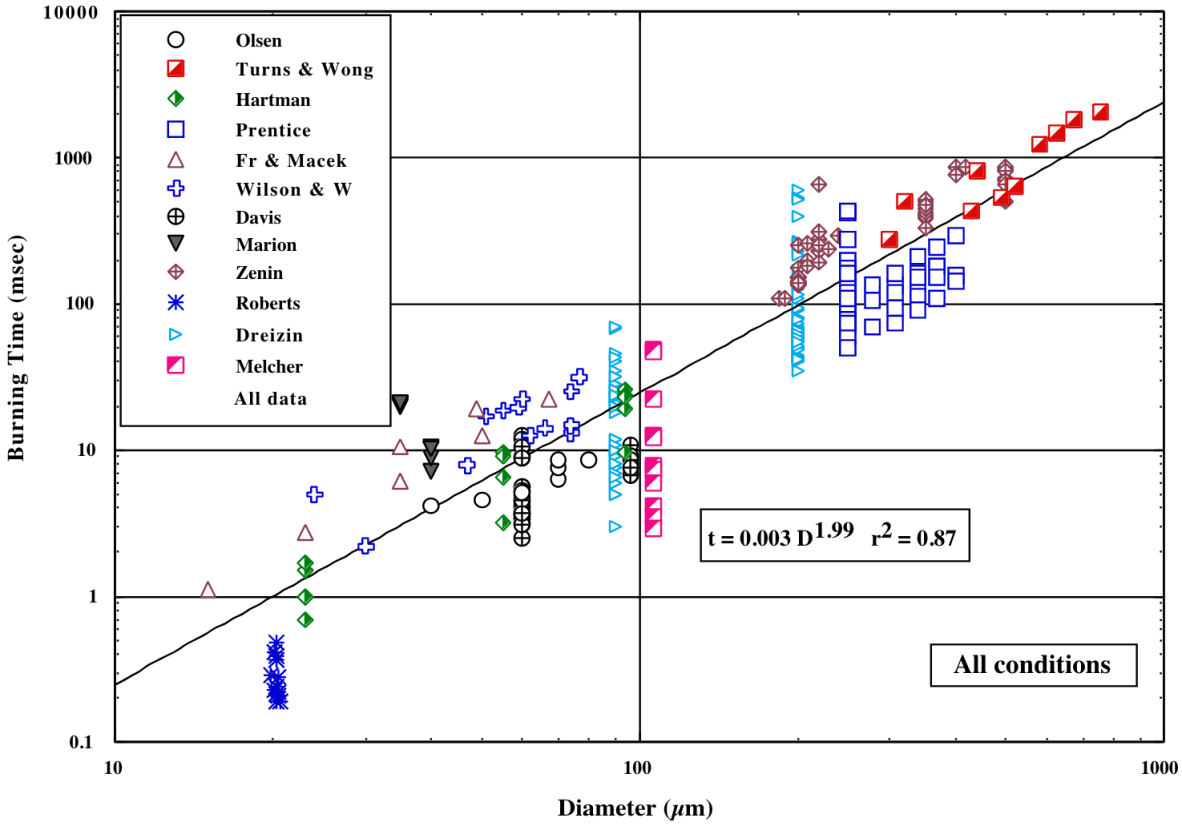

Figure 1.4 – Aluminum burning time measurements from different sources, measured under a wide variety of conditions and test techniques. Figure extracted from [9].

In figure 1.4, it can be observed that the combustion of an aluminum particle follows a modified "d^2" law. The results shown in this figure are for particles with diameter ranging from 10 to 1000 μm. As the particle diameter is reaching a diameter in the range of 1 to 10 μm, the combustion time follow a "$d^{1.8}$" [105].

One of the major interest of retrieving these experimental burning times is to establish an empirical law to be able to predict the burning time as a function of different conditions. Aluminum combustion has historically mainly been used in the arms and space industry in solid propellants. Therefore, these conditions can include pressure, temperature, mass fractions of O_2, H_2O and CO_2 and of course the initial diameter of the particle. Several correlations have been developed through the years, let us give some notable examples. In the same report [9] from which the fig. 1.4 is extracted, Beckstead proposed the following correlation :

$$t_c = \frac{a d_p^n}{\left(X_{O_2} + 0,6X_{H_2O} + 0,22X_{CO_2}\right) P^{0,1} T_0^{0,2}} \tag{1.1}$$

With $a = 0.0244$ for $n = 1.5$ and $a = 0.00735$ for $n = 1.8$. X_{O_2}, X_{H_2O} and X_{CO_2} are the molar fraction for O_2, H_2O and CO_2 respectively. T_0 is the ambient temperature.

One of the most commonly used formula is the one proposed by Brooks et al. [20] :

$$t_c = \frac{a d_p^2}{X_{O_2} + 0,533X_{H_2O} + 0,135X_{CO_2}} \tag{1.2}$$

This model presents a "d^2 law" because it is mostly used for micrometric particles. As the initial particle diameter is getting smaller, the surface reactions (see part 3.4) start playing a major role in the combustion process and the "d^2 law" is no longer valid.

More recently, Braconnier [18] proposed another formulation for the burning time. Indeed, after 428 experimental measurements for different atmospheres:

$$t_c = \frac{a d_p^n}{X_{eff}\, P^{\alpha}} \tag{1.3}$$

with :

$$X_{eff} = \sum e_i X_i = X_{O_2} + 0.2052X_{CO_2} - 0.032X_{N_2} + 0.028X_{CO} \tag{1.4}$$

This model does not account for the ambient temperature and H_2O molar fraction. But it can offer better predictions of the burning time than the one proposed in Eq. (1.1).

Let us analyse further the experimental work from which this last correlation is extracted. This is because the experimental setup used is state of the art regarding experimental combustion of isolated aluminum particles, allowing for the capture of interesting phenomena. This work highlights the importance of the lobe of alumina on the evaporation and therefore the combustion process. Braconnier et al. [19] experimentally studied the self-sustained combustion of 30-120 μm Al particles using an electrostatic levitation system under ambient pressure ranging from 1-31 bar. The particle is ignited using a CO_2 laser beam and its optical signature is recorded using filtered photomultipliers and a high-speed camera. This allows to not only estimate burning time but also the evolution of combustion parameters such as droplet and flame diameters. The schematic representation of the experimental setup is given in figure 1.5.

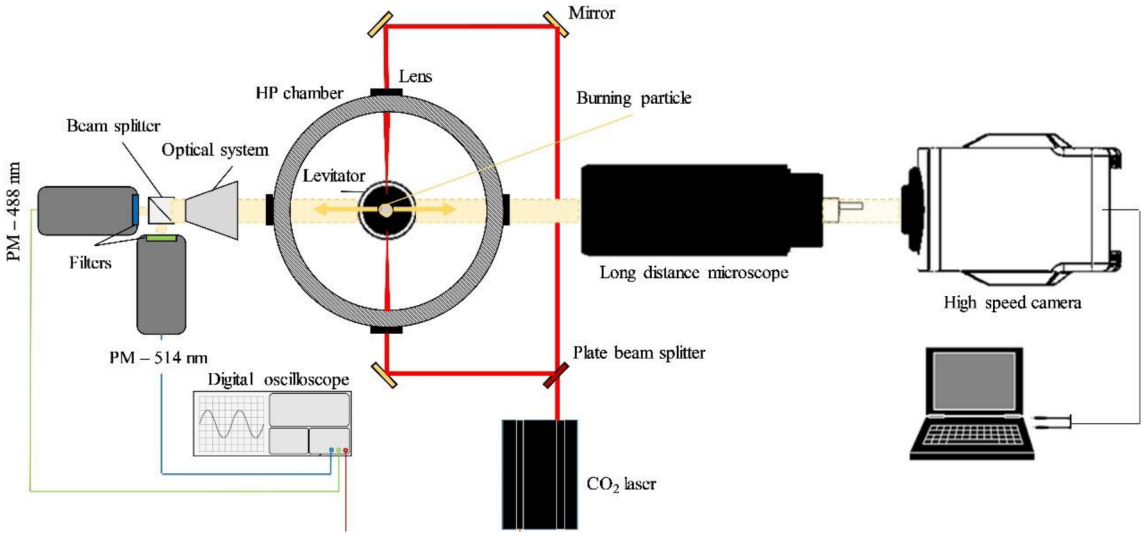

Figure 1.5 – Schematic representation of the experimental setup used by Braconnier et al. [19]. Figure extracted from [19].

The authors captured a phenomenon that highlights the role played by the presence of the lobe on the particle surface, the dissymmetry of the flame surrounding the particle. This is visible in figure 1.6 and is described below.

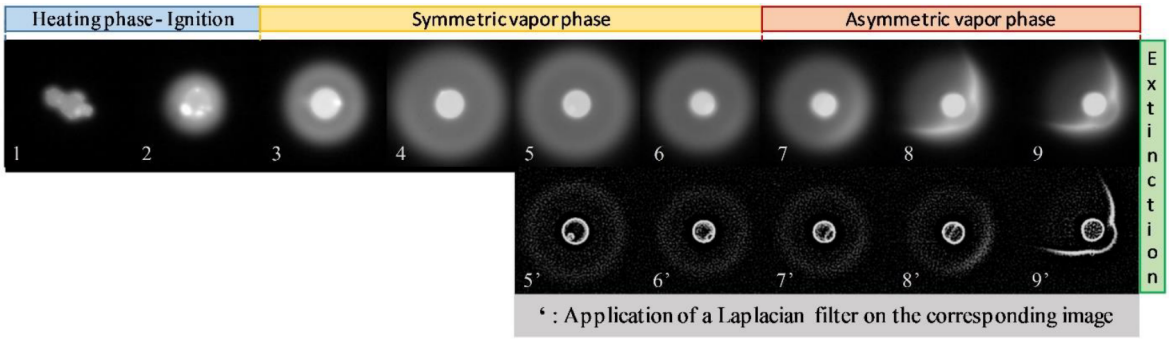

Figure 1.6 – Characteristic combustion sequence of an aluminum particle in air with an initial diameter of 93 μm at 1 bar. Figure extracted from [19].

First, on the frames 1 and 2, the ignition phase is visible with the rupture of the alumina layer into several oxide caps (or lobes) visible on the particle surface. Once this phase is over and the caps have agglomerated into one, a symmetric combustion phase is visible on the frames 3 to 6. During this phase a diffusion flame develops around the particle. This flame grows until it reaches an equilibrium position and becomes totally spherical. But this phase is going to end with the growth of the alumina cap.

This alumina cap can be studied using a contour detection and the application of a Laplacian filter, the result is visible on the frames 5' to 9'. On these frames, the growth of the alumina cap is clearly visible. By covering an increasing part of the aluminum particle, it stops the evaporation process from the surface. The aluminum evaporation rate becomes unsymmetrical and so does the combustion intensity around the particle. Therefore, the combustion enters an asymmetric vapour phase that can be seen on the

frame 7 to 9. This highlights the important role played by the lobe on evaporation and combustion speed.

The growth of the alumina cap for particles in this diameter range has been described in more details in the PhD work of Braconnier [18]. Using the same setup previously detailed here and used in [19], the authors captured the migration of the combustion products from the flame to the alumina cap of the particle. This is visible in figure 1.7.

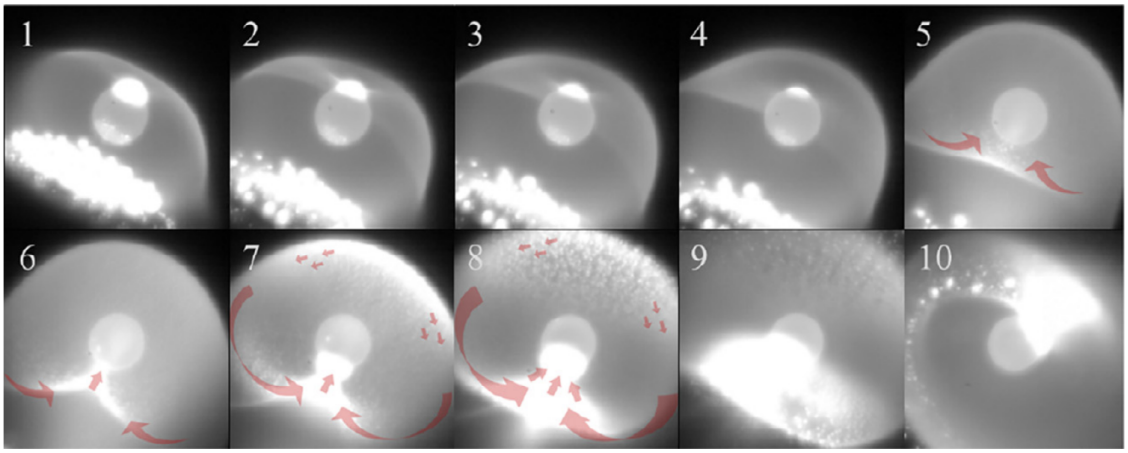

Figure 1.7 – Sequence of a $d_{Al} = 95\mu m$ burning in a 40 $\%CO_2/60\%O_2$ mixture at p=1 atm. Figure extracted from [18, 40].

The combustion products of the gaseous reactions condensate into liquid alumina (Al_2O_3, the same molecule that constitutes the cap on the particle. In figure 1.7, both these combustion products and the alumina cap are visible in white. On the frames 1 to 4, the alumina condensates in the flame zone where they remain. On the frames 5 to 10, the particle spins and as the alumina cap faces the alumina cloud, part of the combustion products is absorbed by he alumina cap. The movement of the alumina cloud toward the particle is indicated by red arrows and is partially responsible for the growth of the alumina cap.

The experimental results presented in this parts gave a first picture of how an isolated aluminum particle burns. The involved phenomena are complex, thus, the use of numerical simulation can help understanding them.

1.1.2 Numerical simulations of an an isolated burning aluminum particle

Another important tool to study the combustion of an isolated aluminum particle is numerical simulation. The aim of studies presented here is to have a detailed modelization of general properties and behaviour around a unique particle. It differs from what has been done in the current work by focusing on having a far better discretization of the domain around the particle. This type of mesh is illustrated for example in figure 1.8.

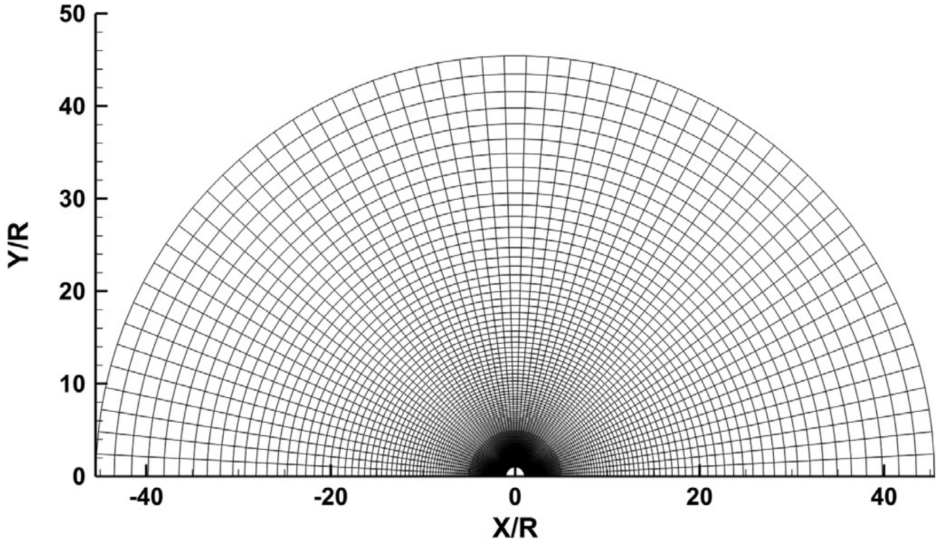

Figure 1.8 – Example of a mesh used by Gallier et al. [41] for the simulation of the combustion of an isolated aluminum particle. Figure extracted from [41].

The reason for introducing here such models is twofold, first to further familiarise the reader to some aspects of aluminum combustion without diving too deep into the details (see chapter 3 for more details). And secondly to introduce some of the models developed for simpler cases reused and adapted in the current work.

One of the first use of such simulation is the work proposed by Beckstead et al. [8]. In this paper, a two-dimensional, unsteady-state, kinetic-diffusion-vaporisation-controlled numerical model for aluminum-particle combustion was presented. The classical conservation equations similar to the simulation of any hydrocarbons droplets were solved. The main specificities of aluminum combustion were also added to the model, mainly, the addition of surface reactions, condensation) and the presence of the lobe on the particle. This is one of the first numerical model accounting for many of these specificities and a schematic of these specificities is given in figure 1.9.

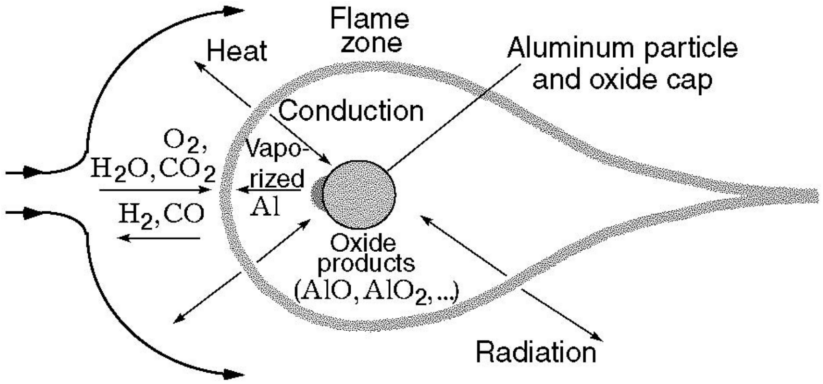

Figure 1.9 – Conceptual schematic of the combustion environment surrounding an aluminum particle. Figure extracted from [8].

In figure 1.9, a burning aluminum particle is schematised. The phenomena at play during this combustion such as vaporisation, conduction or radiation are accounted for.

The presence of the lobe is also illustrated while a gaseous flame is present around the particle. The fine mesh discretization allows to have a complete knowledge of the temperature field around the particle, while accounting for these phenomena. The obtained temperature field is illustrated in figure 1.10.

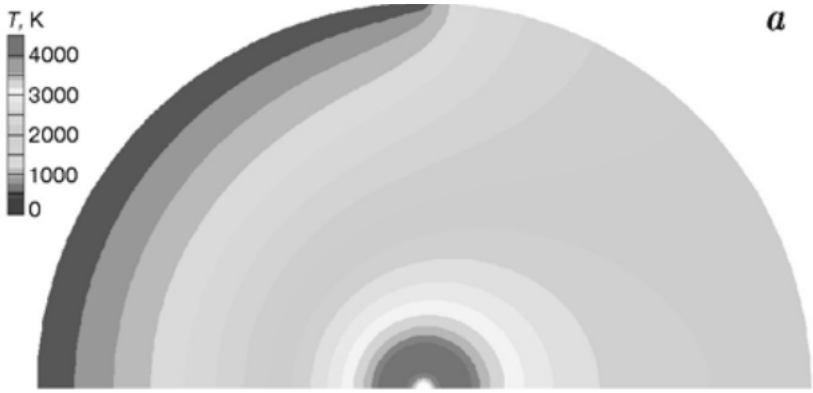

Figure 1.10 – Two-dimensional temperature distribution for aluminum particle (230 μm in diameter) combustion in 79 % Ar +21 % O_2 at $T = 300$ K and $p = 1$ atm. Figure extracted from [8].

In figure 1.10, the temperature field presents a deformation that is induced by some key characteristics of the combustion of isolated aluminum particles. Indeed, according to the authors, the low temperature on the left side of the figure is due to convection, which makes the gases flow from left to right, and the alumina cap, which accumulates on the left side. This is a good demonstration of the impact that the presence of the alumina cap has on the flow around the particle, and more specifically the evaporation and therefore the combustion rate. This is why we have chosen in the current work to implement a sub model to account for the effect of the alumina cap on the evaporation rate.

Having such a detailed mesh also allows the study of the air flow around the particle as illustrated in figure 1.11. This would be impossible in the current work because it requires a full discretization of the gaseous domain.

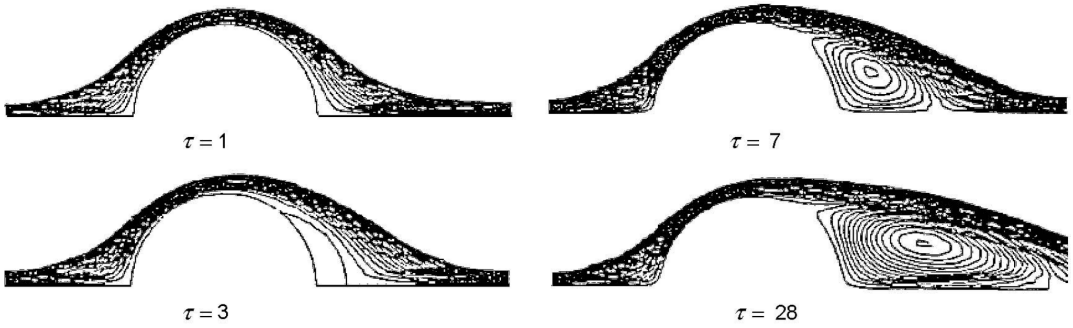

Figure 1.11 – Turbulent wake lengths and profiles for Re=177(streamlines for different times).Figure extracted from [8].

The results shown in figure 1.11 are, according to the authors, very reasonable, and the final length of the turbulent wake is in good agreement with available experimental

data from [67].

Another interesting work using the numerical simulation of a single aluminum particle is the one later published by Glorian et al. [47]. During his PhD thesis, the Glorian focused on the importance of surface reactions for aluminum combustion. An extensive solver, accounting for 49 surface reactions and advanced physical aspects such as surface site availability was developed.

By comparing the physics of aluminum combustion with and without surface reactions, the authors highlighted the importance of these reactions. This experiment would be almost impossible to do without numerical simulation simply because the surface reactions cannot be cut off and on in a real-life setup. The results of this comparison can be observed in figure 1.12.

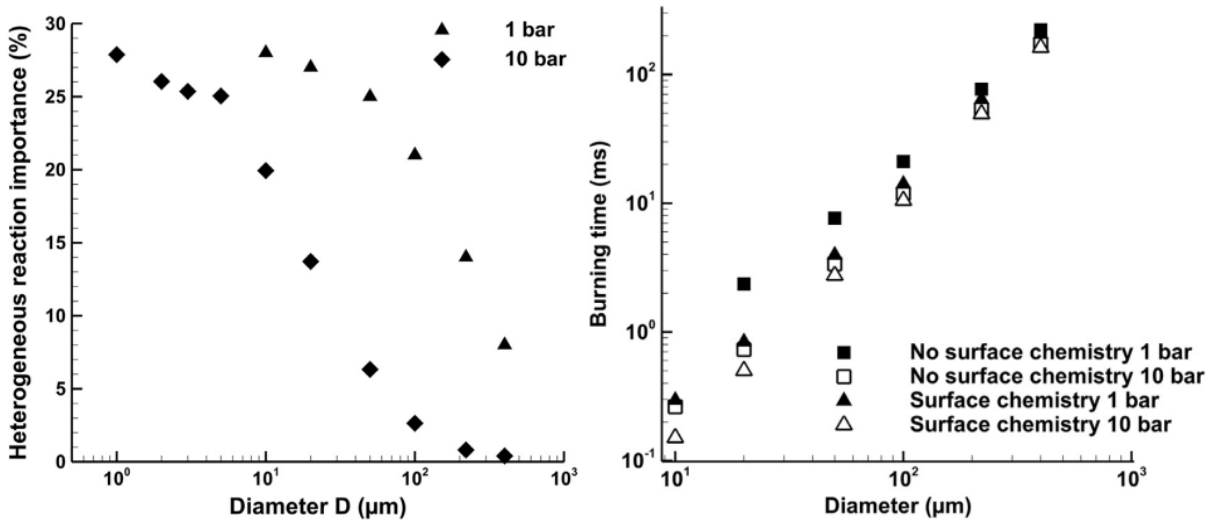

(a) (b)

Figure 1.12 – (a) Relative proportion H of aluminum consumed by heterogeneous reactions (O_2/Ar (21/79), 1 and 10 bar and 300 K). (b) Computed burning times (O_2/Ar (21/79), 1 and 10 bar and 300 K), with and without surface chemistry. Figures extracted from [47].

In figure 1.12a, the heterogeneous reactions importance is plotted for different particle diameters. The importance of these reactions increases as the particle diameter decreases, which is in adequacy with the literature. In the current work, the initial particle diameter will mostly be in the 1 to 10 μm range. The importance of the surface reactions for a particle of 10 μm in diameter is around 28 % of the total oxidation. Which means that in the current work, the surface reactions should account for at least 28 %, if not more as smaller particles are considered.

This work also highlights another really important impact that surface reactions have on combustion. In figure 1.12b, the impact of these reactions increases as the particle diameter decreases. Let us consider the value for particles with a 20 μm diameter given in both figure 1.12a and 1.12b. If the heterogeneous reactions importance is around 28 %,

the combustion time is shortened from 2.5 ms to 0.8 ms, which is a decrease in combustion time of 68 %. This is due to the fact that the energy liberated by the surface reactions will directly heat the particle itself, thus greatly increasing the evaporation rate and the gaseous aluminum available for gaseous reactions. Therefore, by both accounting for near to a third of oxidation for aluminum and reducing by 68 % the combustion time, surface reactions are of high importance. Both these aspects are far from negligible and underline the importance of implementing surface reactions in the current work.

During the work of Gallier et al. [41], the precision of the modelization of the alumina cap was pushed further. The model for predicting the morphology of the alumina cap is reused in the current work and detailed in part 3.2.3. By predicting the shape of the alumina cap, the authors were able to study the behaviour of condensed alumina products migrating to the particle. This work included phoretic motions of the alumina smoke created by the gaseous reactions. The impacts of both thermophoresis and diffusophoresis on the percentage of alumina smoke returning on the particle were tested for different alumina cap sizes.

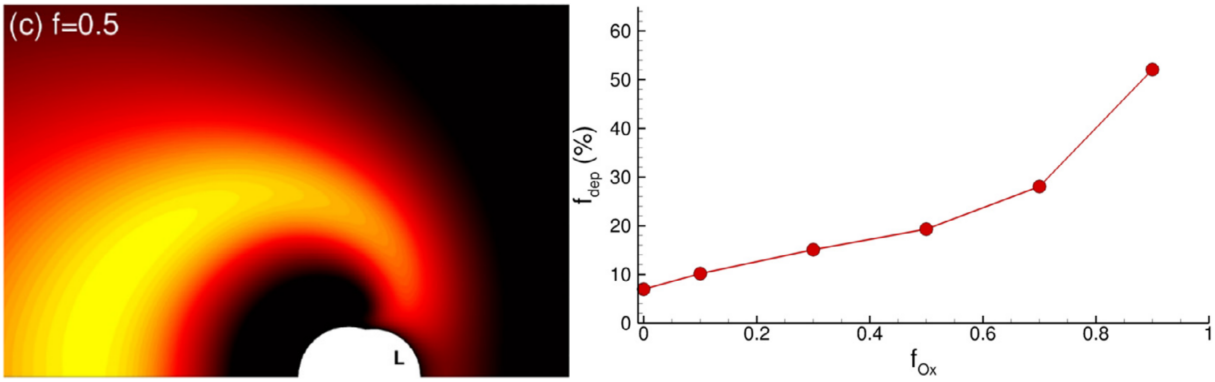

(a) (b)

Figure 1.13 – (a) Oxide smoke mass fraction Y_{ox} for a 70μm aluminum particle with an oxide mass fraction $f = 0.5$. The lobe is indicated by "L" [41]. (b) Fraction f_{dep} of produced alumina deposited on the lobe and particle as a function of lobe size f_{Ox}. Figures extracted from [41].

In figure 6.3a, the spatial distribution of the alumina mass fraction around the particle is plotted. The presence of the alumina cap has a clear impact on this field. Indeed, by stopping evaporation from the surface of the aluminum core it occupies, it deforms the surrounding gaseous flame to bring it closer to the alumina cap. This closeness to the particle makes it easier for the alumina smoke to migrate to the particle.

Furthermore, the evaporation flow of aluminum from the particle to the flame can prevent this migration of alumina smoke to the particle. Since there is no evaporation flow above the alumina cap and the oxide smoke forms closer to the particle surface, the migration of the condensates to the particle is more important for particles with a bigger alumina cap. This results is visible in figure 6.3b.

Finally, the work recently published by Finke et al. [36] is also of high interest in the frame of the current work. It is not a numerical simulation of an isolated aluminum particle but it has been chosen to present it here nonetheless. This is because just like the works previously presented in this section, it shows the potential of using a smaller computational domain to study the impact of the phenomena involved using more advanced models. In their work, the authors combined balance laws for mass and enthalpy with a population balance approach in order to describe the size-resolved condensation of alumina smoke during aluminum combustion above a reactive aluminum surface [36]. The solver was used in the context of a perfectly stirred reactor (PSR) and, subsequently, a partially stirred reactor (PaSR). This was done in a single finite volume cell of a laminar flow simulation.

The model presented here has been reused in the current work and is therefore presented in more details in part 3.5.3. The authors obtained a prediction of the size of the combustion products as well as the characteristic timescales of all the processes involved in the formation of liquid combustion products that are in figure 1.14.

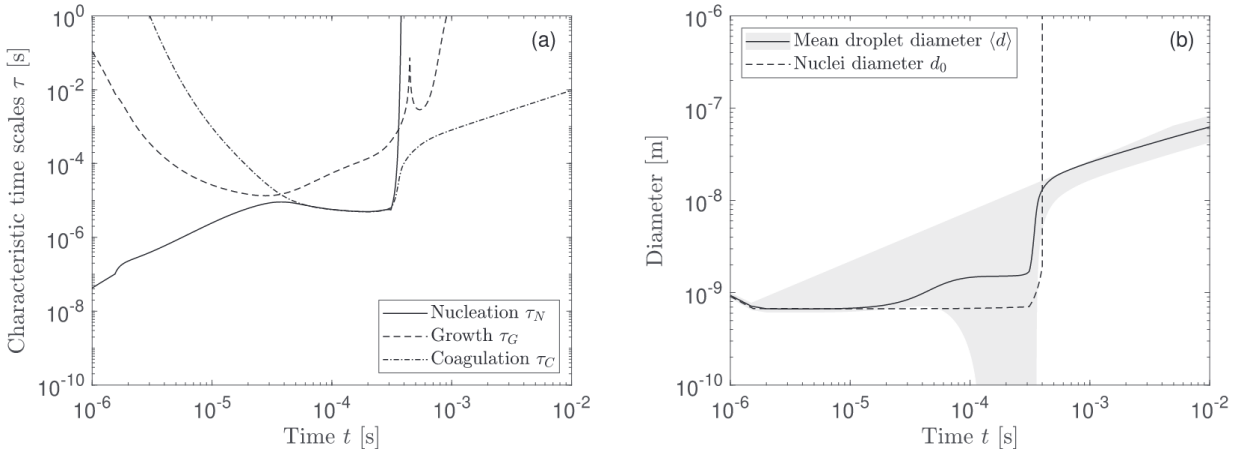

Figure 1.14 – (a) Temporal evolution of the characteristic time scales controlling droplet nucleation, growth and coagulation in a PSR without NOx formation. (b) Time course of the critical nuclei size (dashed line) and the mean droplet diameter (solid line). The shaded area indicates plus/minus one standard deviation from the mean droplet diameter. Figures extracted from [36].

In their analysis of the characteristics time scales available in figure 1.14a, the authors gave great insights regarding the competition of nucleation, growth and coagulation with one another. The process with the smallest time scale is dominant. Until 2×10^{-5} s, nucleation first dominates the global condensation process. As supersaturation increases, the size of the nuclei created by this nucleation process decreases until said nuclei consist of one $Al_2O_3(l)$ molecule. Past that time, growth, meaning the condensation of alumina on the previously created nuclei, and coagulation start having similar time scales. Both these processes will increase the size of the existing particles. Finally, as the combustion is becoming weaker, the available alumina for nucleation in the gas becomes scarce and therefore the growth process becomes weaker and the coagulation is now the dominant process.

The domination of one process over the others directly impacts the diameter of the condensed alumina droplets, as visible in figure 1.14b. The mean diameter of the droplets

is first the same as the one of the nuclei because the characteristic time scale of nucleation is much lower than the others. As growth and coagulation characteristic time scales become comparable to the one of nucleation, these two phenomena are taking a more important role and the mean droplet diameter starts growing past 2×10^{-5} s. Past 4×10^{-4} s, almost no nuclei are created anymore while the existing particles keep growing mainly through coagulation, increasing the mean droplet diameter even further.

The works presented in this section highlight the importance of numerical simulation in studying the combustion of an isolated aluminum particle. Moreover, the models presented were developed and used for simpler cases. One of the main specificities of the current work is to reuse and adapt some of these models for the simulation of more complex configurations, such as 2D dust flames.

Indeed, the model to predict the shape of alumina cap presented in the work of Gallier et al. [41] is reused in the current work (see part 3.2.3). The nucleation, condensation and coagulation models developed by Finke et al. [36] for 0D reactors are reused in the current work (see part 3.5). Finally, if a far simpler model was used in the current work to account for surface reactions, having the results published by Glorian et al. [47] using a multi surface reactions scheme to compare against is of high interest.

1.2 Aluminum dust flames

In the previous section, the presentation of both experimental and numerical studies regarding burning isolated aluminum particles have highlighted some very important characteristics of aluminum combustion. In this section, the aim is to further study aluminum combustion in more complex configurations.

1.2.1 Experimental studies of aluminum dust flames

It is rather difficult to experimentally study aluminum dust flames, thus, not that many studies of these flames have been performed. However, some very interesting works have nonetheless been recently published. In this section, examples of these experimental studies are presented and used to highlight key characteristics of aluminum dust flames.

An interesting way of experimentally studying the key characteristics of aluminum dust flames without having to stabilise said flames, is using a tube in which aluminum particles are resuspended before ignition. One example of such work is the one proposed by Bocanegra et al. [16].

The experimental protocol used in the combustion tube is schematised in figure 1.15.

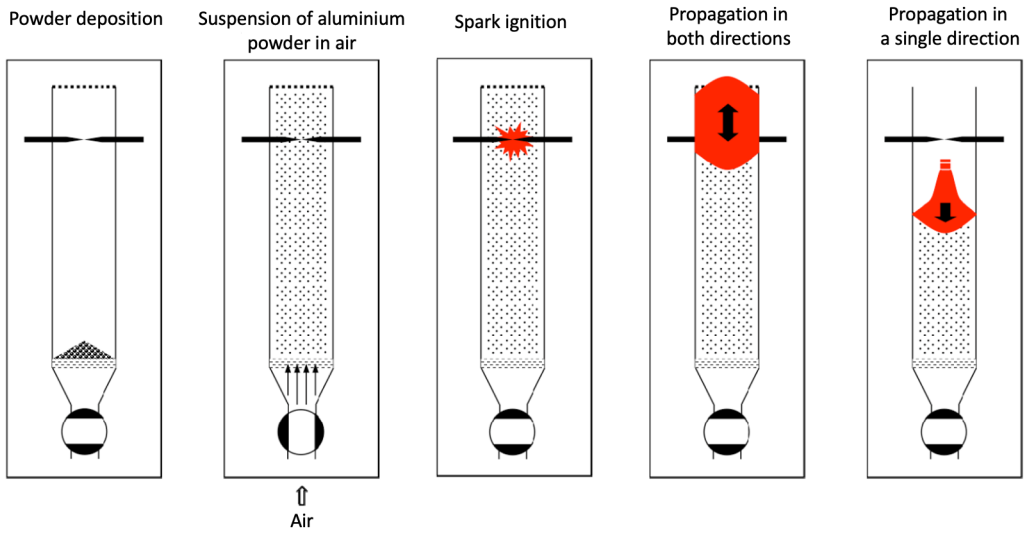

Figure 1.15 – Scheme of the experimental protocol used by Bocanegra et al. [16] in a combustion tube. Figure extracted from [16].

The experimental protocol schematised in figure 1.15 allows for the experimental measurement of flame properties such as flame speed and flame temperature without having to stabilise an aluminum flame.

The experimental setup was used to burn both nanometric and micrometric aluminum particles in several configurations. Using micrometric aluminum powder with an initial diameter of 4.8 ± 1.3 μm at an equivalence ratio of $\Phi = 2$, the maximum flame temperature measured was 3300 ± 100K.

Another important result is the measure of the flame speed which was compared by the authors with previous similar works in figure 1.16.

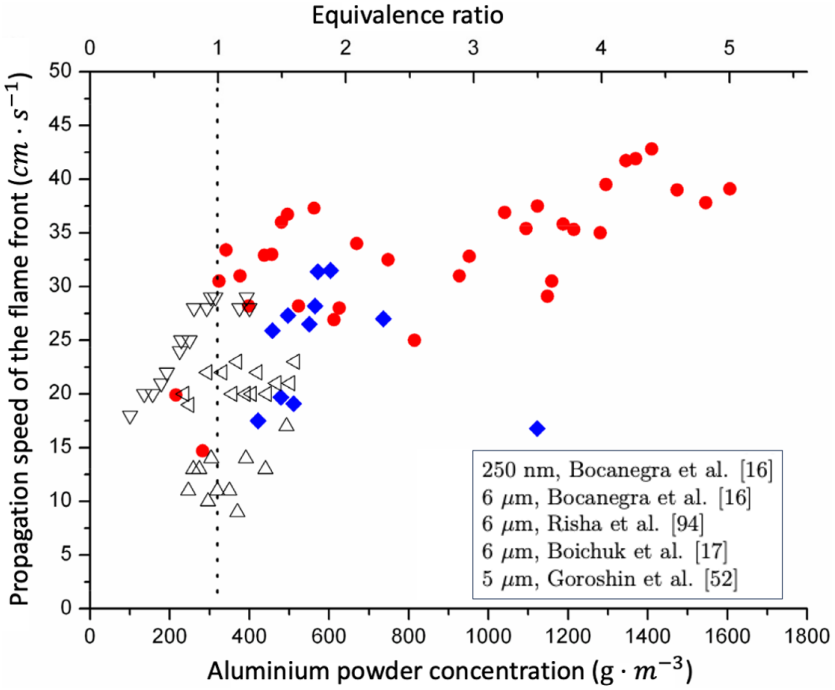

Figure 1.16 – aluminum flame speed obtained experimentally. Figure extracted from Bocanegra et al. [16].

Considering the results in figure 1.16, there is a wide range of values for experimentally measured flame speed. For 6 μm aluminum particles, the flame speed measured by Bocanegra et al. [16] ranges from 17.5 $\mathrm{cm} \cdot \mathrm{s}^{-1}$ at $\Phi = 1.3$ to 32 $\mathrm{cm} \cdot \mathrm{s}^{-1}$ at $\Phi = 1.9$.

Finally, the solid combustion products were also retrieved and analysed. The smaller spherules can be observed in figure 1.17.

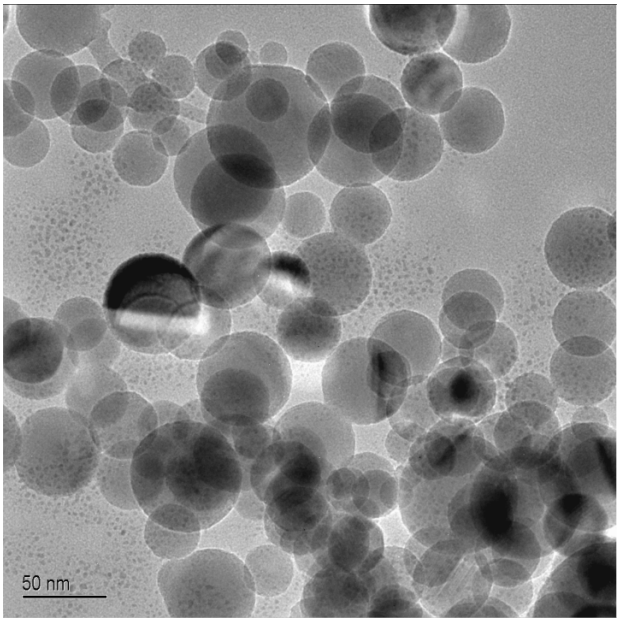

Figure 1.17 – Detailed visualisation of small residuals from the combustion of micrometric aluminum particles. Figure extracted from Bocanegra et al. [16].

The combustion residuals visible in figure 1.17 have an average diameter of 94 μm which is an interesting result within the framework of the current work. Indeed, the model implemented in the current work can predict the size of the combustion products, which can be compared against such experimental results.

Stabilised aluminum dust flames, although difficult to obtain, are useful configurations to study dust flame. Two interesting works that will be later numerically replicated in the current work are the experiments of Lomba et al. [81] and Goroshin et al. [52].

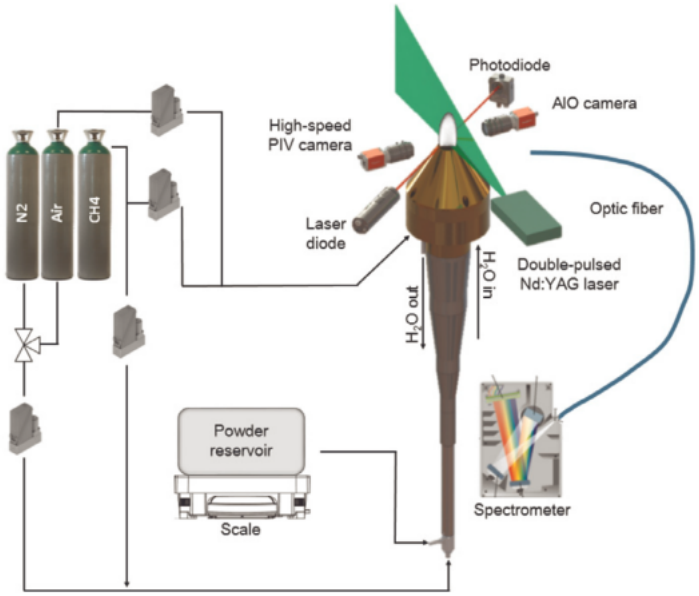

Figure 1.18 – Schematic of the experimental setup proposed by Lomba et al. [81]. Figure extracted from [81].

The experimental setup proposed by Lomba et al. [81] is schematised in figure 1.18. The used aluminum powder has a Sauter mean diameter of 7.1 μm and is stored in a stirred powder reservoir placed on a scale and connected to one end of an ejector nozzle. A depressurisation is created by an air flow supplied to the other end of the ejector nozzle, which creates a suction flow of aluminum particles and atmospheric air, dispersing the powder into the main body of the burner. An annular injector with a thickness of 1.5 mm is used to create a small methane flame responsible for ignition and flame stabilisation. A spectrometer, a tomography setup, a camera and filter set are used to characterise the flame and visualise flame emissions. Finally, using the aluminum particles themselves as trackers, the aerosol flow at the burner exit is characterised by a particle image velocity (PIV). Using this setup, an aluminum-air flame was stabilised and is visible in figure 1.19.

(a) Tomography image of an aluminum-air flame.

(b) Tomography image with lower laser power.

(c) Mean image of the AlO emissions of an aluminum-air flame.

Figure 1.19 – Different visualisation methods for aluminum-air =1.22 flames. Figure extracted from Lomba et al. [81].

This aluminum-air flame was studied for several values of equivalence ratios ranging from $\Phi = 0.99$ to 1.22. Furthermore, an aluminum flame with the addition of hydrocarbons in the main aluminum-air flow has also been studied. All these flames have been stabilised using an annular methane-air pilot flame with a thickness of 1.5 mm. However, this methane-air flame has only a minor impact on the flow with a heat release lower than 3 % of the heat released by the aluminum flame itself [82]. Moreover, the volume flow of this methane-air flame is of only 0.6 l/min versus 53.9 l/min for the aluminum-air main flame.

The authors obtained an average flame temperature of 3146 ± 180K and a flame speed of 28.24 cm/s. This is an interesting experimental work because stabilising an aluminum-air flame for these equivalence ratios without a strong co-flow is not an easy task.

In the current work, a scaled down version of this flame is computed using the implemented model. Therefore more details on this experimental work is given in part 6.1.

Goroshin et al. [52] also proposed a 2D experimental aluminum flame. In their work, a laminar flame was stabilized and self-sustained without any hydrocarbon pilot flame. The aluminum-air flame is premixed at an equivalence ratio of $\Phi = 1.6$ and is injected at a speed of 0.5 m/s. A strong air co-flow was used to stabilize the flame at a similar speed of 0.5 m/s. Photographs of the obtained flames are available in figure 1.20.

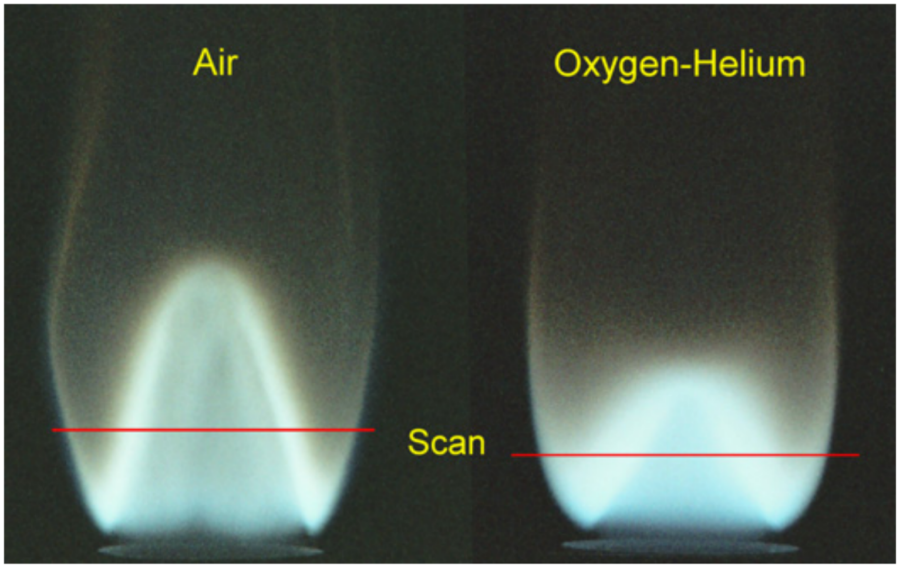

Figure 1.20 – Photographs of Bunsen flames in aluminum air and aluminum–oxygen–helium suspensions stabilised on burner. Figure extracted from Goroshin et al. [52].

The aluminum-air flame in the left part of figure 1.20 presents a "W" shape. This is because the central premixed flame is at an equivalence ratio of $\Phi = 1.6$. Thus, an excess of aluminum does not burn in the central flame but when entering in contact with the oxidiser provided by the strong co-flow, creating an outer flame front. The red line labelled "scan" represents the line where a spatially resolved flame spectra was performed. The measured flame temperature across the flame cone ranges from 2892 to 3312 K. This flame has also been simulated in the current work and more discussions about this experimental work are available in part 6.2.

In this part, experimental dust flames have been rapidly presented. Several key-points have been highlighted. These flames are rather difficult to stabilise and require complex experimental setups. The phenomenology driving these flames is not fully understood, but each of these experimental works is important to improve the understanding of these capricious flames. Due to the difficulty of doing such work, the obtains values can spread over a wide range. This is the case for example for flame speed which can vary from around 10 to close to 40 cm/s for different experimental work. The experimentally obtained flame temperature can also vary but on a smaller order of magnitude. On average, the experimentally obtained flame temperature for aluminum is around 3200 K.

Similarly to the case of the combustion of an isolated aluminum particle, experimental works play a key-role for understanding aluminum combustion. To further understand these complex flames, numerical simulations can be very important and some examples are developed in the next section.

1.2.2 Numerical studies of aluminum dust flames

Numerical simulations of aluminum dust flames are complex to realise and have only recently appeared in the literature for three main reasons. First, as explained in more detail in chapter 3, aluminum combustion involves many phenomena, of which several are essential to stabilise a numerical aluminum dust flame. Furthermore, most of the sub-models necessary for each of these phenomena have been developed only recently and are rather difficult to properly validate. Second, due to a very fast chemistry and high temperature gradients, aluminum flames are numerically unstable. Finally, the use of a Lagrangian solver to track the high aluminum particle population drastically increases calculation cost.

However, by allowing for the study of each of the phenomena involved and their interaction with one another, the simulation of aluminum dust flame can greatly improve the understanding of such flames. Let us study some of these interesting numerical works.

Han et al. [54] proposed the simulation of a propagating aluminum flame in the domain presented in figure 1.21.

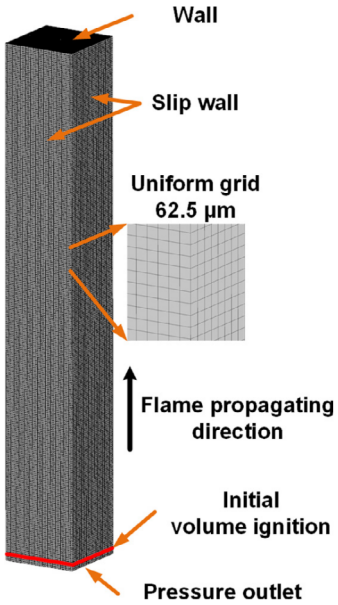

Figure 1.21 – Computational domain and boundary conditions for Al dust combustion. Figure extracted from Han et al. [54].

The numerical domain presented in figure 1.21 is a $2 \times 2 \times 18$ mm square duct. The aim of this simulation is to create an ideal planar flame for particles in the transition regime ranging from 1 to 20 μm. This work is one of the first to study this type of flame on a 3D domain while accounting for both surface reactions and gas-phase reactions. The importance of these surface reactions is highlighted. The burning velocity has values ranging from 11 to 33 m/s with a great sensibility to particle diameter. The obtained flame temperature is sensible to the equivalence ratio and ranges from 2750 K at $\Phi = 2.2$ to 3600 K at $\Phi = 1.0$. Finally, a study of the role of thermophoresis on particle speed was performed. Adding this phenomenon increased the particle residence time inside the

flame zone and resulted in a 13 % increase in burning velocity [54].

More recently, Zhang et al. [114] performed a simulation of the dust flame from Goroshin et al. [52] previously presented. The computational domain is schematised in figure 1.22.

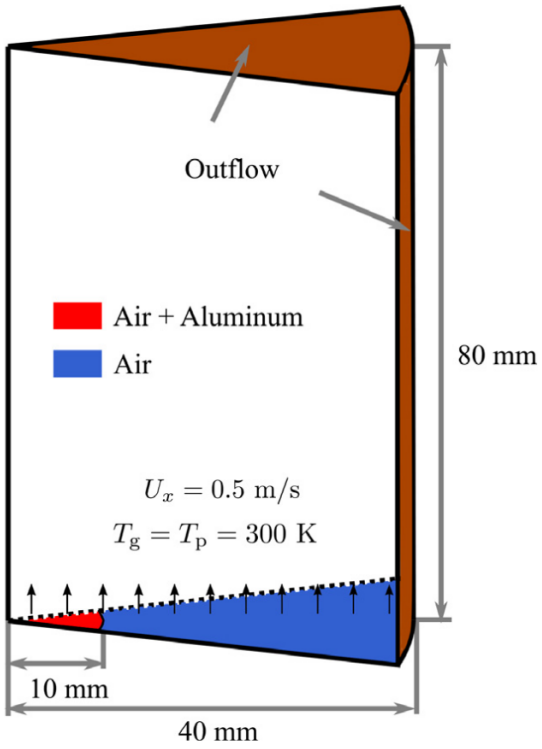

Figure 1.22 – Computational domain and boundary conditions for aluminum particle Bunsen flame. Figure extracted from zhang et al. [114].

To reduce computational cost, the domain is a wedge with an angle of 3° to represent a cylinder with a total radius of 40 mm and a length of 80 mm. This domain is discretized into 200 grid points in the radial direction and 400 grid points in the axial direction, resulting in a mesh resolution of 200 μm.

In this domain, a numerical model for aluminum cloud combustion which includes the effects of interphase heat transfer, phase change, heterogeneous surface reactions, homogeneous combustion, oxide cap growth and radiation within the Euler–Lagrange framework is proposed [114]. The obtained stabilised flame is plotted in figure 1.23.

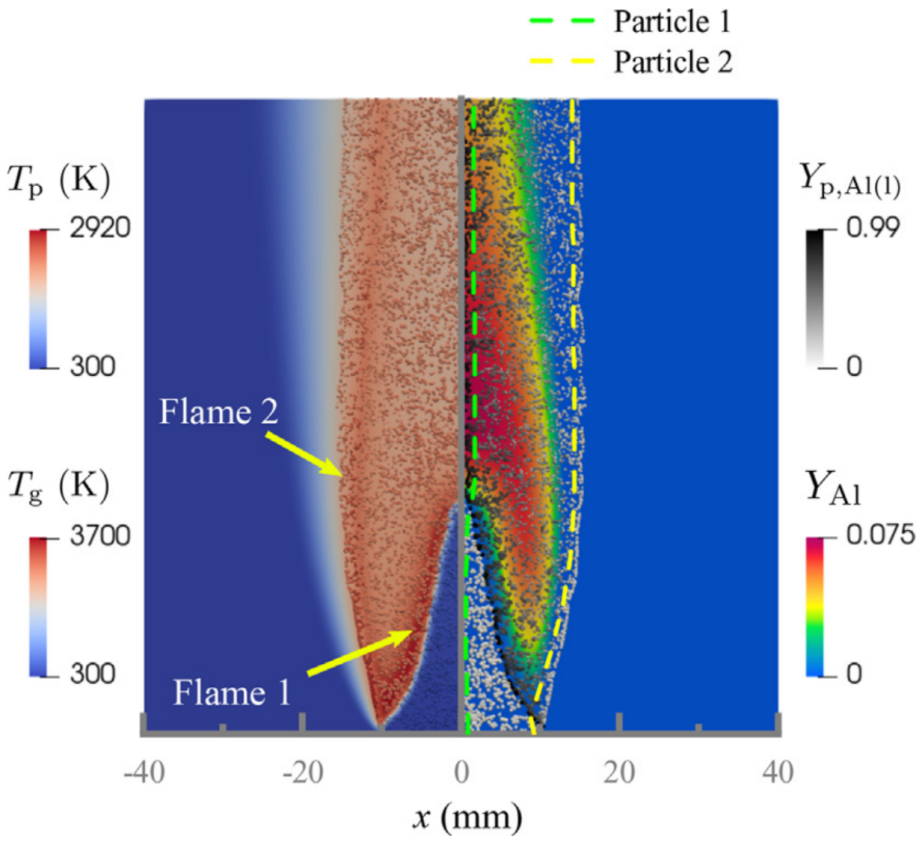

Figure 1.23 – Contour of average gas temperature T_g (left) and average mass fraction of aluminum Y_{Al} (right). Figure extracted from zhang et al. [114].

The "W" flame structure from the experimental work of Goroshin et al. [52] is well reproduced. Moreover, the predicted temperature distribution of the flame is consistent with the experimental measurements. This work is important because it is one of the first stabilising and reproducing correctly an aluminum dust flame with a model including all the sub-model previously mentioned.

Both recent works presented in this part show the possibility of correctly reproducing aluminum dust flame. Yet, this requires the implementation of several sub-models which have not been discussed here in great details. To correctly do so, a whole chapter is necessary which is the chapter 3 of the current work.

After having introduced the general properties of aluminum combustion and before diving into the details of the models used in the current work, an overview of the physical properties of the species must be provided.

1.3 Physical properties of aluminum and its oxides

The properties presented here are extracted from the PhD work of Suarez [105] and have been reused in the current work. Indeed, during his PhD, Suarez implemented in AVBP all the physical properties that necessary for aluminum combustion.

1.3.1 Physical properties of aluminum

Solid aluminum

In its solid state, aluminum has a density of 2701.5 $\mathrm{kg \cdot m^{-3}}$ [110]. Furthermore, aluminum presents a high conductivity of $\lambda = 237\ \mathrm{W \cdot m^{-1} \cdot K^{-1}}$

The physical properties used to predict the melting rate of aluminum are extremely important because they determine how much energy is absorbed by the particle before ignition. Which has a major influence on the ignition delay and therefore on flame properties. The fusion temperature is a function of pressure as indicated in table 1.1

Pressure (MPa)	Fusion temperature (K)
0,1	933
500	963
1000	993
2000	1053
3000	1103
4000	1153

Table 1.1 – Fusion temperature of solid aluminum as a function of pressure. Figure extracted from [105].

In the current work, the pressure will not fluctuate a lot, a fix fusion temperature of 933K is considered. Another important data to quantify the energy required for the melting of the particle is the fusion enthalpy which is taken as $\Delta H_{\mathrm{fusion,\ Al}} = 0.397\ \mathrm{J \cdot kg^{-1}}$ [105, 110].

Liquid aluminum

As aluminum melts, its volume increases by 6.26 %. The relation between temperature and density is available in table 1.2.

Temperature (K)	Density $\left(\mathrm{kg \cdot m^{-3}}\right)$
933	2368
973	2357
1023	2345
1073	2332
1123	2319
1173	2304

Table 1.2 – Density of liquid aluminum as a function of temperature at 1 bar. Figure extracted from [105]

As explained by Suarez in his PhD [105], the melting of aluminum will reduce conductivity to a value between 110 and 115 $\mathrm{W \cdot m^{-1} \cdot K^{-1}}$.

The surface tension of liquid aluminum has been studied by Leitner et al. [79] using electromagnetic levitation and the obtained results are presented in figure 1.24.

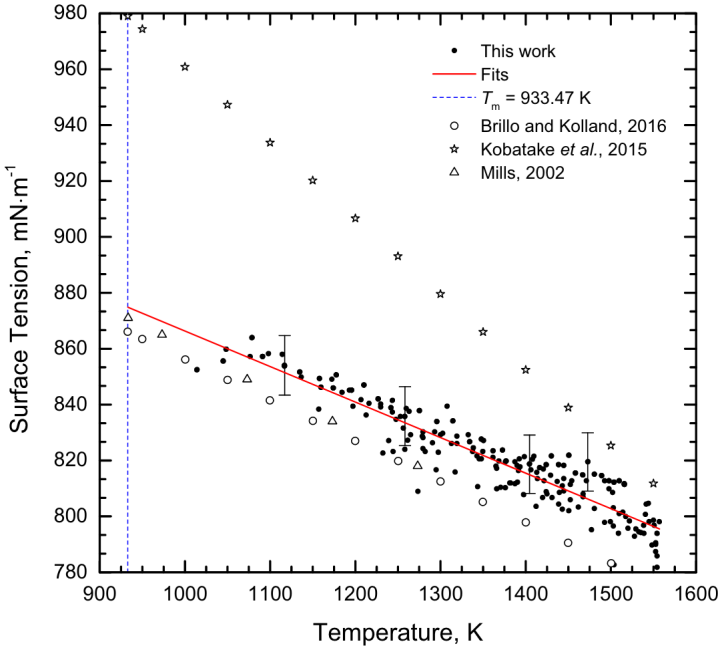

Figure 1.24 – Surface tension of aluminum as a function of temperature. Figure extracted from [79].

In the current work, a surface tension of 0.860 $\mathrm{N \cdot m^{-1}}$ has been selected for all temperatures.

Regarding liquid viscosity, the most commonly used formula in the the literature is the one proposed by Assael et al. [3] :

$$\log\left(\frac{\mu}{\mu^0}\right) = a + \frac{b}{T} \tag{1.5}$$

With $a = -0.7324$, $b = 803.49$ K and $\mu^0 = 1$ mPa $\cdot$ s

For evaporation, it is also very important to correctly determine the boiling point of liquid aluminum. To do so, the method proposed by Suarez in his PhD [105] has been reused. A Clausius-Clapeyron has been used with the reference values of $P_{\text{ref}} = 1$ bar and $T_{\text{ref}} ref = 2793\ K$ calculated by Honig et al. [57] :

$$ln\left(P_{\text{vap}}\right) = \ln\left(P_{\text{ref}}\right) - \frac{M_{Al}\Delta H_{vap,Al}}{R}\left(\frac{1}{T} - \frac{1}{T_{\text{ref}}}\right) \tag{1.6}$$

Moreover, correctly determining the required energy for evaporation is of great importance. The latent heat of vaporization has also been reused from the work of Suarez et al. [105] :

$$\Delta H_{vap,Al} = \Delta H_{vap,Al,ref} + \left(C_{Pl} - C_{Pg}\right)\left(T - T_{ref}\right) \tag{1.7}$$

With the reference values of $\Delta H_{\text{vap,Al,ref}} = 10,76\ \text{kJ} \cdot \text{g}^{-1}$ and $T_{\text{ref}} = 2767$ K taken from [110].

1.3.2 Physical properties of alumina

Alumina is a key species of aluminum combustion. First, in its liquid form, it is the final combustion product that will be tracked using a Lagrangian solver in the current work. Then, the formation of gaseous alumina and its condensation from gaseous to liquid state are both very exothermic phenomena in aluminum combustion.

Therefore, the physical properties of liquid alumina are of primary importance. These physical properties are the same used by Suarez in his PhD work [105]. The properties of the liquid phase of alumina have been obtained using aerodynamic levitation and are summarised in table 1.3 and equation Eq. (1.8)

Property	Value
Molar mass	$102\ \text{g} \cdot \text{mol}^{-1}$
Density	$3000\ \text{kg} \cdot \text{m}^{-3}$ à $T = 2320$ K
Melting point	2350 K at $P = 1$ bar
Boiling point	3800 K at $P = 1$ bar
Surface tension	$0,43\ \text{N} \cdot \text{m}^{-1}$ at $P = 1$bar
Specific heat capacity	$1418,86\ \text{J} \cdot \text{kg}^{-1} \cdot \text{K}^{-1}$
Enthalpy of formation	-1620 kJ/mol

Table 1.3 – Properties of liquid alumina. Figure extracted from [33, 105]

The viscosity of liquid alumina can be obtained using :

$$\mu = AT \exp \frac{B}{T} \tag{1.8}$$

With $A = 6,8 \cdot 10^{-8}\ \text{Pa} \cdot \text{s} \cdot \text{K}^{-1}$ and $B = 13200$ K.

1.3.3 Gaseous properties of aluminum and its oxides

The properties for the gaseous aluminum and its oxides are given through the use of NASA 7-coefficient polynomials. These polynomials gives :

- The molar heat capacity at constant pressure $\hat{c}_p^\circ(T)$ for a range of temperatures at a reference pressure p° :

$$\frac{\hat{c}_p^\circ(T)}{R} = a_0 + a_1 T + a_2 T^2 + a_3 T^3 + a_4 T^4 \tag{1.9}$$

- The molar enthalpy $\hat{h}\left(T^\circ, p^\circ\right)$ at a reference temperature T° and a reference pressure p° :

$$\frac{\hat{h}^\circ(T)}{RT} = a_0 + \frac{a_1}{2} T + \frac{a_2}{3} T^2 + \frac{a_3}{4} T^3 + \frac{a_4}{5} T^4 + \frac{a_5}{T} \tag{1.10}$$

- The absolute molar entropy $\hat{s}\left(T^\circ, p^\circ\right)$ at a reference temperature T° and a reference pressure p° :

$$\frac{\hat{s}^\circ(T)}{R} = a_0 \ln T + a_1 T + \frac{a_2}{2} T^2 + \frac{a_3}{3} T^3 + \frac{a_4}{4} T^4 + a_6 \tag{1.11}$$

The coefficients for these polynomials are available in appendix 6.2.4.

Finally, for simplification, the hypothesis of a unity Lewis number has been made in the current work. A Prandtl value of 0.7 is used for air and the Schmidt numbers of all the gaseous species are considered to have this similar value of 0.7.

In this chapter, the global phenomenology of aluminum combustion has been discussed by presenting the state of the art in this field. If it has been studied for several decades, the interest for this field has greatly increased during the last two decades with both experimental and numerical new publications. These complementary works provide great insights, and discussing them has allowed for the presentation of the key characteristics of aluminum combustion.
Going into further details requires to study each of the involved phenomena and is done in chapter 3, together with their implementations. But before discussing the implementations of these phenomena in the solver, the solver itself and its equations must be presented in chapter 2.

Chapter 2

Conservation equations and general models for the dispersed phase

In the previous chapter, the state of the art of aluminum combustion has been presented. This first chapter also aimed at introducing the general phenomena involved in this type of combustion.
Before detailing how the phenomena of aluminum combustion have been implemented in AVBP, the general equations of the solver have to be detailed. Thus, in this chapter, the Navier-Stokes equations for the gaseous reactive flows are introduced. Then, the general equations involved for the Lagrangian tracking of the particles will be detailed.

Overview

2.1 Equations and models for gaseous reactive flows

2.1.1 Choice of primitive variables

To describe the physics of a reactive flow, several physical variables must be introduced. A species in a mixture can be characterised by:

- Its mass fraction:
$$Y_k = m_k/m \tag{2.1}$$
Where m is the total mass of the mixture and m_k the mass of the species k.

- Its molar fraction:
$$X_k = n_k/n \tag{2.2}$$
Here n is the total amount of substance in the mixture in mol and n_k is the amount of substance of the species k.

- Its molar mass:
$$W_k = m_k/n_k \tag{2.3}$$
The molar mass allows to link both the mass and molar fractions together as:
$$X_k = Y_k W/W_k \tag{2.4}$$
Where W is the molar mass of the mixture.

- Its partial density:
$$\rho_k = m_k/V = \rho Y_k \tag{2.5}$$
Where ρ is the density of the mixture.

- Its heat capacity at constant pressure C_P^k.

- Its sensible enthalpy:
$$h_{s,k} = \int_{T_0}^{T} C_P^k dT \tag{2.6}$$
Where T is the temperature and T_0 a reference temperature. Using its standard enthalpy of formation $\Delta h_{f,k}^0$, the enthalpy of the species can be expressed as:
$$h_k = h_{s,k} + \Delta h_{f,k}^0 \tag{2.7}$$

Using the introduced quantities, the molar mass of the mixture can now be expressed as:

$$W = 1/\sum_{k=1}^{n_{\text{spec}}} Y_k/W_k \tag{2.8}$$

where n_{spec} is the number of species in the gas.

The introduced quantities are also linked by the ideal gas law:

$$p = \sum_{k=1}^{n_{\text{spec}}} p_k = \sum_{k=1}^{N} \rho_k \frac{R}{W_k} T \tag{2.9}$$

where T is the temperature, p the pressure, $p_k = p \cdot Y_k$ the partial pressure of the species k and $R = 8.314$ J/mol/K is the ideal gas constant.

2.1.2 Transport modelling

Before detailing the equations of the system, several transport coefficients have to be introduced.

The coefficient for thermal diffusivity is expressed as:

$$\mathcal{D}_{th} = \frac{\lambda}{\rho C_P} \tag{2.10}$$

with $C_p = \sum_{k=1}^{n_{\text{spec}}} C_{p,k} Y_k$ the heat capacity of the mixture. And λ the coefficient of thermal conductivity that is defined as:

$$\lambda = \frac{\mu C_p}{Pr} \tag{2.11}$$

where Pr is the Prandtl number which is the ratio of the momentum diffusivity to thermal diffusivity and is defined as:

$$Pr = \frac{\mu C_p}{\lambda} \tag{2.12}$$

Furthermore, using a simple power law, the dynamic viscosity can be expressed as:

$$\mu = \mu_{0,R} \left(\frac{T}{T_R} \right)^{c_2} \tag{2.13}$$

Where $\mu_{0,R}$, T_R and c_2 are parameters to calibrate.

Another way to determine the dynamic viscosity is by using the Sutherland law:

$$\mu = \mu_{0,R} \frac{T^{3/2}}{T + c_2} \frac{T_R + c_2}{T_R^{3/2}} \tag{2.14}$$

where $\mu_{0,R}$, T_R and c_2 are given parameters depending on the mixture.

In the current work, the Sutherland law has been used with: $\mu_{0,R} = 1.4614 \cdot 10^{-5} \text{Pa} \cdot \text{s}$, $T_R = 300\text{K}$ and $c_2 = 373.27\text{K}$.

The coefficient of molecular diffusivity $\mathcal{D}_k$ can be expressed according to the kinetic theory of gases [27]:

$$\mathcal{D}_k = \frac{1 - Y_k}{\sum_{j \neq k} \left(X_j / \mathcal{D}_{j,k} \right)} \tag{2.15}$$

The Lewis number of the species k, which is the ratio of the coefficient of thermal diffusivity to the coefficient of molecular diffusivity:

$$\mathcal{L}e_k = \frac{\lambda}{\rho C_P \mathcal{D}_k} = \frac{\mathcal{D}_{th}}{\mathcal{D}_k} \tag{2.16}$$

The Schmidt number of the species k, which is the ratio of momentum diffusivity to the coefficient of molecular diffusivity:

$$\mathcal{S}c_k = \frac{\nu}{\mathcal{D}_k} = \Pr \mathcal{L}e_k \tag{2.17}$$

2.1.3 Navier-Stokes equations

The flow is described using the Navier-Stokes equations. These are composed of the mass, momentum and energy conservation equations, plus a conservation equation for each species. These conservation equations are detailed in this section.

Mass conservation

$$\frac{\partial \rho}{\partial t} + \frac{\partial \rho u_j}{\partial x_j} = S_m^{l \to g} \tag{2.18}$$

Where ρ is the density and u_j the j^{th} velocity component. $S_m^{l \to g}$ is the mass source term of the coupling with the liquid phase.

Momentum conservation

$$\frac{\partial \rho u_i}{\partial t} + \frac{\partial \rho u_i u_j}{\partial x_j} = -\frac{\partial}{\partial x_j} \left(P \delta_{ij} - \tau_{ij} \right) - S_{\text{mmt}}^{l \to g} \ , \text{ for } i = 1, 2, 3 \tag{2.19}$$

Where τ_{ij} is the viscous momentum flux tensor and $P\delta_{ij}$ is the pressure flux tensor. δ_{ij} is the Kronecker symbol equals to 1 when $i = j$ and 0 when $i \neq j$. $S_{\text{mmt}}^{l \to g}$ is the momentum source term of the coupling with the liquid phase.

Energy conservation

$$\frac{\partial \rho E}{\partial t} + \frac{\partial}{\partial x_j} \left(\rho E u_j \right) = -\frac{\partial}{\partial x_j} \left(u_i \left(P \delta_{ij} - \tau_{ij} \right) + q_j \right) + \dot{\omega}_T + \dot{Q} + S_E^{l \to g} \tag{2.20}$$

Where E is the total energy, q_j the energy flux, $\dot{\omega}_T$ the energy source term and $\dot{Q}$ an external energy source term such as a spark or a laser. $S_E^{l \to g}$ is the energy source term of the coupling with the liquid phase.

Species conservation

$$\frac{\partial}{\partial t} \left(\rho Y_k \right) + \frac{\partial}{\partial x_j} \left(\rho Y_k u_j \right) = -\frac{\partial}{\partial x_j} \left(J_{jk} \right) + \dot{\omega}_k + S_k^{l \to g} \ , \text{ for } k = 1, n_{\text{spec}} \tag{2.21}$$

Where Y_k is the mass fraction of species k, $J_{j,k}$ the species diffusive flux and $\dot{\omega}_k$ the k^{th} species source term. $S_k^{l\to g}$ is the species source term of the coupling with the liquid phase.

All the source terms $S_i^{t\to g}$ for the coupling with the Lagrangian tracked liquid phase are detailed in part 2.2.1.

Viscous tensor

The viscous tensor τ_{ij} appearing in Eq. (2.19) and Eq. (2.20) is defined as:

$$\tau_{ij} = -\frac{2}{3}\mu\frac{\partial u_k}{\partial x_k}\delta_{ij} + \mu\left(\frac{\partial u_i}{\partial x_j} + \frac{\partial u_j}{\partial x_i}\right) \tag{2.22}$$

Species diffusion flux

The Hirschfelder and Curtis approximation [62] is used to express the species diffusion flux as:

$$J_{jk} = -\rho\left(\mathcal{D}_k\frac{W_k}{W}\frac{\partial X_k}{\partial x_j} - Y_k V_j^c\right) \tag{2.23}$$

Where the velocity V_j^c is expressed as:

$$V_j^c = \sum_{k=1}^{n_{\text{spec}}} \mathcal{D}_k\frac{W_k}{W}\frac{\partial X_k}{\partial x_j} \tag{2.24}$$

Energy flux

The energy flux is expressed as:

$$q_j = -\lambda\frac{\partial T}{\partial x_j} + \sum_{k=1}^{n_{\text{spec}}} J_{jk}h_{s,k} \tag{2.25}$$

where the first term is for heat conduction while the second term corresponds to the species diffusion.

Energy source term

The energy source term $\dot{\omega}_T$ in the equation of energy conservation is a direct function of the species k source terms $\dot{\omega}_k$ and can be expressed as:

$$\dot{\omega}_T = -\sum_{k=1}^{n_{\text{spec}}} \Delta h_{f,k}^0\dot{\omega}_k \tag{2.26}$$

To obtain both the energy and species source terms, the chemistry is developed in part 2.1.4.

2.1.4 Detailed chemistry

To account for the combustion process in the simulation, a multi-species detailed mechanism given in part 3.3.3 is used. In some cases, solving a conservation equation for each species in the scheme is computationally prohibitive. In these cases where detailed chemistry is to be avoided, other methods are used such as globally reduced chemistry or analytically reduced chemistry.

However, in the current work, the chemistry only involves 10 reactions and 8 species which is not that expensive calculation cost wise. Furthermore, the cost of computing such a small scheme is low in front of the expensive cost of having to numerically track the particle population present in the current work. This is why a detailed chemistry has been used.

A kinetic mechanism is composed of M reactions with a total of n_{spec} species:

$$\sum_{k=1}^{n_{\text{spec}}} \nu'_{kj}\mathcal{M}_k \rightleftharpoons \sum_{k=1}^{n_{\text{spec}}} \nu''_{kj}\mathcal{M}_k \ , \ \text{for } j = 1, M \tag{2.27}$$

where $\mathcal{M}_k$ is symbol for the k^{th} species, ν'_{kj} and ν''_{kj} are the molar stoichiometric coefficients corresponding to the j^{th} reaction involving the k^{th} species.

The species source term $\dot{\omega}_k$ is expressed as:

$$\dot{\omega}_k = \sum_{j=1}^{M} \dot{\omega}_{kj} = W_k \sum_{j=1}^{M} \nu_{kj} Q_j \tag{2.28}$$

With $\nu_{kj} = \nu''_{kj} - \nu'_{kj}$ and Q_j is the progress rate of the j^{th} reaction computed as:

$$Q_j = K_{fj} \prod_{k=1}^{n_{\text{spec}}} \left(\frac{\rho Y_k}{W_k}\right)^{\nu'_{kj}} - K_{rj} \prod_{k=1}^{n_{\text{spec}}} \left(\frac{\rho Y_k}{W_k}\right)^{\nu''_{kj}} \tag{2.29}$$

Where K_{fj} and K_{rj} are the forward and reverse reaction rates of the j^{th} reaction, respectively. The forward rate of reaction j is typically modeled using the Arrhenius law:

$$K_{fj} = \mathcal{A}_j T^{\beta j} \exp\left(-\frac{E_{aj}}{RT}\right) \tag{2.30}$$

Where $\mathcal{A}_j$, βj and E_{aj} are the pre-exponential factor, temperature exponent and activation energy of the j^{th} reaction. The forward and backward reaction are then linked together by the equilibrium constant:

$$K_{eq,j} = \frac{K_{fj}}{K_{rj}} \tag{2.31}$$

Using the equilibrium constant defined by Kuo [72] as:

$$K_{eq,j} = \left(\frac{P_0}{RT}\right)^{\sum_{k=1}^{n_{\text{spec}}} \nu_{kj}} \exp\left(\frac{\Delta S_j^0}{R} - \frac{\Delta H_j^0}{RT}\right) \tag{2.32}$$

Where P_0 is the standard pressure and ΔS_j^0, ΔH_j^0 are respectively the changes in entropy and enthalpy for the j^{th} reaction when transitioning from reactants to products. They are expressed as:

$$\Delta S_j^0 = \sum_{k=1}^{n_{\text{spec}}} \nu_{kj} W_k s_k(T) \tag{2.33}$$

$$\Delta H_j^0 = \sum_{k=1}^{n_{\text{spec}}} \nu_{kj} W_k \left(h_{s,k} + \Delta h_{f,k}^0 \right) \tag{2.34}$$

The reverse rates can finally be computed as:

$$K_{rj} = \frac{K_{f,j}}{\left(\frac{p_a}{RT}\right)^{\sum_{k=1}^{N} \nu_{kj}} \exp\left(\frac{\Delta S_j^0}{R} - \frac{\Delta H_j^0}{RT}\right)} \tag{2.35}$$

2.1.5 Numerics

Numerical tools used in the current work

During this work several tools have used from simpler to more complex ones. To study the chemical kinetics and thermodynamics, Cantera [51], an open-source software, has been used. Another tool that has been used is ARCANE (Analytical Reduction of Chemistry: Automatic, Nice and Efficient) [25], which is a chemistry reduction code based on YARC [90]. If no reduction has been conducted, this tool has been used to analyse important data on the chemical kinetics such as species time scales of formation.

This brings us to the last but not least tool used during this work, AVBP [100]. It solves the fully compressible multi species Navier Stokes equations on unstructured hybrid grids. All the implementations have been performed in AVBP. It is co-developed by CERFACS and IFPEN and can be used on several HPC resources such as CINES (Occigen computer), IDRIS (Turing computeur), CEA-TTGC (Curie and Irene computers) and Kraken the local CERFACS supercomputer. Kraken is composed of 185 compute nodes with 36 intel skylake cores each and 40 compute nodes with 76 IceLake core each. The importance of having a quick and easy access to an onsite computer with a peak capacity of 1 peak Pflop/s cannot be stressed enough.

Numerical schemes

To solve the Navier-Stokes equations written in part 2.1.3, two numerical schemes have been used during this work:

The Two-step Taylor Galerkin scheme [30]: It is a finite element scheme, with an explicit two-step integration in time. It is third order accurate in space and time. This scheme has much better dispersion and dissipation properties than the Lax-Wendroff scheme, but it is around 2.5 times more expensive.

The Lax-Wendroff scheme [76]: It is a finite volume scheme with an explicit single step time integration. It is second order accurate in time and space. It has been used during this work because it presents a lower computational cost than the Two-step Taylor

Galerkin scheme.

Boundary conditions

In the simulations performed during this work, acoustic waves can form and propagate through the domain. If the boundary conditions don't allow the correct evacuation of these acoustic waves in the domain, these waves can reflect and accumulate. This can cause an accumulation of energy which will crash the simulation.

Therefore, the boundary conditions need to both allow for the evacuations of these acoustic waves while respecting the physics of these waves. To do so, AVBP uses the NSCBC (Navier-Stokes Characteristic Boundary Conditions) [91].

Artificial viscosity

The use of centred numerical schemes in AVBP makes the simulations prone to point-to-point oscillations close to regions of steep gradients. Furthermore, the combustion of aluminum is rather extreme, especially during ignition. Indeed, with high energy density and flame temperature often around 3200 K, the ignition process can be brutal and present very steep gradient. To reduce these oscillations, artificial viscosity has been used in this work at ignition.

This strong artificial viscosity is used in all the domain for the ignition until the flame is smoothed and become stable. Once it has stabilised, the artificial viscosity is progressively removed.

2.2 Lagrangian tracking of the dispersed phase

2.2.1 Lagrangian deterministic approach

Lagrangian set of equations

The trajectory, mass variation and temperature of the particles are computed using the following set of equations:

$$\frac{DX_{\mathrm{p},i}}{Dt} = u_{\mathrm{p},i} \tag{2.36}$$

$$\frac{Dm_{\mathrm{p}}u_{\mathrm{p},i}}{Dt} = \mathrm{F}^{\mathrm{ext}}_{i,\mathrm{p}} \tag{2.37}$$

$$\frac{Dm_{\mathrm{p}}}{Dt} = \dot{m}_{\mathrm{p}} \tag{2.38}$$

$$\frac{Dm_{\mathrm{p}}h_{s,\mathrm{p}}}{Dt} = \dot{\Phi}_{\mathrm{p}} \tag{2.39}$$

Where i is the spatial coordinates, X the position, m_{p} the mass of the particle and D/Dt the material derivative. $F^{\mathrm{ext}}_{\mathrm{p}}$ designates the external forces applied to the particle, $\dot{m}_{\mathrm{p}}$ the mass variation and $\dot{\Phi}_{\mathrm{p}}$ the variation of energy of the droplet.

Coupling with the gaseous phase

The coupling of the gaseous phase is modelized through the use of the source terms $\mathrm{S}^{\mathrm{l}\to\mathrm{g}}_{\mathrm{m}}$ for the equation of mass conservation (Eq. (2.18)), $\mathrm{S}^{\mathrm{l}\to\mathrm{g}}_{\mathrm{mmt}}$ for the equation of momentum conservation (Eq. (2.19)), $\mathrm{S}^{\mathrm{l}\to\mathrm{g}}_{\mathrm{E}}$ for the equation of energy conservation (Eq. (2.20)) and $\mathrm{S}^{\mathrm{l}\to\mathrm{g}}_{\mathrm{k}}$ for the equation of species conservation (Eq. (2.21)). These terms are expressed as follow:

$$\mathrm{S}^{\mathrm{l}\to\mathrm{g}}_{\mathrm{m}} = \frac{1}{\Delta V}\sum_{n=1}^{N}\Psi_n\left(x_{\mathrm{p},n}\right)\dot{m}_{\mathrm{p},n} \tag{2.40}$$

$$\mathrm{S}^{\mathrm{l}\to\mathrm{g}}_{\mathrm{qdm,i}} = \frac{1}{\Delta V}\sum_{n=1}^{N}\Psi_n\left(x_{\mathrm{p},n}\right)\left(-m_{\mathrm{p},n}F^{ext}_{i,\mathrm{p},n} + \dot{m}_{\mathrm{p},n}u_{\mathrm{p},n,i}\right) \tag{2.41}$$

$$\mathrm{S}^{\mathrm{l}\to\mathrm{g}}_{\mathrm{F}} = \frac{1}{\Delta V}\sum_{n=1}^{N}\Psi_n\left(x_{\mathrm{p},n}\right)\dot{m}_{\mathrm{p},n} \tag{2.42}$$

$$\mathrm{S}^{\mathrm{l}\to\mathrm{g}}_{\mathrm{E}} = \frac{1}{\Delta V}\sum_{n=1}^{N}\Psi_n\left(x_{\mathrm{p},n}\right)\left(-m_{\mathrm{p},n}\vec{F}^{ext}_{\mathrm{p},n}\cdot\vec{u}_{\mathrm{p},n} + \frac{1}{2}\dot{m}_{\mathrm{p},n}\left\|\vec{u}_{\mathrm{p},n}\right\|^2 - \dot{\Phi}_{\mathrm{p},n}\right) \tag{2.43}$$

Where ΔV is the control volume illustrated in figure 2.1, N the number of particles in said volume and $\Psi_n\left(x_{\mathrm{p}}\right)$ the interpolation function to the mesh.

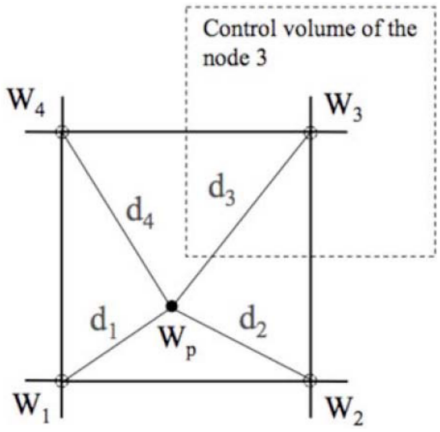

Figure 2.1 – Interpolation of a particle p on the vertices of its encompassing cell. Figure extracted from [89].

The particle is interpolated to the vertices of its encompassing cell. The interpolation is weighed proportionally with the distance d_i of the particle to the vertices using the interpolation function:

$$\Psi_{n,j}\left(x_p\right) = \frac{1/d_j}{\sum\limits_{k'=1}^{N_\mathrm{v}} 1/d_{k'}} \tag{2.44}$$

Where j is the index of each vertices while N_v is the total number of these vertices.

2.2.2 Dynamic of an isolated particle

When studying the dynamic of an isolated particle, the particle is considered as a non-evaporating rigid sphere whether it is solid or liquid. This neglects the evaporation effect on the droplet trajectory, indeed evaporation can be non-uniform and therefore can induce thrust, thus modifying the trajectory. This hypothesis greatly simplify the study of the particle dynamic. The external forces exerted on the particle are obtained by integrating the Navier-Stokes equations around the particle surface.

Several forces can constitute the term $F_{i,\mathrm{p}}^{\mathrm{ext}}$ in equation Eq. (2.37). Buoyancy and gravity forces can be combined into:

$$\vec{F}_{\mathrm{g+buoyancy}} = \rho_\mathrm{l} V_\mathrm{p} \vec{g} \left(1 - \frac{\rho_\mathrm{g}}{\rho_\mathrm{l}}\right) \tag{2.45}$$

Where ρ_l and ρ_g are the liquid and gaseous densities, V_p is the volume of the particle and $\vec{g}$ the gravity. Since the ratio of densities $\rho_\mathrm{g}/\rho_\mathrm{l}$ is extremely low for aluminum in air, the buoyancy force can be neglected. Furthermore, the change of the relative velocity between the particle and the gas creates the unsteady virtual mass effect and Basset force. But once again, both these forces are negligible [29] due to the the density ratio value in the case of aluminum particles in air. This leaves us with the most important force, the drag force.

2.2.3 Drag force

A droplet moving at a velocity $\vec{u}_\mathrm{p}$ in gas, which is at velocity $\vec{u}_\mathrm{g}$, is subjected to a drag force that can be expressed as:

$$\vec{F}_\mathrm{D} = \frac{1}{2}\rho_\mathrm{g} C_\mathrm{D} s \left\|\vec{u}_g - \vec{u}_p\right\| \left(\vec{u}_g - \vec{u}_p\right) \tag{2.46}$$

Where $s = \pi d_p^2/4$ is the projected area of the spherical particle while C_D is the drag coefficient. The drag coefficient is a function of the velocity difference between the particle and the gas. This is visible in figure 2.2 which shows the evolution of C_D as a function of the Reynolds number number expressed as:

$$Re_\mathrm{p} = \frac{\rho_\mathrm{g} d_\mathrm{p} \left\|\vec{u}_\mathrm{g} - \vec{u}_\mathrm{p}\right\|}{\mu_\mathrm{g}} \tag{2.47}$$

where d_p is the diameter of the particle while μ_g is the gaseous dynamic viscosity.

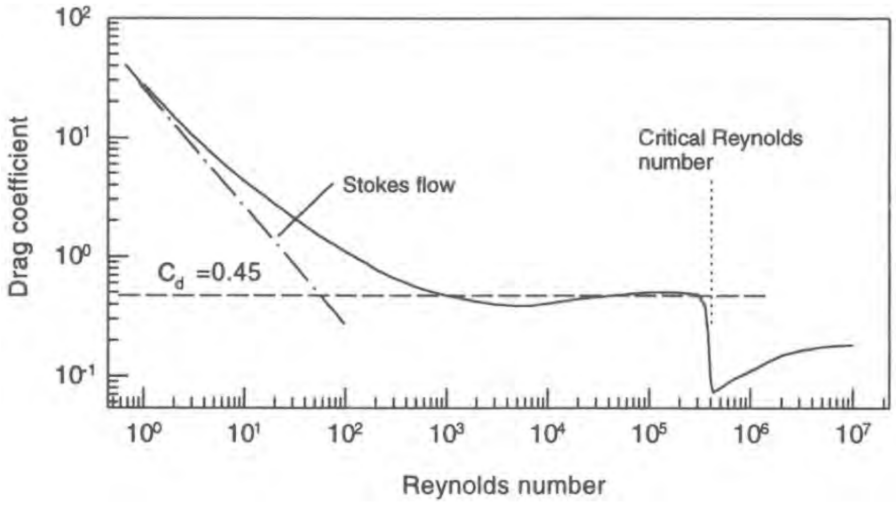

Figure 2.2 – Drag coefficient C_D as a function of the Reynolds number. Figure extracted from [29, 31].

The drag coefficient is calculated using the empirical relation proposed by Schiller and Naumann [99]:

$$C_\mathrm{D} = \frac{24}{Re_\mathrm{p}} \left(1 + 0,15 Re_\mathrm{p}^{0,687}\right) \tag{2.48}$$

2.2.4 Stochastic approach and control of the number of particles

In the deterministic approach, each physical particle is represented by one numerical particle. The problem with this approach is that the population of numerical particles can not be controlled and is directly controlled by the population of physical particles. This can create two types of problems for numerical simulation. First, as illustrated on figure 2.3, if the number of particles is too low, some cells can be empty of particles represented in red. Therefore, only part of the nodes are interpolated upon (represented in green)

while the rest of the node are not (represented in blue). This can happen if the Eulerian phase requires a really fine mesh while the physical particles population is low.

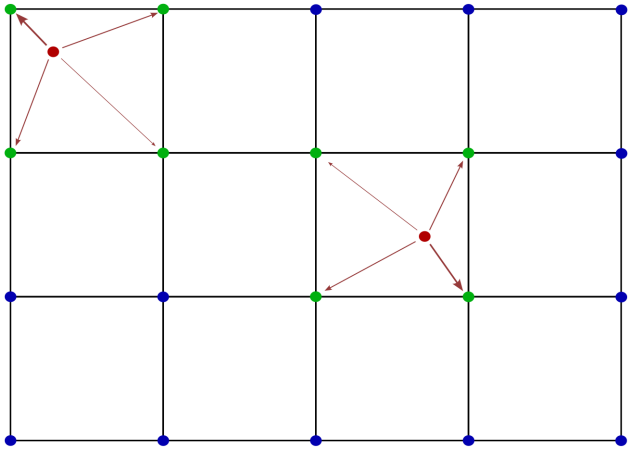

Figure 2.3 – Schematic representation of a case where the particles in red are too few and only interpolates on the green nodes, leaving cells empty.

In this case, it can present resolution problems or it can even crash the simulation. Indeed, if the evaporation rate is too high in one cell while low in the other ones, it can induce too high of an evaporation source term, which can disrupt stability.

On the other hand, the particle density can be too high in the cells as illustrated on the left part of figure 2.4. The population is therefore needlessly high and since each one of the particles is tracked individually, the calculation cost is needlessly increased.

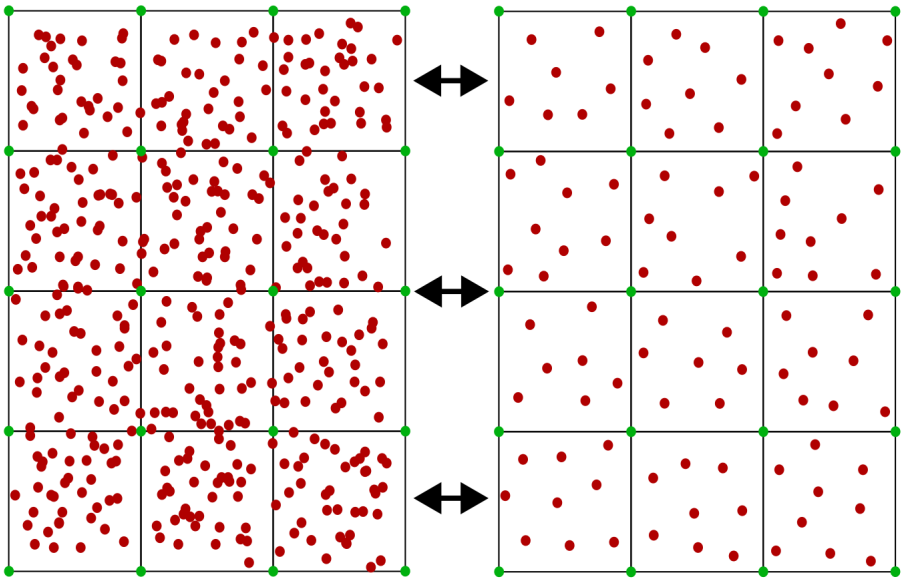

Figure 2.4 – Schematic representation of a case where the particles in red are too many in each cell on the left hand-side. This is physically equivalent to the case on the right hand-side where each numerical particles represents a higher number of physical particles

The stochastic approach can correct both these problems by allowing the numerical particles to represent a certain number of physical particles. Each numerical particle is assigned a statistical weight (ω_p) that is equal to the number of physical particles it represents. By doing so, the number of numerical particles can be reduced while leaving the physical particle population untouched.

For example, in figure 2.4, the right part is equivalent to the left part while reducing the number of numerical particles, and therefore the calculation cost. In the right part each numerical particles simply has a higher statistical weight and accounts for several physical particles. Because the numerical particle population is this still high enough, information such as position, morphology or temperature are consistent while the source terms interpolated to the nodes are similar. This notion of keeping a high enough numerical particle population is crucial to maintain statistical convergence and therefore ensuring that the lower number of numerical particles correctly represents the physical particle population. Otherwise, the model doesn't represent said physical population with extreme cases leaving cells empty and crashing the simulation as discussed previously and illustrated in figure 2.3.

Due to flow variations or evaporation of the particles, the numerical particle density can change during the simulation, yielding empty cells or cells with too many particles. Thus, a population control tool can be used in AVBP to ensure that the population density of numerical particles stays within an adequate range. This is the merge and split tool, which uses a constant-number approaches [103].

In this method, a maximum number of particle per cell is defined as $N^{\max}$. If the number of particles in the cell is higher than $N^{\max}$, the numerical particles can merge together to form particles with higher statistical weight and the average of the properties of the merged particles. Meanwhile, if the number of particles in the cell is lower than $N^{\max}/2$, the numerical particles can split into more numerical particles with a lower statistical weight. This is illustrated in figure 2.5 for $N^{\max} = 10$ ptcls/cell, the number of numerical particles is maintained between 10 and 20 ptcls/cell while the statistical weight ω_p is adjusted accordingly to conserve the population of physical particles.

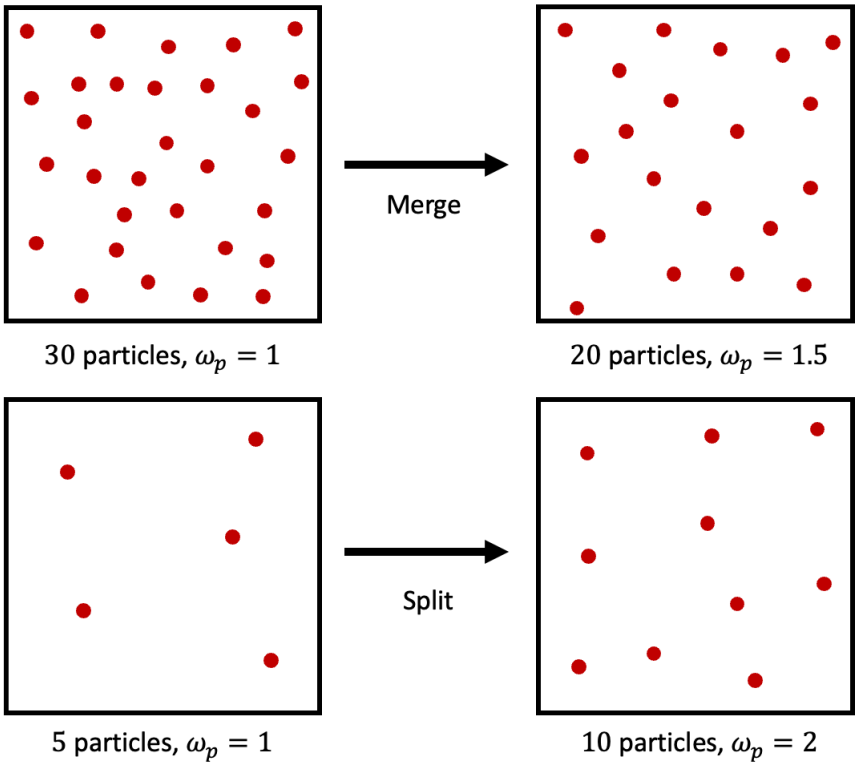

Figure 2.5 – Example of a merge and split algorithm for $N^{\max} = 20$ ptcls/cell.

Several methods exist to merge particles together, the constant-number approach [103] is popular because by maintaining the number of numerical particles under a maximum number, it allows for a better control of the computational cost.

Another method not used here is the random particle removal [55, 80, 85], but by removing particle randomly without considering its properties, it can be detrimental to statistical convergence.

A better method is the Garg, Narayanan, and Subramaniam (GNS) method [43]. It is as fast as random removal while being more accurate. This method removes the particle with the lowest statistical weight because its removal will have less of an impact than a particle with a higher weight [38, 43].

The method used in the current work is a modified version of GNS and has been first implemented in AVBP by Gallen during his PhD [38]. This method is the MGNS method introduced by Tofighian et al. [107]. In this approach, the properties of the removed particle are not equally distributed over every other particles in the cell, but proportionally to the proximity of their properties to the removed particles [38]. This approach is schematised in figure 2.6.

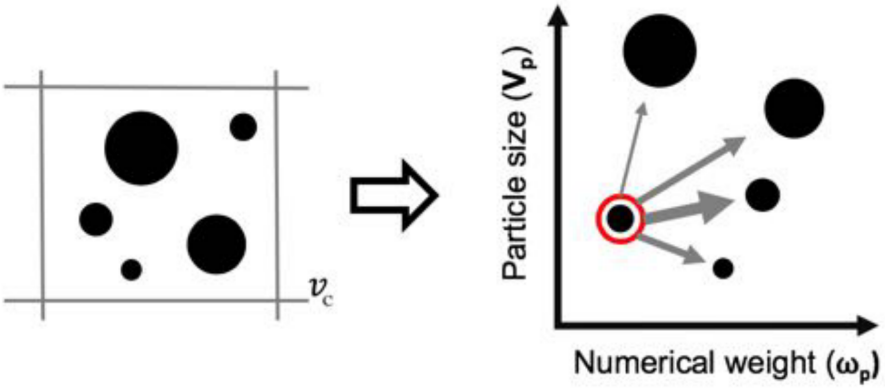

Figure 2.6 – Schematic representation of MGNS merging procedure in a control volume. Figure extracted from [38].

In the current work, there are two numerical populations separated in two different subsets. The first population is the aluminum particles and the second one is the condensed combustion products made of liquid alumina.

The aluminum particles have a constant statistical weight that is given at the injection and varies for each cases according to the mesh resolution and flow speed. This statistical weight varies from 25 to 150 in the current work. This drastically reduces the calculation cost while keeping a dense enough numerical particle population to ensure statistical convergence.

The combustion products, liquid alumina is condensed from the gaseous phase using a nucleation/condensation algorithm (detailed in part 3.5.3). This algorithm nucleates at each iteration in the cell a numerical particle with a statistical weight representing the number of physical particles predicted by the nucleation theory. Thus, the number of numerical particles increases at each iteration and needs to be controlled. To do so, the MGNS method is used on the nucleated alumina droplets.

Finally, once the aluminum particle has burnt all its aluminum and is only made of alumina, it is moved from the first to the second subset. Therefore, once the combustion is over, the remains of the aluminum particles population is now controlled, with the rest of the liquid alumina, by the MGNS algorithm, which greatly reduces the overall calculation cost.

In this chapter, the Navier-Stokes equations for the gaseous reactive flows have been introduced alongside the general equations involved for the Lagrangian tracking of the particles.
Both the general phenomenology of aluminum and the general equations of AVBP have been introduced. Each phenomenon constituting the general phenomenology of aluminum can now be detailed alongside its implementation in the current work.

Chapter 3

Models and implementation of aluminum combustion

The state of the art of aluminum combustion has been presented in the first chapter while the fundamental equations of AVBP have been introduced in the second one. In this third chapter, each phenomenon involved in aluminum combustion are physically detailed alongside the role that they play during combustion. Then, the sub-models available in the literature for each phenomenon are detailed together with the ones chosen in the current work.

Overview

3.1 General phenomenology

As explained in chapter 1, aluminum combustion is a complex process involving several phenomena. To understand this process, one must study the phenomena one by one. To do so, the figure 3.1 is proposed in order to understand and recapitulate what is happening during the combustion of an aluminum particle. The burning of a particle is described in this section by explaining chronologically how these phenomena happen. In the rest of this chapter, each of these individual aspects will be explained in more details. Especially, their role in the global combustion process and how they have been implemented in the code are described.

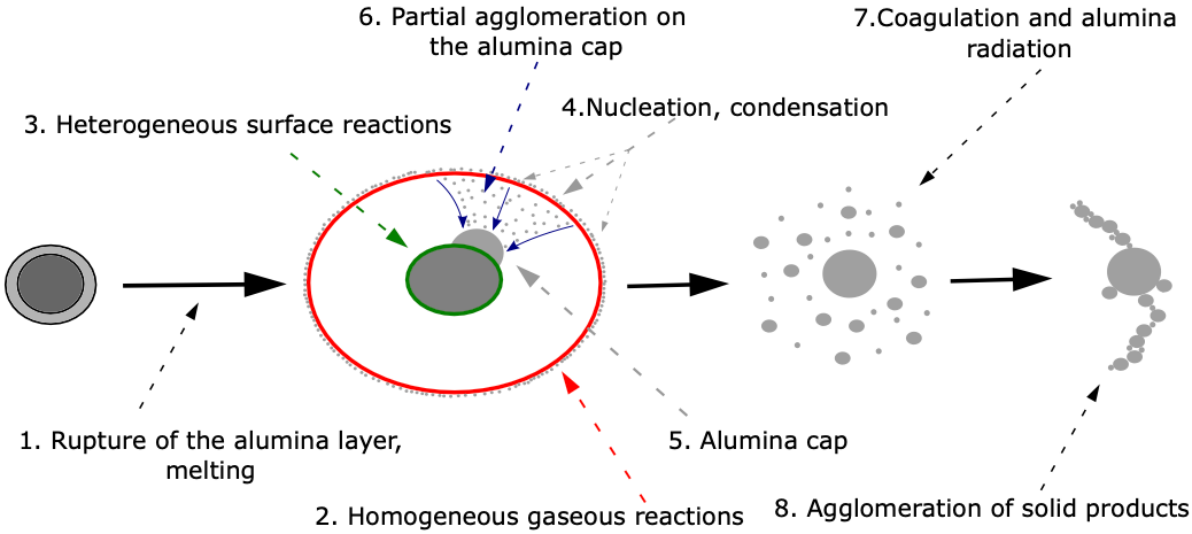

Figure 3.1 – Schematic of the phenomena involved in the combustion of an aluminum particle.

Before entering the flame zone, the particle is in a solid state. It is composed of an aluminum core surrounded by a thin alumina layer. As the particle is rising in temperature, the aluminum core starts to melt and the external alumina layer, which requires higher temperature to melt, breaks under the pressure exerted by the growing volume of the liquid aluminum core (1 in figure 3.1). After the ignition process, the particle is composed of a spherical melted aluminum core with an alumina cap on it (5 in figure 3.1). These two aspects are discussed further in part 3.2 of this chapter.

The liquid aluminum then evaporates and burns through homogeneous gaseous reactions just like a classical hydrocarbon droplet would do. This aspect is the point 2 in figure 3.1 and is detailed in part 3.3 of this chapter.

A major difference with the combustion of a hydrocarbon droplet resides in the presence of heterogeneous surface reactions. These reactions between liquid aluminum and gaseous oxidizer play a key role during the combustion of micrometric aluminum droplets. This aspect is the point 3 in figure 3.1 and is detailed in part 3.4 of this chapter.

The gaseous combustion products, mostly alumina, condensate instantaneously to form small alumina droplets. This process, together with its impact on combustion chemistry, is very exothermic and is a key process in aluminum combustion. This is the point 4 in figure 3.1 and is detailed in part 3.5 of this chapter.

The formed alumina droplets then either agglomerate on the surface of the aluminum particle (6 in figure 3.1) or coalesce into bigger radiating droplets (7 in figure 3.1). All these combustion products are going to solidify and agglomerate into bigger aggregates that will be the final combustion products (8 in figure 3.1). These aspects are detailed in part 3.6 of this chapter.

Thus, the complexity of aluminum combustion resides in the fact that it involves many phenomena that must be individually considered and modeled. The associated sub-models are presented hereafter.

3.2 Rupture of the alumina layer and formation of the alumina cap

3.2.1 Description of the physical phenomenon

Before ignition, the particle is composed of an aluminum core surrounded by a thin alumina layer. This layer prevents any contact between aluminum and air, therefore preventing any reaction. This contributes to the stability of micrometric aluminum particles during storage. The melting temperature of aluminum is 933 K while alumina only melts at 2350 K [105]. Without an alumina layer, the particle would start evaporating and burning in the gaseous phase as soon as the core would liquefy at 933 K. However as the external layer melts at a higher temperature, it needs to be broken first. As the core is melting, it expands, exerting pressure and breaking the external layer. When the particle reaches 2350 K, the external alumina layer melts and forms droplets on the particle surface which accumulate into a lobe. This ignition process is visible on the experimental image in figure 1.2. Therefore, the presence of the external layer has the major effect of increasing the ignition temperature. According to [59], the size of the external layer is dependent on the radius of the particle. Therefore, the ignition temperature is also a function of the particle radius. Huang et al. [59] proposed a summary of the different ignition temperatures obtained experimentally and shown in figure 3.2.

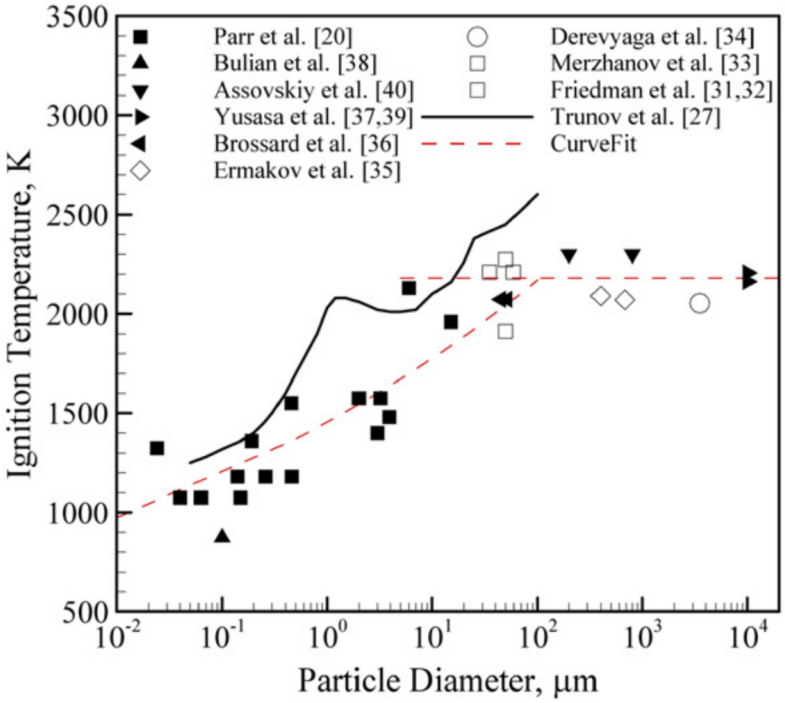

Figure 3.2 – Ignition temperature of aluminum particle as a function of particle diameter in oxygen-containing environments. Figure extracted from [59].

According to Trunov et al. [109], for particles in the range of 1 to 100 μm, the ignition temperature can vary from 1300 K to 2300 K. This is consistent with the curvefit in figure

3.2. In the current work, it is chosen to ignite the particle at a temperature consistent with the curvefit given in fig. 3.2.

Once the particle has ignited, it burns through both homogeneous gaseous reactions (see part 3.3) and heterogeneous surface reactions (see part 3.4). The particle is now composed of a liquid aluminum sphere with a liquid alumina lobe on its surface. This alumina lobe grows mainly due to the combustion products forming at the surface. Its size and shape are also functions of the surface tension of both liquids [41]. Several models describing the evolution of the alumina lobe during the combustion process have been proposed in the literature and will be discussed in the next section. This is of great interest because predicting these characteristics of the lobe allows to predict the fraction of the aluminum core that is not covered by alumina, i.e, the non-covered fraction of surface available for both surface reactions and evaporation. Therefore, the lobe and its shape directly impact the combustion speed.
This ignition process with the particle liquefying from a solid aluminum particle surrounded by an external layer of alumina to a a liquid aluminum particle partly covered by an alumina lobe can be observed in figure 1.2.

Finally, the latent heat of fusion of the particle has to be considered because it represents a non-negligible amount of energy that delays ignition.

3.2.2 Models proposed in the literature

One of the first to account for the presence of the lobe on the aluminum particle in numerical simulation was Beckstead et al. [8]. To do so, the authors used a simple model of oxide-cap geometry as illustrated in figure 3.3.

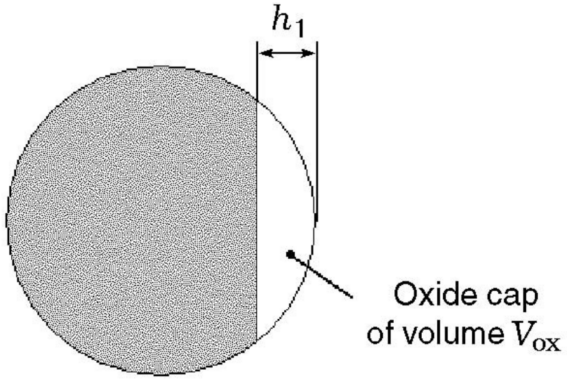

Figure 3.3 – Scheme of oxide deposition on the aluminum particle surface. Figure extracted from [8].

The deposition height h_1 is described by the equation:

$$h_1^3 - 3Rh_1^2 + \frac{3V_{ox}}{\pi} = 0 \tag{3.1}$$

where V_{OX} is the alumina cap volume and R is the droplet radius. In this model, the alumina cap inhibits aluminum evaporation from the portion of the sphere that is covered.

This is justified by the fact that the alumina has almost twice the density of the metal and the metal cannot diffuse through the oxide [8].

The model of Beckstead et al. [8] was developed to describe aluminum combustion in rocket motors. The ignition is assumed to have already occurred and is therefore not included in the model which focuses on the combustion itself.

More advanced methods were later used to have a more realistic representation of the ignition, melting and geometry of the alumina cap.

A recent example is the use of the model first proposed in [70, 112] and reused by Zhang et al. [114]. In this model a more complex geometry is considered for the modelization of the alumina cap, as illustrated in figure 3.4.

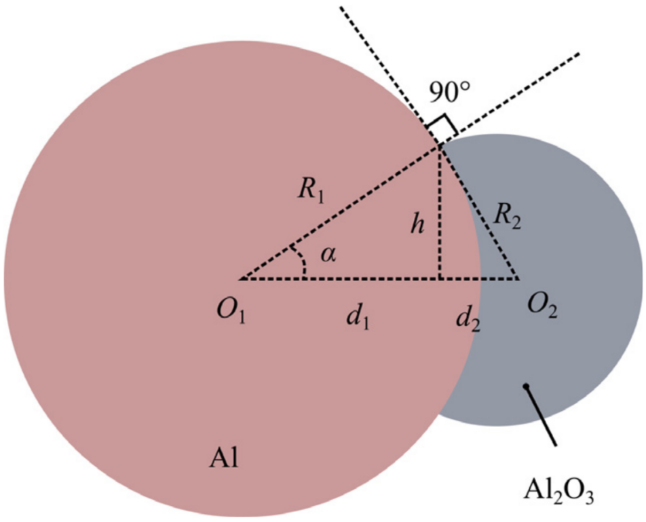

Figure 3.4 – Geometry of aluminum droplet with alumina cap. Figure extracted from [112, 114].

From the figure 3.4, the authors proposed the following equations:

$$V_{Al_2O_3} = \frac{4}{3}\pi R_2^3 - \frac{1}{3}\pi\left(R_1 - d_1\right)^2\left(2R_1 + d_1\right) - \frac{1}{3}\pi\left(R_2 - d_2\right)^2\left(2R_2 + d_2\right) \tag{3.2}$$

$$d_1^2 = R_1^2 - h^2 \tag{3.3}$$

$$d_2^2 = R_2^2 - h^2 \tag{3.4}$$

$$h = \frac{R_1 R_2}{d_1 + d_2} \tag{3.5}$$

with R_1 the particle radius of the aluminum core and $V_{Al_2O_3}$ the volume of the Al_2O_3 cap which is, in the model of Zhang et al. [114], made of the heterogeneous surface reactions products. The angle α is determined as:

$$\alpha = \arcsin\left(\frac{h}{R_1}\right) \tag{3.6}$$

which yields the solid angle of the oxide cap ϑ as:

$$\vartheta = 2\pi(1 - \cos\alpha) \tag{3.7}$$

Finally, the fraction of the aluminum sphere covered with oxide can be determined as:

$$\beta = \frac{\vartheta}{4\pi} = \frac{1}{2}(1 - \cos\alpha) \tag{3.8}$$

Regarding ignition, in the model proposed by Zhang et al. [114], both the solid and liquid phases are accounted for in the particle using their respective mass fractions. As soon as the particle reaches the melting temperature of one of its component, aluminum or alumina, the particle temperature stop rising as the energy is absorbed in the melting process. The melting rate of this process is determined as:

$$\dot{m}_{\text{p, melt}} = -\frac{\dot{Q}_{\text{p, melt}}}{h_{\text{p, melt}}} = \frac{\dot{Q}_{\text{p, inter}} + \dot{Q}_{\text{p, HSR}} + \dot{Q}_{\text{p, evap}} + \dot{Q}_{\text{p, rad}}}{h_{\text{p, melt}}} \tag{3.9}$$

where $\dot{Q}_{\text{p,inter}}$, $\dot{Q}_{\text{p,HSR}}$, $\dot{Q}_{\text{p, evap}}$ and $\dot{Q}_{\text{p,rad}}$ are the heat due to convection, surface reactions, evaporation and radiations respectively. $\dot{Q}_{\text{p, melt}}$ is the heat due to melting and $h_{\text{p, melt}}$ is the latent heat of fusion obtained from [28].

3.2.3 Chosen model and implementation

Initially, the particle is made of both aluminum and alumina. In the current work, the bi-composition of the particle has been implemented by calculating in each particle the mass fractions of both aluminum and alumina. These mass fractions change through both evaporation and heterogeneous surface reactions. Using these mass fractions, the mass and volume of aluminum and alumina are computed as:

$$m_{\text{Al}} = m_{\text{p}}\, Y_{\text{Al}} \tag{3.10}$$

$$m_{\text{Al}_2\text{O}_3} = m_{\text{p}}\, Y_{\text{Al}_2\text{O}_3} \tag{3.11}$$

where m_{p} is the mass of the particle, m_{Al} and $m_{\text{Al}_2\text{O}_3}$ are the mass of aluminum and alumina respectively and Y_{Al} and $Y_{\text{Al}_2\text{O}_3}$ their respective mass fractions. From the mass, the volume of both phases can then be easily retrieved as:

$$V_{\text{Al}} = \frac{m_{\text{Al}}}{\rho_{\text{Al}}} \tag{3.12}$$

$$V_{\text{Al}_2\text{O}_3} = \frac{m_{\text{Al}_2\text{O}_3}}{\rho_{\text{Al}_2\text{O}_3}} \tag{3.13}$$

with: $\rho_{\text{Al}} = 2236\ \text{kg} \cdot \text{m}^{-3}$ and $\rho_{\text{Al}_2\text{O}_3} = 3000\ \text{kg} \cdot \text{m}^{-3}$ the density of aluminum and alumina, respectively.

This allows to have all the necessary data properties of the particles while only adding two mass fractions to the particle, therefore maintaining a low calculation cost increase.

As explained in part 3.2.1, predicting the shape of the alumina lobe is of high interest. In the current work, the model proposed by Gallier et al. [41] is used. This model has been chosen because it can predict the shape of the lobe by accounting for the surface tension of both components. Doing so allows to predict the effective surface S_{eff}, which is the surface that is not covered by the alumina cap and therefore available for evaporation and surface reactions.

The particle geometry used for this model is represented in figure 3.5.

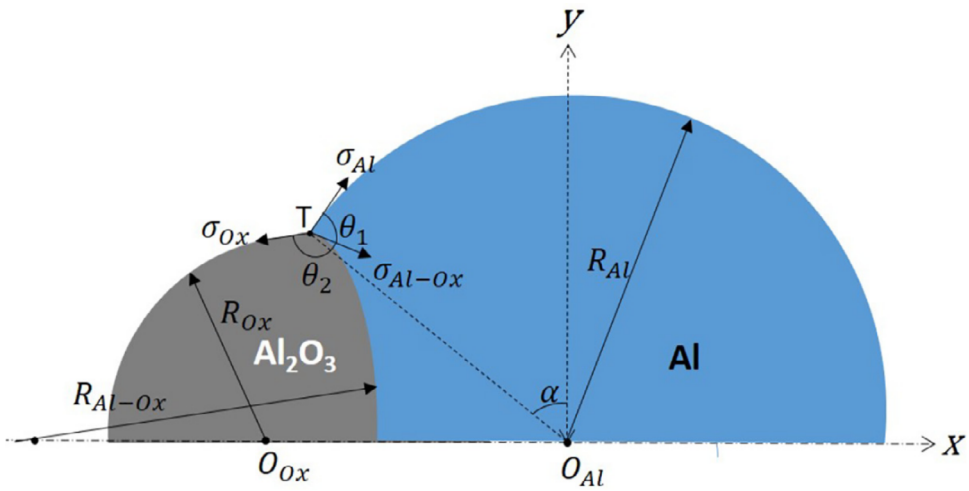

Figure 3.5 – Aluminum droplet (blue) with its oxide lobe (grey). Figure extracted from [41].

The exact shape of the lobe is obtained using the equilibrium of the triple line T between surrounding gas, aluminum (Al) and alumina (Ox) which yields the following equations.

$$\sigma_{\text{Al-ox}} + \sigma_{\text{ox}} \cos\theta_2 + \sigma_{\text{Al}} \cos\theta_1 = 0 \tag{3.14}$$

$$\sigma_{\text{Al-0x}} \cos\theta_2 + \sigma_{\text{ox}} + \sigma_{\text{Al}} \cos(\theta_1 + \theta_2) = 0 \tag{3.15}$$

$$\sigma_{\text{Al-ox}} \cos\theta_1 + \sigma_{\text{ox}} \cos(\theta_1 + \theta_2) + \sigma_{\text{Al}} = 0 \tag{3.16}$$

where α, δ, θ_1 *and* θ_2 are geometric angles defined in figure 3.5 and σ_i are the surface tensions expressed as:

$$\sigma_{\text{Al}} = 1.267 - 2.6 \cdot 10^{-4}(T - 933) \quad [83] \tag{3.17}$$

$$\sigma_{\text{ox}} = 0.66 - 6 \cdot 10^{-5}(T - 2327) \quad [48] \tag{3.18}$$

$$\sigma_{\text{Al-ox}} = 0.687 - 1.6 \cdot 10^{-4}(T - 933) \quad [5] \tag{3.19}$$

The angles θ_i can be expressed using surface tension as:

$$\cos\theta_1 = \frac{\sigma_{\text{ox}}^2 - \sigma_{\text{Al-ox}}^2 - \sigma_{\text{Al}}^2}{2\sigma_{\text{Al-ox}} \cdot \sigma_{\text{Al}}} \tag{3.20}$$

$$\cos\theta_2 = \frac{\sigma_{\mathrm{Al}}^2 - \sigma_{\mathrm{Al-ox}}^2 - \sigma_{\mathrm{ox}}^2}{2\sigma_{\mathrm{Al-ox}} \cdot \sigma_{\mathrm{ox}}} \tag{3.21}$$

The authors [41] then introduced the angle α to define the position of the triple line, from which the following relation is obtained:

$$R_{\mathrm{Al}} \cos\alpha = R_{\mathrm{ox}} \cos(\alpha - \delta) = R_{\mathrm{Al-ox}} \cos(\theta_1 - \alpha) \tag{3.22}$$

with $\delta = \theta_1 + \theta_2 - \pi$

Finally, using simple geometry, the two following equations are proposed:

$$\begin{aligned} V_{\mathrm{Al}} = \frac{\pi}{3} R_{\mathrm{Al}}^3 \Bigg[& \Big((1+\sin\alpha)^2(2-\sin\alpha)\Big) - \frac{\cos^3\alpha}{\cos^3(\theta_1-\alpha)} \\ & \times (2+\sin(\theta_1-\alpha))\,(1-\sin(\theta_1-\alpha))^2 \Bigg] \end{aligned} \tag{3.23}$$

$$\begin{aligned} V_{\mathrm{Al_2O_3}} = \frac{\pi}{3} R_{\mathrm{Al}}^3 \Bigg[& \frac{\cos^3\alpha}{\cos^3(\alpha-\delta)} (1-\sin(\alpha-\delta))^2 (2+\sin(\alpha-\delta)) \\ & + \frac{\cos^3\alpha}{\cos^3(\theta_1-\alpha)} (2+\sin(\theta_1-\alpha))\,(1-\sin(\theta_1-\alpha))^2 \Bigg] \end{aligned} \tag{3.24}$$

Using Eq. (3.20) and Eq. (3.21), θ_1 and θ_2 can be obtained as a function of temperature.

The system composed of Eq. (3.22), Eq. (3.23) and Eq. (3.24) can now be solved for α, R_{Al} and R_{ox}. Once the system is solved, it is possible to obtain the surface of aluminum as:

$$S_{\mathrm{eff}} = 2\pi R_{\mathrm{Al}}^2 (1+\sin\alpha) \tag{3.25}$$

This model was originally developed for the simulation of a single particle in the work of Gallier et al. [41]. In the current work, the aim is to simulate dust flames with up to several million particles. Thus, solving a system of three equations for each particle at each iteration is cost-prohibitive. To keep a reasonable computing cost, this system of equations has been solved prior to the simulation using a python script and the Sympy package [86] for temperature ranging from 900 K to 3800 K and Y_{Al} ranging from 0 to 1. The results are stored in a 2D table composed of 25 values for temperature and 30 values for Y_{Al}, that is simply loaded and used by the flame simulation code which interpolates the result at any values of temperature and Y_{Al}.

Using this surface for both the evaporation rates (see part 3.3) and the heterogeneous surface reaction rate (see part 3.4) instead of the particle surface accounts for the impact of the alumina lobe on these phenomena.

Latent heat of fusion

The model implemented by Suarez [105] in AVBP during his PhD work to account for the latent heat of fusion has been reused in the current work. The sensible enthalpy of the species have been adjusted to account for the energy consumed by the melting of the particle. For temperatures $T_p < T_{fus}$, the latent heat of fusion is added to the latent

heat of vaporization in order to determine the sensible enthalpy of the particle. Figure 3.6 illustrates the variation of the particle sensible enthalpy with temperature using two functions f_1 and f_2 to represent the latent heat fusion and evaporation, respectively, and given in Eq. (3.26) and Eq. (3.27). This added latent heat due to fusion implies that more energy has to be given to the solid particle compared to a liquid droplet, therefore allowing for a more physical approach.

$$f_1(T) = H_{s,g} - \Delta H_{vap} - C_{P,l}l\,(T_{vap} - T_{liq}) - \Delta H_{fus} - C_{P,s}\,(T_{fus} - T) \tag{3.26}$$

$$f_2(T) = H_{s,g} - \Delta H_{vap} \; - C_{P,l}\,(T_{vap} \; - T) \tag{3.27}$$

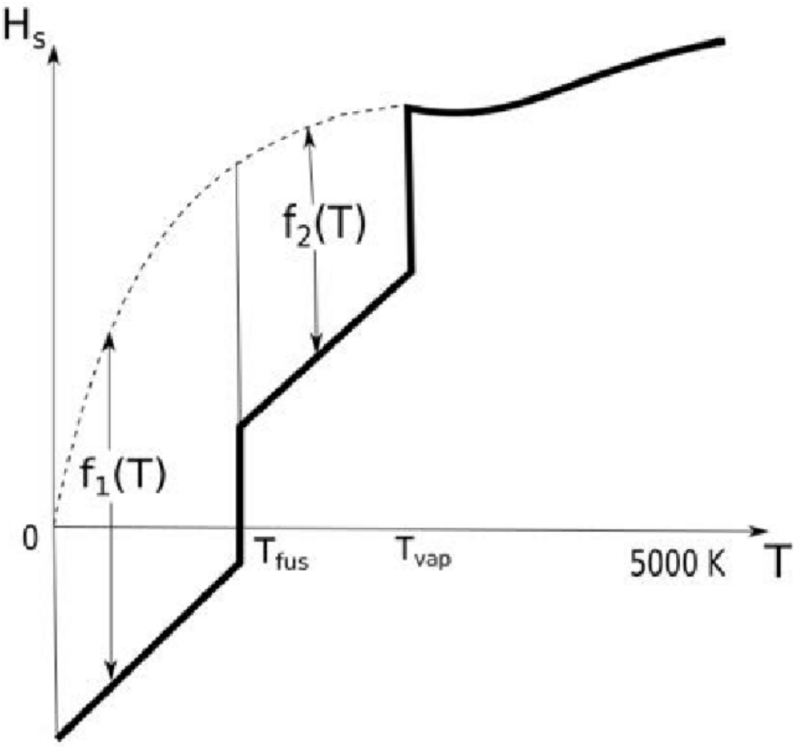

Figure 3.6 – Evolution of the sensible enthalpy with temperature for different phases (in solid line) superimposed with the sensible enthalpy for the gaseous phase (dashed line). Figure extracted [105].

This method presents the advantage of accounting for the phase change energy without having to introduce a notion of liquid/solid state for each particles which would be costly.

Ignition temperature

Finally, both the evaporation and the heterogeneous surface reactions can only occur for temperatures higher than the ignition temperature T_{ign}. This ignition temperature is mainly a function of the initial diameter of the particle, as shown in figure 3.2. The

simulations performed in this work are mainly done for particle diameters ranging from 1 to 10 μm, therefore the ignition temperature will vary from 1450 K to 1750 K.

In the current work, to determine the ignition temperature of the aluminum particles, the formula proposed by Han et al. [54] based on the work of Huang et al. [59] has been used :

$$T_{\text{ign}} = \exp\left(0.087 \times \ln\left(d_{\text{p}} \cdot 10^{6}\right) + 7.28\right) \tag{3.28}$$

where d_{p} is the initial diameter of the aluminum particle.

Once the particle has fully burned through homogeneous gaseous reactions (see part 3.3) and heterogeneous surface reactions (see part 3.4), the alumina cap remains. Meanwhile, the rest of the liquid alumina products created by the condensation process are contained in a second subset of particles in the Lagrangian solver (see part 3.5.3 for more details on the condensation model). To account for the interaction between alumina particles that are remaining from the alumina cap with the rest of the alumina particles, they are moved to the second subset as soon as the mass fraction of aluminum in the fuel particles reaches zero.

As soon as the mass fraction of aluminum in the fuel particles reaches zero, these particles are moved to the second subset. This is done for two reasons. First, to account for the interaction between alumina particles that are the remaining of the alumina cap with the rest of the alumina particles. Second, to reduce calculation cost by having all the combustion products submitted to the merge algorithm, which is applied only to the second subset (see part 2.2.4 for more details).

3.3 Evaporation and homogeneous gaseous combustion

3.3.1 Description of the physical phenomenon

An important part of the combustion takes place in the same way as it does for liquid fuel droplets, with few differences. So, let us first quickly introduce the specificities of combustion for these liquid fuel droplets before studying the similarities and differences with the combustion of aluminum particles regarding evaporation and homogeneous gaseous reactions.

For two-phase flames, evaporation plays a major role. According to Collin et al. [31], a characteristic evaporation time τ_{ev} can be introduced to better quantify the phenomenology of spray flames:

$$\tau_{\text{ev}} = \frac{\rho_{\text{l}} d_{\text{p}}^2}{8\rho_{\text{g}} D_F \ln\left(1 + B_M\right)} \tag{3.29}$$

where ρ_{l} and ρ_{g} are the liquid and gaseous densities, d_{p} the droplet diameter, D_F the fuel diffusivity an B_M the Spalding mass transfer number.

By comparing this time to the characteristic residence time τ_{res} of the droplets, one can study the flame structure as a function of the ratio $\tau_{\text{ev}}/\tau_{\text{res}}$. To easily do so, 1D two-phase laminar flames are a good case study. Three flames are presented for three different ratios $\tau_{\text{ev}}/\tau_{\text{res}}$ in figure 3.7. s_{l}^{tp} and δ_{l}^{tp} are the two-phase flame velocity and thickness respectively. In this case, the residence time is: $\tau_{\text{res}} = L/\delta_{\text{l}}^{tp}$, where L is is the length of evaporation in the fresh gases, as illustrated in figure 3.7.

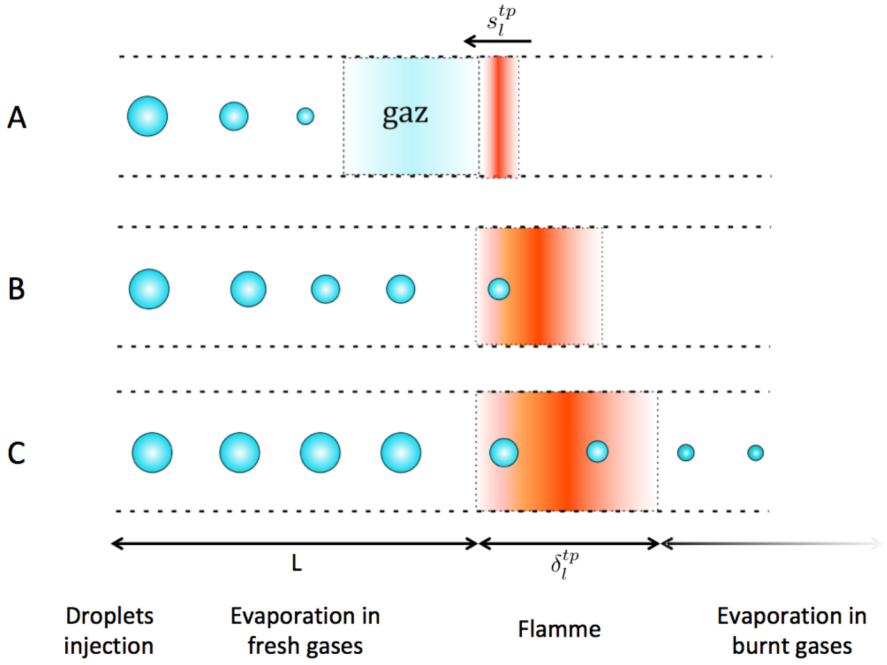

Figure 3.7 – Two-phase laminar flame topology depending on τ_{ev}. Figure extracted from [31].

As explained by Collin [31] in his PhD work, there are three cases described in figure 3.7:

- For case A, $\tau_{ev}/\tau_{res} < 1$. In this scenario, the droplets have completely evaporated by the time they reach the flame front, resulting in a flame that behaves like a gaseous flame. If the gaseous fuel and air mix quickly, the flame is premixed. Meanwhile, if the mixing process is slow, a non-premixed flame occurs.
- For case B, $\tau_{ev}/\tau_{res} \approx 1$. Droplets mostly evaporate within the flame preheat zone and cannot cross the flame front. However, beside pre-vaporized fuel, the reactive zone of the flame also contains fuel droplets that modify the flame structure.
- For case C, $\tau_{ev}/\tau_{res} > 1$. This can happen when droplets are very large or when the droplets velocity is significantly higher than the gas velocity. In such cases, droplets do not fully evaporate even after crossing the flame front and continue evaporating in the burnt gases. As gaseous fuel is present in the burnt gas, it can burn if oxidiser is still available, leading to a thicker flame.

A micrometric aluminum particle partially burns through the same evaporation and homogeneous gaseous combustion as a liquid fuel droplet. The flame envelope around the particle can clearly be seen in figure 3.8. The particle is visible in grey in the middle of the frame with a flame envelope around the particle in lighter grey.

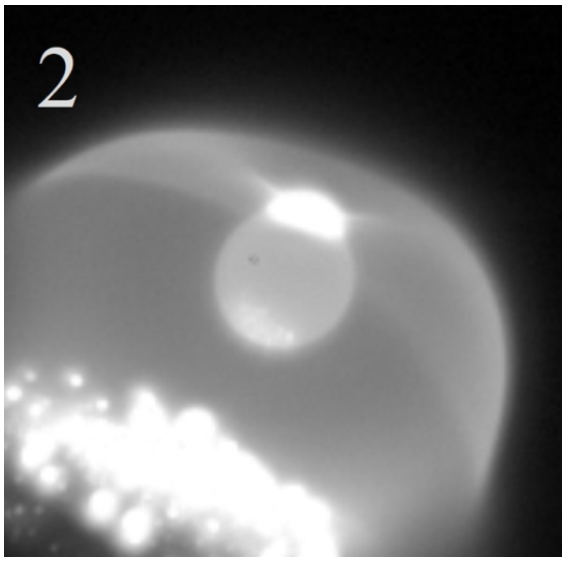

Figure 3.8 – Experimental image of a burning aluminum particle with an initial diameter of 95 μm. Figure extracted from [19].

However there are also major differences, as for aluminum, part of these three above cases almost never happen. Indeed, as explained in part 3.2.1, the aluminum particle is first in a solid state surrounded with an alumina solid layer. The energy that needs to be given for the preheating, but also liquefaction and breaking of the external layer to the aluminum particle is much higher than for liquid fuel droplets. Therefore, the pre-heating time is much higher for aluminum particles.

Furthermore, once the particle is ignited, it is partially covered by the alumina cap which limits the evaporation. This is clearly visible in figure 3.8, where the aluminum liquid core is in grey while the alumina cap on it is white, and the flame envelope is in lighter grey. This flame envelope is not a sphere as it would be for a fuel droplet, it is deformed by the alumina cap, and closer to it due to the lack of evaporation from this part of the particle. In our cases, for particle with an initial diameter ranging from 1 to 10 μm, the combustion time follows a $d^{1.8}$ law [105] instead of the standard d^2 law for liquid fuel which derives from Eq. (3.29). Therefore, the presence of the lobe also increases the combustion time.

Therefore, because of both the liquefaction and the presence of the lobe, τ_{ev} is considerably increased. Furthermore, the burning particle never totally disappears and always crosses the flame front because it keeps the alumina cap once all of the aluminum has burned. This is why the case A of figure 3.7 is almost non existent for micrometric aluminum particle combustion and the flame front is much thicker for aluminum flame. Indeed, according to Han et al.[54], the average flame thickness for an aluminum flame is around 2mm and Lomba et al. [82] obtained a flame thickness of 1.2 mm.

3.3.2 Models proposed in the literature

Several evaporation models have been used in the literature. They are generally similar to a Spalding model that is detailed in part 3.3.3.

In most of the recent simulations of aluminum/air combustion available in the literature, the kinetic mechanism proposed by Catoire et al. [24] is used. It dates back to 2003 and is made of 16 reactions to be used in ram accelerators and is available in appendix 6.2.4. For aluminum/air combustion, all the reactions with carbon species are removed and the obtained scheme is available in figure 3.1

N°	Reactions	$A_{f,j}$ (mol.cm.s)	β (-)	$E_{a,j}/R$ (K)
1	$Al(g) + O_2 = AlO + O$	9.72e14	0	80.5
2	$Al(g) + O + M = AlO + M$	3.00e17	-1	0
3	$AlO + O_2 = AlO_2 + O$	4.62e14	0	10008
4	$AlO_2 = AlO + O$	1.0e15	0	44564
5	$Al_2O = Al + AlO$	1.0e15	0	67035
6	$Al_2O_2 = AlO_2 + Al(g)$	1.0e15	0	74937
7	$Al_2O_2 = 2\ AlO$	1.0e15	0	59336
8	$Al_2O_2 = Al_2O + O$	1.0e15	0	52466
9	$Al_2O_3(g) = Al_2O_2 + O$	3e15	0	49144
10	$Al_2O_3(g) = AlO_2 + AlO$	3e15	0	63915

Table 3.1 – Kinetic scheme for aluminum/air combustion first proposed by Catoire et al. [24] without carbon species.

This scheme has the advantages of having only 10 reactions while needing to transport only 9 species (including N_2).

3.3.3 Chosen model and implementation

In the current work, an adapted version of the Spalding model [73, 102, 104] has been used. Let us first describe this model.

This model aims at determining the evaporation rate from a liquid droplet, in order to determine the particle mass variation $\dot{m}_\mathrm{p} = dm_\mathrm{p}/dt$. The following hypotheses are necessary for simplification:

- The droplet is considered as an isolated sphere, meaning that the interactions of the droplets with others are neglected.
- The thermal conductivity in the droplet is infinite, therefore the temperature inside the droplet is uniform. This hypothesis is justified by the fact that the thermal conductivity of a liquid is greater than the one of air by at least one order of magnitude, the difference is even greater for liquid aluminum. This allows to avoid having to solve the internal flow of the droplet and to only consider the thermal exchange at the surface of the particle.
- Both the gas environment and the droplet are at rest and the evolution of the gas phase is quasi-static.

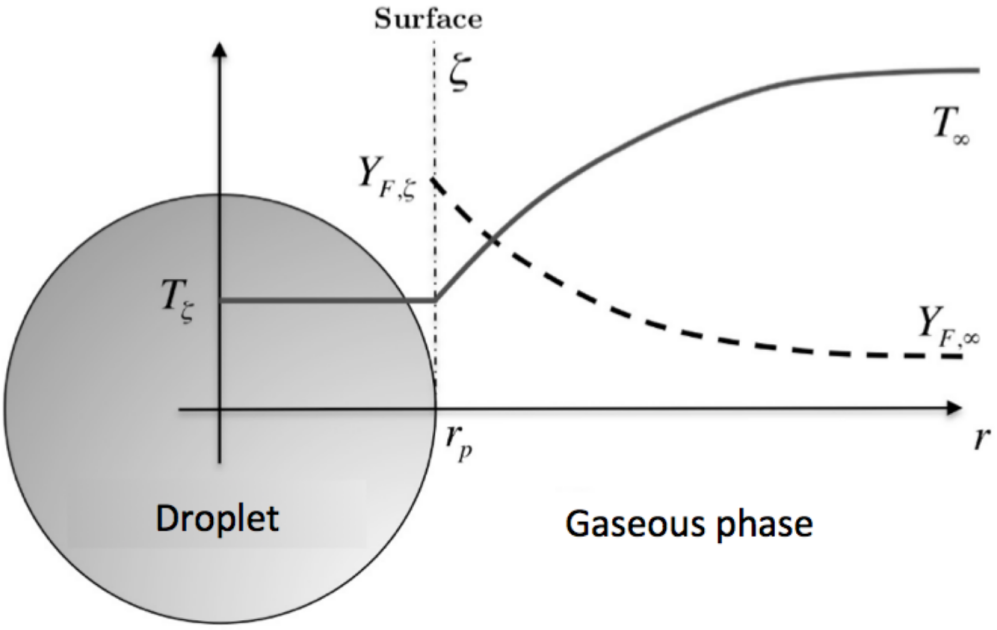

Figure 3.9 – Radial profile of temperature T and fuel mass fraction Y_F around a droplet.

Because of these hypotheses, the equations for the gaseous phase can be treated as quasi-static in spherical coordinates. Only the radial coordinates are considered as defined in figure 3.9. The equations for the conservation of momentum, species and gaseous energy are written at the surface of the droplet, denoted ζ, and at the infinity ∞:

$$\rho_\mathrm{g} u_\mathrm{g} r^2 = \text{ constant } = \frac{\dot{m}_F}{4\pi} \tag{3.30}$$

$$\rho_{\mathrm{g}} u_{\mathrm{g}} r^2 \frac{dY_F}{dr} = \frac{d}{dr}\left(r^2 \left[\rho_{\mathrm{g}} D_F\right] \frac{dY_F}{dr}\right) \tag{3.31}$$

$$\rho_{\mathrm{g}} u_{\mathrm{g}} r^2 \frac{dC_P T}{dr} = \frac{d}{dr}\left(r^2 \frac{\lambda}{C_P} \frac{dC_P T}{dr}\right) \tag{3.32}$$

where r is the radial coordinate, Y_F the fuel mass fraction, C_p the heat capacity of the mixture and λ the thermal diffusivity. $\dot{m}_F$ is the gaseous fuel flux at the surface, D_F the fuel diffusivity, and T the gas temperature. $\rho_{\mathrm{g}} D_F$ and λ/C_p are evaluated at infinity and are supposed constant along the radial profile. Miller et al. [87] improved this model by proposing to evaluate these values between the droplet surface and the infinity with a 1/3-2/3 law. The reference temperature T_R and fuel mass fraction $Y_{F,R}$ at which transport and thermodynamic properties are evaluated as:

$$T_R = T_\zeta + \frac{1}{3}\left(T_\infty - T_\zeta\right) \tag{3.33}$$

$$Y_{F,R} = Y_{F,\zeta} + \frac{1}{3}\left(Y_{F,\infty} - Y_{F,\zeta}\right) \tag{3.34}$$

$\rho_{\mathrm{g}} D_F$ and λ/C_p can be expressed as functions of the Schmidt number Sc and the Prandtl number Pr:

$$\rho_{\mathrm{g}} D_F = \frac{\mu\left(T_R\right)}{Sc} \tag{3.35}$$

$$\frac{\lambda}{C_P} = \frac{\mu\left(T_R\right)}{\mathrm{Pr}} \tag{3.36}$$

From these equations, the first step is to obtain the mass variation of the droplet. Since the liquid/gas interface does not have a mass, any steam flow is the direct result of mass loss for the liquid droplet. This mass conservation can be written as $\dot{m}_F = -\dot{m}_{\mathrm{p}}$, where $\dot{m}_{\mathrm{p}}$ is the mass variation of the droplet. By integrating twice Eq. (3.31), the mass variation can be obtained as:

$$\dot{m}_{\mathrm{p}} = -2\pi d_{\mathrm{p}} \left[\rho \mathcal{D}_F\right] \ln\left(B_M + 1\right) \tag{3.37}$$

where B_M is the mass Spalding transfer number that can be expressed as:

$$B_M = \frac{Y_{F,\zeta} - Y_{F,\infty}}{1 - Y_{F,\zeta}} \tag{3.38}$$

$Y_{F,\zeta}$ can be obtained by considering the Clausius-Clapeyron relation and supposing that the droplet interface is at thermodynamic equilibrium.

The d^2 law for evaporation previously mentioned can now be easily obtained. Indeed, the evaporation rate of the droplet can be expressed as:

$$\dot{m}_{\mathrm{p}} = \frac{d}{dt}\left[\frac{4}{3}\pi \rho_{\mathrm{l}} r_{\mathrm{p}}^3\right] \tag{3.39}$$

Using both this expression of $\dot{m}_{\mathrm{p}}$ and Eq. (3.37) the following expression can be obtained:

$$d_p^2 = d_{\mathrm{p},0}^2 - \frac{8\rho_\mathrm{g}\mathcal{D}_F}{\rho_\mathrm{l}} \ln\left(B_M + 1\right) \times t \tag{3.40}$$

Using Eq. (3.40), a characteristic time for evaporation τ_ev after which the droplet has evaporated, giving that $d_\mathrm{p} = 0$, is expressed as:

$$\tau_\mathrm{ev} = \frac{\rho_\mathrm{l} d_{\mathrm{p},0}^2}{8\rho_\mathrm{g} D_F \ln\left(B_M + 1\right)} \tag{3.41}$$

The energy required for the evaporation process is a function of the evaporated mass.

Finally, to compute the B_M coefficient, two parameters must be used: the Prandtl number Pr and the Schmidt number Sc. In the current work, the values computed by Suarez et al. [105] have been reused. According to the calculations from their work, the authors obtained a Prandtl number for gaseous aluminum of 0.2 by considering $C_p = 798.46\ \mathrm{J \cdot kg^{-1} \cdot K^{-1}}$ and $\lambda = 0.22\ \mathrm{W \cdot m^{-1} \cdot K^{-1}}$. Using the unitary Lewis hypothesis, $Sc = Pr = 0.2$.

All these values are obtained using the NASA polynomials introduced in part 1.3.3 for a temperature of 3000 K.

In the current work, the Spalding model has been modified to account for the specificities of the combustion of an aluminum particle. Indeed, the presence of the alumina cap on the surface of the particle has to be considered because by covering part of the aluminum core, it impacts the area of the surface available for evaporation. This area is the effective surface, S_eff, that is computed using the sub-model presented in part 3.2.3.

While the particle is constituted of both aluminum and alumina, only the aluminum evaporates at flame temperature. Furthermore, the alumina cap is covering a spherical aluminum core with a form schematized in figure 3.10.

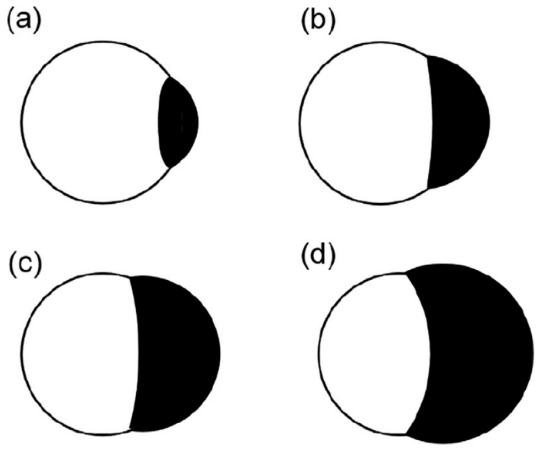

Figure 3.10 – Aluminum (white)/alumina (black) droplet geometry for four alumina mass fractions $\mathrm{Y_{Al_2O_3}} = 0.1$(a),0.3(b),0.5(c), and 0.7(d). Figure extracted from [41].

Therefore, in the evaporation model used in the current work, the Spalding model has been applied to the aluminum core as if it was a particle. The evaporation rate is then

reduced by a percentage proportional to the area covered by the alumina cap. To do so, the Spalding model is used on the aluminum core without considering the presence of alumina on the particle to compute the evaporation mass flux of aluminum in equation Eq. (3.37).

The obtained aluminum mass flux does still not account for the presence of the alumina cap. The shape of this cap has been determined in part 3.2.3 and the effective surface S_{eff} available for evaporation is determined using equation Eq. (3.25). S_{eff} is then used to determine the fraction of the surface particle that is not covered by the alumina cap as:

$$F_{\text{eff}} = \frac{S_{\text{eff}}}{S_{\text{Al}}} \tag{3.42}$$

F_{eff} is then used to limit evaporation as follow:

$$\dot{m}_{\text{p,eff}} = F_{\text{eff}} \cdot \dot{m}_{\text{p}} \tag{3.43}$$

Once gaseous aluminum has evaporated from the particle, it reacts with gaseous oxygen. To modelize the occurring chemical reactions, a detailed chemistry scheme has been used. This detailed chemistry scheme uses classical Arrhenius laws:

$$K_{fj} = \mathcal{A}_j T^{\beta_j} \exp\left(-\frac{E_{\text{a}j}}{RT}\right) \tag{3.44}$$

The coefficients may vary depending on the scheme used. For more details on the chemistry model, please see part 2.1.4.

In the current work, two chemical schemes have been considered, but only one was finally used. The first one is the one proposed by Catoire et al. [24] and is presented in figure 3.1. The second one has been recently proposed by Saba et al. [95] and constitutes a more complete kinetic scheme with 76 reactions. This mechanism has been obtained using state of the art chemistry numerical tools. Indeed, as explained by the authors, quantum chemical calculations have been performed to obtain molecular structures of intermediates on the reaction pathways. DFT level calculation has been applied to search intermediates and transition states, and CBS-QB3 method has been applied to calculate highly accurate potential energies. The rate coefficients of each reaction paths were also calculated based on VTST or RRKM theory for constructing the detailed chemical kinetic model. [95].

This kinetic scheme also accounts for the formation of large aluminum oxides Al_xO_y for sizes up to Al_8O_{12}. A model accounting for the pathway of formation of clusters composed of Al_2O_3, which is presented in part 3.5, is already used in the current work. Therefore, the chemical pathways leading to the creation of Al_xO_y molecules bigger than Al_2O_3 have been ignored.

There is a major criterion for the use of such kinetic schemes in a simulation using a fully compressible multi species reactive flow solver like AVBP [100]. It is the stiffness of the scheme: the smaller the characteristic time of formation of the species is, the smaller the time step of the simulation will have to be, thus increasing calculation cost.

Using ARCANE [26], an evaluation of the characteristic time of formation of the species has been performed on both the kinetic schemes of Catoire et al. [24] and Saba et al. [95]. The obtained results are available in figure 3.11 for the first one and figure 3.12 for the second one.

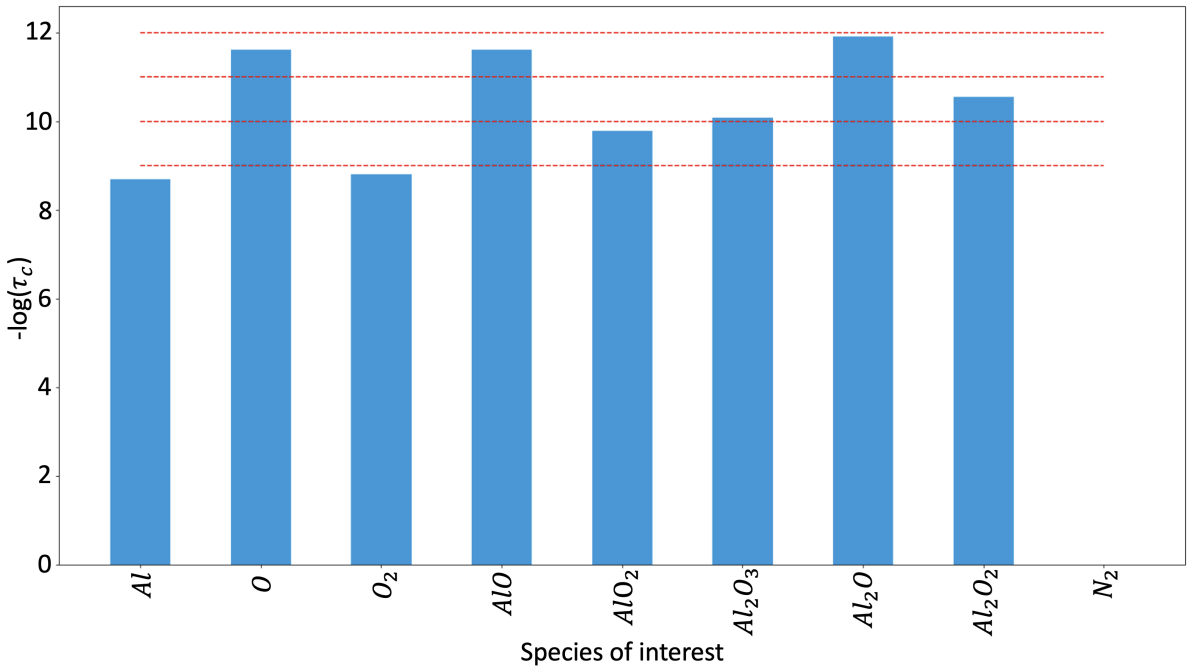

Figure 3.11 – Evaluation of the characteristic time τ_c of the species in the scheme proposed by Catoire et al. [24].

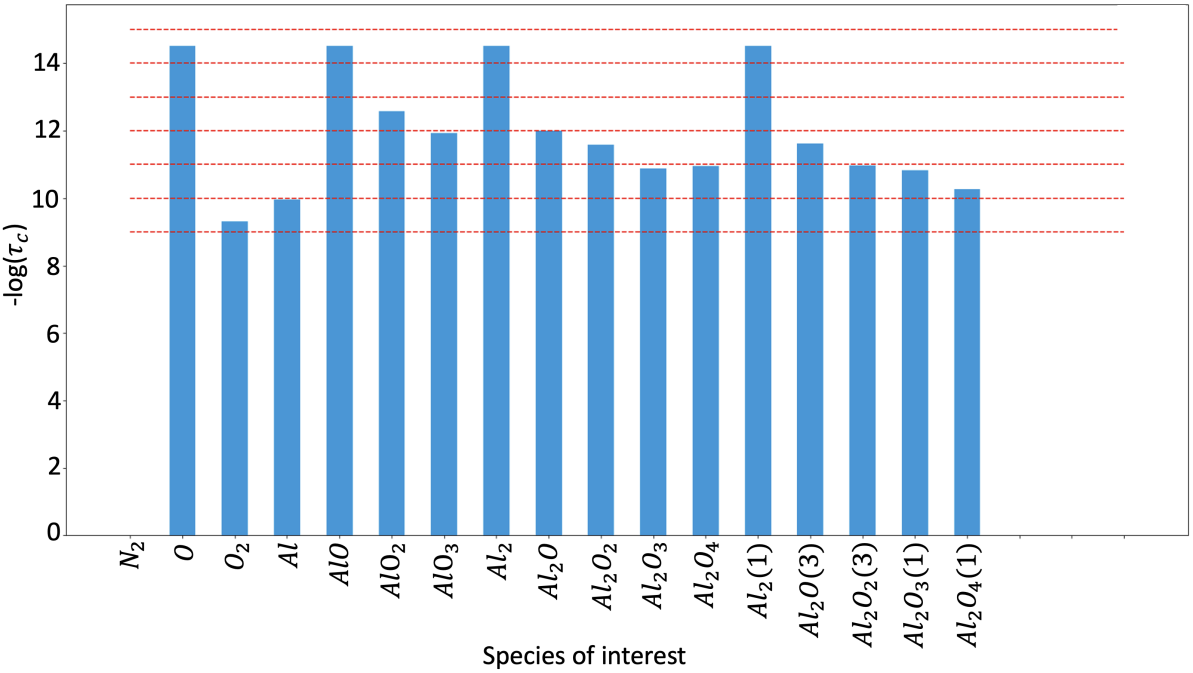

Figure 3.12 – Evaluation of the characteristic time τ_c of the species in the scheme proposed by Saba et al. [95].

In figure 3.11, the stiffest species is Al_2O with a characteristic time τ_c below 10^{-12}. Two other stiff species are AlO and O with characteristic times of $10^{-11.5}$. Therefore, this kinetic scheme is already extremely stiff and costly for a use in AVBP.

In figure 3.12, the stiffest species are O, AlO and Al_2 with a characteristic time τ_c of $10^{-14.5}$. Thus, this kinetic scheme is way too stiff to be used in AVBP without incurring prohibitive computational costs.

For this reason, only the scheme of Catoire et al. [24]has been retained. Please note that the scheme proposed by Saba et al.[95] might be much more accurate and is very promising. It should be considered in other works where calculation cost is less of an issue. Furthermore, reductions of this scheme that would render it less stiff for the use in explicit solver could be of great interest.

Finally, because the scheme of Catoire et al. [24] is still extremely stiff, chemical sub-cycling has been used in the current work.

3.4 Heterogeneous surface reactions

3.4.1 Description of the physical phenomenon

Depending on the initial particle diameter, aluminum particles can burn either through evaporation and then homogeneous gaseous reactions (see part 3.3), or through heterogeneous surface reactions. "Heterogeneous" means here that the gaseous oxidiser directly reacts with the liquid aluminum at the particle surface. According to Han et al. [54], if the particle diameter is greater than 100 μm, it essentially burns through evaporation and gaseous reactions. Meanwhile a small nanometric particle with a diameter smaller than 100 nm only burns though surface reactions. In the case of the current work, for particles with a diameter ranging from 1 to 10 μm, both types of reactions are to be accounted for. One must keep in mind that these diameter ranges are not exact simply because it is difficult to experimentally determine which reaction regime is dominant.

Glorian et al. [45, 47] did a whole PhD on heterogeneous surface reactions and found that for particle with a diameter smaller than 10 μm, at least 30 % of the aluminum is consumed through surface reactions. Furthermore, the energy from the surface reactions essentially goes into heating up the particle which considerably accelerating the evaporation. The gaseous combustion is controlled by the evaporation and diffusion of the gaseous aluminum because the gaseous reactions are extremely fast. Thus, by accelerating the evaporation, the surface reactions considerably increase the combustion speed. Therefore, the surface reactions are not only responsible for about a third of the oxidation but they also diminish the combustion time by 68 %.

For all these reasons, it is extremely important to account for these surface reactions when studying the combustion of aluminum particles with diameters ranging from 1 to 10 μm.

3.4.2 Models proposed in the literature

To account for these surface reactions, several models have been proposed during the last decades.

Beckstead et al. [8] was one of the first to implement surface reactions in his numerical model for the simulation of an isolated burning aluminum particles. The following reaction was used [8]:

$$\mathrm{Al(l) + AlO(g) \rightarrow Al_2O(g)} \tag{3.45}$$

More recently, Glorian et al. [46] studied extensively these surface reactions. The authors proposed a kinetic model for surface reactions with 57 reversible reactions and 58 species. This is a very interesting paper to go deeper into the complexities of surface reactions.

Lately, authors like Han et al. [54] and Zhang et al. [114] used for the simulation of aluminum dust flame a single surface reactions in the form:

$$\mathrm{Al(l)} + \mathrm{O_2(g)} \rightarrow \mathrm{Al_2O_3(l)} \tag{3.46}$$

where the obtained $Al_2O_3(l)$ is directly produced and deposited on the particle.

3.4.3 Chosen model and implementation

The complete model with 57 reversible reactions and 58 species proposed by Glorian et al. [45], was used for the simulation of mono-particle only. In the scope of this project, aiming at simulating 2D dust flames with potentially several millions particles, using such a model is cost prohibitive and it was chosen to use the model first proposed by Gurevich et al. [53], and also used by Zhang et al. [114]. The model consists of a single reaction between liquid aluminum and gaseous oxygen:

$$\mathrm{Al} + \frac{3}{4}(\mathrm{O_2} + 3.76\mathrm{N_2}) \rightarrow \frac{1}{2}\mathrm{Al_2O_3} + 2.82\mathrm{N_2} \tag{3.47}$$

The consumption rate of liquid Al by the particle surface reaction is :

$$\dot{m}^{\mathrm{Al}}_{\mathrm{p,HSR}} = S_{\mathrm{eff}} \rho_{\mathrm{s}} Y_{\mathrm{O_2,s}} A_{\mathrm{r}} \exp\left(-\frac{E_{\mathrm{a}}}{R T_{\mathrm{p}}}\right) \tag{3.48}$$

where S_{eff} is the effective surface computed in section 3.2.3, ρ_{s} is the gas density at the particle surface, $Y_{\mathrm{O_2}}$ is the mass fraction of oxygen. $A_{\mathrm{r}} = 1.5{\cdot}10^4$ m/s, and $E_{\mathrm{a}} = 83.72$ kJ/mol are the Arrhenius coefficients for the surface reaction. R is the universal gas constant and T_p is the particle temperature.

The heat released by the reaction is computed by Zhang et al. [114] as:

$$\dot{Q}_{\mathrm{p,HSR}} = \dot{m}^{\mathrm{Al}}_{\mathrm{p,HSR}} h_{\mathrm{p,HSR}} \tag{3.49}$$

with

$$\dot{m}_{\mathrm{p,HSR}} = \dot{m}^{\mathrm{Al}}_{\mathrm{p,HSR}} - 0.5 \frac{W_{\mathrm{Al_2O_3}}}{W_{\mathrm{Al}}} \dot{m}^{\mathrm{Al}}_{\mathrm{p,HSR}} \tag{3.50}$$

and

$$h_{\mathrm{p,HSR}} = h_{\mathrm{Al}}\left(T_{\mathrm{p}}\right) - 0.5 \frac{W_{\mathrm{Al_2O_3}}}{W_{\mathrm{Al}}} h_{\mathrm{Al_2O_3}}\left(T_{\mathrm{p}}\right) \tag{3.51}$$

where $h_{\mathrm{p,HSR}}$ is the enthalpy of the surface reaction.

Finally, $W_{\mathrm{Al_2O_3}}$ and W_{Al} are the molar masses of Al_2O_3 and Al, respectively, while $h_{\mathrm{Al_2O_3}}(T_{\mathrm{p}})$ and $h_{\mathrm{Al}}(T_{\mathrm{p}})$ are their enthalpy.

In the current work, the heat produced is finally accounted for via a variation of the particle temperature given by :

$$\frac{dTp}{dt}_{HSR} = \frac{\dot{Q}_{\mathrm{p,HSR}}}{C_{p,l} \cdot m_p} \tag{3.52}$$

where $C_{p,l}$ is the specific heat capacity of the liquid aluminum.

3.5 Condensation of gaseous alumina

3.5.1 Description of the physical phenomenon

In the gaseous phase, aluminum reacts with oxidizers, in the current work, dioxygen. These reactants mix to produce intermediate aluminum oxides and finally alumina or Al_2O_3. This gaseous alumina has a boiling temperature of 3800K and cannot stay in a gaseous state for temperature below 3800K [59]. Because aluminum flame temperatures are lower than this, the gaseous alumina condensates in the flame to form liquid alumina. This phenomenon of condensation of alumina into fine droplets can be observed in figure 3.13

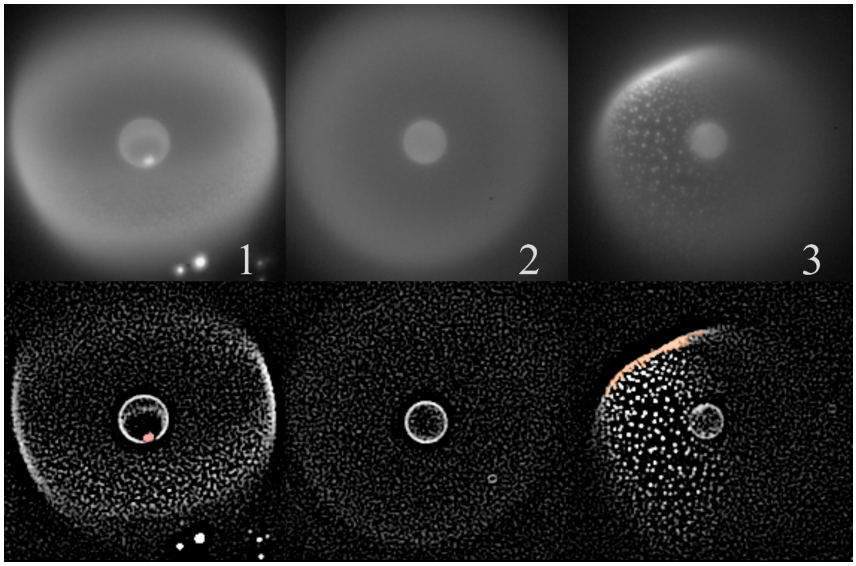

Figure 3.13 – Sequence images of a burning aluminum particle in a $40\%N_2/60\%O_2$ mixture. Figure extracted from [18]

On the three upper images in figure 3.13, the flame envelope around the particle is clearly visible in grey. On the bottom three images, the condensed alumina particles are visible in the form of white dots. The position of the white dots and the flame coincide because gaseous alumina directly condensates in the flame as it is produced.

The condensation itself is responsible for a rise in temperature of several hundred degrees [105]. Moreover, this condensation process has a very important impact on the gaseous chemistry. To better understand this, let us consider Eq. (3.53) which illustrates the pathway followed by aluminum burning through gaseous reactions.

$$Al(g) + O_2(g) \rightarrow Al_xO_y(g) \underbrace{\rightarrow}_{\text{I}} Al_2O_3(g) \underbrace{\rightarrow}_{\text{II}} Al_2O_3(l) \tag{3.53}$$

The condensation process (II in Eq. (3.53)) removes alumina from the gaseous phase, which tends to form again from other intermediate aluminum oxides (I in Eq. (3.53)). As a consequence, the gaseous chemical equilibrium is shifted toward the production of more aluminum oxides. In the end, the only remaining gaseous species downstream a stoichiometric aluminum-air flame is nitrogen because all the oxygen has reacted with

the gaseous aluminum to finally condensate into liquid alumina, which is the only final combustion product.

This means that the condensation rate not only drives the condensation itself but also indirectly the final chemical equilibrium state by impacting the reactions I in Eq. (3.53). Knowing that this last reaction is one of the most exothermic phenomenon in aluminum combustion, this shows the importance of having a good model for this condensation rate.

Retrieving and recycling liquid alumina produced by the combustion of aluminum is key in order to use aluminum as a clean fuel. Indeed, the only combustion product of aluminum combustion is solid alumina. This alumina can be turned back into aluminum, making aluminum a renewable energy vector.

To do so, it is important to understand the morphology of the final combustion products. The condensation speed is a key predictor of the alumina spherules size. These spherules will then coagulate into larger combustion products.

Because of both the exothermic impact of condensation and its key role in determining the morphology of the combustion products, correctly modelizing this condensation process is of high importance.

3.5.2 Models proposed in the literature

A simple model is to ignore the existence of alumina in the gas phase, creating directly liquid alumina through the kinetic scheme. The produced liquid alumina is then tracked as the rest of the gaseous species using the Eulerian solver. This approach has been used by Han et al. [54] who used the reduced scheme presented in figure 3.2.

No	Reactions	A[cm3/mols]	E[cal/mol]
1	$Al + O_2 = AlO + O$	9.72E13	159.95
2	$Al_2O_3 = AlOAlO + O$	3.0E15	97649.99
3	$AlOAlO = AlO + AlO$	1.0E15	117900
4	$AlOAlO = AlOAl + O$	1.0E15	104249.94
5	$AlOAl = AlO + Al$	1.0E15	133199.94

Table 3.2 – Reduced reaction kinetics of Al/O system used by Han et al. [54]. Figure extracted from [54].

In the scheme presented in figure 3.2, the Al_2O_3 species is in liquid state. This is a good cost effective way of accounting for the condensation energy if the condensation process is supposed to be infinitely fast. However, gaseous alumina is totally neglected and no information on the morphology of the liquid alumina phase can be extracted from this model.

Another commonly used method is to track alumina as a gaseous species while considering alumina condensation to be infinitely fast. Zhang et al. [114] used this type

of method and accounted for condensation using a single infinitely fast reaction. This condensation reaction is directly added to the kinetic scheme available in figure 3.3.

No.	Reaction	$A\left(\text{ cm}^3/(\text{mol}\cdot\text{s})\right)$	n	E(cal/mol)
1	$Al + O_2 = AlO + O$	9.72×10^{13}	0	159.95
2	$Al + O + M = AlO + M$	3.00×10^{17}	-1	0
3	$AlO + O_2 = AlO_2 + O$	4.62×10^{14}	0	19885.9
4	$Al_2O_3 = Al_2O_2 + O$	3.00×10^{15}	0	97649.99
5	$Al_2O_3 = AlO_2 + AlO$	3.00×10^{15}	0	126999.89
6	$Al_2O_2 = AlO + AlO$	1.00×10^{15}	0	148900
7	$Al_2O_2 = Al + AlO_2$	1.00×10^{15}	0	104249.94
8	$Al_2O_2 = Al_2O + O$	1.00×10^{15}	0	88549.86
9	$AlO_2 = AlO + O$	1.00×10^{15}	0	133199.94
10	$Al_2O = AlO + Al$	1.00×10^{15}	0	0
11	$Al_2O_3 = Al_2O_3(l)$	1.00×10^{14}	0	0

Table 3.3 – Kinetic scheme for Al/O system used by Zhang et al. [114]. Figure extracted from [114].

The infinitely fast condensation reaction in this scheme is the number 11 in figure 3.3. This way of accounting for the condensation is also a cost effective way of accounting for the condensation energy if the condensation process is supposed to be infinitely fast. It accounts for the existence of a gaseous alumina phase but still does not permit the tracking of the morphology of condensed products.

During his PhD work, Suarez et al. [105] proposed to track the alumina products using the Lagrangian solver of AVBP. In his work, a germination method was used. The main advantage of this method is to track particles without having to implement a nucleation algorithm in the code, which is hard to implement. Without the use of a nucleation method, the gaseous alumina has no physical support on which it can condensate. The germination method consists in injecting said physical support with a diameter extremely small (1 nm) so that the injected mass of alumina is negligible.

Suarez et al. [105] injected one alumina nucleus for each injected aluminum particle at the inlet. As the fuel particle evaporates and burns it produces gaseous alumina that can condensate on the available alumina nuclei. This method is schematized in figure 3.14.

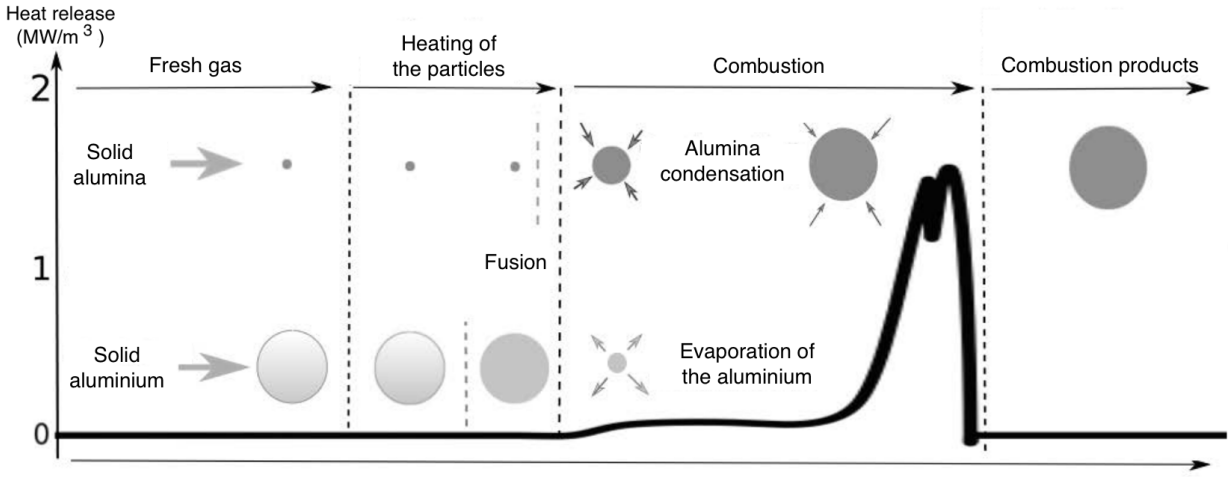

Figure 3.14 – Schematic of the germination method used by Suarez et al. [105]. Figure extracted and translated from [105].

The diameter of the injected alumina nuclei is 1 nm which is extremely small in comparison to the micrometric diameter of the injected aluminum particles. Therefore the mass quantity of alumina added to the system is negligible.

The condensation speed used by Suarez et al. [105] on the alumina nuclei is based on the Spalding model but with a mass flow $\dot{m}_{\mathrm{p}}$ going from gas to liquid. To do so, the Spalding mass transfer number is computed using Eq. (3.38) with $Y_{F,\zeta} < Y_{F,\infty}$, and is therefore negative. This yields a positive mass flow $\dot{m}_{\mathrm{p}}$ that is used to compute the new particle mass m_{p}.

This germination method is a simple way to track the liquid alumina combustion products using the Lagrangian solver. However, the condensation speed is dependent on the number of injected nuclei per aluminum particle, which is arbitrary.

Condensation can be categorized into two categories. The most common one, heterogeneous condensation is condensation on already existing supports. This first type of condensation can occur at low saturation values of the condensing gaseous phase. A good example of this type of phenomenon is the contrails left behind commercial air planes illustrated in figure 3.15. The particulates emitted by the aircraft engines can form condensation nuclei onto which water vapor can condense and produce larger cloud particles [6].

Figure 3.15 – Contrails created by a 4 jet engines aircraft. Figure extracted from [22].

However, if the gaseous species is at a high supersaturation state, condensation can occur without a heterogeneous support. At such high saturation, the gaseous species will form condensation nuclei on which condensation can occur. This is known as homogeneous condensation and the creation of such nuclei is known as nucleation.

Liquid alumina condensates directly in the flame through homogeneous condensation. Therefore, a physical model is required to predict both the morphology and rate of creation of the nuclei created from the gaseous alumina.

Most of the models that can predict these physical characteristic are based on the classical nucleation theory [7] or CNT. This theory is therefore detailed hereafter.

Classical nucleation theory (CNT)

To introduce the classical nucleation theory, an abbreviated version of chapter 3 from the book *Nucleation theory* [66] is presented here. None of the material presented here is original work, and it has all been taken from this book [66]. The reader is referred to the original document for further details.

Nucleation occurs when a gaseous phase is pushed to a non-equilibrium metastable state. In such a state, the chemical potential of the liquid phase $\mu_{\mathrm{l}}(p_{\mathrm{v}}, T)$ is lower than the chemical potential of the gaseous phase $\mu_{\mathrm{v}}(p_{\mathrm{v}}, T)$. Here, the vapor pressure p_{v} exceeds the saturation vapor pressure. This makes it thermodynamically favorable for the gaseous phase to condensate due to the chemical potential difference:

$$\Delta\mu = \mu_{\mathrm{v}}(p_{\mathrm{v}}, T) - \mu_{\mathrm{l}}(p_{\mathrm{v}}, T) > 0 \tag{3.54}$$

At a gaseous state, the environment is at a metastable state A. This physically means that it stays stable against small variations of the thermodynamic variables. Consequently, to reach a stable state B, the gaseous phase must overcome an energetic barrier corresponding to a local maximum of free energy to reach a global minimum of free energy. This phenomenon is illustrated in figure 3.16

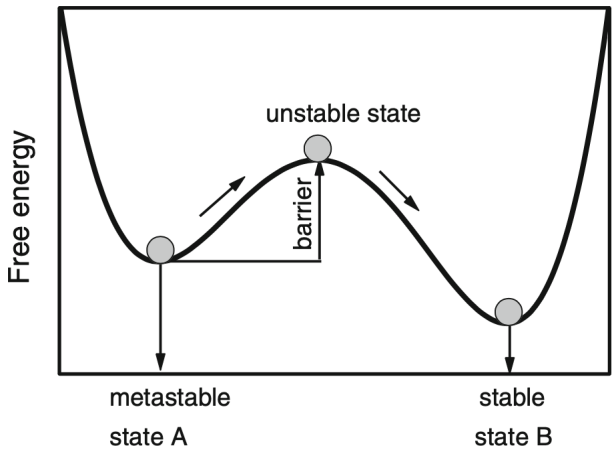

Figure 3.16 – Sketch of the free energy as a function of the order parameter. Local minimum corresponds to the metastable state A (supersaturated vapor). The global minimum corresponds to the stable state B (bulk liquid). Figure extracted from [66].

Considering the liquid phase as incompressible and knowing that $d\mu = -sdT + vdp$, $\Delta\mu$ can be rewritten as:

$$\Delta\mu \approx \left[\mu_{\mathrm{v}}\left(p_{\mathrm{v}}, T\right) - \mu_{\mathrm{sat}}(T)\right] - \frac{1}{\rho_{\mathrm{l,sat}}}\left(p_{\mathrm{v}} - p_{\mathrm{sat}}\right) \tag{3.55}$$

where $\rho_{\mathrm{l,sat}}$ is the liquid density at saturation and $\mu_{\mathrm{sat}}(T)$ is the chemical potential at a saturation state, at temperature T. By introducing the compressibility factor of the liquid phase at saturation $Z_{\mathrm{l,sat}} = \dfrac{p_{\mathrm{sat}}}{\rho_{\mathrm{l,sat}} k_{\mathrm{B}} T}$, $\Delta\mu$ can be expressed as:

$$\Delta\mu = k_{\mathrm{B}} T \ln S - k_{\mathrm{B}} T Z_{\mathrm{l,sat}} \left(\frac{p_{\mathrm{v}}}{p_{\mathrm{sat}}} - 1\right) \tag{3.56}$$

with S the supersaturation ratio which is expressed as:

$$S = \exp\left(\frac{\mu_{\mathrm{v}}\left(p_{\mathrm{v}}, T\right) - \mu_{\mathrm{sat}}(T)}{k_{\mathrm{B}} T}\right) = \frac{p_{\mathrm{v}}}{p_{\mathrm{sat}}} \tag{3.57}$$

For $T \neq T_{\mathrm{c}}$, where T_{c} is the critical temperature, $Z_{\mathrm{l,sat}} \approx 10^{-6} - 10^{-3}$, which means that the second term of Eq. (3.56) is negligible and therefore:

$$\Delta\mu = k_{\mathrm{B}} T \ln S \tag{3.58}$$

Let us now determine the minimum work required for the formation of a cluster made of n monomers. To do so, the authors [66] propose to use general thermodynamic considerations following Debenedetti [32].

The system is in contact with a reservoir. In its initial state, it is constituted of vapor and has an internal energy noted $U_{v,0}$. In its final state, after the formation of a liquid droplet, it is constituted of both vapor and a liquid droplet. Thus, its internal energy at final state U_f can be expressed as:

$$U_f = U_{v,f} + U_{\mathrm{l}} + U_{\mathrm{exc}} \tag{3.59}$$

with $U_{v,f}$ the internal energy of the bulk vapor, $\mathrm{U_l}$ the internal energy of the bulk liquid and U_{exc} the internal energy of surface (excess) contribution.

The variation of the internal energy of the system due to changes in the physical state is a function of:

- The work W exerted by the exterior on the system.
- The work performed by the reservoir to create a droplet which is: $p_{\mathrm{r}}\Delta V_{\mathrm{r}}$
- The energy received by the system from the reservoir: $-T_{\mathrm{r}}\Delta S_{\mathrm{r}}$

where T_{r} and p_{r} are the temperature and pressure of the reservoir respectively. Therefore, the variation of internal energy of the system can be written as:

$$\Delta U = W + p_{\mathrm{r}}\Delta V_{\mathrm{r}} - T_{\mathrm{r}}\Delta S_{\mathrm{r}} \tag{3.60}$$

According to the second law of thermodynamics, the change in entropy of both the system and the reservoir must be positive:

$$\Delta S_{\mathrm{r}} + \Delta S \geq 0 \tag{3.61}$$

From Eq. (3.60), the variation of entropy of the reservoir can be expressed as:

$$\Delta S_{\mathrm{r}} = -\frac{\Delta U}{T_{\mathrm{r}}} + \frac{W}{T_{\mathrm{r}}} + \frac{p_{\mathrm{r}}\Delta V_{\mathrm{r}}}{T_{\mathrm{r}}} \tag{3.62}$$

Using this expression of ΔS_{r} in equation Eq. (3.61) and knowing that $T_{\mathrm{r}} \geq 0$:

$$-\Delta U + W + p_{\mathrm{r}}\Delta V_{\mathrm{r}} + T_{\mathrm{r}}\Delta S \geq 0 \tag{3.63}$$

The total volume of the reservoir and the system remains unchanged, thus: $\Delta V_{\mathrm{r}} = -\Delta V$ and:

$$W \geq \Delta U - T_{\mathrm{r}}\Delta S + p_{\mathrm{r}}\Delta V \tag{3.64}$$

The equality sign corresponds to the minimum work to form the droplet. Supposing that the transformation happens at a constant temperature $T = T_{\mathrm{r}}$ and a constant pressure $p_{\mathrm{v}} = p_{\mathrm{r}}$:

$$W_{\mathrm{min}} = \Delta U - T\Delta S + p_{\mathrm{v}}\Delta V = \Delta G \tag{3.65}$$

where G is the Gibbs free energy. Therefore, the minimum work required for the formation of a cluster is equal to the variation of Gibbs free energy. Let us now determine this value.

The variation of internal energy can be expressed as:

$$\Delta U = (U_{\mathrm{v,f}} - U_{\mathrm{v},0}) + U_{\mathrm{l}} + U_{\mathrm{erc}} \tag{3.66}$$

By integrating $dU = TdS - pdV + \mu dN$ using Euler's theorem for homogeneous functions:

$$U_{\mathrm{v},0} = TS_{\mathrm{v},0} - p_{\mathrm{v}}V_{\mathrm{v},0} + \mu_{\mathrm{v}}N_{\mathrm{v},0} \tag{3.67}$$

$$U_{\mathrm{v,f}} = TS_{\mathrm{v,f}} - p_{\mathrm{v}}V_{\mathrm{v,f}} + \mu_{\mathrm{v}}N_{\mathrm{v,f}} \tag{3.68}$$

$$U_{\mathrm{l}} = TS_{\mathrm{l}} - p_{\mathrm{l}}V_{\mathrm{l}} + \mu_{\mathrm{l}}N_{\mathrm{l}} \tag{3.69}$$

$$U_{\mathrm{exc}} = TS_{\mathrm{exc}} + \sigma(\mathrm{R})s(\mathrm{R}) + \mu_{\mathrm{exc}}N_{\mathrm{exc}} \tag{3.70}$$

where $\sigma(\mathrm{R})$ is a surface tension at the dividing surface R with a surface area $s(\mathrm{R})$, and N refers to the number of moles.

The volume change of the system is:

$$\Delta V = (V_{\mathrm{v,f}} + V_{\mathrm{l}}) - V_{\mathrm{v},0} \tag{3.71}$$

By substituting Eq. (3.66) - Eq. (3.70) into Eq. (3.65) and knowing that because of the conservation law of matter, $N_{\mathrm{v},0} = N_{\mathrm{v,f}} + N_{\mathrm{l}} + N_{\mathrm{exc}}$:

$$\Delta G = (p_{\mathrm{v}} - p_{\mathrm{l}})\, V_{\mathrm{l}} + \sigma s + N_{\mathrm{l}} \left[\mu_{\mathrm{l}}\left(p_{\mathrm{l}}\right) - \mu_{\mathrm{v}}\left(p_{\mathrm{v}}\right)\right] + N_{\mathrm{exc}} \left[\mu_{\mathrm{exc}} - \mu_{\mathrm{v}}\left(p_{\mathrm{v}}\right)\right] \tag{3.72}$$

This is the expression for Gibbs free energy of cluster formation without specifying the location of a dividing surface. By choosing the equimolar surface $\mathrm{R_e}$, the last term is removed. Moreover, by considering the phase to be incompressible:

$$\mu_{\mathrm{l}}\left(p_{\mathrm{l}}\right) = \mu_{\mathrm{l}}\left(p_{\mathrm{v}}\right) + v_{\mathrm{l}}\left(p_{\mathrm{l}} - p_{\mathrm{v}}\right) \tag{3.73}$$

with v_{l} the molecular volume of the liquid phase. Finally, by substituting Eq. (3.73) into Eq. (3.72):

$$\Delta G = -n\Delta\mu + \sigma_{\mathrm{e}} s_{\mathrm{e}} \tag{3.74}$$

with $n \equiv N_l$, σ_{e} is the surface tension of the equimolar surface and s_{e} the area of this surface.

The so-called capillarity approximation is now introduced. This is a key part of CNT [7] and it relies on the following hypotheses:

- Clusters are considered as homogeneous spherical droplets with a defined radius and bulk liquid properties inside them. Moreover, bulk vapor properties are considered outside the droplets.
- The liquid phase is considered as incompressible.
- The surface tension of a cluster containing n molecules can be evaluated as the product of the planar interfacial tension at the temperature T, $\sigma_{\mathrm{l}}(T)$ and the surface area of the cluster s_{l}.

Those hypotheses yield the following expression for ΔG:

$$\Delta G = -n\Delta\mu + \sigma_{\mathrm{l}} s_{\mathrm{l}} \tag{3.75}$$

Since the cluster is considered as a sphere, its surface can be expressed as:

$$s_{\mathrm{l}} = 4\pi r_{\mathrm{l}}^2 \tag{3.76}$$

where r_{l} is the radius of the cluster which can be expressed as:

$$r_\mathrm{l} = r_1 n^{1/3} \tag{3.77}$$

where r_1 is the Wigner-Seitz radius of a monomer and is therefore expressed as:

$$r_1 = \left(\frac{3v_1}{4\pi}\right)^{1/3} \tag{3.78}$$

Moreover, knowing that $\Delta\mu = k_\mathrm{B}T \ln S$, ΔG can be expressed as:

$$\Delta G = -\underbrace{n k_\mathrm{B} T \ln S}_{\text{bulk}} + \underbrace{\sigma_\mathrm{l} s_1 n^{2/3}}_{\text{surface}} \tag{3.79}$$

where s_1 is the surface of a monomer expressed as:

$$s_1 = (36\pi)^{1/3} (v_1)^{2/3} \tag{3.80}$$

The variation of ΔG as a function of the number of monomers is plotted in figure 3.17

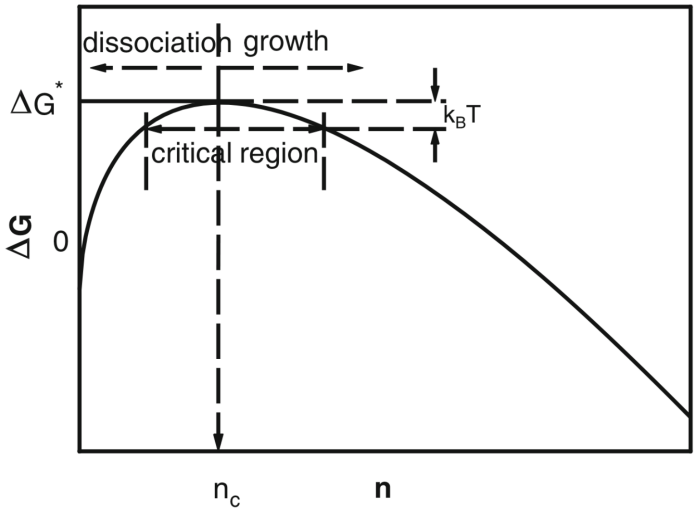

Figure 3.17 – Gibbs free energy of cluster formation ΔG as a function of the number of monomers. Figure extracted from [66].

In figure 3.17, n_c is the number of monomers in a critical cluster. For a number of monomers $n < n_\mathrm{c}$, the cluster will dissociate while for $n > n_\mathrm{c}$, the cluster will grow. The Gibbs free energy associated to this critical cluster is noted $\Delta\mathrm{G}^* = \Delta\mathrm{G}(n_\mathrm{c})$

This critical value corresponds to the maximum of ΔG and can therefore be determined as:

$$\frac{\partial G}{\partial n} = 0 = -k_\mathrm{B}T \ln S + \frac{2}{3}\sigma_\mathrm{l} s_1 n^{-1/3} \Rightarrow n_\mathrm{c} = \left(\frac{2}{3}\frac{\sigma_\mathrm{l} s_1}{k_\mathrm{B}T \ln S}\right)^3 \tag{3.81}$$

Using Eq. (3.77) the critical cluster radius can be expressed as:

$$r_\mathrm{c} = \frac{2}{3}\frac{r_1 \sigma_\mathrm{l} s_1}{k_\mathrm{B}T \ln S} \tag{3.82}$$

Using this value of n_c, the value which corresponds to the energetic barrier to overcome for nucleation to happen can be determined as:

$$\Delta G^* = \Delta G\left(n_c\right) = \frac{16\pi}{3}\frac{\left(v_1\right)^2 \sigma_l^3}{\left(k_B T \ln S\right)^2} \tag{3.83}$$

Now that the size and Gibbs free energy of these critical clusters are known, the speed at which these nuclei are created, the nucleation rate, is to be determined.

A cluster can either gain or lose monomers, this is schematized in figure 3.18.

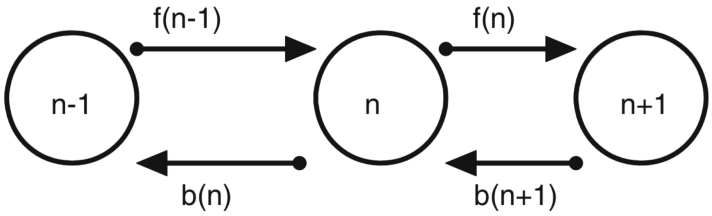

Figure 3.18 – Schematic representation of the kinetics of homogeneous nucleation; f(n) is the forward rate which corresponds to condensation while b(n) is the backward rate which corresponds to evaporation. Figure extracted from [66].

The nucleation rate of clusters composed of n monomers can be defined as:

$$I(n,t) = \mathrm{f}(n)\rho(n,t) - \mathrm{b}(n+1)\rho(n+1,t) \tag{3.84}$$

where $\rho(n,t)$ is the number density of clusters with n monomers at time t.
At equilibrium, $I(n,t) = 0$ and Eq. (3.84) can be written as:

$$0 = \mathrm{f(n)}\rho_{\mathrm{eq}}\mathrm{(n)} - \mathrm{b(n+1)}\rho_{\mathrm{eq}}\mathrm{(n+1)} \Rightarrow \mathrm{b(n+1)} = \mathrm{f(n)}\frac{\rho_{\mathrm{eq}}\mathrm{(n)}}{\rho_{\mathrm{eq}}\mathrm{(n+1)}} \tag{3.85}$$

Substituting this last equation into Eq. (3.84) gives the following expression for $I(n,t)$:

$$I(n,t)\frac{1}{\mathrm{f}(n)\rho_{\mathrm{eq}}(n)} = \frac{\rho(n,t)}{\rho_{\mathrm{eq}}(n)} - \frac{\rho(n+1,t)}{\rho_{\mathrm{eq}}(n+1)} \tag{3.86}$$

The nucleation process rapidly reaches a permanent regime after a very small relaxation time. $I(n,t)$ can therefore be expressed as:

$$I(n,t) = I \quad \forall n, (t \to \infty) \tag{3.87}$$

The terms from Eq. (3.86) can be summed from $n = 1$ to N which gives:

$$I\sum_{n=1}^{N}\left[\frac{1}{\mathrm{f}(n)\rho_{\mathrm{eq}}(n)}\right] = \frac{\rho(1)}{\rho_{\mathrm{eq}}(1)} - \frac{\rho(N+1)}{\rho_{\mathrm{eq}}(N+1)} \tag{3.88}$$

As explained in the original document [66], for small clusters, the free energy barrier is dominated by the "surface" term in Eq. (3.79), which means that the number of small clusters keeps its equilibrium value despite the constant depletion by the flux I:

$$\frac{\rho(n)}{\rho_{\mathrm{eq}}(n)} \to 1 \quad \text{as } n \to 1^{+} \tag{3.89}$$

Meanwhile, for large values of n, the cluster is favorable to condensation because it is more thermodynamically stable. When n grows, $\rho_{\mathrm{eq}}(n)$ increases while the true distribution $\rho(n)$ remains finite. Therefore:

$$\frac{\rho(n)}{\rho_{\mathrm{eq}}(n)} \to 0 \quad \text{as } n \to \infty \tag{3.90}$$

Thus, by choosing large enough clusters, the term $\dfrac{\rho(N+1)}{\rho_{\mathrm{eq}}(N+1)}$ can be neglected in Eq. (3.88). Extending summation to infinity:

$$I = \left[\sum_{n=1}^{\infty} \frac{1}{\mathrm{f}(n)\rho_{\mathrm{eq}}(n)}\right]^{-1} \tag{3.91}$$

In the summation from Eq. (3.91), the most important contribution comes from the terms close to n_{c}. Moreover, for large values of n_{c}, there is a large enough number of these summation terms so that the difference between the successive terms is small. This summation can therefore be considered as an integral:

$$I = \left[\int_{1}^{\infty} \frac{\mathrm{d}n}{\mathrm{f}(n)\rho_{\mathrm{eq}}(n)}\right]^{-1} \tag{3.92}$$

Before computing the value of this integral, ρ_{eq} can be expressed as a function of ΔG given by Kalikmanov [66] as:

$$\rho_{\mathrm{eq}}(n) = \rho_1 \exp\left(-\frac{\Delta G(n)}{k_{\mathrm{B}}T}\right) \tag{3.93}$$

In the critical region around n_c, $\Delta G(n)$ can be approximated as the parabolic form:

$$\Delta G(n) \approx \Delta G^{*} + \frac{1}{2}\Delta G''\left(n_{\mathrm{c}}\right)\left(n - n_{\mathrm{c}}\right)^2 \tag{3.94}$$

by substituting this expression in Eq. (3.93):

$$\begin{aligned}\rho_{\mathrm{eq}}(n) &= \rho_1 \exp\left(-\frac{\Delta \mathrm{G}^{*}}{\mathrm{k_B T}} + \frac{\Delta \mathrm{G}''\left(\mathrm{n_c}\right)}{2\mathrm{k_B T}}\left(\mathrm{n} - \mathrm{n_c}\right)^2\right) \\ &= \rho_{\mathrm{eq}}\left(n_{\mathrm{c}}\right) \exp\left(\frac{\Delta G''\left(n_{\mathrm{c}}\right)}{2k_{\mathrm{B}}T}\left(n - n_{\mathrm{c}}\right)^2\right)\end{aligned} \tag{3.95}$$

Finally, this expression of $\rho_{\mathrm{eq}}(n)$ can be re-injected into Eq. (3.93) to obtain the following expression of I for $n = n_{\mathrm{c}}$:

$$I = \left[\frac{1}{\mathrm{f}\left(n_{\mathrm{c}}\right)\rho_{\mathrm{eq}}\left(n_{\mathrm{c}}\right)} \int_{1}^{\infty} \exp\left(-\frac{1}{2}\frac{1}{k_{\mathrm{B}}T}\Delta G''\left(n_{\mathrm{c}}\right)\left(n - n_{\mathrm{c}}\right)^2\right)\right]^{-1} \tag{3.96}$$

A Gaussian integration of this last expression yields:

$$I = \underbrace{\sqrt{-\frac{1}{2\pi}\frac{1}{k_{\mathrm{B}}T}\Delta G''\left(n_{\mathrm{c}}\right)}}_{Z\text{: Zeldovich factor}} \mathrm{f}\left(n_{\mathrm{c}}\right)\rho_{\mathrm{eq}}\left(n_{\mathrm{c}}\right) \tag{3.97}$$

By using the expression of ΔG given in Eq. (3.79) and the expression for n_{c} given in Eq. (3.81), the Zeldovich factor can expressed as:

$$Z = \sqrt{\frac{\sigma_{\mathrm{l}}}{k_{\mathrm{B}}T}}\frac{1}{2\pi\rho_1 r_{\mathrm{c}}^2} \tag{3.98}$$

Moreover, for a transition from gas to liquid, the term f(n) is a function of the rate of collisions between the gaseous monomers and the surface of the cluster, this term can be expressed as:

$$\mathrm{f}\left(n_{\mathrm{c}}\right) = \nu s\left(n_{\mathrm{c}}\right) \tag{3.99}$$

where ν is the flux of monomers by surface units which is determined by gas kinetics [75]:

$$\nu = \frac{p_{\mathrm{v}}}{\sqrt{2\pi m_1 k_{\mathrm{B}}T}} \tag{3.100}$$

where m_1 is the mass of one monomer. Finally, the nucleation rate can be expressed as:

$$I = I_0 \exp\left(-\frac{\Delta G^*}{k_{\mathrm{B}}T}\right) \tag{3.101}$$

with:

$$I_0 = Z\nu s\left(n_{\mathrm{c}}\right)\rho_{\mathrm{v}} \tag{3.102}$$

where $\rho_{\mathrm{v}} \approx \rho_1$ is the density of the supersaturated vapor. The term $\nu s\left(n_{\mathrm{c}}\right) = \mathrm{f}\left(n_{\mathrm{c}}\right)$ is the rate at which the molecules bound to critical size cluster. By substituting the expression for I_0 of Eq. (3.102) in Eq. (3.98), Eq. (3.100) and using the ideal gas law:

$$I_0 \approx \frac{\left(\rho_{\mathrm{v}}\right)^2}{\rho_{\mathrm{l}}}\sqrt{\frac{2\sigma_{\mathrm{l}}}{\pi m_1}} \tag{3.103}$$

In conclusion, CNT predicts for a gaseous phase undergoing homogeneous condensation two important values. The first one is the size of the created nuclei which is given in Eq. (3.82). The second one is the nucleation rate, which is the number of these nuclei created in one cubic meters per second. This term is given in Eq. (3.101).

CNT is a fundamental theory which is supposed to be valid and used for any species. Let us now see how it has been used more specifically to predict the condensation of alumina.

Models derived from CNT available in the literature

Several numerical studies have been using CNT-derived models to account for the condensation of combustion products. All the models hereafter presented have been developed for the simulation of the combustion of an isolated particle. In the following, an

example of model is first presented, before introducing the model chosen in the current work and its implementation in the CFD code 3.5.3.

One of the first studies that used CNT to account for the condensation of alumina is the work of Beckstead et al. [10]. The authors considered that the use of a simple kinetic mechanism for the production of alumina was insufficient. Therefore, a two-step process was proposed as follows:

$$aC_m + bC_n \xrightarrow{k_r} \mathrm{Al_2O_3(g)} \xrightarrow{r_{\mathrm{cond}}} \mathrm{Al_2O_3\ (l)} \tag{3.104}$$

The first step can be any of the chemical reaction that generates alumina which are the following in the work of Beckstead et al. [8]:

$$\begin{aligned}
\mathrm{2AlO} + \frac{1}{2}\mathrm{O_2} &\xrightarrow{k_{11}} \mathrm{Al_2O_3} \\
\mathrm{2AlO} + \mathrm{CO_2} &\xrightarrow{k_{12}} \mathrm{Al_2O_3} + \mathrm{CO} \\
\mathrm{2AlO} + \mathrm{H_2O} &\xrightarrow{k_{13}} \mathrm{Al_2O_3} + \mathrm{H_2} \\
\mathrm{Al_2O} + \mathrm{O_2} &\xrightarrow{k_{14}} \mathrm{Al_2O_3} \\
\mathrm{Al_2O} + \mathrm{2CO_2} &\xrightarrow{k_{15}} \mathrm{Al_2O_3} + \mathrm{2CO} \\
\mathrm{Al_2O} + \mathrm{2H_2O} &\xrightarrow{k_{16}} \mathrm{Al_2O_3} + \mathrm{2H_2} \\
\mathrm{AlO_2} + \mathrm{AlO_2} &\xrightarrow{k_{17}} \mathrm{Al_2O_3} + \frac{1}{2}\mathrm{O_2}
\end{aligned} \tag{3.105}$$

These reactions are and can therefore be described using an Arrhenius reaction:

The reactions constants of each of these reactions are computed following an Arrhenius law. The rate of these expressions can then be expressed as:

$$\dot{\omega}_1 = k_r C_m^a C_n^b \tag{3.106}$$

The second step is the homogeneous condensation process that is based on CNT. Just as described in more details in the previous part, if a nucleus reaches a size greater than the critical radius, it can grow into a droplet. This critical radius corresponds to the radius for which the Gibbs function has a maximum for a given supersaturation [8, 113]. This radius value for the critical cluster is expressed in Eq. (3.82).
For this second step which corresponds to the nucleation process, the rate expression is:

$$\dot{\omega}_2 = C_c r_{\mathrm{cond}} \tag{3.107}$$

with r_{cond} the nucleation rate. This nucleation rate is obtained using CNT and is similar to the rate obtained in equation Eq. (3.101). Beckstead et al. [8] expressed it as:

$$\begin{aligned}
r_{\mathrm{cond}} = &\left(\frac{\alpha_i^* p_{\mathrm{v}}}{k_{\mathrm{B}} T}\right)\left(\frac{2\sigma_{\mathrm{l}}}{\pi m_1}\right)^{1/2}\left(\frac{m_1}{\rho_{\mathrm{l}}}\right) n_1 \\
&\times \exp\left[-\frac{16\pi\sigma_{\mathrm{l}}^3 v^2}{3k_{\mathrm{B}}^3 T^3 (\ln S)^2}\right],
\end{aligned} \tag{3.108}$$

where α_i^* is the condensation coefficient, σ_{l} is the surface tension, n_1 the number of critical-size nuclei per unit volume, v the volume of a molecule in the liquid state, S the

supersaturation of the vapor phase and finally, p_v is the pressure in the saturated vapor of the condensed phase. The total rate for the two-step condensation process is finally expressed by the authors as:

$$\begin{aligned}\dot{\omega}_\mathrm{cond} =& \frac{1}{1/\dot{\omega}_1 + 1/\dot{\omega}_2} = \frac{C_c k_r r_\mathrm{cond} C_m^a C_n^b}{k_r C_m^a C_n^b + C_c r_\mathrm{cond}} \\ =& \frac{r_\mathrm{cond} C_m^a C_n^b}{C_m^a C_n^b / C_c + r_\mathrm{cond}/k_r}\end{aligned} \tag{3.109}$$

Next, the authors assumed that the denominator in equation Eq. (3.109) does not change significantly during condensation. Therefore, they rewrote the total rate as:

$$\dot{\omega}_\mathrm{cond} = K r_\mathrm{cond} C_m^a C_n^b \tag{3.110}$$

where K is an empirical constant.

Usually, the supersaturation of the vapor phase is expressed as:

$$S = \frac{p_\mathrm{v}}{p} \tag{3.111}$$

Here, the authors assumed that alumina dissociates before it vaporises and therefore $p_\mathrm{v} = 0$ rendering Eq. (3.111) unusable. Thus, the following expression for the supersaturation was used:

$$S = 1 + \frac{\sum\limits_i p_i}{p_\mathrm{Al}} \tag{3.112}$$

where p_i is the partial pressure of the aluminum sub-oxides.

This condensation model is interesting because it is one of the first to use CNT to determine a condensation rate for alumina in a numerical simulation of the combustion of an isolated aluminum particle.

3.5.3 Chosen model and implementation

In the current work, the model recently proposed by Finke et al. [36] has been used. This state-of-the art model for alumina condensation has been applied in a 0D reactor using a population balance approach. The goal here is to extend this model to dust flames using a Lagrangian solver to track the created liquid combustion products.

Finke et al. [36] combined a population balance approach with detailed chemistry to model the condensation of oxide smoke during aluminum combustion in spatially homogeneous reactors. This model for nucleation and condensation is also based on CNT. It is derived from the equations previously presented but modified to account for the physical properties of alumina. The model, as well as its implementation in AVBP, are described hereafter.

To compute the nucleation rate, the classical nucleation theory has been used but it is amended by Courtney's correction and corrected for internal consistency [36] (internally consistent classical theory [44, 66, 97]). This yields:

$$I = \left(\frac{p_\mathrm{v}}{k_\mathrm{B}T}\right)^2 v_1 \sqrt{\frac{2\sigma_\mathrm{l}}{\pi m_1}} \times \exp\left(-\frac{16\pi\sigma_\mathrm{l}^2 v_1^3}{3k_\mathrm{B}^3 T^3 (\ln S)^2} - \frac{s_1\sigma_\mathrm{l}\ln S}{k_\mathrm{B}T}\right) \tag{3.113}$$

where p_v is the partial pressure of Al_2O_3, k_B is the Boltzmann constant. v_1, m_1 and s_1 are respectively the volume, mass and surface of a single-molecule droplet, σ_l is the surface tension of alumina.

This rate corresponds to the number of nuclei created in a cubic meter in one second.

Usually, the supersaturation is defined as:

$$S = \frac{p_\mathrm{v}}{p_\mathrm{e}} \tag{3.114}$$

In the context of the work presented by Finke et al. [36], p_v is defined as:

$$p_\mathrm{v} = p_{\mathrm{Al_2O_3}} + p_{\mathrm{Al_2O_3c}} = (X_{\mathrm{Al_2O_3}} + X_{\mathrm{Al_2O_3c}})\, p \tag{3.115}$$

where $p_{\mathrm{Al_2O_3}}$ and $X_{\mathrm{Al_2O_3}}$ are the partial pressure and molar fraction of Al_2O_3, while $p_{\mathrm{Al_2O_3c}}$ and $X_{\mathrm{Al_2O_3c}}$ are the partial pressure and molar fraction of Al_2O_3c. Because in the current work the isomer of alumina Al_2O_3c has not been accounted for, its impact on the supersaturation is ignored and the following expression for p_v is used:

$$p_\mathrm{v} = p_{\mathrm{Al_2O_3}} \tag{3.116}$$

In the work of Finke et al. [36], the approach used to evaluate S is rooted in the difference between chemical potentials as a driving force of the phase change. This accounts for the physical properties of alumina in the computation of S. This alternative formulation of the supersaturation is developed hereafter, following the exact same reasoning as in the Supplementary material S.1 of Finke et al. [36].

According to Kalikmanov [66] and Vehkamäki [111], the thermal state (p, T) and the mole fraction X_i of gas species i control the difference between the chemical potential μ_v^i of a bulk gas molecule of species i and the one of a bulk liquid molecule μ_l^i:

$$\Delta\mu^i = \mu_\mathrm{v}^i\,(p, X_i, T) - \mu_\mathrm{l}^i(p, T) \tag{3.117}$$

In a supersaturated vapor of species i, $\Delta\mu^i$ is positive, meaning that the system favors the conversion of the gas to liquid. In a multi-component ideal gas, each species i behaves as if it were alone at pressure $p_\mathrm{v}^i = X_i p$. Therefore, the chemical potential of the gaseous species i can be approximated as the one of a pure gaseous substance: $\mu_\mathrm{v}^i\,(p, X_i, T) \approx \mu_\mathrm{v}^{i,\mathrm{pure}}\left(p_\mathrm{v}^i, T\right)$. Thus, Eq. (3.117) can be recast as:

$$\Delta\mu^i = \mu_\mathrm{v}^{i,\ \mathrm{pure}}\left(p_\mathrm{v}^i, T\right) - \mu_\mathrm{l}^{i,\ \mathrm{pure}}\,(p, T) \tag{3.118}$$

Using the Gibbs-Duhem equation, the chemical potential of both the liquid and gaseous phases can be evaluated as:

$$d\mu^{\mathrm{pure}}\,(p, T) = -S_1(p, T)dT + v_1(p, T)dp \tag{3.119}$$

where S_1 and v_1 are respectively the entropy and the volume per molecule. Because the chemical potential is evaluated at a different pressure while maintaining the same temperature, $dT = 0$ and equation Eq. (3.119) becomes:

$$d\mu^{\text{pure}} = v_1 dp \tag{3.120}$$

Integrating Eq. (3.120) over the pressure range $[p_0, p_1]$ gives:

$$\int_{p_0}^{p_1} d\mu^{\text{pure}}(p,T) = \mu^{\text{pure}}(p_1,T) - \mu^{\text{pure}}(p_0,T) = \int_{p_0}^{p_1} v_1(p,T)dp \tag{3.121}$$

Using the ideal gas law, the vapor phase $v_1(p,T)$ can be expressed as:

$$v_1(p,T) = \frac{k_{\text{B}}T}{p} \tag{3.122}$$

Substituting this last relation into Eq. (3.121) gives for the gaseous phase:

$$\mu_{\text{v}}^{\text{pure}}(p_1,T) = \mu_{\text{v}}^{\text{pure}}(p_0,T) + k_{\text{B}}T \ln\left(\frac{p_1}{p_0}\right) \tag{3.123}$$

For a liquid phase, $v_1 = v_{\text{l}} = \text{const}$, Eq. (3.121) thus becomes:

$$\mu_{\text{l}}^{\text{pure}}(p_1,T) = \mu_{\text{l}}^{\text{pure}}(p_0,T) + v_1(p_1 - p_0) \tag{3.124}$$

Rewriting Eq. (3.123) and Eq. (3.124) with $p_1 = p_{\text{v}}$ and $p_1 = p$ respectively and substituting them into Eq. (3.117), Finke et al. [36] finally obtained for the change in chemical potential on transition of a pure Al_2O_3 or Al_2O_3c molecule from the gaseous to the bulk liquid phase:

$$\Delta\mu = \mu_{\text{v}}^{\text{pure}}(p_0,T) + k_{\text{B}}T \ln\left(\frac{p_{\text{v}}}{p_0}\right) - \mu_{\text{l}}^{\text{pure}}(p_0,T) - v_1(p - p_0) \tag{3.125}$$

The only difference with the present work is that instead of condensing from gaseous Al_2O_3 or Al_2O_3c, here condensation applies only to Al_2O_3 and not its isomer.

This also means that instead of expressing $\mu_{\text{v}}^{\text{pure}}$ as:

$$\mu_{\text{v}}^{\text{pure}} = \frac{X_{\text{Al}_2\text{O}_3}\mu_{\text{Al}_2\text{O}_3}^{\text{pure}} + X_{\text{Al}_2\text{O}_3\text{c}}\mu_{\text{Al}_2\text{O}_3\text{c}}^{\text{pure}}}{X_{\text{Al}_2\text{O}_3} + X_{\text{Al}_2\text{O}_3\text{c}}} \tag{3.126}$$

in the present work $\mu_{\text{v}}^{\text{pure}}$ is computed as:

$$\mu_{\text{v}}^{\text{pure}} = \mu_{\text{Al}_2\text{O}_3}^{\text{pure}} \tag{3.127}$$

For a pure species, the chemical potential is equal to the Gibbs free energy $G(p,T)$ [4, 101], and at standard pressure p_0, it writes:

$$\mu^{\text{pure}}(p_0,T) = \mu^0(T) = G^0(T) = H^0(T) - TS^0(T) \tag{3.128}$$

where H^0 and S^0 are respectively the enthalpy and entropy at standard pressure. According to [15, 66, 106, 111], $\Delta\mu$ and S are linked by the relation:

$$k_{\text{B}}T \ln S = \Delta\mu \quad \Leftrightarrow \quad S = \exp\left(\frac{\Delta\mu}{k_{\text{B}}T}\right) \tag{3.129}$$

Eq. (3.125) can finally be substituted into Eq. (3.129) to obtain:

$$\begin{aligned} S =& \exp\left(\frac{\mu_{\mathrm{v}}^{\mathrm{pure}}\ (p_0,T) + k_{\mathrm{B}}T\ln\left(\frac{p_{\mathrm{v}}}{p_0}\right) - \mu_{\mathrm{l}}^{\mathrm{pure}}\ (p_0,T) - v_1\,(p-p_0)}{k_{\mathrm{B}}T}\right) \\ =& \frac{p_{\mathrm{v}}}{p_0}\exp\left(\frac{\mu_{\mathrm{v}}^{\mathrm{pure}}\ (p_0,T) - \mu_{\mathrm{l}}^{\mathrm{pure}}\ (p_0,T) - v_1\,(p-p_0)}{k_{\mathrm{B}}T}\right) \end{aligned} \tag{3.130}$$

This formulation of the supersaturation accounts for the physical properties and is a function of the enthalpy and entropy at standard pressure that are used to compute the chemical potential using Eq. (3.128). In the current work, both the enthalpy and entropy are computed using NASA 7 polynomials [1, 84]:

$$\frac{\hat{h}^{\circ}(T)}{\bar{R}T} = a_0 + \frac{a_1}{2}T + \frac{a_2}{3}T^2 + \frac{a_3}{4}T^3 + \frac{a_4}{5}T^4 + \frac{a_5}{T} \tag{3.131}$$

$$\frac{\hat{s}^{\circ}(T)}{\bar{R}} = a_0\ln T + a_1 T + \frac{a_2}{2}T^2 + \frac{a_3}{3}T^3 + \frac{a_4}{4}T^4 + a_6 \tag{3.132}$$

where $\hat{h}^{\circ}(T)$ is the molar enthalpy and $\hat{s}^{0}(T)$ is the absolute molar entropy.

The coefficients of these NASA polynomials are obtained from the database of Burcat and Ruscic [21] in the current work.

By substituting the expression of S given in Eq. (3.130) into Eq. (3.113), the nucleation rate I is finally obtained. This rate corresponds to the number of nuclei created in a cubic meter in one second.

After the calculation of the nucleation rate, the last step is to consider the morphology of the nuclei.

To determine the radius of the created nuclei, the number of molecules in a critical cluster given in Eq. (3.81) is used:

$$n_c = \left(\frac{2}{3}\frac{\sigma_{\mathrm{l}} s_1}{k_{\mathrm{B}}T\ln(S)}\right)^3 \tag{3.133}$$

Since in the context of CNT [7], the nucleus is considered as spherical, the radius is obtained as:

$$r_c = \frac{2}{3}\frac{r_1\sigma_{\mathrm{l}} s_1}{k_{\mathrm{B}}T\ln S} \tag{3.134}$$

Once the particles have been created through the nucleation process, they are available for homogeneous condensation. Thereforethey grow at a certain rate that is also given by Finke et al. [36] and has been used in the current work. The model is presented hereafter as it is presented in [36].

Kinetically, the condensation process on the nuclei is controlled by collisions. The growth rate is therefore determined by the type of kinetic environment in which the particles evolve.

The environment and flow regime are characterized by the Knudsen number:

$$Kn = \frac{\lambda}{L} \tag{3.135}$$

where λ is the mean free path and L is a representative physical length scale. Here L is equal to the radius r of a droplet. According to [14, 36], the mean free path of a gas mixture can be computed as:

$$\bar{\lambda} = \sum_k X_k \lambda_k \tag{3.136}$$

with λ_k the species-specific mean free path obtained as the ratio of the mean thermal speed and the average collision frequency:

$$\lambda_k = \frac{k_\mathrm{B} T \bar{c}_k}{p \sum\limits_l X_l \pi \sigma_{kl}^2 \bar{c}_{kl}} \tag{3.137}$$

where $\bar{c}_k = \sqrt{8RT/(\pi W_k)}$ is the mean thermal speed of molecules of species, $\sigma_{kl} = (\sigma_k + \sigma_l)/2$ is the total collision diameter and $\bar{c}_{kl} = \sqrt{8RT\,(W_k + W_l)/(\pi W_k W_l)}$ represents the relative mean thermal speed of molecules of species k and l.

The Knudsen number can afterwards be used to know in which transport regime the gas is. The collision theory considers the existence of three different transport regimes [36, 37, 101]:

Kinetic regime: The radius of the droplet is small compared to the mean free path of the ambient gas, meaning that Kn $\gg 1$. In this regime, the droplet exists in a rarefied medium and its transport properties can be obtained from the kinetic theory of gases. In this regime, the volumetric growth rate can be expressed as [36]:

$$\left(\frac{dv}{dt}\right)_{\mathrm{kin}} = \frac{\alpha v_1 \left(p_\mathrm{v} - p_\mathrm{e}^r\right) \pi}{\sqrt{2\pi m_1 k_\mathrm{B} T}} \sqrt{\frac{v_1}{v} + 1}\, (d + d_v)^2 \tag{3.138}$$

The parameter α is the accommodation coefficient, it represents the likelihood for a colliding molecule to stick to the droplet. As explained by Finke et al. [36], in the absence of data on this coefficient in the literature, $\alpha = 1$ in his work as well as in the current work.

In Eq. (3.138), p_e^r is the equilibrium vapor pressure over a droplet. To obtain this pressure, the expression of S in Eq. (3.114) is equalized to the one in Eq. (3.130) to obtain the equilibrium vapor pressure over a flat surface as:

$$p_\mathrm{e} = p_0 \exp\left(-\frac{\mu_\mathrm{v}^{\mathrm{pure}}\ (p_0, T) - \mu_\mathrm{l}^{\mathrm{pure}}\ (p_0, T) - v_1 (p - p_0)}{k_\mathrm{B} T}\right) \tag{3.139}$$

Since the interface at the particle surface is curved, its equilibrium pressure can be expressed using the Kelvin's equation as [36]:

$$p_\mathrm{e}^r \equiv p_\mathrm{e} \underbrace{\exp\left(\frac{2\sigma_\mathrm{l} v_1}{r k_\mathrm{B} T}\right)}_{\geq 1} \tag{3.140}$$

This expression of p_e^r can now be used in Eq. (3.138) to obtain the volumetric growth rate in the kinetic regime.

Continuous regime: The radius of the droplet is big compared to the mean free path of the ambient gas, meaning that $Kn \ll 1$. In this regime, the continuum hypothesis is applied. The growth is based on the diffusive transport of the gaseous molecules towards the droplet surface and can be obtained as the solution of a diffusion equation [36]. The volumetric growth rate can be obtained using the diffusive flux evaluated at the droplet surface [36, 37]:

$$\left(\frac{dv}{dt}\right)_{\text{con}} = \frac{2\pi d\mathcal{D}v_1 \left(p_\text{v} - p_\text{e}^r\right)}{k_\text{B}T} \tag{3.141}$$

Here, $\mathcal{D}$ is the diffusion coefficient of Al_2O_3 into the gas mixture and is obtained using the Hirschfelder and Curtiss approximation [56].

Transition regime: The radius of the droplet is in same order of magnitude than the mean free path of the ambient gas, meaning that Kn ~ 1. In this regime, the growth rate is obtained by interpolating the growth rates of the kinetic and continuous regimes [101]. In the current work, as in Finke et al. [36] the harmonic averaging of Pratsinis [93] is adopted:

$$\frac{dv}{dt} = \frac{\frac{dv}{dt}_{\text{con}} \cdot \frac{dv}{dt}_{\text{kin}}}{\frac{dv}{dt}_{\text{con}} + \frac{dv}{dt}_{\text{kin}}} \tag{3.142}$$

As determining for each particle at each iteration the regime using the Knudsen number would be too costly, and because the interpolation approach of Eq. (3.142) is consistent with either the kinetic or continuum regimes, it is used for all the particles in the domain regardless of their size [88, 93]. This simplification was also made in Finke et al. [36].

Integration of nucleation and condensation in AVBP

The nucleation algorithm determines the nucleation rate in each cell of the mesh. The nucleation rate I expressed in Eq. (3.113) gives the number of nuclei created in a cubic meter per second. By multiplying this rate by the cell volume V_{cell} and the time step Δt we obtain:

$$I_{\text{cell,th}} = IV_{\text{cell}}\Delta t \tag{3.143}$$

where I is the nucleation rate given by Eq. (3.113), V_{cell} and Δt the time step.

This new rate $I_{\text{cell,th}}$ corresponds to the number of particles nucleated in the cell at each iteration. To create said nucleated particles at a low cost, a statistical approach (see part 2.2.4) is used where each numerical particle accounts for multiple physical particles via a statistical weight, allowing to retrieve the population statistics while maintaining a low computational cost. Therefore, at each iteration, a numerical particle with a numerical weight $\omega = I_{\text{cell}}$ is created. In other words, the physical information that is the number of nucleated particles is contained in the statistical weight. Still the number of numerical particles may increase too much, and to control this number a merge algorithm (see

part 2.2.4) is also used, that allows to delete numerical particles without altering statistics.

Furthermore, the mass of alumina removed from the gas phase as well as the energy generated by the condensation process must be accounted for. However nucleation can be very fast and consume in one time step more gaseous alumina than available, leading to negative mass fraction of alumina. Since this is unacceptable, a limiter has been put in place to prevent to guarantee a positive mass fraction of alumina.

First, the mass of alumina available in the cell is evaluated as:

$$m_{Al_2O_3} = \rho Y_{Al_2O_3} V_{\text{cell}} \tag{3.144}$$

Meanwhile, starting from $I_{\text{cell,th}}$ that gives the number of nuclei created in an iteration in the cell,multiplying by the mass of these nuclei that is, the mass of one molecule of alumina m_1 times the number of said molecules in the nucleus n_c, the mass of alumina consumed by the nucleation $\dot{m}_{\text{nucl}}$ in one time step is obtained:

$$m_{\text{nucl}} = I_{\text{cell}} m_1 n_c \tag{3.145}$$

By using Eq. (3.144) and Eq. (3.145) at their maximum values, one obtains:

$$m_{Al_2O_3,\text{max}} = m_{\text{nucl,max}} \Rightarrow \rho Y_{Al_2O_3} V_{\text{cell}} = I_{\text{cell,max}} m_1 n_c \Rightarrow I_{\text{cell,max}} = \frac{\rho Y_{Al_2O_3} V_{\text{cell}}}{m_1 n_c} \tag{3.146}$$

Thus, the value used in the nucleation is obtained as:

$$I_{\text{cell,max}} = min(I_{\text{cell,max}}, I_{\text{cell,th}}) \tag{3.147}$$

Finally, it is important to avoid creating new numerical particles with a null statistical weight where no gaseous alumina is present, i.e., before combustiont. To do so, no particles are created in cells with temperature lower than 933 K or mass fractions of alumina lower than 0.0001.

The mass consumed in the cell expressed in Eq. (3.145) is directly removed from the gas. The energy given to the system by the nucleation process is obtained by multiplying the mass by the latent heat of condensation L_v:

$$Q_{\text{nucl}} = \dot{m}_{\text{nucl}} L_v \tag{3.148}$$

This heat is added to the gas energy equation.

The volume condensation growth rate is multiplied by the density to obtain the mass variation as:

$$\frac{dm_p}{dt}_{\text{cond,th}} = \frac{dv}{dt} \cdot \rho_{Al_2O_3} \tag{3.149}$$

This mass variation is added to the particle. Similarly to nucleation, a limiter is added to prevent the condensation process from over-consuming gaseous alumina. The amount

of mass in the cell is determined using Eq. (3.144). Since the mass variation of a particle determined in Eq. (3.149) is known, the maximum mass variation is easily calculated as:

$$\frac{dm_p}{dt}_{\text{cond,max}} = m_{Al_2O_3} = \rho Y_{Al_2O_3} V_{\text{cell}} \tag{3.150}$$

The used value for the particle mass variation is:

$$\frac{dm_p}{dt}_{\text{cond}} = \min\left(\frac{dm_p}{dt}_{\text{cond,th}}, \frac{dm_p}{dt}_{\text{cond,max}}\right) \tag{3.151}$$

Finally, the feedback of condensation on the gaseous phase is done using mass and energy source terms in the same way as for nucleation described previously.

There is one flaw inherent to the use of such an advanced condensation model in complex configurations such as those targeted in the current work. In the simplified configuration of one isolated particle, the region around the particle can be precisely discretized using a mesh similar to the one presented in figure 1.8. This gives accurate information on the gaseous environment around the particle and in particular gives the real value of $Y_{Al_2O_3}$ at the particle surface to be used in the nucleation and condensation models. This level of discretization is unachievable in the simulation of aluminum dust flames, where particles are represented as point sources in the Lagrangian solver. Thus, the nucleation and condensation source terms that are non linear functions of $Y_{Al_2O_3}$ are computed using diluted values of $Y_{Al_2O_3}$ in the cell containing the particle point source. This introduces an error in the model and should be kept in mind. A solution to correct this error without solving the particle surrounding flow is currently studied for future implementations.

3.6 Coagulation, agglomeration and radiation of the alumina products

3.6.1 Description of the physical phenomenon

The combustion product of aluminum combustion is alumina. Indeed, this combustion product comes from two different pathways which correspond to the two combustion modes of micrometric aluminum particles (see part 3.5.1).

The first pathway corresponds to homogeneous combustion. For this mode, aluminum evaporates from the liquid particle to burn with the oxidizer, forming intermediate aluminum oxides. These oxides are then converted into gaseous alumina that in turn condensates into liquid alumina. In the end, the liquid alumina is the only combustion product. This pathways is schematized in equation Eq. (3.152).

$$Al(g) + O_2(g) \rightarrow Al_xO_y(g) \rightarrow Al_2O_3(g) \rightarrow Al_2O_3(l) \tag{3.152}$$

This first burning pathway produces small nanometric alumina particles.

The second pathway is heterogeneous surface reactions. For this type of oxidation, the liquid aluminum reacts directly with the gaseous oxidizer to form liquid alumina directly at the surface of the particle that merges with the alumina cap. This second pathway is schematized in Eq. (3.153)

$$Al(l) + O_2(g) \rightarrow Al_2O_3(l) \tag{3.153}$$

This second burning pathway produces particles that are the size of the alumina cap. Therefore, the size of these residues is bigger if the surface reactions are predominant during combustion, and smaller if the homogeneous gaseous reactions are dominant. Thus, this residual size can range from nanometric to micrometric.

It is important to note that part of the alumina from gaseous reactions can move and coagulate on the alumina cap as can be seen on the experimental results of figure 1.7. This phenomenon increases the size of the alumina cap while reducing the number of alumina particles created by the gaseous reactions. In their work, Gallier et al. [41] explained these phenomena by a combination of aerodynamic and thermophoretic effects. A simplified model for mono-particle combustion was proposed and found to be in good agreement with experiment. A correlation between particle size and the fraction of alumina particles that is deposited on the alumina cap has been established and can be observed on figure 3.19.

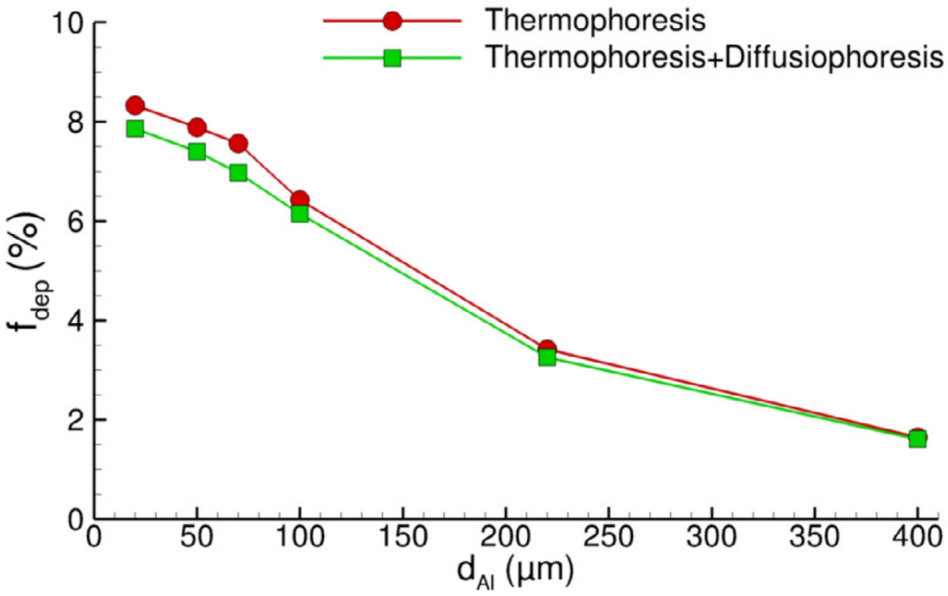

Figure 3.19 – Fraction of produced alumina deposited on a burning aluminum particle of diameter d_{Al} including thermophoresis only and thermophoresis + diffusiophoresis. Figure extracted from [41]

It can be observed in figure 3.19 that up to around 8 % of the alumina produced through gaseous reactions migrate to the alumina cap. This value is for a particle with a diameter of 20 μm. As the particle diameter increases, this percentage decreases. This can be explained by the fact that the bigger the particle is, the further away the flame envelope is from the particle. Thus, the alumina particles that nucleate in the flame are themselves further away from the particle, decreasing the number that can migrate to the burning aluminum particle.

This graph is for particles with a higher diameter than the ones used in the current work. Having such higher diameters means that in the work of Gallier et al. [41], the surface reactions are negligible and not accounted for. However, in the current work, these surface reactions play a major role.

It is difficult to predict exactly the impact of smaller burning particles with surface reactions on the fraction of alumina particles coming back to the burning aluminum particle. However, an hypothesis of a reduction in diameter is presented hereafter.

First, for smaller aluminum particles, the flame envelope is closer, which means that the alumina particles nucleate closer to the particle surface, favoring their migration to said surface.

Second, as previously discussed, surface reactions products migrate to the alumina cap, increasing its size. According to Gallier et al. [41], the thermophoresis flow has to go against the Stephan flow created by evaporation. However, since evaporation is inhibited by the presence of the alumina lobe on the surface of the aluminum core, this Stephan flow is expected to be weaker above the alumina cap. Therefore, by limiting the evaporation flow, the alumina cap makes the migration of combustion products from the gaseous phase to the particle surface easier, and the bigger it is, the more these products can migrate to the surface. Therefore, by increasing the alumina cap size, the heterogeneous surface

reactions may increase the flow of alumina particles going from the flame envelope to the burning particle.

Finally, still according to Gallier et al. [41], the thermophoresis-induced flow is by far more important than diffusiophoresis for the migration of alumina particles to the burning aluminum particle. This is illustrated in figure 3.19. Furthermore, thermophoresis is due to the existence of a gradient of temperature between the burning particle, that is cooled down by evaporation, and the surrounding flow. This gradient can be of several hundred degrees and can reach a thousand degrees depending on the burning conditions of the particle. But for smaller particles, the energy given by the surface reactions can considerably increase the particle temperature, reducing this gradient and therefore reducing the thermophoretic-driven flow of alumina products to the burning particle.

Without further investigation, it is difficult to evaluate which of these three effects induced by smaller burning particles most impact the migration of alumina products to the alumina cap.

In the current work, this migration has been neglected mainly due to the difficulty of including such an effect in the modeling of a dust flame. Furthermore, adding a thermophoretic effect for each particle would increase the calculation cost by a fair amount. Finally, this phenomenon would only slightly impact the flame properties as well as the morphology of the combustion products. However, this simplification must be kept in mind when analyzing the results.

Both the combustion products from the homogeneous gaseous reactions and the heterogeneous surface reactions are liquid alumina droplets of different radiuses. They interact with one another to form bigger particles, as schematized in figure 3.20 and described hereafter.

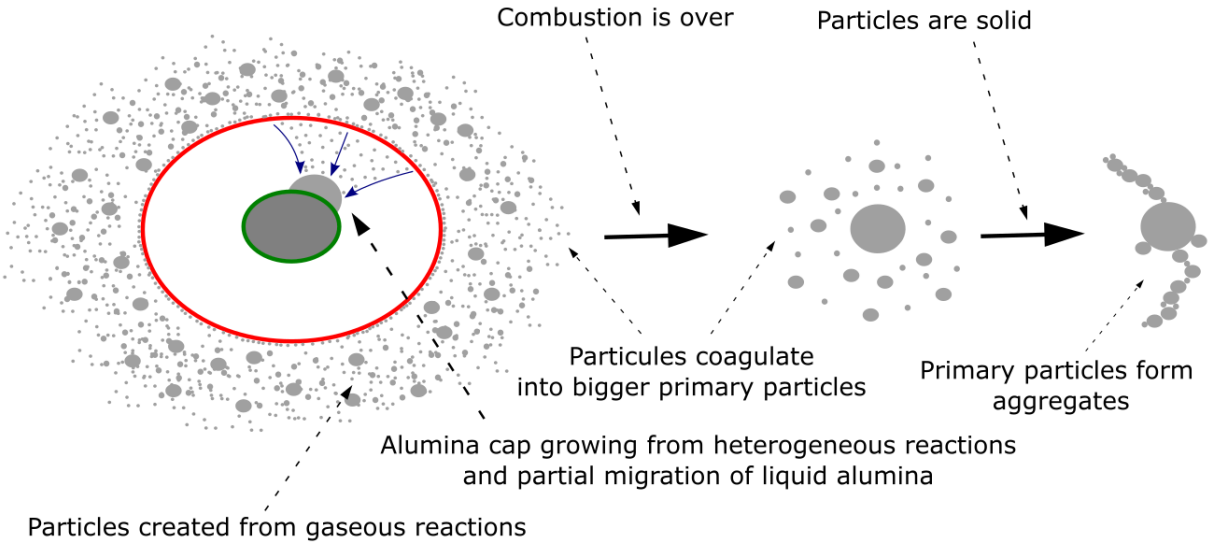

Figure 3.20 – Scheme of the process leading to the formation of alumina aggregates.

As long as the particle temperature remains above 2350 K, which is the fusion temperature of alumina, it stays liquid. As these liquid droplets meet one another, they coagulate into bigger liquid droplets. These spherical droplets are called primary particles.

These particles lose energy mostly through radiation and solidify as they reach a temperature of 2350 K. Once solid, these particles can still collide with one another but no longer coagulate into bigger spherical particles. Instead, when these solid particles collide they form aggregates.

Therefore, the final product of aluminum combustion is constituted of micrometric aggregates of nanometric primary particles. These aggregates have been experimentally observed and are visible in figure 3.21.

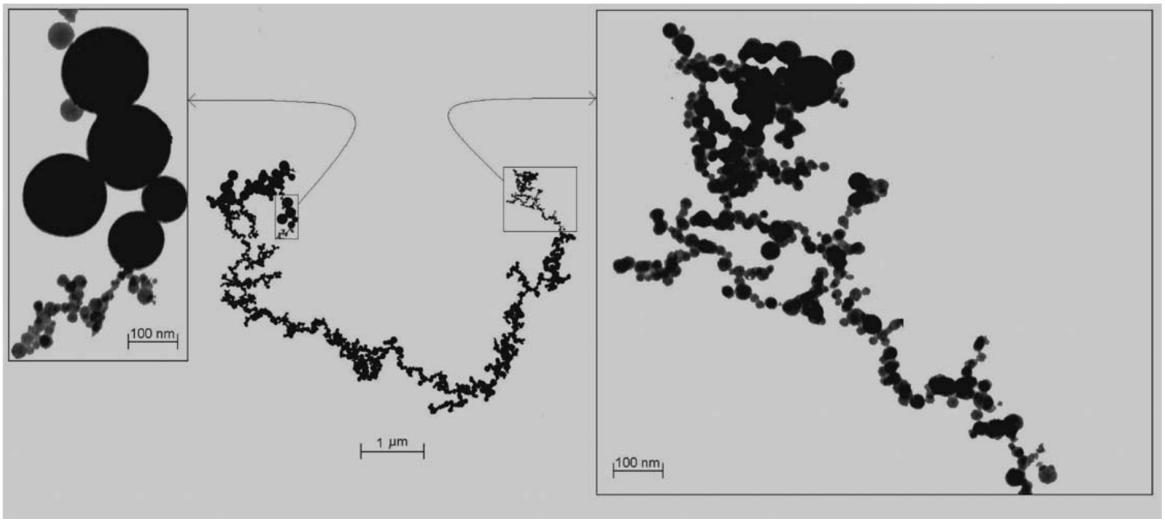

Figure 3.21 – TEM image of Al_2O_3 aggregate. Figure extracted from [68].

Finally, the combustion products are in the flame at a high temperature. Thus, they emit a lot of energy through thermal radiation.

3.6.2 Chosen model and implementation

The theoretical model chosen in the current work for the implementation of the coagulation of the liquid alumina is the exact same one proposed by Finke et al. [36]. It is described hereafter as it is in the original paper.

Just as for the condensation process, coagulation is driven by the collision theory and its rate is a function of the regimes that are in the number of three, characterized by the Knudsen number.

Kinetic regime: For $Kn \gg 1$, the coagulation kernel is based on the collision rate obtained using the kinetic theory of gases. It is therefore calculated in a similar way as the condensation rate expressed in equation Eq. (3.138). This coagulation rate is expressed as[36]:

$$\beta_{\text{kin}} = \mathcal{W}_{\text{kin}} \sqrt{\frac{\pi k_{\text{B}} T}{2\rho_l}} \sqrt{\frac{1}{v} + \frac{1}{w}} (d(v) + d(w))^2 \tag{3.154}$$

with d(w) the collision diameter computed as:

$$d(v) = \sqrt[3]{\frac{6v}{\pi}} \tag{3.155}$$

where $\mathcal{W}_{\text{kin}}$ is an enhancement factor that is detailed after.

Continuum regime: For $Kn \ll 1$, coagulation is caused by the diffusive Brownian motion of the collision partners. The coagulation kernel is computed as:

$$\beta_{\text{con}} = \mathcal{W}_{\text{con}} \frac{2k_{\text{B}}T}{3\mu} \left(\frac{C(v)}{d(v)} + \frac{C(w)}{d(w)} \right) (d(v) + d(w)) \tag{3.156}$$

where μ in the laminar dynamic viscosity of the gas mixture which is, in the current work, computed using the Sutherland law (see part 2.1.2). $C(v)$ is the Cunningham slip correction factor which results from an amendment to Stokes drag law [36]:

$$C = 1 + \text{Kn} \left(1.257 + 0.4 \times \exp\left(-\frac{1.1}{Kn} \right) \right) \tag{3.157}$$

Transition regime: For $Kn \sim 1$, the harmonic averaging, proposed by Pratsinis[93], of the two previous regimes is used to obtain :

$$\beta = \frac{\beta_{\text{kin}}\, \beta_{\text{con}}}{\beta_{\text{kin}} + \beta_{\text{con}}} \tag{3.158}$$

Using the same reasoning as for condensation, the harmonic averaging of equation Eq. (3.158) has been used for all the coagulating particles, just like in the work of Finke et al. [36].

Enhancement factors

These coagulation kernels are solely based on Brownian motion. The attractive or repulsive interactions dictated by the interstitial gas or electro-magnetic fields have to be accounted for. These interactions can either promote or impede collisions, which is accounted for using the enhancement factors calculated by Finke et al. [36]. The expression of said factors is given as :

$$\mathcal{W}(r_1, r_2, T) = 1 + (\alpha_1 + \alpha_2 T) \exp\left(\alpha_3 \ln\left(\frac{r_1}{r_2} \right)^2 \right) \times (\alpha_4 (r_1 + r_2) + 1)^{\alpha_5} \tag{3.159}$$

where the coefficients of the nonlinear fits are given in table 3.4.

Coefficients	Kinetic regime	Continuum regime
α_1	1.44	-2.85×10^{1}
α_2	-1.26×10^{-4}	-1.57×10^{-5}
α_3	-1.29×10^{-1}	-1.21×10^{-1}
α_4	4.84×10^{5}	3.54×10^{6}
α_5	-0.5	7.81×10^{-2}

Table 3.4 – Coefficients of the nonlinear fits of the coagulation enhancement factors. Table extracted from [36]

Using these coefficients in equation Eq. (3.159) gives the enhancement factors that can be used to compute $\mathcal{W}_{\text{kin}}$ and $\mathcal{W}_{\text{con}}$ in equations Eq. (3.154) and Eq. (3.156).

The calculated value of β in equation Eq. (3.158) is used in the Lagrangian tracking approach in the same way as in the work from Gallen et al. [39]:

1. In each cell, β is computed for each pair of particles and the maximum $\beta_{\max}$ is determined.
2. The acceptance-rejection method [42] is used: coagulation of a given pair of particles occurs if $r \leq \beta/\beta_{\max}$, where r $\in [0, 1]$ is a random number. If not, the pair does not coagulate, the operation is repeated until one coagulating pair is found [71].
3. The selected coagulation event is realized using the constant-number method [71] which is detailed below.

This coagulation process has been first implemented and used in AVBP by Lucien Gallen for the treatment of soot particles coagulation. The model is detailed in his PhD manuscript [38] and is described similarly hereafter.

The coagulation process follows the constant number approach, meaning that the number of numerical particles remains unchanged while their size and numerical weight are modified. A coagulation event for a pair of particles (i, j) characterized by their volume (v_i, v_j) and their numerical weight (ω_i, ω_j) is described in figure 3.22.

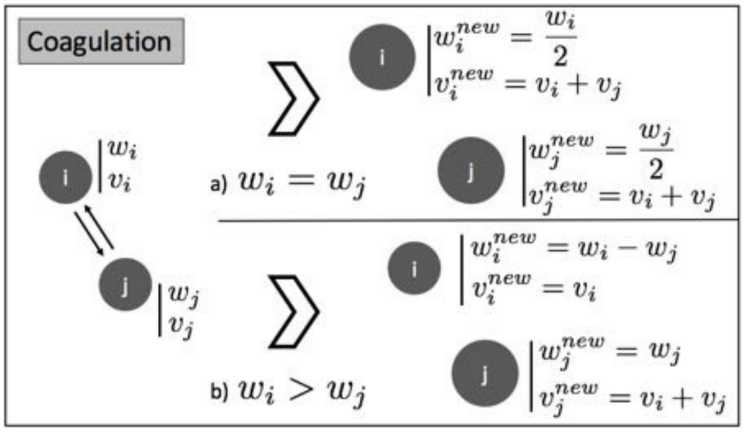

Figure 3.22 – Description of a coagulation event between two numerical (weighted) particles. Figure extracted from [38].

In figure 3.22, two cases are considered depending on the numerical weights of the colliding particles:

1. Both particles have the same numerical weight ($\omega_i = \omega_j$): half of the physical particles represented by the numerical particles collide. For both colliding numerical particles, coagulation induces a reduction by half of their numerical weight and a gain in mass which becomes the sum of the mass of both particles.
2. Different numerical weights ($\omega_i \neq \omega_j$): the entirety of the physical particles represented by the numerical particle with the smaller weight collide. After collision, the particle i has a numerical weight of $\omega_i - \omega_j$ and the particle j sees an increase in mass to ensure total mass conservation.

This process allows the coagulation process to be efficient in terms of computational cost while not affecting the density of the alumina particle population.

According to Gallen [38], an important limitation of such model is that it may underestimate the collision rate if the control volume and the numerical timestep are too big. This, in the case of Gallen [38] was not a problem since the simulation of turbulent sooting flames requires a fine mesh discretization, which induces in a compressible flow a very small acoustically-driven timestep.

In the current work, for aluminum combustion, the very stiff chemistry imposes a very small chemically-driven timestep coupled with a fine mesh. Therefore, the coagulation model is used in the correct setting.

Finally, due to a lack of time, no thermal radiation model for the combustion products has been implemented. If the impact on the flame characteristics is less important than for the sub-models implemented, it plays a major role in predicting the morphology of the combustion products. This is why a thermal radiation sub-model should be the next sub-model to be implemented.

In this chapter, the aluminum combustion phenomena have been studied in great detail. Each phenomenon involved in aluminum combustion has been discussed, along with the role it plays during combustion and their modeling. The implementations of these models in the current work has been presented. Several of these models have been developed for an isolated burning particle and were never used in a global model geared toward the numerical simulation of more complex dust flames. This will be done in the next chapters.

Chapter 4

Simulation of the combustion of an isolated aluminum particle

Previously, the phenomenology of aluminum combustion, as well as its implementation have been detailed. The obtained model is now first tested on the combustion of isolated aluminum particles to validate it as well as studying the many aspects implicated in this type of combustion.

Overview

4.1 Computational configuration

In this chapter, the combustion of an isolated aluminum particle is computed. The aim here is to validate the implemented model and to study the key aspects of this type of combustion.

To do so, the numerical particle is introduced into a cubic domain constituted of a single cubic cell of dimension $L \times L \times L$ with $L = 0.6$ mm and a domain volume $V = L^3 = 0.216$ mm^3. The particle is introduced at an initial temperature $T_{\mathrm{p},i}$ in air at temperature T_{g} and pressure p as illustrated in figure 4.1.

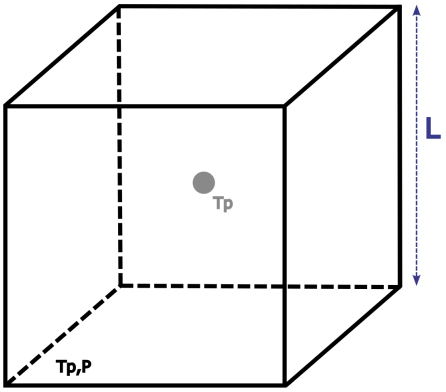

Figure 4.1 – Schematic of the single particle case used in this chapter

To obtain stoichiometry, the statistical weight of the numerical particle is adjusted. The determination of this statistical weight is detailed hereafter for a particle with a diameter of 7 μm at $T_{\mathrm{g}} = 2000K$.

The global reaction for aluminum combustion is:

$$4\mathrm{Al} + 3\mathrm{O_2} \rightarrow 2\mathrm{Al_2O_3} \tag{4.1}$$

The mass stoichiometric ratio can therefore be computed as:

$$s = \frac{Y_{\mathrm{O_2}}}{Y_{\mathrm{Al}}}\Big)_{st} = \frac{W_{\mathrm{O_2}}}{W_{\mathrm{Al}}}\frac{\nu_{\mathrm{O_2}}}{\nu_{\mathrm{Al}}}\Big)_{\mathrm{st}} = \frac{0.03199}{0.02698} \cdot \frac{3}{4} \approx 0.89 \tag{4.2}$$

Then, the equivalence ratio is equal to:

$$\Phi = s\frac{Y_{\mathrm{Al}}}{Y_{\mathrm{O_2}}} = s\frac{m_{\mathrm{Al}}}{m_{\mathrm{O_2}}} \tag{4.3}$$

The total mass of oxygen can be easily obtained because the gas phase is air:

$$m_{\mathrm{O_2}} = Y_{\mathrm{O_2}} m_{\mathrm{a}} \tag{4.4}$$

where m_{a} is the mass of air in the domain computed using the ideal gas law:

$$PV = nRT \Rightarrow m_{\mathrm{a}} = \frac{PVW_{\mathrm{a}}}{RT} = 3.7626 \cdot 10^{-11} \text{ kg} \tag{4.5}$$

The total mass of aluminum in the domain can be expressed as:

$$m_{\mathrm{Al}} = n_{\mathrm{p}} m_{\mathrm{p,Al}} \tag{4.6}$$

where n_{p} is the total number of particles in the domain while $m_{\mathrm{p,Al}}$ is the mass of aluminum contained in each particle. According to Zhang et al. [114], the thickness of the external alumina layer is 4 nm. Therefore, for a particle of 7 μm in diameter, which is the diameter used in the present work, unless otherwise mentionned:

$$V_{\mathrm{p}} = V_{\mathrm{p,Al}} + V_{\mathrm{p,Al_2O_3}} \tag{4.7}$$

where $V_{\mathrm{p,Al}}$ and $V_{\mathrm{p,Al_2O_3}}$ are the volume in each particles of aluminum and alumina respectively which, because the aluminum core is spherical, can be computed as:

$$V_{\mathrm{p}} = \frac{4}{3}\pi(3.5 \cdot 10^{-6})^3 = 1.7959 \cdot 10^{-16}\ \mathrm{m}^3 \tag{4.8}$$

$$V_{\mathrm{p,Al}} = \frac{4}{3}\pi(3.496 \cdot 10^{-6})^3 = 1.7898 \cdot 10^{-16}\ \mathrm{m}^3 \tag{4.9}$$

$$V_{\mathrm{p,Al_2O_3}} = V_{\mathrm{p}} - V_{\mathrm{p,Al}} = 6.1 \cdot 10^{-19}\ \mathrm{m}^3 \tag{4.10}$$

The mass of aluminum $m_{\mathrm{p,Al}}$ and alumina $\mathrm{m_{p,Al_2O_3}}$ in each particle are easily obtained as:

$$m_{\mathrm{p,Al}} = V_{\mathrm{p,Al}} \cdot \rho_{\mathrm{Al}} = 1.7898 \cdot 10^{-16} \cdot 2236 = 4.0020 \cdot 10^{-13}\ \mathrm{kg} \tag{4.11}$$

$$m_{\mathrm{p,Al_2O_3}} = V_{\mathrm{p,Al_2O_3}} \cdot \rho_{\mathrm{Al_2O_3}} = 6.1 \cdot 10^{-19} \cdot 3000 = 1.83 \cdot 10^{-15}\ \mathrm{kg} \tag{4.12}$$

$$m_{\mathrm{p}} = m_{\mathrm{Al}} + m_{\mathrm{Al_2O_3}} = 4.0203 \cdot 10^{-13}\ \mathrm{kg} \tag{4.13}$$

From these masses, the mass fractions of each species in each particle can be computed:

$$Y_{\mathrm{p,Al}} = \frac{4.0020 \cdot 10^{-13}}{4.0203 \cdot 10^{-13}} = 0.9954 \tag{4.14}$$

$$Y_{\mathrm{p,Al_2O_3}} = 1 - Y_{\mathrm{p,Al}} = 0.0046 \tag{4.15}$$

Thus, it is interesting to note that for most of the cases in the current work, the particle is composed of 99.54 % of aluminum in its initial state. This initial composition could therefore be neglected in the simulations without having an important impact on the results. Since the ability to account for both species has already been implemented to account for presence of the lobe (see part 3.2), it is easy to account for the initial dual-composition of the particle.

Finally, Eq. (4.3) can be rewritten and using the values previously computed for a particle with a diameter of 7μm at $\mathrm{T_g} = 2000\mathrm{K}$ as an example gives:

$$\Phi = s\frac{n_{\mathrm{p}} m_{\mathrm{p,Al}}}{m_{\mathrm{O_2}}} \Rightarrow n_{\mathrm{p}} = \frac{\Phi m_{\mathrm{O_2}}}{s m_{\mathrm{p,Al}}} = 24.53\ \mathrm{ptcls} \tag{4.16}$$

Therefore using the stochastic approach, the number of physical particles can be adjusted to the different conditions needed without having to change the size of the domain or the number of numerical particles.

4.2 Temperature and mass fractions

The first study case is at a gaseous temperature of 2000 K with an initial particle temperature of 300 K. The aim here is to replicate a particle transported by fresh gases arriving in a hot flame front. Figure 4.2 represents the evolution in time of the temperature of both the aluminum particle and the gas phase, as well as the mass fractions of both aluminum $Y_{p,Al}$ and alumina Y_{p,Al_2O_3} in the particle.

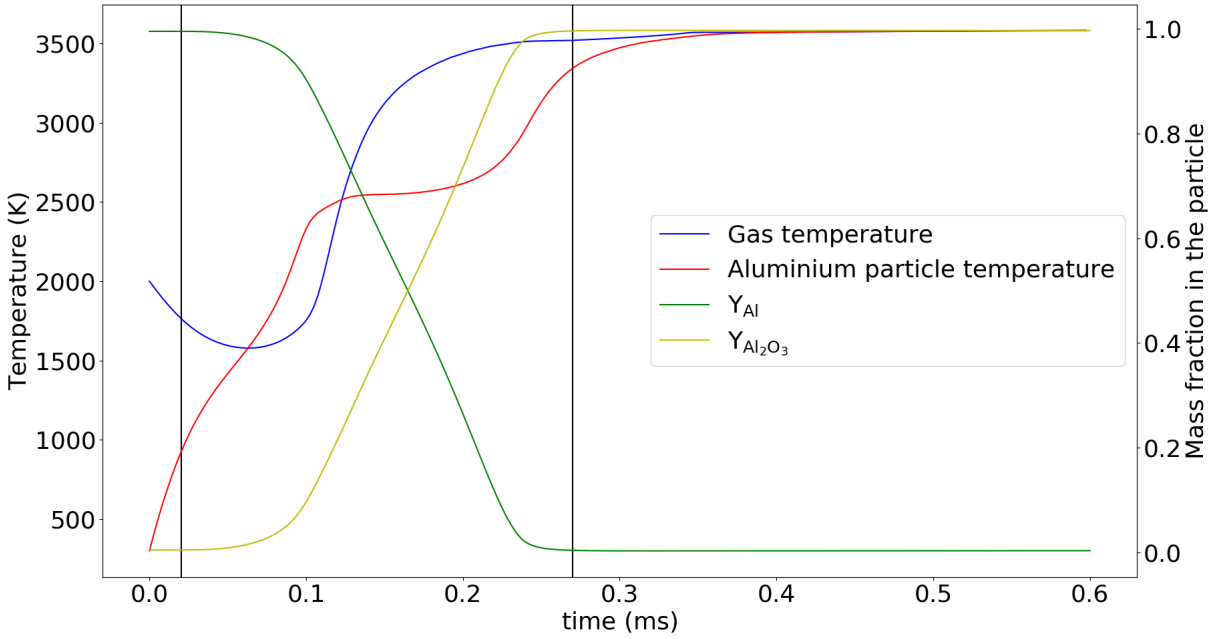

Figure 4.2 – Evolution of the gas temperature and the mass fractions of Al and Al_2O_3 during the combustion of an aluminum particle. The black vertical lines delimit the combustion time.

Figure 4.2 shows that the gas temperature starts at 2000 K but slowly decreases as the particle absorbs energy during its preheating phase. When the particle temperature reaches 933 K, the heterogeneous surface reactions start, which contributes to an increase of particle temperature. The surface reaction consumes liquid aluminum and gaseous oxygen and produces liquid alumina on the particle surface. Therefore, the aluminum mass fraction decreases, while the alumina mass fraction increases.

The aluminum particle temperature keeps increasing while the gas temperature keeps decreasing until a minimum is reached at 1579 K. From this point, the particle in turn heats up the gas thanks to the surface reaction which produces heat. Once the particle reaches the temperature of 1718 K, which corresponds to the empirical ignition temperature, the evaporation process starts and so do the homogeneous gaseous reactions.

The increase of the particle temperature slows down as the evaporation rate increases, therefore absorbing a lot of the energy generated by the surface reaction. Meanwhile the evaporated aluminum keeps reacting in the gaseous phase. Thus, the temperature of the gaseous phase continues to increase and becomes greater than the temperature of

the particle, which then receives again heat from the gas. Finally, both gas and particles reach the same temperature of 3569 K.

After the particle has finished burning and its mass fraction of aluminum is zero, the gas temperature keeps slowly increasing. This is due to the condensation model that slows down when the gaseous mass fraction of alumina decreases. Moreover, the concentration of Al_2O_3 in the gas has a major impact on the gaseous chemistry and the gas temperature. We believe that this is unrealistic and an improvement in the implementation of the condensation model proposed in the current work should be proposed in future work. However, this only creates a minor temperature variation.

Please note that in the current case, the particle is not transferred to the second subset. This is because there is no need to reduce calculation cost in 0D by transfering the particle to the second subset. For the simulations in Chapter 5 and of the current work, once the aluminum particle has fully become an alumina particle, it is transferred to the second subset.

4.3 Characteristic combustion time

As explained in part 1.1, the characteristic burning time for an isolated aluminum particle has been experimentally studied and is considered as a key result for this type of combustion. From these experimental results, several correlations have emerged to empirically predict the characteristic combustion time as a function of the initial values of gaseous environment composition, temperature or pressure. It is interesting to compare the characteristic combustion time obtained in the current work to these empirical relations.

An aluminum particle with a smaller diameter than 1 μm exclusively burns through heterogeneous surface reactions while for particles with a diameter larger than 10 μm, homogeneous gaseous reactions are dominant. For the nanometric particles, Huang et al. [58] proposed a correlation but this is not applicable here due to the presence of gaseous reactions.

For particles with a diameter higher than 10 μm, the correlation proposed by Beckstead et al. [11] is often used. This characteristic combustion time can be expressed for combustion in air as:

$$\tau_{\text{Beckstead}} = 0.00735 \frac{d_p^{1.8}}{X_{O_2} T_g^{0.2}} \tag{4.17}$$

with d_p in μm, and X_{O_2} the oxygen mole fraction. The characteristic combustion time $\tau_{\text{Beckstead}}$ is expressed in ms.

As explained in part 1.1, a more recent formulation for the characteristic burning time of aluminum has been proposed by Braconnier et al. [18], which for combustion in air is expressed as:

$$\tau_{\text{Braconnier}} = \frac{0.002 d_p^{1.75}}{(X_{O_2} - 0.032 X_{N_2}) P^{0.007}} \tag{4.18}$$

with d_p in μm, X_{O_2} and X_{N_2} the oxygen and nitrogen mole fraction and P the pressure in Pascal.

For the particles studied in the current work, both the surface and gaseous reactions come into play and none of the previously mentioned correlations are directly applicable. It is indeed difficult to obtain an expression for the characteristic combustion time that would cover the transition regime where both the surface reactions and the gaseous reactions have an impact. However the comparison to the combustion time obtained in the current work and delimited by the black lines in figure 4.2 is interesting. It is found equal to $\tau_{num} = 0.25$ ms, i.e., close to the values of 0.254 ms and 0.301 ms obtained with the correlations proposed by Beckstead and Braconnier, respectively. This constitutes a first validation of the proposed model.

It is important to keep in mind that both of these correlations are here outside their application range, but not by a lot. Yet, they give similar results to the characteristic combustion time obtained in the current work.

4.4 Heat release and temperature

Let us now quickly consider the heat release rate plotted in figure 4.3.

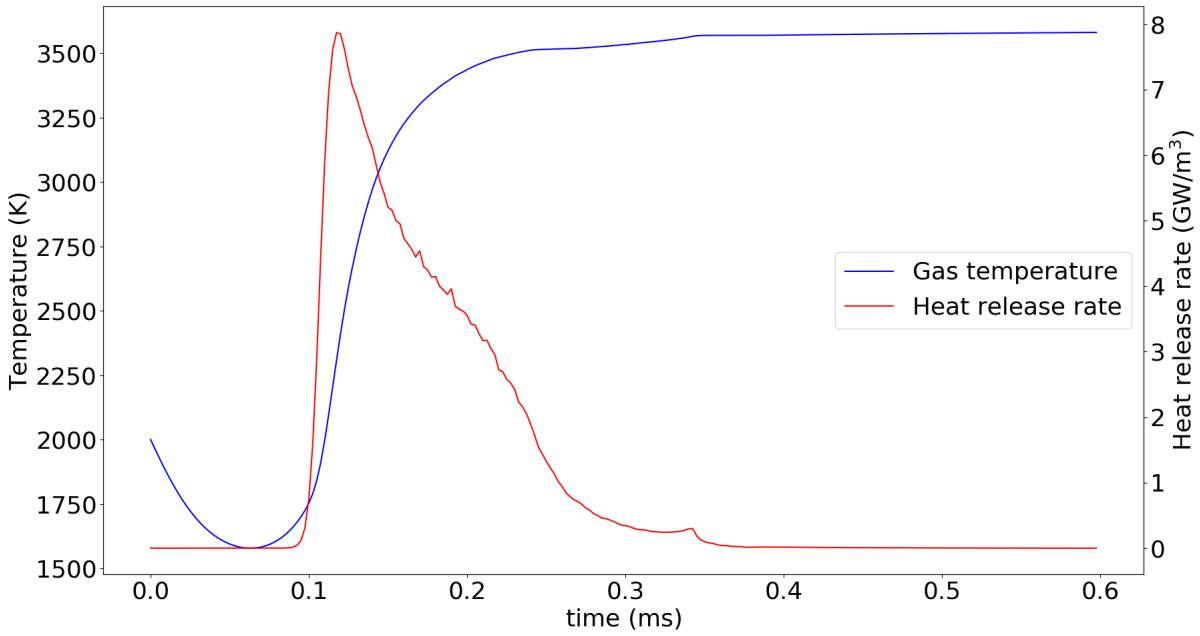

Figure 4.3 – Evolution of the gas temperature and the heat release rate during the combustion of an isolated aluminum particle.

The initial decrease in temperature in figure 4.3 is due to the warming up of the particle. As the evaporation starts, the heat release rate becomes increasing extremely fast as the evaporation is sustained by the heat from the surface reactions while the gaseous reactions are extremely fast. The total heat release rate finally peaks at 7.87 GW/m^3 at t = 0.117 ms. Finally, the total heat release rate then decreases progressively to reach zero while the gas temperature reaches its maximum.

4.5 Evolution of the aluminum particle, importance of the surface reactions

The general morphology of the burning aluminum particle is studied here. To do so, the evolution of the diameter of the particle and the liquid mass fractions of aluminum and alumina are plotted in figure 4.4

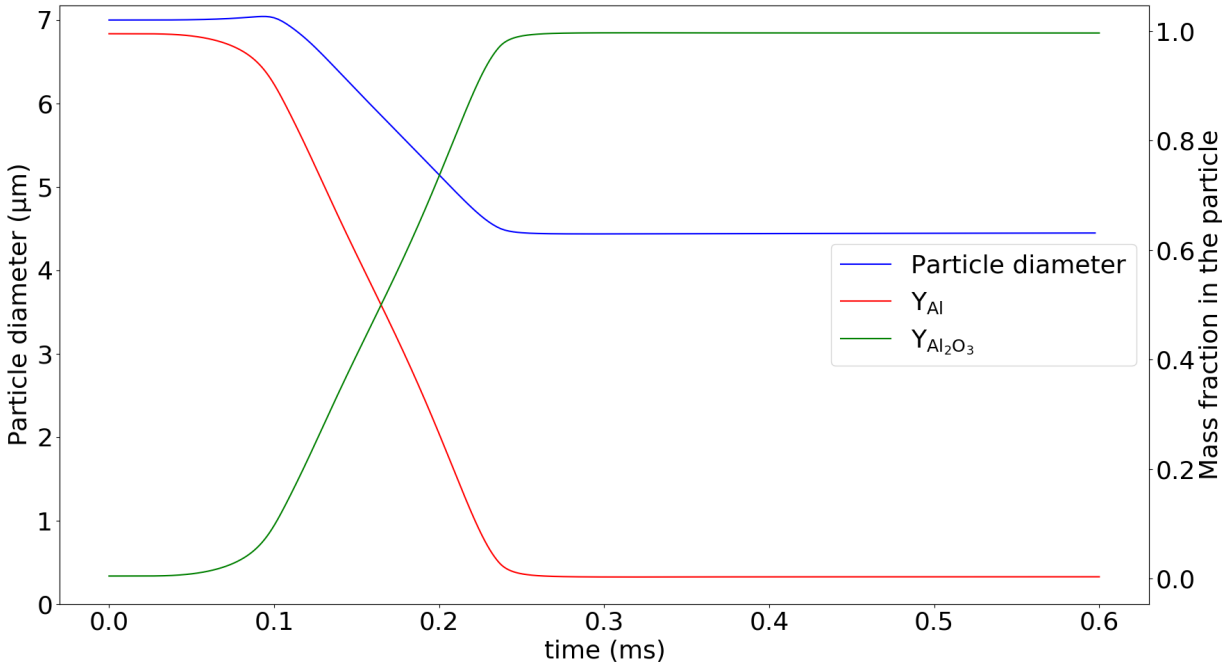

Figure 4.4 – Evolution of the particle diameter and the mass fractions of aluminum and alumina in the particle.

In figure 4.4, at first, the surface reactions consume the liquid aluminum with gaseous oxidiser to produce liquid alumina on the particle. Thus, the mass of aluminum atoms in the particle stays constant while gaseous oxygen is absorbed to form alumina, increasing the diameter of the particle. Furthermore, alumina has a greater density at $\rho_{Al_2O_3} = 3000\text{kg} \cdot \text{m}^{-3}$ than aluminum at $\rho_{Al} = 2236\text{kg} \cdot \text{m}^{-3}$, therefore, even as the evaporation slowly begins to happen, the particle diameter keeps growing. Once the gaseous reactions become clearly dominant, the radius of the particle starts decreasing. It keeps doing so as all the aluminum is either evaporated or consumed by surface reactions.

As the particle reaches its final diameter $d_p = 4.44\ \mu\text{m}$, all the aluminum has been consumed while only the alumina from the surface reactions and the initial external layer remain. In reality, a part of the condensed alumina in the gas phase would migrate to the particle lobe. Since it is not the case here, and the quantity of initial alumina from the external layer is known, the obtained final diameter may be used to deduce which percentage of the combustion has happened in the form of surface reactions or gaseous reactions. Indeed, as calculated in part 4.1, the initial mass of aluminum in a particle is $m_{p,Al}^{init} = 4.0020 \cdot 10^{-13}$ kg and the initial mass of alumina in the particle is

$m^{init}_{p,Al_2O_3} = 1.83 \cdot 10^{-15}$ kg. The global reaction for aluminum at stoichiometry is:

$$4Al + 3O_2 \rightarrow 2Al_2O_3 \tag{4.19}$$

meaning that at stoichiometry, which is the case here, 4 moles of Al will produce 2 moles of Al_2O_3. Therefore, the total amount of Al_2O_3 produced can be computed as:

$$n^{end}_{Al_2O_3} = \frac{1}{2} n^{end}_{Al} = \frac{1}{2} \frac{m^{init}_{p,Al}}{W_{Al}} = 7.4165 \cdot 10^{-12} \text{mol} \tag{4.20}$$

Meanwhile, the obtained final quantity of Al_2O_3 in the particle can be computed from the final diameter as:

$$n^{end}_{p,Al_2O_3} = \frac{V^{end}_{p,Al_2O_3} \cdot \rho_{Al_2O_3}}{W_{Al_2O_3}} = 1.348 \cdot 10^{-12} \text{mol} \tag{4.21}$$

Since all the obtained alumina in the particle is either the product of the surface reactions or the initial alumina layer from before the combustion, the percentage of the part of alumina created from these surface reactions can be obtained as:

$$\frac{n^{end}_{p,Al_2O_3} - n^{init}_{p,Al_2O_3}}{n^{end}_{Al_2O_3}} \cdot 100 = 17.9 \ \% \tag{4.22}$$

According to Glorian et al. [47], for particles with an initial diameter of 10 μm, the surface reactions account for 28 % of the combustion (see figure 1.12a). Since the importance of the surface reactions diminishes as the initial diameter of the particles gets smaller, in the current case, the surface reactions should account for a little bit more than 28 % of the combustion. Therefore, with only 17.9 % of the combustion coming from surface reactions, the model implemented in the current work undermines the importance of surface reactions.

Let us now analyze further the impact and behavior of these surface reactions.

4.6 Key role of heterogeneous surface reactions

To better understand the role of these surface reactions, the energy source terms for surface reactions $\dot{Q}_{HSR}$, thermal transfer $\dot{Q}_{th}$ and evaporation $\dot{Q}_{evap}$ are plotted in figure 4.5.

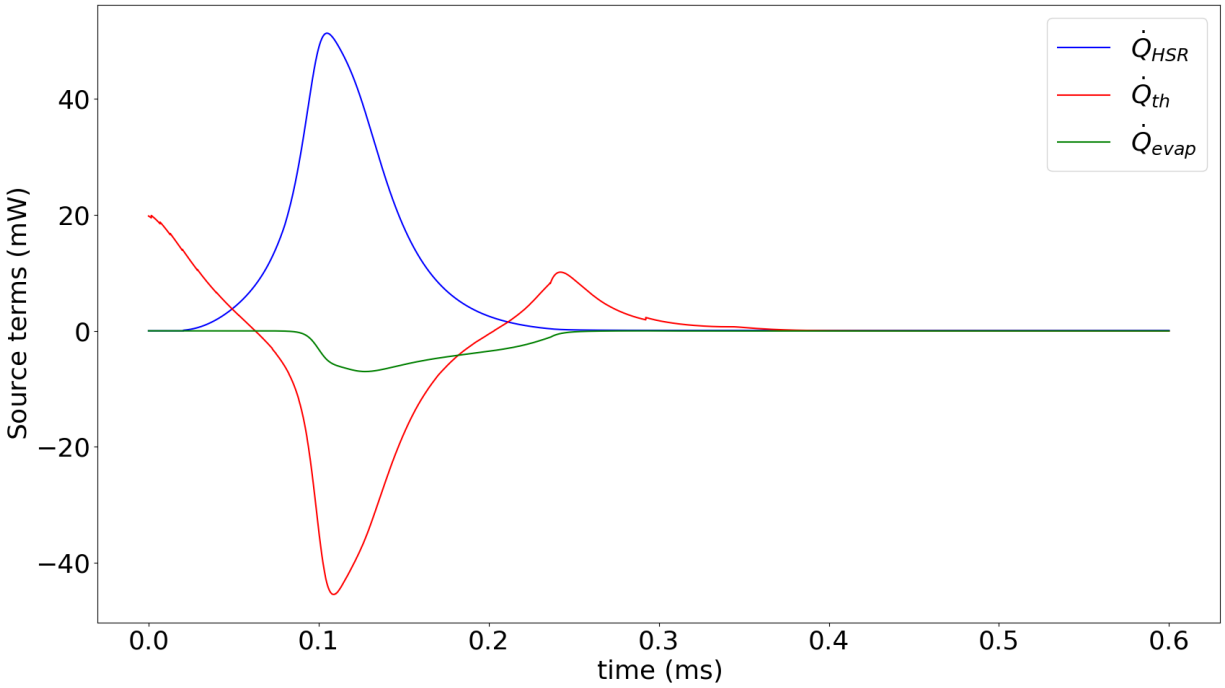

Figure 4.5 – Evolution of the energy source terms for surface reactions $\dot{Q}_{HSR}$, thermal transfers $\dot{Q}_{th}$ and evaporation $\dot{Q}_{evap}$.

In figure 4.5, we can see the role of the three source terms having an impact on the particle temperature.

The first source term $\dot{Q}_{HSR}$ corresponds to the heating of the particle by heterogeneous surface reactions (HSR) and is computed using equation Eq. (3.49). The second source term $\dot{Q}_{th}$ corresponds to the thermal transfer of the particle with the gaseous phase. This transfer includes conduction, convection and radiation. The last source term $\dot{Q}_{evap}$ is the energy required for evaporation.

At first, as can be seen in figure 4.2, the particle temperature is lower than the gaseous temperature. Thus, $\dot{Q}_{th}$ is positive as the gas is heating up the particle. The term $\dot{Q}_{HSR}$ starts growing at $t = 2.05 \cdot 10^{-2}$ms, heating the particle, this term is always positive. Due to this last source term, the particle temperature goes higher than the temperature of the gaseous phase at $t = 6.27 \cdot 10^{-2}$ms. Therefore, $\dot{Q}_{th}$ becomes negative at that time as the particle is now giving energy to the gas phase. It is interesting to note that as $\dot{Q}_{HSR}$ increases, so does proportionally inversely $\dot{Q}_{th}$, meaning that the excess energy of the surface reactions is indirectly heating up the gas. As expected, the evaporation source term $\dot{Q}_{evap}$ is negative and largely dominated by $\dot{Q}_{HSR}$, highlighting the fact that the evaporation is accelerated by the surface reactions. Finally, when the gas temperature becomes higher than the particle temperature, $\dot{Q}_{th}$ becomes positive again until both temperatures equilibrate with one another.

This underlines the double role of heterogeneous reactions. First, they indirectly heat the gas phase. Second, they accelerate considerably the evaporation of the particle by heating it.

4.7 Combustion without heterogeneous surface reactions

A simple way to study the impact of surface reactions on the simulation is to simply remove them and see the direct effect. To compare with and without surface reactions, we need to modify the initial conditions because if we consider a particle at a temperature $T_p = 300K$ in a gaseous phase at a temperature $T_g = 2000K$, the combustion simply cannot happen as illustrated on figure 4.6

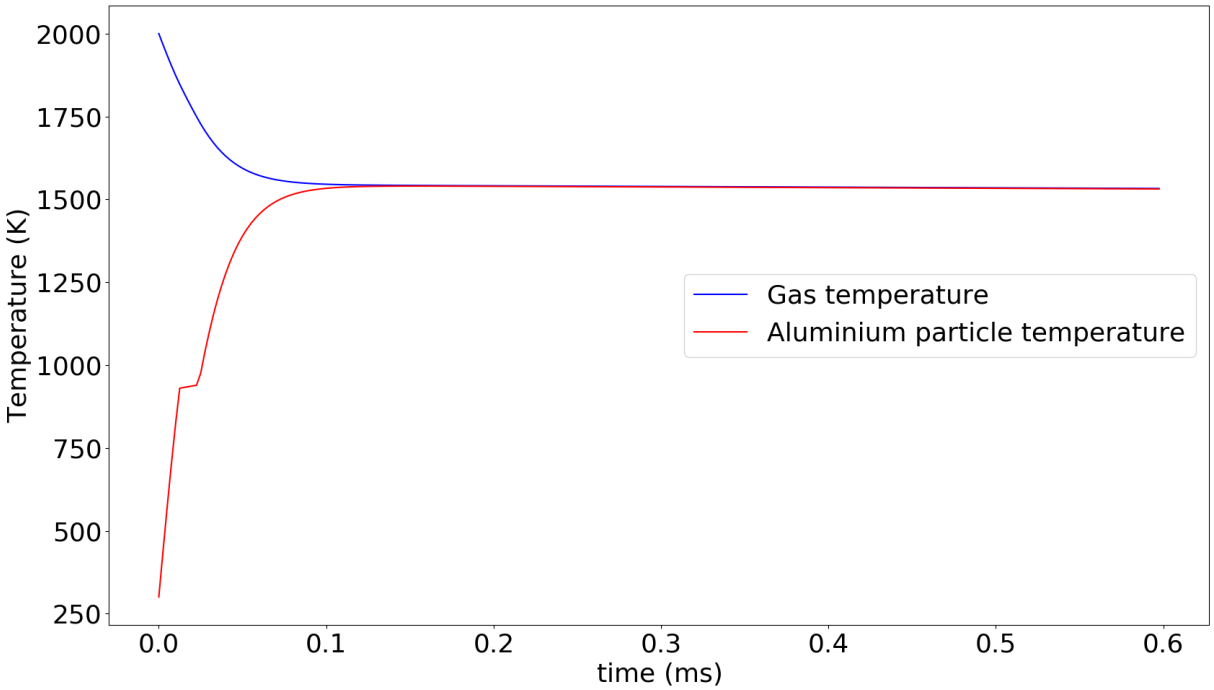

Figure 4.6 – Evolution of the gas and particle temperature without heterogeneous reactions.

The figure 4.6 is shown here to underline the importance of the surface reactions in the ignition process. Indeed, at 933 K, the aluminum core of the particle melts which leads to an increase in its volume which in turn starts breaking the outer alumina layer. The partially exposed aluminum surface can then react via surface reactions therefore increasing the particle temperature up to 1718 K, which corresponds to the empirical ignition temperature of aluminum. In the simulation without surface reactions, the gas temperature decreases as it heats the liquid particles. The temperature of said particle increases to reach a temperature of 933 K where in the complete model the surface reactions would start heating up the particle to the empirical ignition temperature, as illustrated in figure 4.2. In the current simulation, the surface reactions are not accounted for and nothing happens past $T_p = 933K$ to further heat the particle. The particle temperature keeps rising due to heat exchange with the gas phase until its temperature reaches an equilibrium with the gas phase at 1542 K, which is lower than the ignition temperature. Therefore, the surface reactions play a key role in the ignition of the particle.

To compare the combustion with and without surface reactions, the initial conditions need to be changed in order to reach the ignition temperature even without surface reactions. To do so, the initial temperature of the particles have been modified from 300 K to 2000 K so the particles can ignite at t_0.

The obtained comparison between the cases with and without heterogeneous surface reactions (HSR) is visible in figure 4.7.

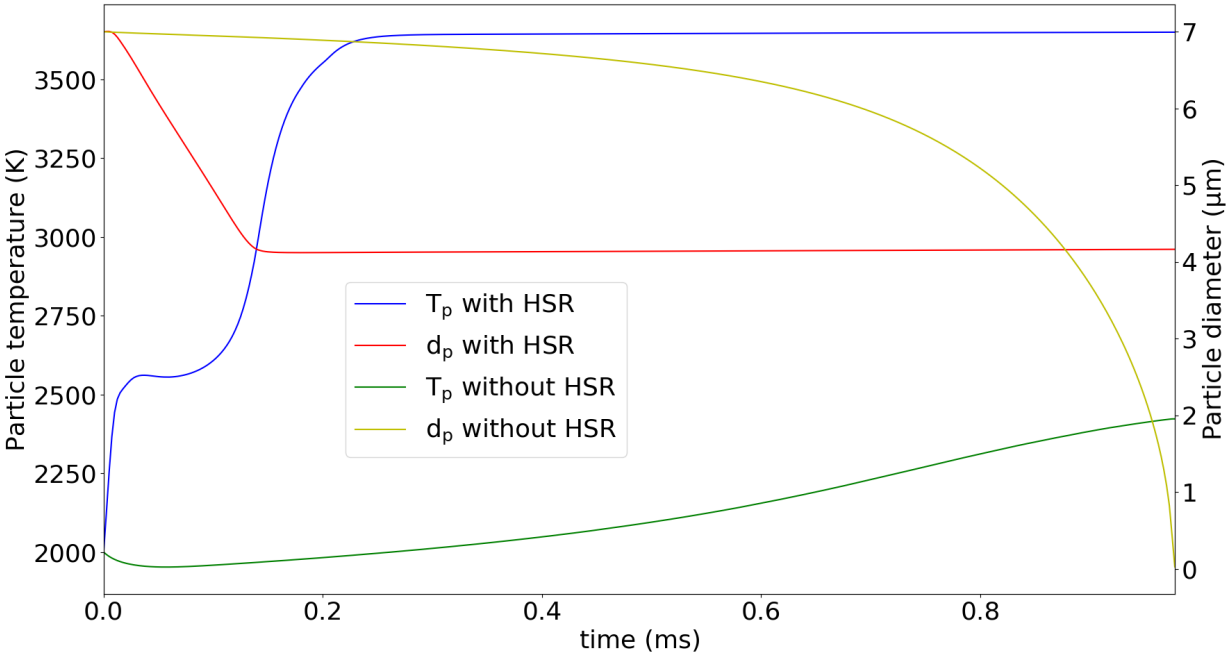

Figure 4.7 – Evolution of the diameter and temperature of an aluminum particle burning with and without heterogeneous surface reactions (HSR).

In figure 4.7, the impact of the surface reactions is clearly visible. Indeed, without the surface reactions, the particle temperature first drops 48 degrees due to the energy required by the evaporation process. Once the homogeneous gaseous reactions start, they heat up the particle which compensates for evaporation. The particle then slowly heats up as it keeps burning up to 2422 K where it finishes evaporating.

In comparison, the temperature of the burning particles with surface reactions rises sharply due to the heat provided by these reactions. The evaporation is therefore also much faster and so are the gaseous reactions that are controlled by this evaporation rate. This results in a much faster global combustion rate and shorter characteristic combustion time.

For the characteristic combustion time without surface reactions, let us consider the combustion to have ended when all the aluminum has evaporated because of the fast chemistry. The only remaining of the particle burning without surface reactions is the alumina from the initial alumina layer while the remaining of the particle with surface reactions also contains the alumina produced by these reactions. In these conditions, the combustion time for particles with surface reactions is 0.218 ms versus 0.978 ms without surface reactions.

4.8 Impact of condensation of alumina on the flame

As explained in part 3.5, condensation of alumina plays a major role in aluminum combustion. First, the energy released by the condensation process itself increases the flame temperature by several hundred degrees. Then, by removing alumina from the gas phase, it enhances the conversion of all the other intermediary oxides into alumina through exothermic reactions.

Regarding the energy generated by the condensation process itself, the heat release of the nucleation and condensation processes are plotted and compared to the gaseous heat release in figure 4.8.

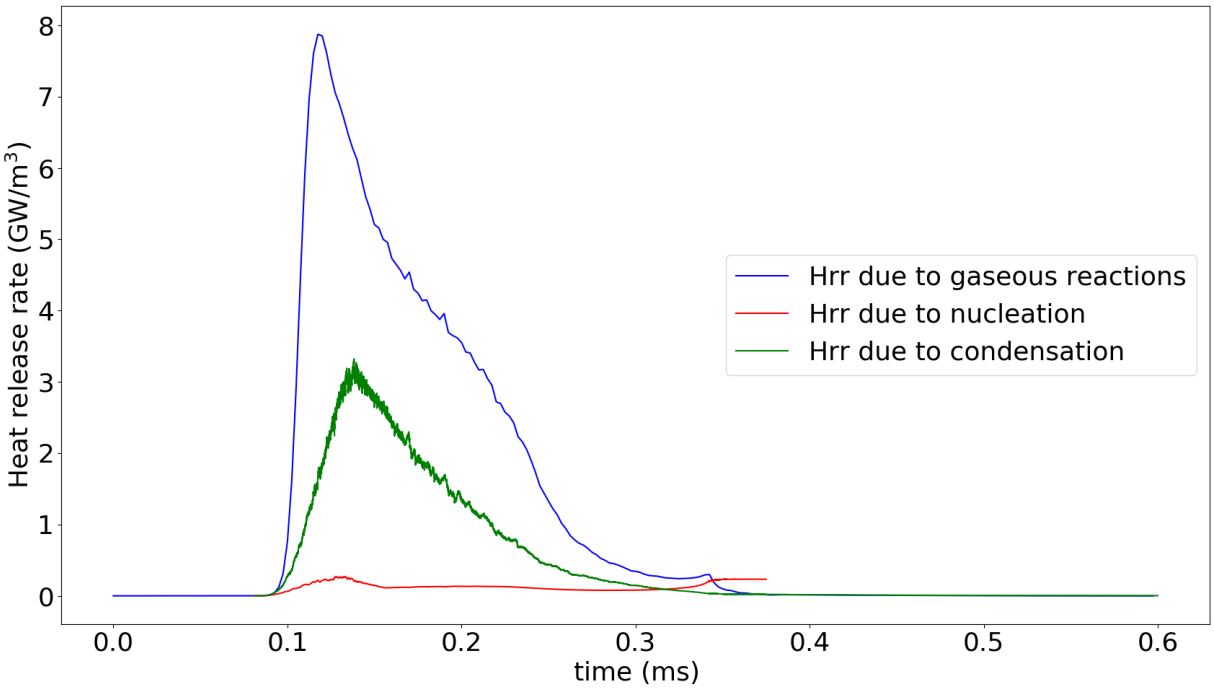

Figure 4.8 – Evolution of the heat release rates (Hrr) due to the gaseous reactions, nucleation and condensation.

In figure 4.8, the heat release rate of the gaseous reactions is compared to the heat release rates of nucleation and condensation that account together for the energy released by the global condensation of the gaseous alumina into liquid droplets.

First, if nucleation is essential for condensation to happen, the associated heat release rate is negligible in comparison to condensation and reactions. Therefore this contribution could be neglected with almost no impact on the flame.

Secondly, the heat release rate due to condensation is about half the heat release due to the gaseous reactions. This highlights the importance of accounting for the heat release rate of condensation.

Another way of directly measuring the impact of condensation on the combustion is to simply remove it. In figure 4.9, the combustion characteristics of an isolated aluminum particle in the same conditions as in figure 4.2 but without nucleation and condensation, are presented.

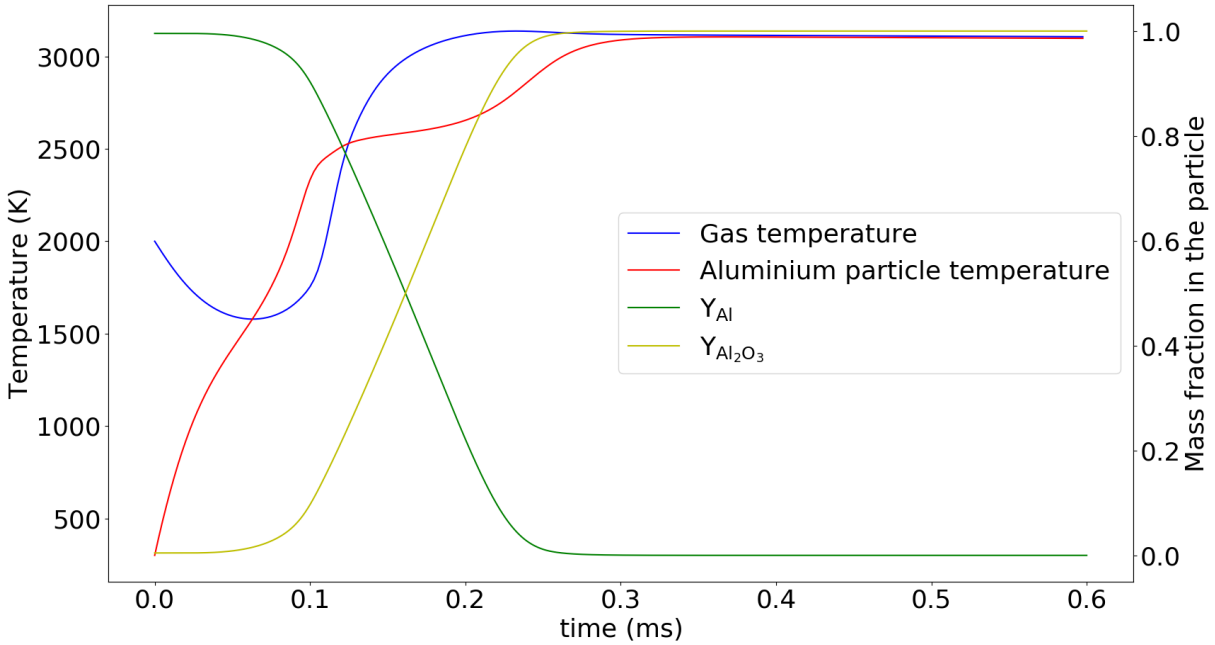

Figure 4.9 – Evolution of the gas temperature and the mass fractions of Al and Al_2O_3 during the combustion of an aluminum particle without nucleation or condensation.

Comparing figure 4.9 with figure 4.2 shows that condensation most important impact is on the final temperature, which is of 3114 K without condensation vs 3569 K with condensation. This means that condensation is directly and indirectly responsible for a rise in temperature of 455 K in the present case. "Directly" refers to the energy released by the condensation itself and visible in figure 4.8 while "indirectly" refers to the impact that condensation has on the gaseous chemistry.

4.9 Final equilibrium and condensation

It is of high interest to study the concentration of species during the reactions. Furthermore, a major argument for aluminum combustion as a renewable fuel is the fact that the only combustion product remaining is liquid alumina at stoichiometry (see part 3.5).

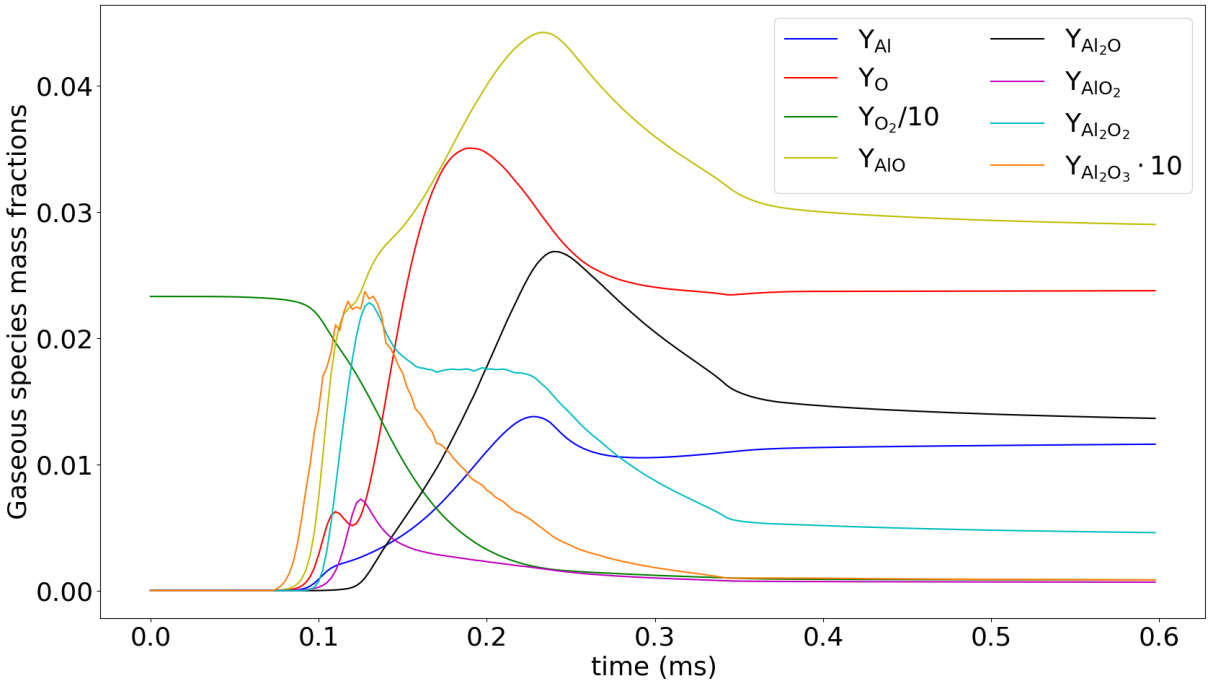

Figure 4.10 – Evolution of the gaseous species mass fractions during the combustion of an aluminum particle.

The evolution of the species mass fractions during the combustion is plotted in figure 4.10. As may be seen, at the end of calculation, several species and especially AlO remain in the gas phase with mass fractions up to 0.03 despite the fact that there is no longer any gaseous alumina in the gas phase. There should not be any residuals in the gas phase once the combustion is over. In the literature, the kinetic scheme is used with an instantaneous condensation reaction (see table 3.3 as an example) of the type:

$$Al_2O_3(g) \rightarrow Al_2O_3(l) \tag{4.23}$$

with Arrhenius coefficients $A = 10^{14}$ and an activation energy of zero. Trying to understand why residuals are left in the current work, we have done a similar simulation for which the results are plotted in figure 4.10. This time, we did not use our nucleation/condensation model and instead used a similar instantaneous condensation reaction as what is used in the literature. The only difference is that the Arrhenius coefficients have been decreased down to $A = 10^{10}$ to prevent numerical stiffness. The gaseous species mass fractions obtained with this instantaneous condensation are available in figure 4.11.

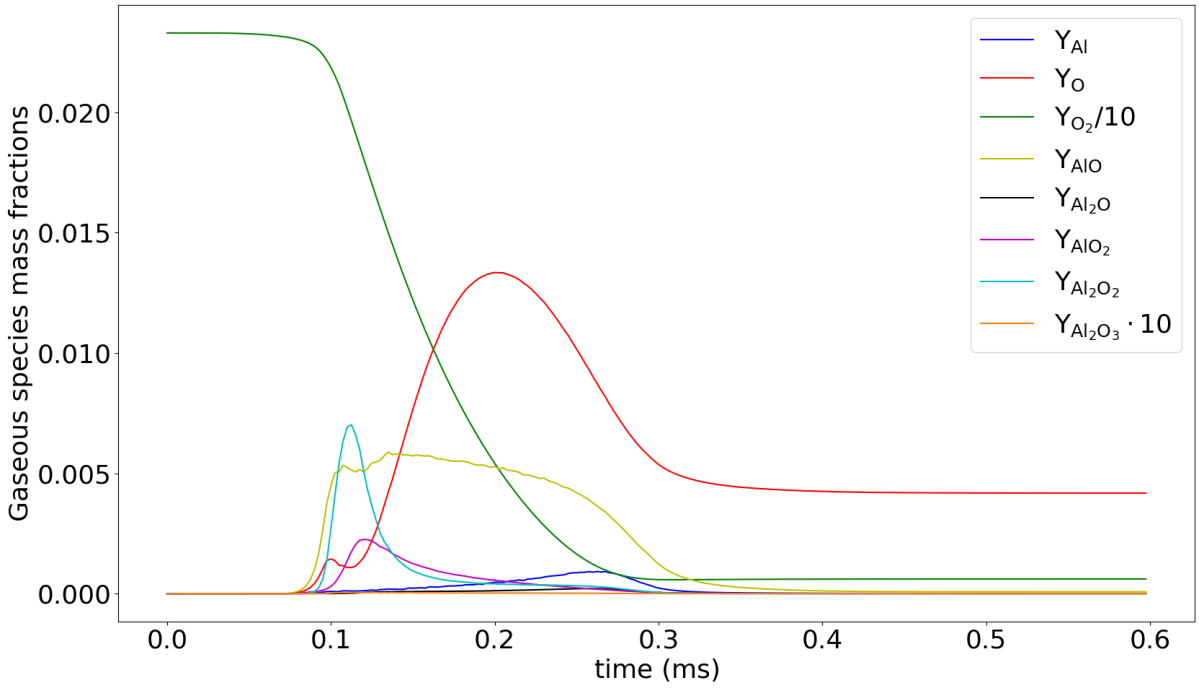

Figure 4.11 – Evolution of the gaseous species mass fractions during the combustion of an aluminum particle using an instantaneous condensation reaction instead of the model proposed in the current work.

Figure 4.11 shows that by using an instantaneous condensation and therefore maintaining a mass fraction of alumina to zero, the mass fractions of residual intermediates are far lower. Indeed, except for O, which does not contain aluminum, all the intermediate mass fractions never rise above 0.0075 and are null at the end of the simulation.

This tends to indicate that the presence of residual species at the end of the simulation is due to the fact that the oondensation model allows for the presence of gaseous alumina to exist in small quantities in the mix. Because alumina exists in the gaseous phase, the chemical equilibrium allows for the creations of intermediates in larger quantities. Since the current kinetic scheme was not designed to be used with such condensation model, it does not include chemical pathways to remove the intermediates once created in large quantities.

Further investigation is needed, but if this hypothesis is correct, a modification to this scheme to remove the presence of aluminum intermediates in the air once created in larger quantities could be of high interest to ensure a correct final equilibrium.

These results highlight the major influence of the condensation of gaseous alumina on the chemical equilibrium and therefore the combustion. Thus, it is important to have as precise and realistic of a condensation model as possible.

Another way of highlighting the importance of the condensation on final chemical equilibrium is to simply remove any condensation model.

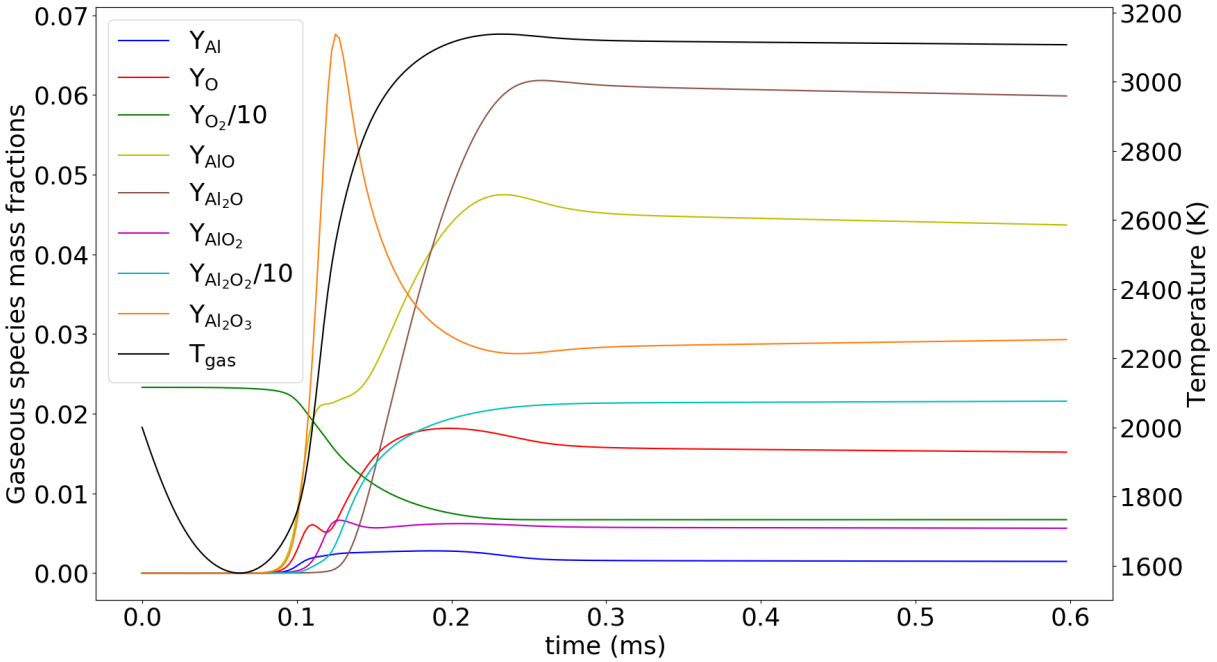

Figure 4.12 – Evolution of the gaseous species mass fractions during the combustion of an aluminum particle without any condensation model.

In figure 4.12, the condensation of alumina has been removed. Since there is no removal of alumina from the gas phase, the final chemical equilibrium is drastically modified. Thus, the final gaseous temperature of 3114 K is 455 K lower than the final temperature obtained with the condensation model. As explained in more detailed in part 3.5, this is due to two factors. Firstly, the energy of condensation is no longer available because the alumina stays in the gas phase, amounting for close to 3 % of the gas phase. Secondly, if alumina is not removed from the gaseous phase, other intermediates are not transformed into this final product through exothermic reactions. All the intermediates present significantly higher final concentrations with Al_2O_2 accounting for than 20 % of the gaseous mass at the end of combustion. Transforming these intermediates into alumina would yield a lot of energy to the system.

4.10 Morphology of the combustion products

One important improvement of the current model compared with the models available in the literature is that it can track the evolution of the morphology of the condensed combustion products. Indeed, the current model describes the coalescence of particles. Coagulation is not needed because the temperature never goes below 2350 K, which is the fusion temperature of alumina. Therefore, the particles do not aggregate.

The impact of nucleation, condensation and coagulation are discussed in the current part. The obtained results are not compared here with the experimental results in the literature. This will be done in part 5.9 alongside the results obtained on a 1D flame because the latter are more comparable with the experimental results.

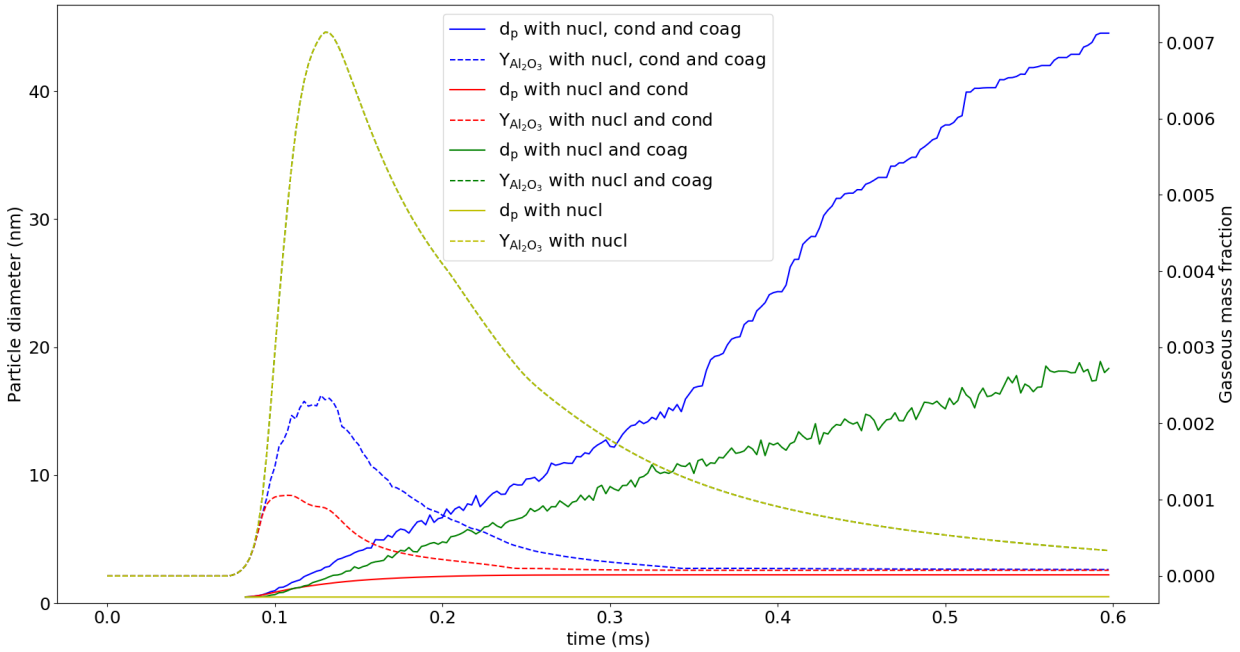

Figure 4.13 – Evolution of the average diameter of the alumina particles and the alumina gaseous mass fractions with different parts of the model activated.

Figure 4.13 enables the comparison of the impact of nucleation, condensation and coagulation on the average diameter of the alumina particles and the alumina gaseous mass fraction.

A first conclusion is that with nucleation only, the averaged particle diameter stays constant at 0.48 nm. In this case, the particle diameter is not modified by condensation or coagulation and corresponds to the diameter of the nucleated particles. This diameter is predicted by classical nucleation theory (CNT) but is capped at a minimum of 0.48 nm which corresponds to the diameter of an alumina molecule. This is consistent with the results obtained in the literature by Savel'ev et al. [98] who underlined that CNT incorrectly describes this parameter.

As expected, both condensation and coagulation increase the diameter of the particles. Coagulation brings a stronger increase than condensation with a diameter of 18.35 nm vs 2.27 nm at t = 0.6 ms. This is due to the extremely high particle density in the medium which considerably increases the probability of collision. Combining both condensation and coagulation further increases the particle diameter to a diameter of 44.5 nm.

Since the global condensation only consumes alumina, the gaseous mass fraction of alumina plotted in figure 4.13 gives information regarding the speed and intensity of global condensation. It can be observed that nucleation alone consumes far less alumina than condensation. This is in adequacy with the results of figure 4.8. Indeed, the quantity of matter transformed to liquid is directly proportional to the heat release rate, which is much weaker for nucleation than for condensation.

The curve of alumina mass fraction with nucleation only is superposed to the one with

both nucleation and coagulation. This is expected because coagulation does not transform gaseous alumina into liquid. But it does not mean that its impact is limited to an increase in particle size. By increasing the average particle size while reducing the particle population and conserving the global mass of liquid in the domain constant, coagulation reduces the sum of the surfaces of all the particles in the domain. Meanwhile, the speed of the condensation model is a direct function of this total surface of the particles in the domain and the condensation speed decreases as the total surface does the same. This explains why in figure 4.8, the surface mass fraction of alumina is lower with only condensation than with both condensation and coagulation because more alumina is consumed in the first case.

In conclusion, both condensation and coagulation greatly influence global condensation speed and products morphology. Meanwhile, nucleation obviously can not be neglected because it creates the necessary nuclei without which the two first phenomena can not happen. Thus, it is important to implement all three sub-models.

In this first attempt to simulate aluminum combustion, the phenomena, as well as the corresponding sub-models, implicated in the combustion of an isolated aluminum particle have been applied and studied. The essential roles of global condensation and heterogeneous surface reactions have been demonstrated. Furthermore, the importance of having a more realistic condensation model has been highlighted and the importance of accounting for nucleation, condensation and agglomeration has been demonstrated. If the implemented sub-model for surface reactions under-predicts the importance of these reactions, it greatly increases combustion speed, which is consistent with previous results in the literature. Moreover, the global model produces gaseous aluminum residues which should have been condensed into liquid alumina, reasons and possible corrections have been proposed. Despite these points that need improvements, the final temperature and characteristic combustion time are coherent with the results available in the literature. This is very encouraging and needs to be tested on more complex dust flames.

Chapter 5

Results: 1D dust flame

In the previous chapter, the behavior of an isolated burning particle has been studied in detail. This allowed for a better understanding of the importance of each of the individual phenomena involved in aluminum combustion. In the current chapter, 1D dust flames are simulated to validate the implemented combustion model and to study aluminum dust flames in more detail.

Overview

5.1 Computational configuration

To simulate 1D aluminum flames, a simple linear domain has been used. It is composed of square cells in line as illustrated in figure 5.1.

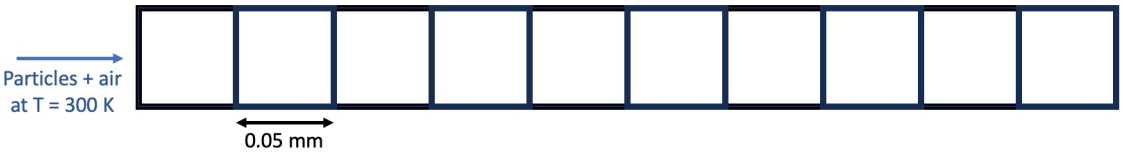

Figure 5.1 – Schematic of the 1D mesh

As illustrated in figure 5.1, the cell edges are 0.05 mm long and their volume is therefore 0.0025 mm^2. There is a total of 600 cells for a total domain length of 30 mm. A point injection is used for the aluminum particles that are injected at a temperature of $T_p = 300$ K in air, which is at a similar temperature of $T_g = 300$ K. The upper and lower parts of the domain are symmetries.

Unless precised otherwise, the flame is at stoichiometry. The injection parameters are computed as follows to meet this condition.

The global reaction for aluminum combustion is given in Eq. (4.1) while the mass stoichiometric ratio is equal to s = 0.89 as computed in Eq. (4.2). The air mass flow is first computed as:

$$\dot{m}_{\text{air}} = \rho_{\text{air}} \cdot u_{\text{air}} \cdot S \tag{5.1}$$

where ρ_{air} is the air density which is equal to 1.177 kg/m^3 at $T_g = 300\ K$, u_{air} is the gas speed at the inlet, and S is the injection section. The oxidiser mass flow is easily retrieved from the air mass flow:

$$\dot{m}_{O_2} = \dot{m}_{\text{air}} \cdot Y_{O_2} \tag{5.2}$$

Finally, the mass flow of aluminum for a given equivalence ratio can be obtained as:

$$\Phi = s\frac{\dot{m}_{\text{Al}}}{\dot{m}_{O_2}} \Rightarrow \dot{m}_{\text{Al}} = \frac{\Phi}{s} \cdot \dot{m}_{O_2} \tag{5.3}$$

5.2 Ignition process

The combustion of aluminum is more complex and unstable than the combustion of classical hydrocarbons. This is mainly due to a much higher flame temperature as well as a much stiffer chemistry (see part 3.3.3). Therefore, the stabilisation of aluminum dust flames is no easy task and the numerical ignition procedure can easily lead to code crashes.

Thus, strategies have been developed in the current work to ignite flame as smoothly as possible. For the 1D flames, the following ignition, illustrated in figure 5.2, has been used.

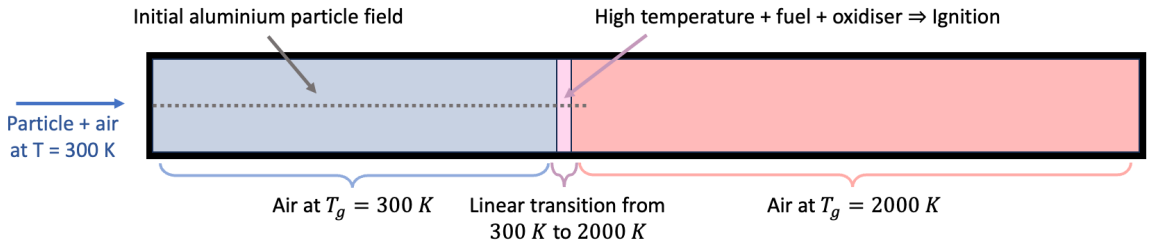

Figure 5.2 – Schematic of the ignition process for a 1D aluminum flame.

The ignition process schematized in figure 5.2 is generally similar to the one used for the ignition of liquid hydrocarbon. However, the stiffer properties of aluminum combustion require adjustments to achieve a softer ignition. The domain is initially filled with air at a temperature of $T_g = 300$ K on the left side and at $T_g = 2000$ K on the right side, with a linear temperature transition in between. Lagrangian particles are injected along a line that goes from the cold air zone to the beginning of the hot air zone, thus crossing the smooth temperature transition region, where particles are in contact with both high temperature and oxidizer, allowing their ignition.

As this could still be too stiff, artificial viscosity was applied in the whole domain during ignition and removed once the flame has been stabilised, therefore not affecting the results shown hereafter.

5.3 Properties of 1D aluminum dust flame at stoichiometry

In the case studied here, the flame is at stoichiometry and the initial aluminum particle diameter is $d_p = 7$ μm. The flame is stabilised by injecting the fresh air with particles at the flame speed which is here 29.67 cm $\cdot$ s^{-1} and is further discussed in part 5.5.

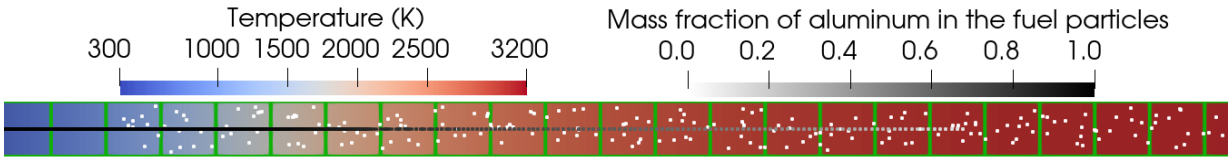

Figure 5.3 – Visualization of a 1D aluminum-air flame front: field of temperature and particles colored by their aluminum mass fraction.

In figure 5.3, a visualization of a 1D aluminum flame is given, with the gaseous temperature field in the background ranging from 300 K in the cold air to more than 3100 K in the hot air. The cells are represented by the green squares. The black particles are the fuel particles and the dispersed white particles are the nucleated alumina particles.

The aluminum particles are injected at a point in the middle of the left border and penetrate far in the domain along a linear trajectory, while their content in aluminum decreases. The radius of these particles goes from 3.5 μm to 2.1 μm as the particles evaporate. Once all the aluminum contained in the particle has evaporated, only alumina

remains and the particle is transferred to the second subset of particles (in white in figure 5.3) that contain alumina only.

The alumina particles are dispersed in the cells because they are randomly nucleated in each cell. They start to appear in the flame as soon as gaseous alumina is produced by the gaseous reactions and thus available for nucleation.

The results are further detailed with the evolution of gas temperature and heat release rate plotted in figure 5.4.

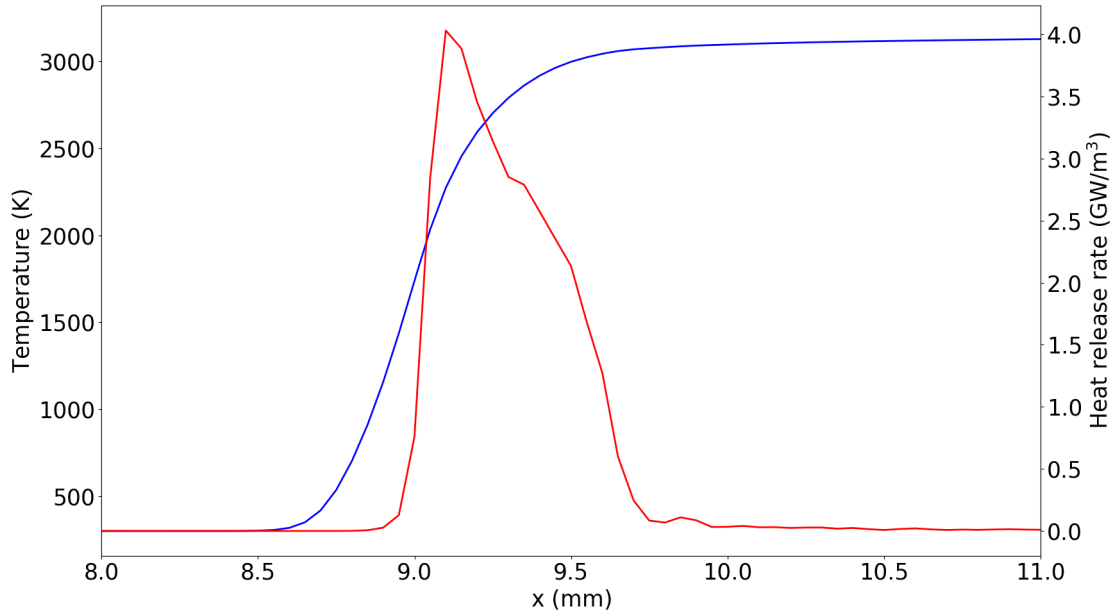

Figure 5.4 – Evolution of the gas temperature (in blue) and of the heat release rate (in red) across the flame.

The gas temperature initially at 300 K starts to rise at position 9.2 mm. Because the particles need first to liquefy and then reach a temperature of 1718 K to evaporate, the heat release rate stays zero in this heating up and melting phase. As soon as evaporation starts, the heat release rate sharply rises to reach a peak of 4.03 GW/m^3 which brings a huge amount of energy to the flame. Thus, the temperature further increases to reach a burnt gas temperature of 3127 K. This flame temperature is slightly lower, but in good agreement with the experimental measurement from Lomba et al. [82] who obtained an experimental temperature of 3146 ± 180 K in similar conditions, as shown in figure 5.5.

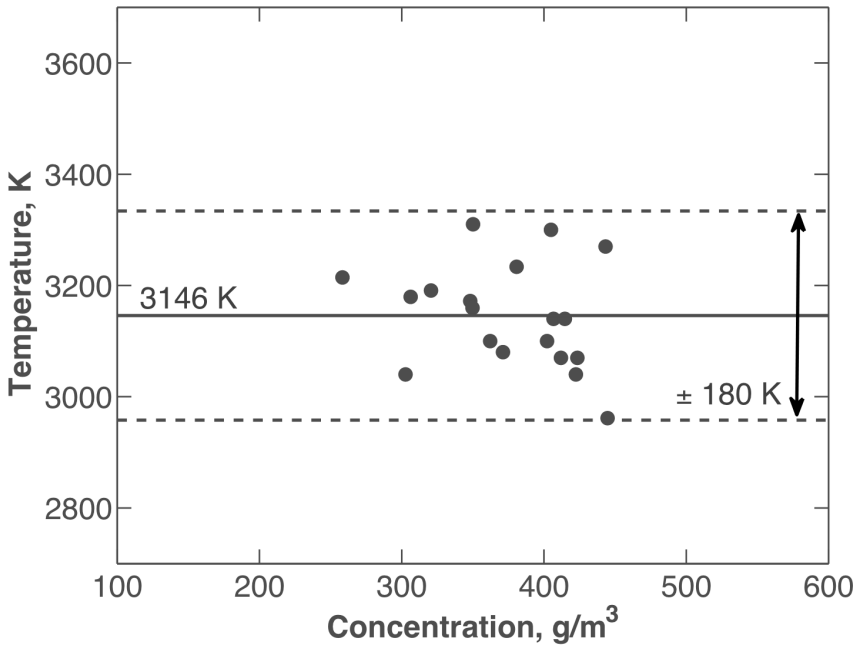

Figure 5.5 – Flame temperature as a function of the aluminum concentration for dust flames. Figure extracted from [82]

It is important to mention again that thermal radiation of the condensed combustion products was not included in the current work. In reality, the temperature after the flame front should decrease as these alumina droplets radiate.

5.4 Evaporation and growth of alumina particles.

The evolution of the aluminum and alumina particle diameters are illustrated in figure 5.6.

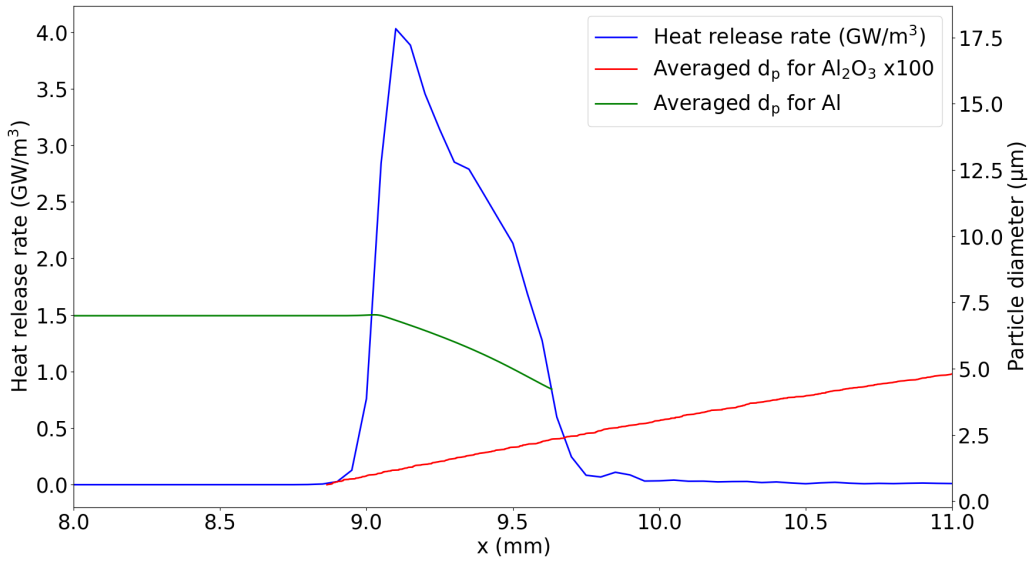

Figure 5.6 – Evolution of heat release rate and the averaged particle diameters d_p of both aluminum and alumina across the flame.

In figure 5.6, it is interesting to see the transfer of mass from the first subset of aluminum particles to the second subset of alumina particles through the flame. Indeed, as the heat release rate increases, i.e., as the particles enter the flame zone, they start evaporating and their diameter therefore decreases.

At the same position, the homogeneous gaseous reactions produce gaseous alumina that condensates as it is produced. Thus, the averaged alumina particles diameter of the second subset increases. This is due to both the global condensation of the combustion products and the coagulation of the particles with others.

It can be noted that the heat release rate, i.e., the gaseous reactions, starts rising slightly before the particle starts evaporating. This is simply due to a small diffusion of gaseous aluminum upstream which, due to the very reactive chemistry, reacts despite its low amount.

5.5 Laminar flame speed

The 1D aluminum flame is the easiest configuration to study the flame speed. Indeed, since the flow and therefore the flame, can only move in one direction, the flame speed is the injection speed aused to stabilise the flame front.

In the current work, for an aluminum flame in air at $\Phi = 1$ with a particle diameter $d_p = 7\mu$m, this injection speed and therefore flame speed is 29.67 cm $\cdot$ s^{-1}. In their work,

Lomba et al. [82] experimentally obtained a flame speed of 28.24 $cm \cdot s^{-1}$ in similar conditions.

5.5.1 Impact of the equivalence ratio on flame speed

Many experimental measurements of flame speed have been reported in the literature. These measurements have been realized for several equivalence ratios and the measured flame speeds are presented in figure 5.7.

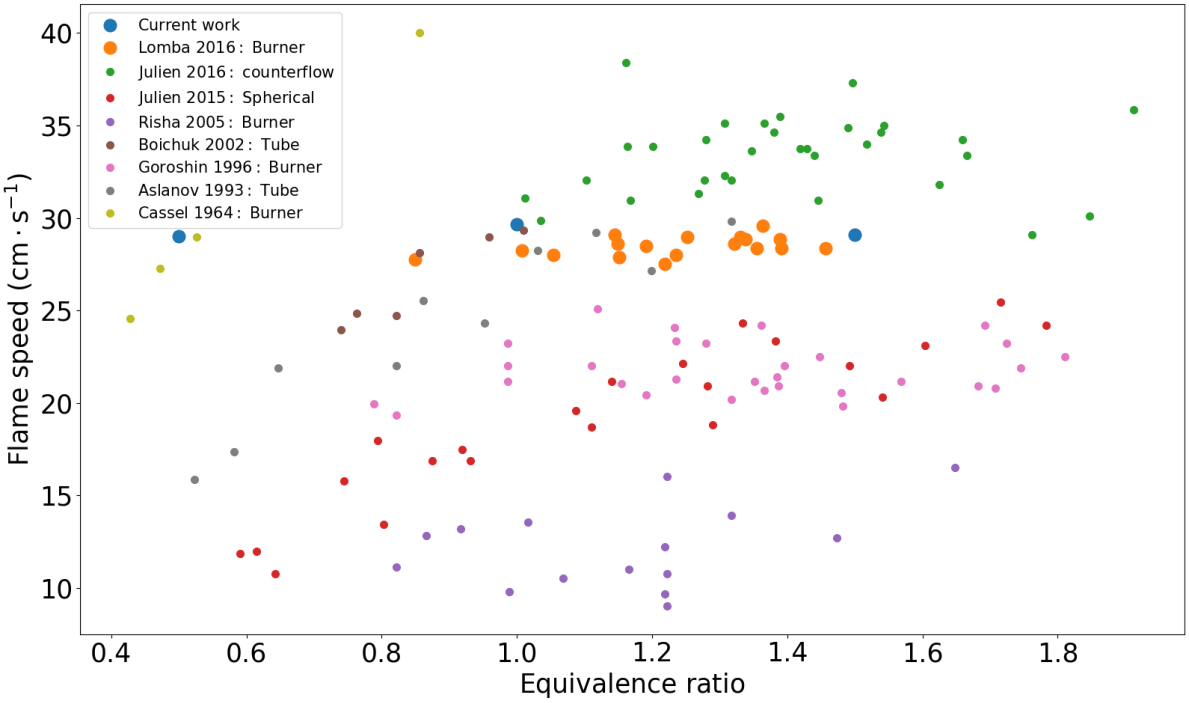

Figure 5.7 – Comparison between the flame speed values obtained in the current work and experimental values from different works.

Boichuk et al. [17] studied the propagation of a flame in a tube and found that aluminum flame speed increases with the equivalence ratio. Risha et al. [94] and Julien et al. [64] measured aluminum flame speeds in spherical flames. Finally, another type of experimental setup used to measure flame speeds is a burner, Julien et al. [65] or Lomba et al. [82] used such burners.

For comparison, the flame speeds obtained in the current work are also reported in figure 5.7. The computed values are within the cloud of the experimental data. Moreover, they are in good agreement with the morst recent experimental work of Lomba et al. [82] which was done for a similar particle diameter. Indeed, the flame speed obtained in the current work ranges from 29 $cm \cdot s^{-1}$ to 29.5 $cm \cdot s^{-1}$ for values of Φ ranging from 0.5 to 1.5 while the flame speeds from Lomba et al. [82] are found in the range 27.8 to 29.6 $cm \cdot s^{-1}$ for a similar range of equivalence ratio.

5.5.2 Impact of the particle diameter on the flame speed

In order to study the impact of initial aluminum particle diameter on flame speed, statistical convergence (see part 2.2.4 for more details) is reached by adjusting the statistical weight ω of the particles. It is reminded that ω_i is the number of physical particles represented by one numerical particle. Changing the particle diameter while keeping the same mass flow of aluminum at the inlet means that the number of aluminum particles will be impacted. Thus, ω must be adjusted as follows to keep the same number of injected numerical particles.

The aluminum mass flow can be expressed as a function of the radius:

$$\dot{m}_{Al} = \dot{n}_p^{\text{physical}} m_p^{\text{Al}} \tag{5.4}$$

$$\Rightarrow \dot{m}_{\text{Al}} = \dot{n}_p^{\text{num}} \omega \frac{4}{3} \pi r_p^3 \rho_{\text{Al}} \tag{5.5}$$

$$\Rightarrow \dot{n}_p^{\text{num}} = \frac{3\dot{m}_{\text{Al}}}{4\omega\pi r_p^3 \rho_{\text{Al}}} \tag{5.6}$$

where $\dot{m}_{\text{Al}}$ is the mass flux of injected aluminum and m_p^{Al} is the mass of aluminum in one particle. $\dot{n}_p^{\text{physical}}$ and $\dot{n}_p^{\text{num}}$ are the particle injection rates (number of particle injected per second) of physical and numerical particles respectively.

Considering $\dot{n}_p^{\text{num}}$ constant from an injection of particles with a diameter of $\mathrm{d_{p,a}}$ and a statistical weight ω_a to an injection of particles with a diameter of $\mathrm{d_{p,b}}$ and a statistical weight ω_b, the following relation is obtained:

$$\omega_b = \left(\frac{d_{p,a}}{d_{p,b}} \right)^3 \cdot \omega_a \tag{5.7}$$

To give an order of magnitude, particles of diameter 7μm with a statistical weight of $\omega = 25$ represent the same mass as particles of diameter 3μm, with a statistical weight ω equal to:

$$\omega_{\mathrm{i}} = \left(\frac{7}{3} \right)^3 \cdot 25 \approx 318 \tag{5.8}$$

This weight adjustment is extremely important to prevent either too high calculation cost or too few numerical particles to achieve statistical convergence.

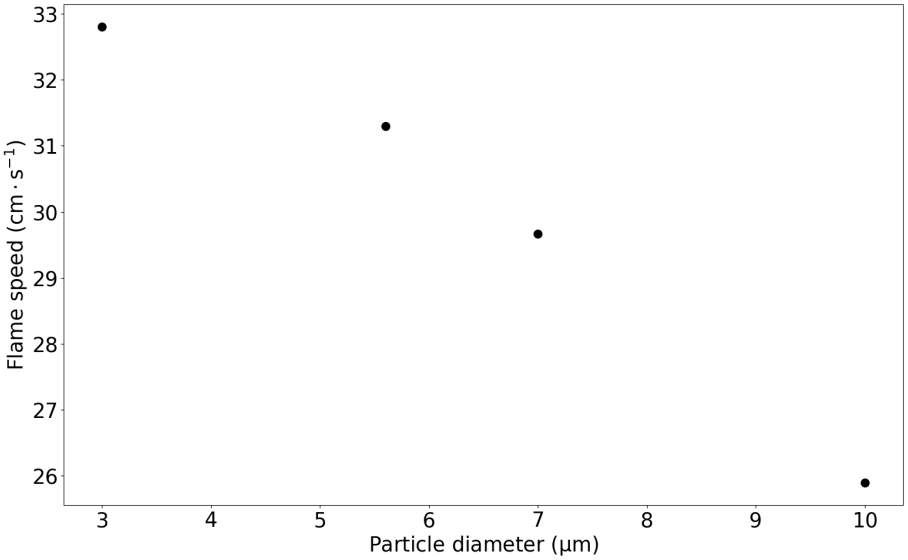

Figure 5.8 – Evolution of the flame speed of 1D aluminum flame as a function of the initial diameter of the aluminum particles using the combustion model implemented in the current work.

In figure 5.8, the evolution of the flame speed in a 1D aluminum flame is plotted as a function of the initial diameter of the aluminum particles. As the particle size is reduced, the flame speed increases up to $32.8\text{cm} \cdot \text{s}^{-1}$ while it is reduced to $25.9\text{cm} \cdot \text{s}^{-1}$ as the particle size is increased. This is due to the fact that reducing the particles size while conserving the same global stoichiometric ratio increases the surface available for both evaporation and surface reactions.

5.6 Impact of the equivalence ratio on flame temperature

As previously explained, the flame temperature $T_f = 3127$ K for an equivalence ratio $\Phi = 1$ and a particle diameter $d_p = 7$ μm obtained in the current work is in good agreement with the experimental work of Lomba et al. [82]

In figure 5.9, the flame temperature obtained in the current work for several equivalence ratios is plotted.

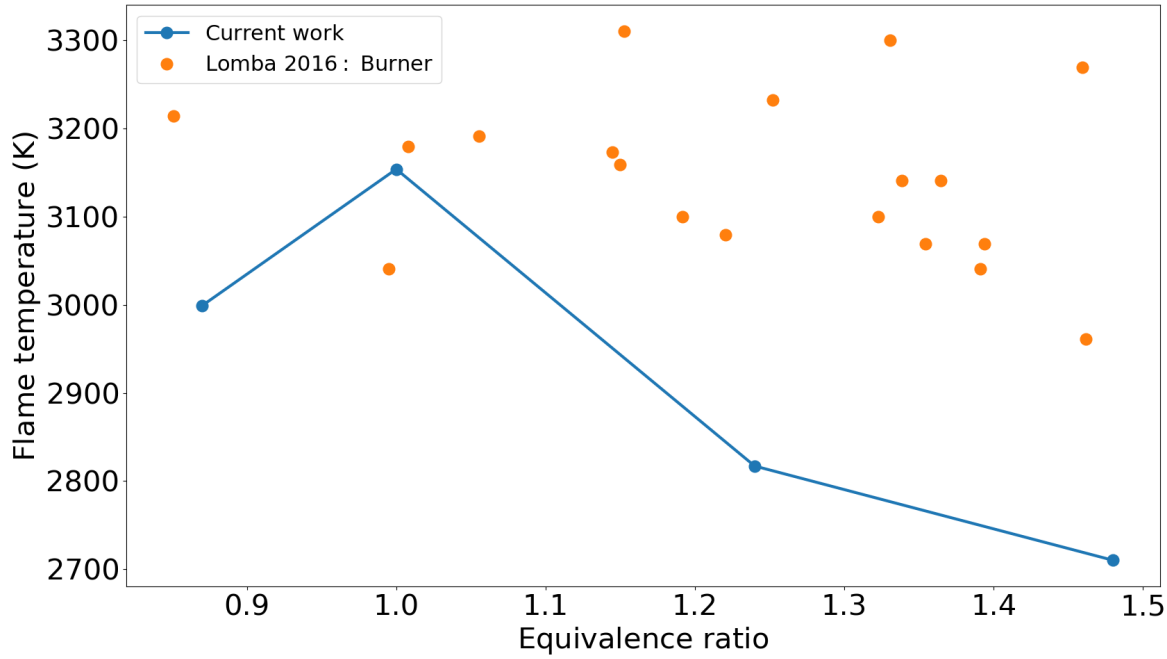

Figure 5.9 – Evolution of the flame temperature of a 1D aluminum flame as a function of equivalence ratio. Comparison between the current work and experimental data from [82].

The experimental flame temperature obtained by Lomba et al. [82] is within an interval of 360 K for Φ ranging from 0.87 to 1.48 with a minimum of 2961 K and a maximum of 3310 K. There is no clear impact of the variation of the equivalence ratio for this experimental data set.

However, in the current work, the flame temperature varies clearly with the equivalence ratio. While the flame temperature at $\Phi = 1$ is 3127 K, it drops significantly as the equivalence ratio takes lower or higher values. For $\phi = 0.87$, the flame temperature is 2999 K while dropping as low as 2710 K for $\Phi = 1.48$.

If this dependence of the flame temperature on the equivalence ratio is inconsistent with the experimental values from Lomba et al. [82] it has been observed in the numerical work of Han et al. [54]. This is illustrated in figure 5.10.

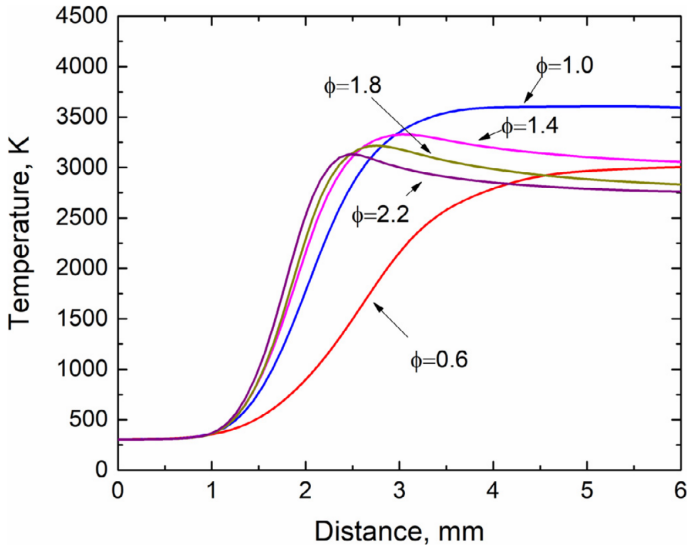

Figure 5.10 – Temperature profiles near flame zone at different equivalence ratios on a numerical aluminum-air flame obtained by Han et al. [54]. Figure extracted from [54].

As visible in figure 5.10, Han et al. [54] also obtained a reduction in flame temperature for both increases and decreases of the equivalence ratio in similar proportion to what is obtained in the current work. Further investigation is required to understand the difference between the experimental results from Lomba et al. [82] and the numerical works from both Han et al. [54] and the current work.

5.7 Gas composition through the flame

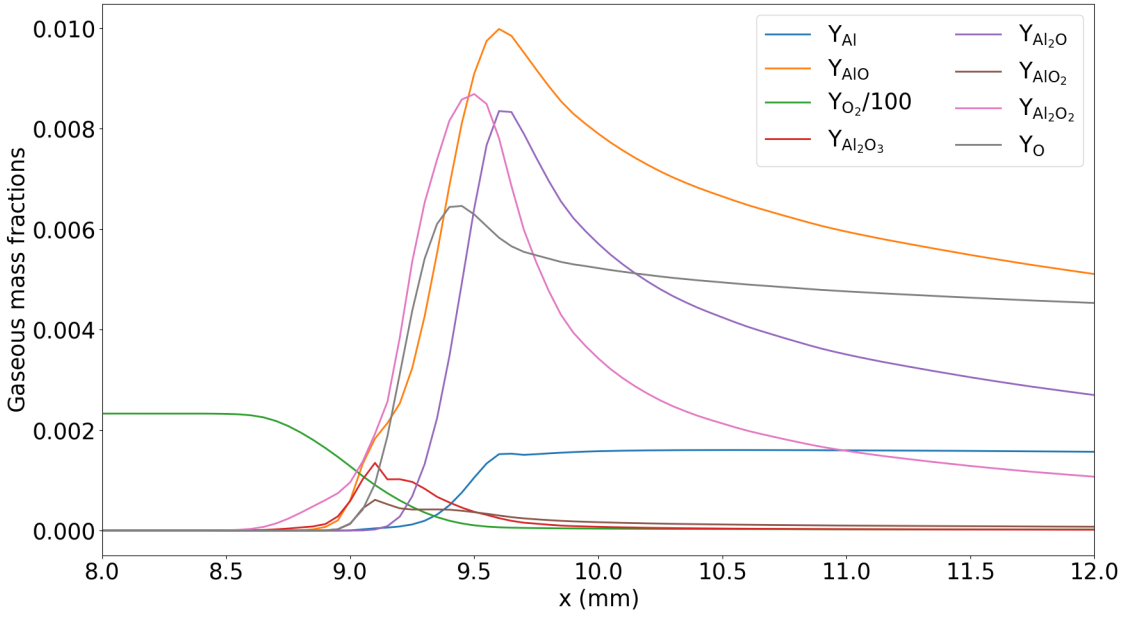

Figure 5.11 – Gaseous species mass fractions profiles in a 1D aluminum flame.

In figure 5.11, the profiles of mass fractions of the gaseous species are plotted through the flame.

First, Y_{O_2} starts varying slightly before the other gaseous species. This is because the surface reactions only consume O_2 and occur before the evaporation and therefore before the gaseous reactions (see part 3.4).

The first species to appear is Al_2O_2, followed by all the other aluminum oxides while the oxygen is depleted through the flame front.

In part 4.9, the fact that the condensation model did not transform gaseous alumina into liquid fast enough was highlighted. This allowed for the presence of gaseous aluminum oxides in the combustion products, which is physically incorrect. In the current 1D flame, the mass fractions of alumina never rises above 0.0014, thus, the mass fractions of aluminum oxides stays under 0.01. The evolution of the sum of the mass fractions of all the molecules containing aluminum, oxygen and nitrogen is plotted in figure 5.12.

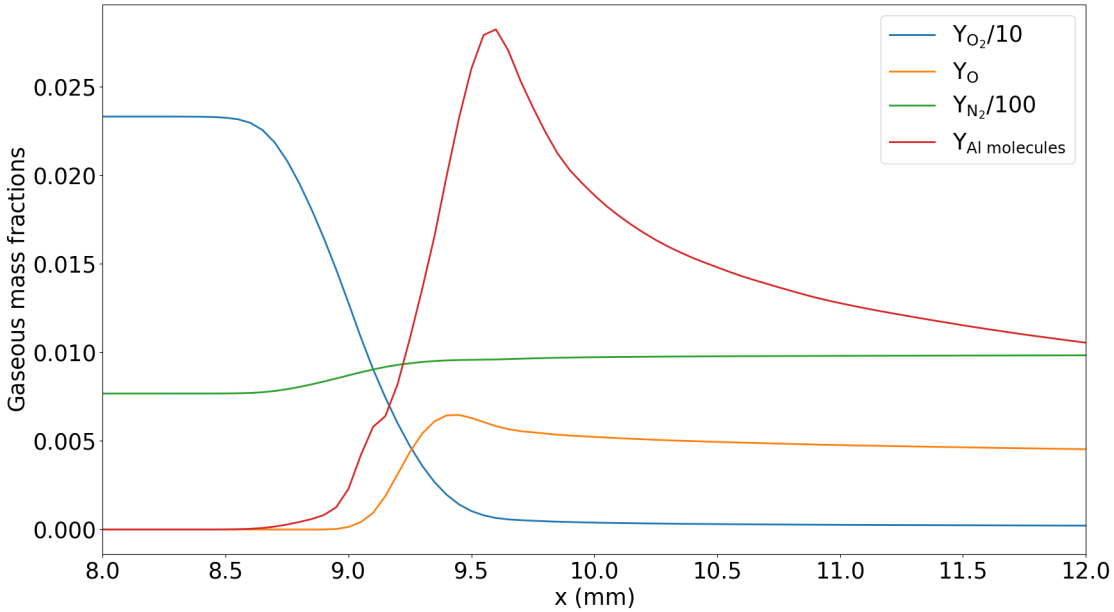

Figure 5.12 – Comparison of the sum of the gaseous mass fractions of species containing aluminum (noted $Y_{Al\ molecules}$) with the mass fractions of other gaseous species through a 1D flame.

In figure 5.12, the sum of the mass fractions of all the species containing aluminum never surpasses 0.028 and accounts for slightly above 1 % of the mass of the combustion products. The rest of the gaseous phase after the flame front is composed at 99 % of nitrogen and traces of O and O_2. In reality, the aluminum oxides mass fraction should be negligible after the flame front. However, this final composition is far more satisfactory and closer to reality than the one obtained in part 4.9 where the sum of all the species containing aluminum constituted 6 % of the mass of the combustion products.

5.8 Impact of the condensation of alumina

It is important to study the condensation of alumina for two reasons. Firstly, the condensation itself releases a lot of energy which has an important impact of the flame. Furthermore, the removal of alumina from the gaseous phase has a major impact on the gas phase chemistry.

Secondly, because the use of aluminum as a clean energy vector would require to recycle the condensation products back to aluminum, it is interesting to be able to predict the morphology of these products.

5.8.1 Impact of the condensation on flame structure

As previously discussed in more details in part 3.5, aluminum contributes greatly to the heat released in the flame. A good way of studying the role of the condensation on the flame properties is to simply remove the condensation model and to compare the flame behavior with and without the condensation model.

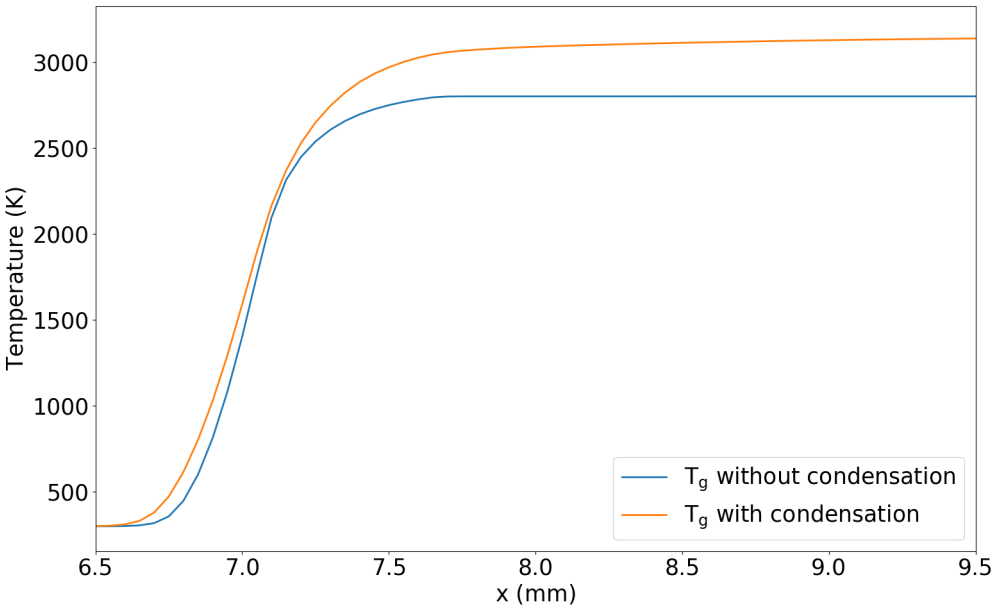

Figure 5.13 – Comparison of the evolution of the gas temperature (T_g) through the flame with and without condensation

In figure 5.13, the evolution of the temperature through the flame is plotted with and without condensation. As expected, the final temperature is lower by 337 K for the case without condensation. The reason is twofold. First, the condensation process itself is exothermic, as studied in figure 4.8. Second, condensation has an indirect effect on the heat release rate, as visible in figure 5.14.

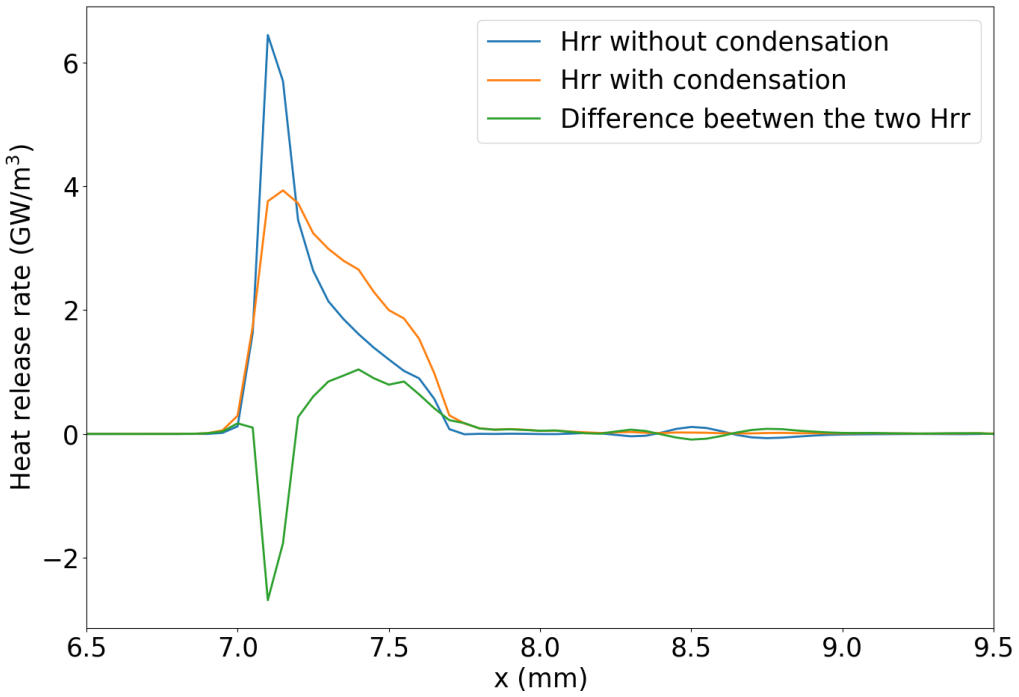

Figure 5.14 – Comparison of the evolution of the heat release rates (Hrr) through the flame with and without condensation with the difference between the two.

In figure 5.14, the heat release rate of a flame without condensation is compared to the heat release rate of a flame with the condensation model implemented in the current work. There are two important observations to make from this figure.

The first one is that the heat release rate of the flame without condensation is much stiffer than the one with condensation with a peak at 6.45 GW/m^3 instead of 3.93 GW/m^3. Furthermore, small ondulations appear after the flame front without condensation. Because the energy from combustion is released more brutally, the simulation may be numerically less stable. Furthermore, this stiffer energy release means that the combustion happens faster, accelerating the flame speed that goes from 29.67 $cm \cdot s^{-1}$ with condensation to 33.75 $cm \cdot s^{-1}$ without condensation, despite a lower flame temperature.

The second observation is that despite the fact the heat release rate peaks higher, the total heat release rate is lower without condensation than with condensation. Indeed, by integrating the green curve in figure 5.14 that represents the difference between the heat release rate with and without condensation, the total heat release difference is obtained. Dividing the obtained difference by the total heat release with condensation gives a value of 0.132, meaning that the total heat release is reduced by 13.2 % without condensation.

This is mainly due to the fact that the final chemical equilibrium is drastically modified by the condensation which is highlighted in the next part.

5.8.2 Impact of the condensation on the composition of the burnt gases

The condensation process consumes gaseous alumina, thus modifying the gas composition. As alumina is removed from the gaseous phase, the chemistry is shifted toward the production of more alumina through the consumption of aluminum intermediate oxides. This process should continue until no aluminum oxides are left in the gaseous phase. In the current work traces of these oxides are still left in the gas as discussed in part 5.7.

Without any condensation a large amount of these aluminum oxides are left after the flame front as visible in figure 5.15.

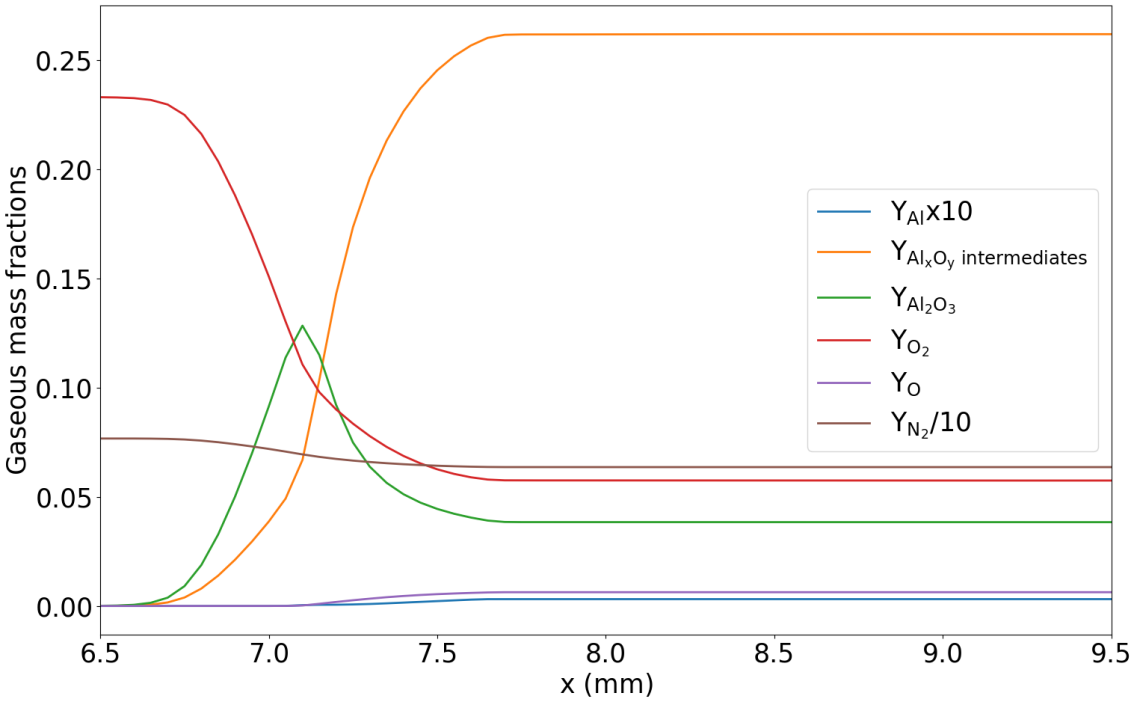

Figure 5.15 – Evolution of the gaseous species mass fractions through a 1D flame without condensation

In figure 5.15, the composition of the gas phase is very different without condensation than the one with condensation that can be observed in figure 5.12. Because of the absence of condensation, alumina concentration rises in the flame front to reach a mass fraction value of 0.13 before reducing to 0.04, its final value. Due to the presence of this alumina, the intermediates aluminum oxides (noted Al_xO_y intermediates in figure 5.15) are not transformed into more alumina to replace the condensed alumina. Thus, these intermediates aluminum oxides accumulate in the gas phase to reach a final mass fraction of 0.26 which is a substantial quantity. Moreover, the transformation of these intermediates into alumina consumes oxygen. The reduction of these reactions also leaves behind a mass fraction of unconsumed dioxygen of 0.06. Therefore, without condensation, the burnt gases composition is non-physical.

Finally, the limitation of the exothermic reactions by the absence of condensation described previously explains the reduction of the heat release rate observed in part 5.8.1.

This section discussed the observed key role of condensation on the aluminum flame properties, as well as the correct prediction of the combustion products composition. The tight link between condensation and chemistry in an aluminum flame highlights the importance of using realistic models for the simulation of aluminum combustion.

5.9 Morphology of the condensed alumina particles

The combustion models available in the literature for aluminum use instantaneous condensation and track the liquid combustion products as gaseous species (see part 3.5.2). Contrary to these models, the model used in the current work is able to describe the morphology of these combustion products. As explained in part 4.10, the current model allows for the coalescence of particles but not for coagulation. This does not matter for the 1D flame simulations of this chapter because the temperature never goes under 2350 K, which is the fusion temperature of alumina. Therefore, the particles never coalesce together.

In reality, a lot of energy is lost after the flame front through thermal radiation, which is not accounted for in the current work. Adding the radiation of the liquid combustion products and considering a longer domain allowing for the particles to lose enough energy to solidify in the domain would enable the study of the morphology of aggregates, illustrated in figure 5.17. Due to lack of time, this has not been implemented in the code and will be done in future work. However, the current model is able to determine the diameter of the spherules constituting these aggregates, which is of high interest and has been also experimentally studied.

Before comparing the simulation results with experimental data regarding spherule radius, it is important to discuss the physical mechanisms that influence the size of the spherules.

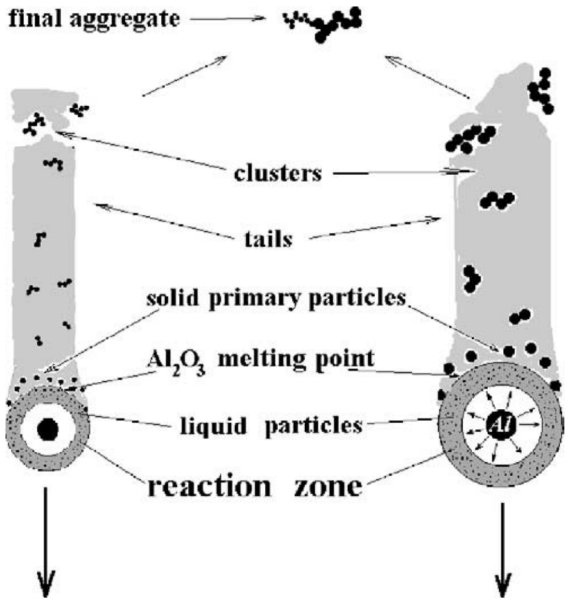

Figure 5.16 – Scheme of the Al2O3 coagulation process. Figure extracted from [69].

In figure 5.16, two isolated burning aluminum particles are schematized. Inside the part labelled "reaction zone", the temperature is above 2350 K, which is the melting temperature of alumina [105], so that the particles are liquid. In this zone, when the liquid droplets collide with one another, they simply form a larger liquid droplet: this phenomenon is known as coalescence. As these droplets exit this zone and pass the frontier labelled "Al_2O_3 melting point", they enter the "tails" zone in which the temperature is lower than their melting point. Thus, these particles solidify into spherules. Now, when two spherules collide, they stick together to form a cluster of spherules: this phenomenon is known as aggregation. These clusters then collide together and with other spherules to form the "final aggregate".

Therefore, the size of the spherules is a direct function of the relative importance of coalescence compared to aggregation. The higher the residence time of the alumina particles in the zone hotter than their melting point, that is now called coalescence zone, the bigger the spherules. Following a similar reasoning, the higher the residence time of the these particles in the zone colder than their melting point, now called aggregation zone, the larger the number of spherules forming the final aggregates.

Figure 5.16 explains the phenomena for the case of an isolated burning particle. Extension to an aluminum dust flame is now discussed.

For an aluminum dust flame , after the flame front, the gas temperature is above the melting point of alumina. Thus, the coalescence zone is much larger than in the previous case, extending downstream the flame front to a point where gas temperature becomes lower than alumina melting point. Past this point, the particles enter in the colder aggregation zone. Because in this case the coalescence zone is larger, the residence time of the particles in this zone is much higher, resulting in final aggregates with fewer but bigger spherules.

Knowing that the residence time of the combustion products is driving the combustion products morphology, a review of experimental results of the literature regarding this morphology is proposed below.

First, Glotov et al. [50] experimentally studied burning aluminum particles detaching from burning propellants. An example of a retrieved final aggregate is visible in figure 5.17.

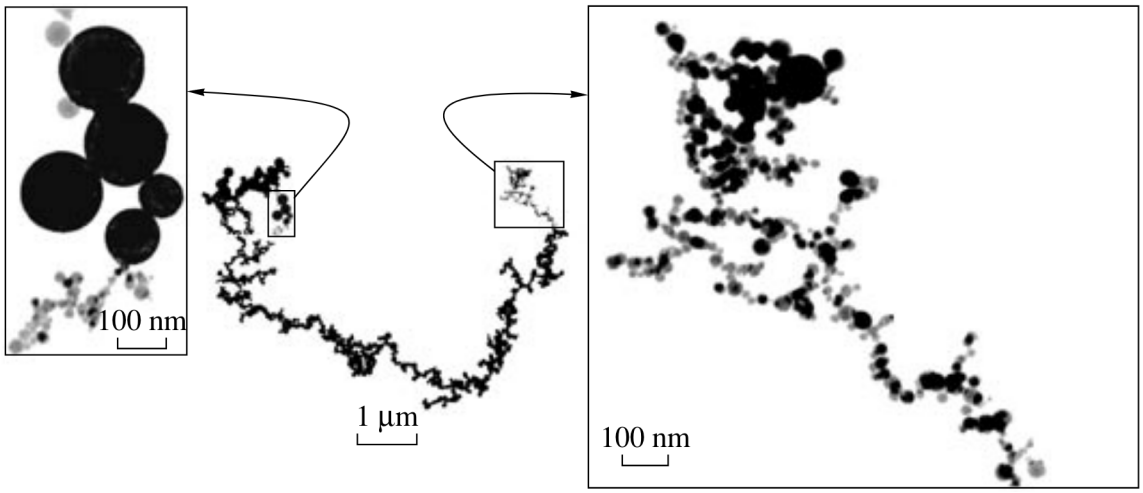

Figure 5.17 – Aggregate of nanosized alumina particles produced by combustion of an aluminized propellant. In different regions of the aggregate, spherules differ considerably in size. Figure extracted from [50].

This experiment was realised for several initial aluminum particle diameters. The size of the spherules composing the retrieved aggregates as a function of the initial aluminum particle diameters is plotted in figure 5.18

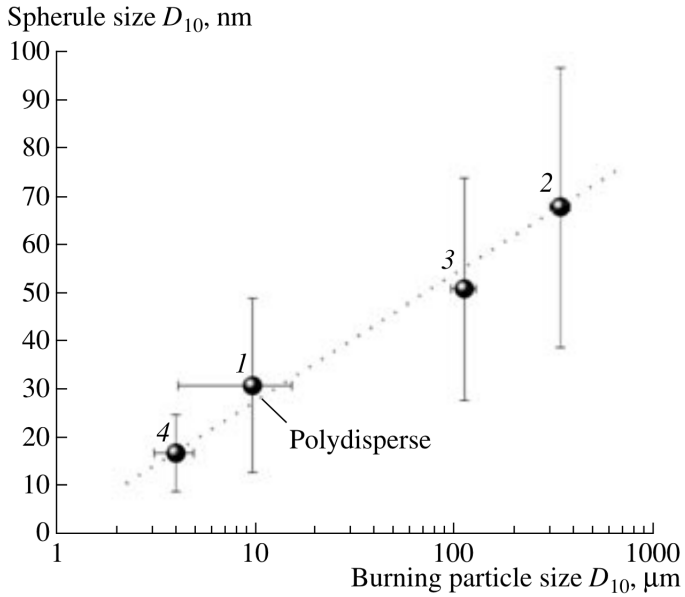

Figure 5.18 – Alumina spherule size vs. the burning particle size. The numbers at the data points are the numbers of series. Figure extracted from [49].

The results in figure 5.18 are for isolated burning aluminum particles which is closer to the case schematized in figure 5.16. The combustion products of dust flames have been analyzed in other experimental works such as the one of Bocanegra et al. [16] with visualization of these products presented in figure 1.17. The mean Sauter diameter of residual particles was around 94 nm [34] for an initial aluminum particle diameter of 4.8 μm.

Poletaev et al. [92] used the experimental setup schematized in figure 5.19.

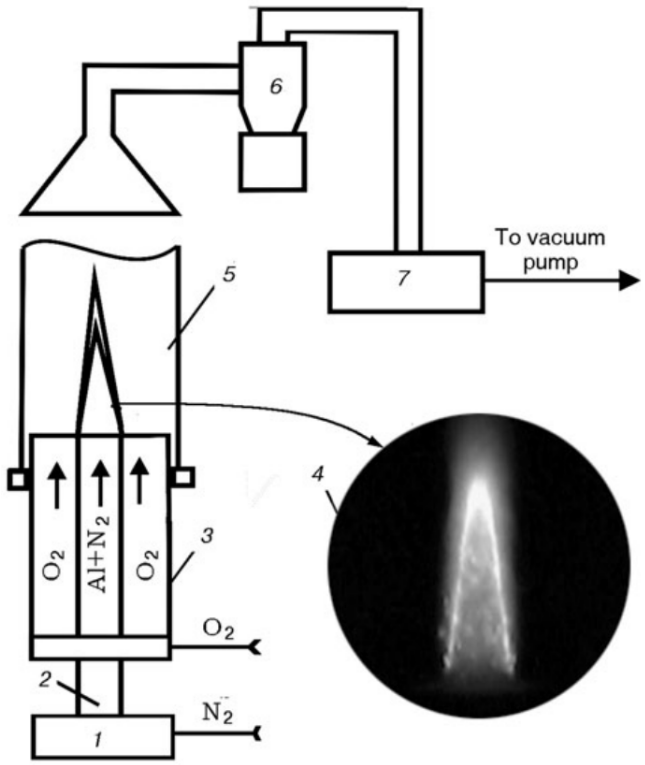

Figure 5.19 – Diagram of the dust burner used by Poletaev et al. [92]: 1) dispersion unit; 2) inner burner tube; 3) outer burner tube; 4) flame; 5) protective quartz tube; 6) trapping system; 7) fabric filter. Figure extracted from Poletaev et al. [92].

The experimental setup proposed in figure 5.19 has been designed for the capture and analysis of the solid combustion products. The particles can be injected either with only nitrogen in the central tube and react with the oxidizer provided by the coaxial tube, or with both nitrogen and the oxidizer. Once the flame has been stabilised, the combustion products are retrieved and analyzed using the trapping system.

Different results have been obtained for different values of aluminum particles concentrations and different oxidizer concentrations in the central injectors. The obtained alumina particles range from 63 nm to 107 nm in diameter. None of the configurations correspond to a flame without co-flow at $\Phi = 1$, which would be closest to the 1D flame configuration performed in the current work, nevertheless the comparison remains interesting.

Finally, Lomba et al. [81] captured the combustion products and quickly discussed them in the PhD manuscript of Lomba [82]. They found alumina spherules of diameter approximately 200 nm with some having a diameter up to 1μm. Although no exact average value was given, these results obtained in experimental conditions that are closest to the 1D simulation realised in the current work are of high interest.

The heat loss that reduces the gas temperature after the flame front is due to the thermal radiation of the condensed particles of alumina. Because thermal radiation model of these particles is not included in the current work, the gas temperature after the flame front remains constant, which means that the whole post-flame zone is a region of coalescence. Therefore, the spherules keep growing instead of stop growing due to solidification, and it is difficult to compare their diameter with experimental results. However, an indirect comparison allowing for a discussion of these results is propsed in fig 5.20.

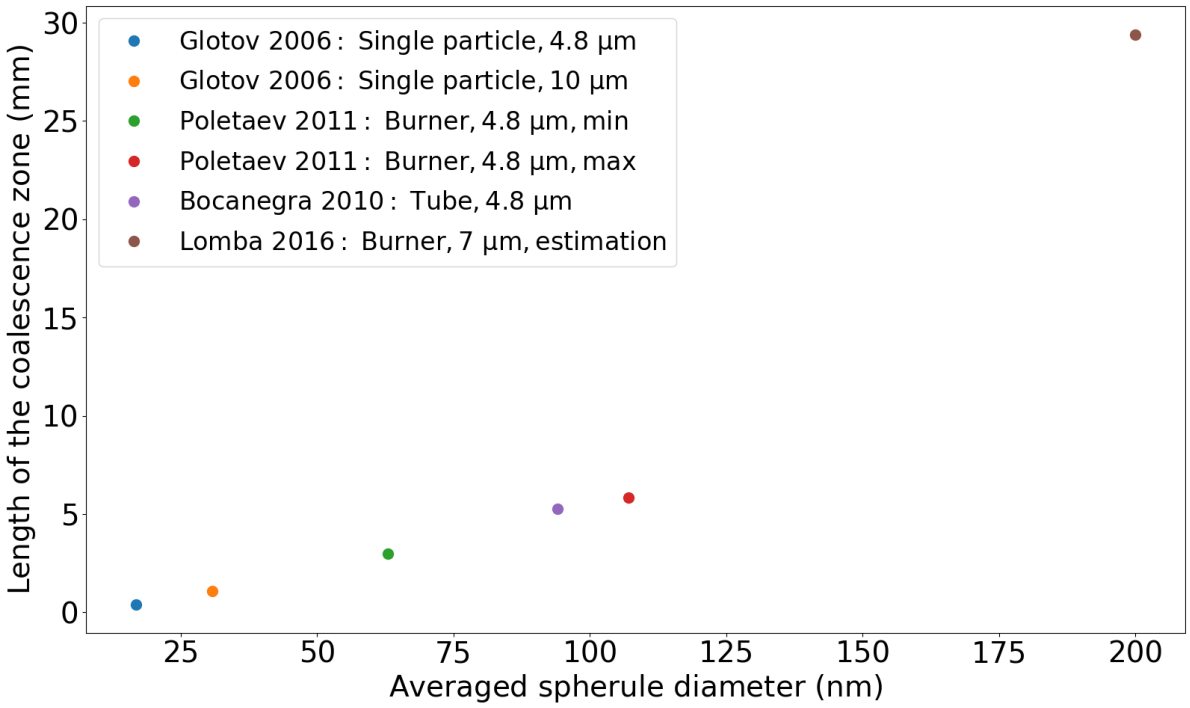

Figure 5.20 – Length of the coalescence zone in the current work for which the obtained averaged spherule diameter corresponds to different experimental results.

The length of the coalescence zone in the current work for which the obtained averaged spherule diameter corresponds to different experimental results is plotted in figure 5.20. The objective here, is to estimate if the modeled coalescence rate is in adequacy with the experimental data available in the literature. Again, without knowing the experimental gas temperature profile, and the point at which the spherules solidify, only qualitative estimations can be made.

The spherule diameter values of 16.8 nm and 30.8 nm from Glotov and al. [49] are obtained in the 1D flame for coalescence zone lengths of 0.39 and 1.09 mm. Remember that these results were obtained in the case of an isolated burning aluminum particle

for which the coalescence zone is close to the size of the flame envelope, as illustrated in figure 5.16. This flame envelope typically varies from 2 to 5 times the particle radius which is much smaller than 0.39 or 1.09 mm. However the experimental conditions are too far from the 1D flame for a direct comparison, which has been put on the plot only to illustrate the role of the coalescence zone length on the diameter of the spherules.

The results of Poletaev et al. [92] were obtained for a dust flame in closer but not similar conditions with the 1D flame simulations performed here. The experimentally obtained spherule diameter values ranging from 63 to 107 nm are obtained in the 1D flame for coalescence distances of 2.99 and 5.84 mm. Despite the lack of experimental data on the temperature profile, these distances seem to be in the correct order of magnitude but rather low. Indeed, 5.84 mm seems to be a too small distance for the temperature to drop by more than 1000 K.

Finally, Lomba et al. [82] found alumina spherules of diameter approximately 200 nm. This was not given as an averaged measured value, but rather as an observation of some spherules. The value of 200 nm is recovered in the current work for a coalescence distance of 29.4 mm, whichis again in the right order of magnitude and is plausible for the gas phase to drop to 2350 K.

Although no quantitative validation can be drown from this comparison, it can be concluded that the averaged dimension of the spherules obtained numerically in the current work is in the same order of magnitude than the experimental data available in literature. This is an encouraging result, and motivates further validation after the implementation of both an aggregation and a thermal radiation model.

In this chapter, the complete aluminum combustion model implemented in the current work has been studied and compared with experimental data available in the literature. The model yields good results regarding key elements such as flame speed and flame temperature. The role of the sub-models has been studied further, highlighting their individual importance. The necessity of the implementation of more sub-models such as aggregation and thermal radiation of the alumina particles has been also shown, in particular to capture their solidification. Nevertheless, without such sub-models the obtained results are promising regarding the capacity of the model to describe the combustion products morphology. The general model can now be used to study more complex 2D flames.

Chapter 6

Simulation of 2D dust flames

After testing the implemented model on basic configurations in chapters 4 and 5, the model is now applied to 2D aluminum-air dust flames. The two simulations presented here are performed in similar conditions with experimental burners from the literature, thus allowing a comparison between experimental and numerical results. Furthermore, the 2D configurations allow for the study and discussion of the phenomena happening in the flame and their interactions.

Overview

6.1 Scaled down simulation of an experimental burner at stoichiometry

6.1.1 Computational configuration

In this section, a 2D numerical flame is stabilized to reproduce the experimental aluminum dust flame from Lomba et al. [82]. It is a simple aluminum-air jet burner for particles of diameter 7.1 μm.

A mix of air and aluminum particles at stoichiometry is injected through a circular tube of diameter 32 mm. It is surrounded by an annular injector with a thickness of 1.5 mm which sustains a methane-air flame used for ignition and aluminum flame stabilization. As this pilot flame has a very low mass flow it has a negligible impact on the aluminum flame structure. Indeed, its heat release is lower than 3 % of the heat released by the aluminum flame [82].

Therefore in the current numerical work this annular pilot flame is omitted which significantly simplifies the configuration, avoiding in particular to include methane chemistry in the kinetic scheme.

Even with the concept of weighted numerical particles presented in section 2.2.4, the calculation cost of the real configuration remains too high. To reduce this cost, the geometry is scaled down to a 7 mm - diameter injector, while conserving the injection velocity at 0.912 $m \cdot s^{-1}$, i.e., decreasing the flow rate by the same injection surface ratio. The particles flow rate is adjusted to maintain an equivalence ratio of 1. The computational domain is schematized in figure 6.1.

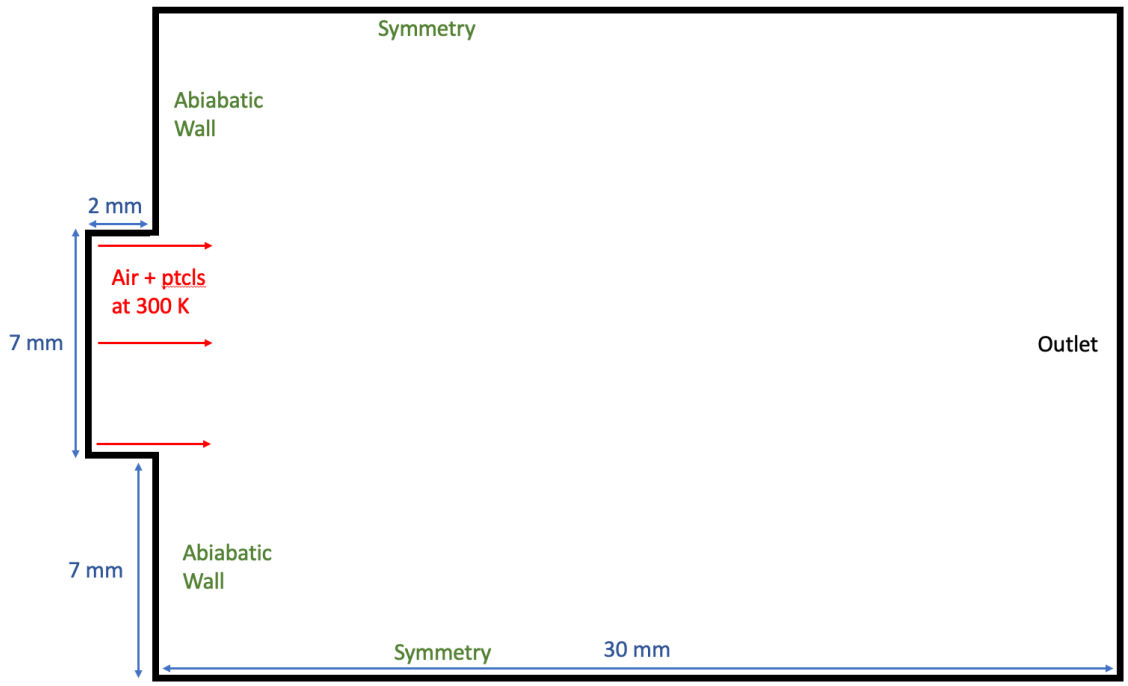

Figure 6.1 – Computational domain and boundary conditions for the scaled down 2D aluminum-air flame at stoichiometry.

The domain is discretized with 592398 triangular cells with 0.05 mm edges.

In all the 2D simulations, the transfer of the consumed aluminum particles from the first to the second subset is deactivated, due to a difficulty in the implementation of this transfer in the code. Therefore, once all the aluminum particles have fully evaporated, the remaining alumina particles are removed. If this has no influence on the flame and combustion itself, the residual alumina particles constituted from the lobes on the burned particles are not accounted for, which impacts the morphology of the combustion products.

6.1.2 Ignition and flame stabilization

Three characteristics of aluminum combustion make the ignition of these flames more challenging than gaseous or spray flames. The first challenge is the stiffness of the gaseous chemistry that has been discussed in part 3.3.3. The second is the flame temperature of aluminum, which is above 3000 K. Going from 300 K to such a high temperature at ignition may trigger important numerical instabilities. Third, because the particles are initially in a solid state, they need to absorb more energy from the gas phase before igniting than liquid hydrocarbon droplets.

The solution to the first two problems could be to apply a softer ignition with a lower temperature but the third problem forbids such an approach. Thus, the three above particularities imposes a ignition at high temperature.To ensure stability despite the induced stiffness, artificial viscosity is applied in the entire domain.

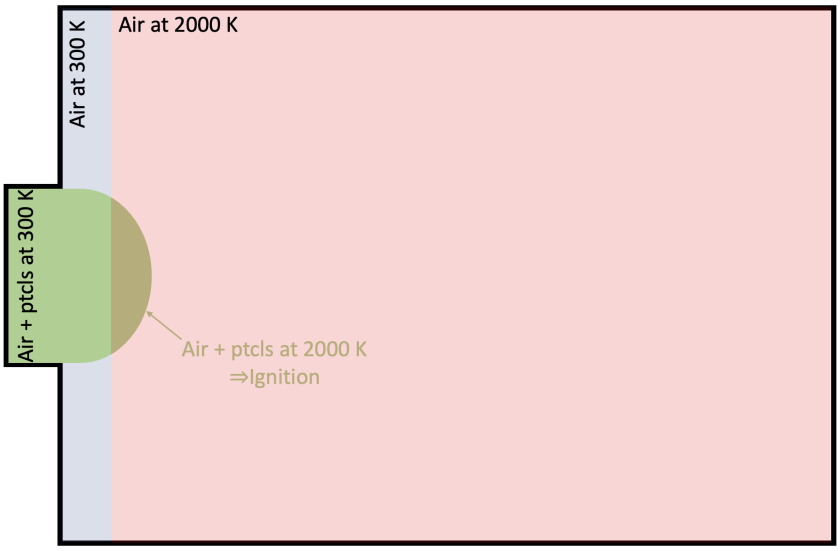

Figure 6.2 – Schematization of the ignition process used in the domain.

The ignition process is schematized in figure 6.2. At first, particles are injected with air at 300 K in a domain containing only air at the same temperature. Once the particles are far enough from the inlet, artificial viscosity is added and the temperature is increased to 2000 K. Once the flame is stabilized, the artificial viscosity is progressively removed and the final flame is obtained. This ignition process requires a high calculation cost of 70 000 cpu hours.

6.1.3 Key characteristics of the stoichiometric flame

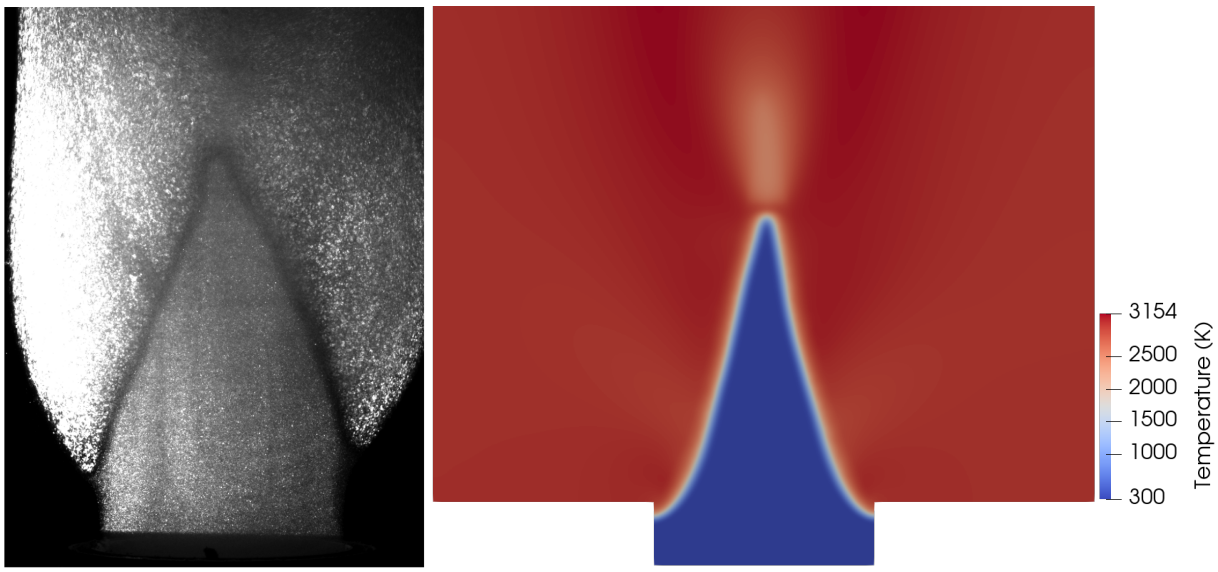

(a) (b)

Figure 6.3 – (a) Tomography image of an experimental aluminum-air flame. Figure extracted from [82]. (b) Temperature field of the numerical aluminum-air flame obtained in the current work.

In figure 6.3, the shape obtained in the current simulation is compared to the experimental flame from [82]. The two flames are overall similar but differ from each other in some aspects. The numerical flame is slightly longer than the experimental one and exhibits more concave sides. Moreover, the experimental flame is detached from the burner lips while the numerical flame is attached inside the injector. These differences indicate that particles heat up and ignite too fast in the simulation.

Several explanations for this behavior are possible. First, the heat transfer between the gas and the particles maybe be overestimated and a more accurate model could be used. Second, accounting for the existence of both liquid and solid aluminum and alumina in the particles would more realistically account for the fusion enthalpy. Third, the simplified surface reaction model might be too fast. Furthermore, in the current model, the surface reaction happens when the particle reaches 934 K, when the aluminum core melts and breaks the alumina layer. However in reality, if parts of the aluminum core are exposed to the oxidizer at this temperature not all the aluminum surface is immediately exposed to surface reaction.

The flame temperature is 3154 K, which is in good agreement with the flame temperature of 3146 ± 180 K obtained by Lomba et al. [82]. Slightly lower temperatures of 2900 K at the lower sides of the flame and a lower temperature of 2400 K at the top of the flame are observed. These local temperature drops are due to the difference in velocity between the particles and the gas, which creates local variations in equivalence ratio. Figure 6.4 illustrates this particular behavior.

The field of Y_{O_2} plotted in figure 6.4a shows an excess of O_2 on the lower sides of the flame, with mass fraction up to 0.05 close to the flame front, where a reduction in

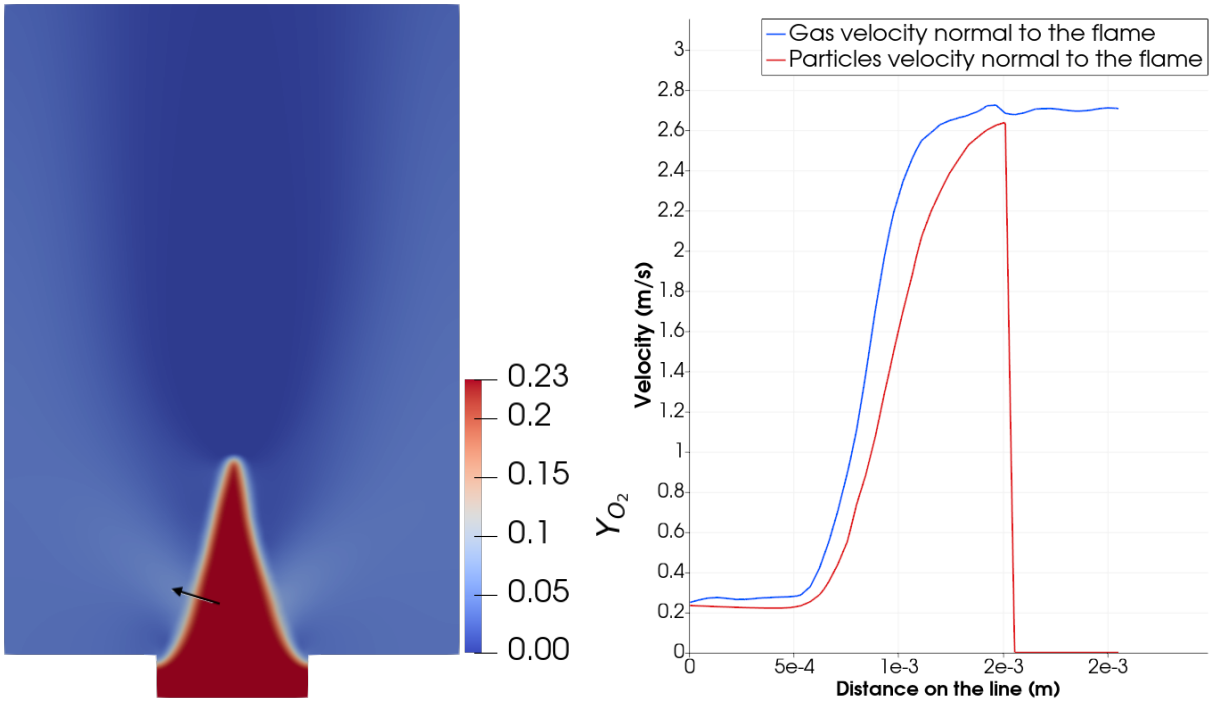

(a) (b)

Figure 6.4 – (a) Mass fraction field of O2 in the numerical domain. (b) Evolution of gas and particles velocity along the arrow in the left subplot.

temperature to 2900 K was also observed. In this region, the velocities of the gas and particles normal to the flame front along the black arrow in figure 6.4a are plotted in figure 6.4b. The gas accelerated by the heat release in the direction normal to the flame front, has a higher velocity than the particles which accelerate less due to their inertia. Therefore, the particles tend to keep a trajectory more aligned with the vertical axis while air is more ejected to the sides of the flame, locally modifying the equivalence ratio. Injected at stoichiometry, the reactive mixture then becomes locally rich while excess air is found in the burnt gas side. The temperature therefore decreases, down to 2900K. This effect cumulates along the flame sides, until the rich mixture reaches the top of the flame, where the temperature dips to 2400K and unburnt aluminum crosses the flame front. As the height above burner increases, this excess of aluminum finally mixes with the excess of oxidizer released along the flame sides, and burns to finally reach the expected flame temperature.

6.1.4 Aluminum particle distribution and statistical convergence

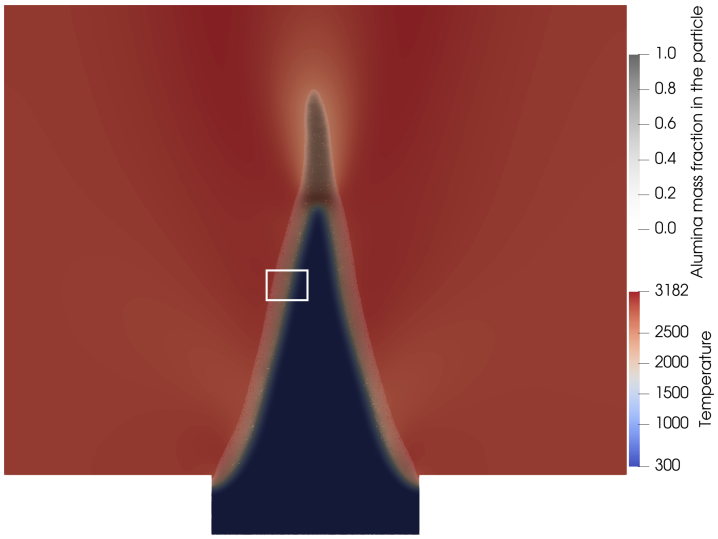

Figure 6.5 – Distribution of the aluminum mass fraction in the fuel particles superimposed to the gaseous temperature field. The white rectangle in the flame represents the zoomed domain shown in figure 6.6.

The aluminum mass fraction in the fuel particles is shown together with the gaseous temperature field in figure 6.5. As the particles enter the flame zone, their aluminum mass fraction diminishes due to evaporation and surface reactions. This process happens over a length of 0.81 mm along the flame. However, at the top of the flame which presents a lower temperature, the particles take longer to react and evaporate.

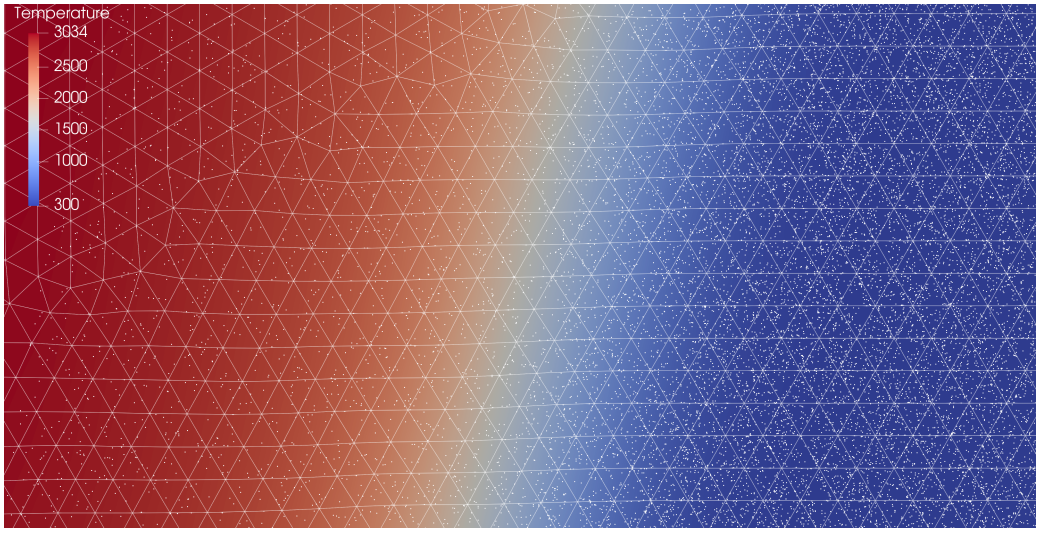

Figure 6.6 – Zoom on the white box of figure 6.5 : aluminum fuel particles, gas temperature and mesh.

In the current model, each numerical particle represents a number of physical particles that correspond to the statistical weight of the numerical particle. This point is

extensively discussed in part 2.2.4 but it is important to stress here that an insufficient number of numerical particles may induce statistical and model inaccuracy. Meanwhile, increasing the number of numerical particles increases the calculation cost. Thus having an unnecessary large population of numerical particles is detrimental. Through a flame, the gas accelerates which reduces the particle density and to compensate this effect, a larger than necessary particle density must be injected in the fresh gas. If this behavior already appears in hydrocarbon flames, it is re-enforced by the higher flame temperature in aluminum dust flames.

In figure 6.6, the fuel particles are represented as white dots through the flame front. In the fresh gas region, a concentration of around 30 particles per cell is observed which is more than enough to correctly represent the population of fuel particles with a constant initial diameter. In the flame, this density drastically drops as the temperature rises but remains on average around 5 particles per cell. Even if a few cells are empty, this particle density is a good compromise between numerical stability, physical representation and calculation cost.

6.1.5 Morphology of the combustion products

The current model allows for the tracking of the liquid combustion products. However due to the lack of a radiation and coagulation sub-models, only the size of the spherules can be predicted. This aspect was detailed in part 5.9.

The averaged diameter of the alumina particles in each cell is plotted in figure 6.7 for the entire domain.

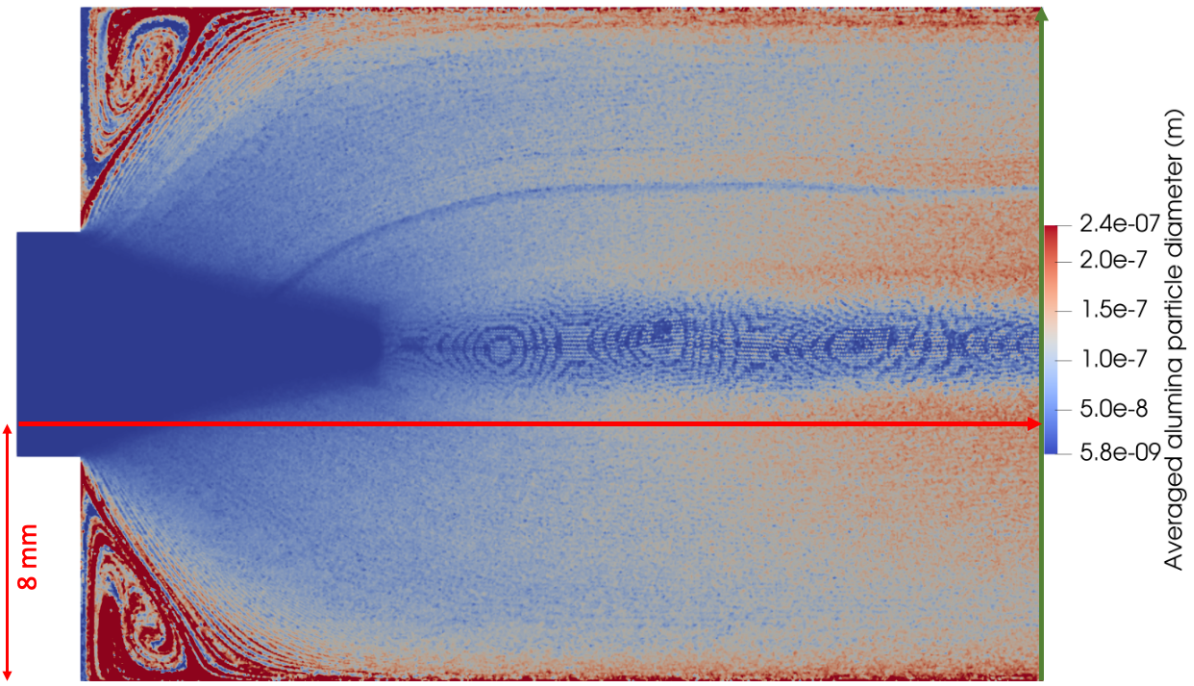

Figure 6.7 – Distribution of the averaged alumina particle diameter in the domain. The red and green arrows represent the plot-over-lines shown in figure 6.8 and 6.9, respectively.

The distribution of the averaged alumina particle diameter in the domain is heterogeneous for several reasons.

First, in the top and bottom left corners, re-circulation zones create an accumulation of particles that can be trapped here with diameters of up to 2 μm.

Second, some of these particles escape the re-circulation zone and leave the domain by traveling along the top and bottom limits of the domain. These particles can present diameters of up to 870 nm. These two first diameter variations are due to the boundaries of the domain and should be ignored because they are non-physical. This could be corrected simply by using better boundary conditions, which will be done in future work. Having realized this weakness of the computational domain, the 2D flame presented in section 6.2 has been computed with outlet boundary conditions as illustrated in figure 6.10. Thus, these anomalies are not present in figure 6.15.

Third, the heterogenization of the equivalence ratio created by the speed difference between the gas and the particles that is discussed in part 6.1.3 has a clear impact on the diameter of the alumina particles. Indeed, in the wake of the top of the flame where combustion was diminished by a higher equivalence ratio, less gaseous alumina was produced. Therefore, the condensation upon these particles is weaker, which results in a zone with smaller particles. A similar phenomenon happens in lesser proportion on the sides of the flames where the equivalence ratio is lower.

As the excess aluminum from the top of the flame meets the excess of oxidizer from the sides of the flame, gaseous alumina is produced. The produced alumina condenses on the particles, which results in bigger alumina particles. Furthermore, because this area is in the wake of the part of the flame at stoichiometry that already produced higher particles diameter, the particles with the highest averaged diameters are found here.
Please note that a thin zone spreading from the top left zone of the flame to the outlet presents abnormally low diameter values. No explanation for this zone has been found yet and is probably the result of a numerical error. This will be investigated and corrected in future work.

The averaged diameter is further characterized with its profile along the red arrow in figure 6.7.

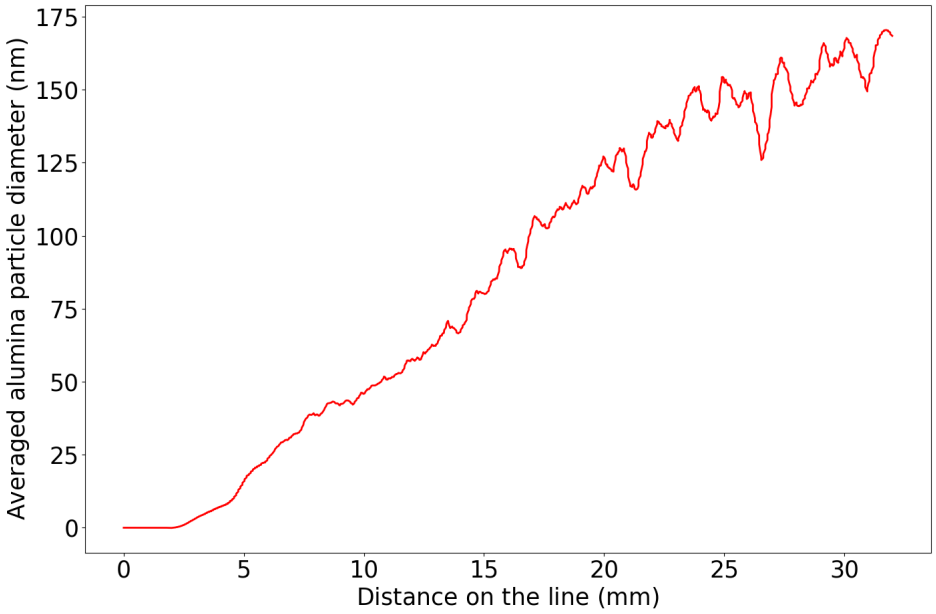

Figure 6.8 – Evolution of averaged alumina particle diameter along the red arrow in figure 6.7.

Along the red arrow, figure 6.8 shows that the averaged alumina particle diameter steadily grows to reach a value of 170.4 nm at the outlet, i.e., 29.6 mm downstream the flame front. This value is in the same order of magnitude as the results obtained in the 1D aluminum-air flame 5.9 where a value of 200 nm at 29.4 mm after the flame front was found. This difference with the 1D flame could be due to the physical differences between the setups. It could also be explained by the absence of the transfer of the alumina lobe to the second particle subset. Indeed, the residual alumina particles from the lobe contain the alumina from surface reactions and have higher diameters, increasing the averaged alumina particle diameter.

However this result is obtained for a specific line in an in-homogeneous distribution of diameters and to better study this quantity, it is interesting to consider the plot on figure 6.9.

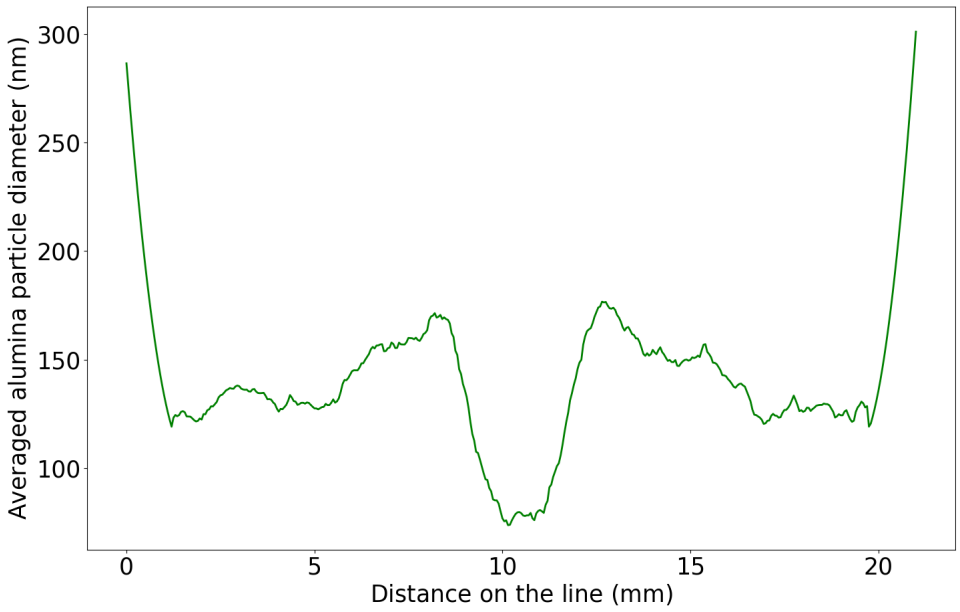

Figure 6.9 – Profile of averaged alumina particle diameter along the green arrow in figure 6.7.

The evolution of alumina particle diameters along the green arrow is shown in figure 6.9. This gives the averaged diameter distribution of alumina particles along the outlet. Ignoring the maximums at the extremities that are due to the boundary conditions of the domain, the distribution varies from 72.6 nm to 176.2 nm. The reasons for these variations have already been developed earlier in this section. In the zones that are not in the wake of the variations in equivalence ratio, the averaged particle diameter is around 130 nm, which is in a coherent order of magnitude with the experimental values presented in part 5.9.

Finally, if some of these variations in the distribution of the particle size are due to nonphysical phenomena, these results clearly show the potential of the model to track and study complex heterogeneous particle morphology distribution.

6.2 Scaled down simulation of an experimental burner at $\Phi = 1.6$

6.2.1 Computational configuration

In this section, a 2D numerical flame is stabilized to reproduce the experimental aluminum dust flame from Goroshin et al. [52]. This burner was introduced in part 1.2.1 and photographs of flames obtained on this burner are visible in figure 1.20. The flame of interest is the aluminum-air flame. The aluminum particles are injected together with air in a central tube at an equivalence ratio of $\Phi = 1.6$ with a speed of $u = 0.5$ m/s. This central injector with a diameter of 20 mm is surrounded by an air co-flow injected at a similar speed of $u = 0.5$ m/s to stabilize the main flame and oxide the aluminum excess. Finally, the injected particles are smaller than in the burner of Lomba et al. [82] with an average diameter $d_p = 5.6$ μm. The used numerical domain is schematized in figure 6.10.

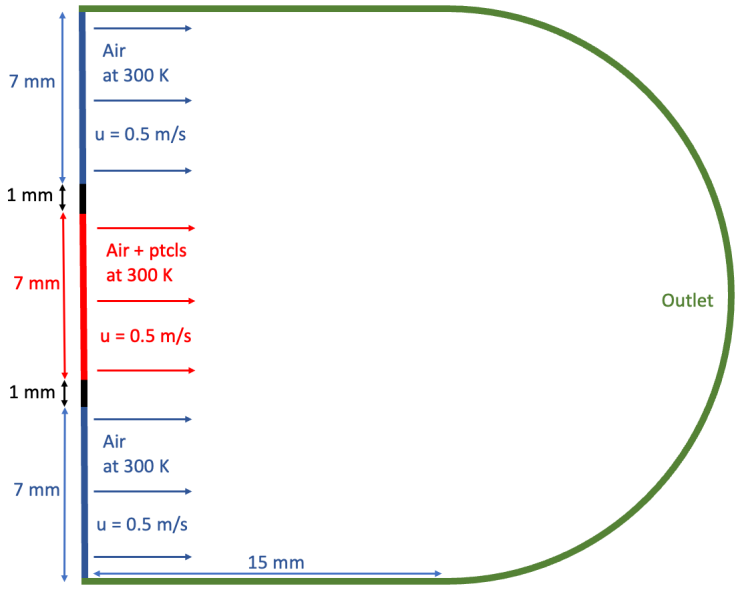

Figure 6.10 – Computational domain and boundary conditions for the scaled down 2D aluminum-air flame at $\Phi = 1.6$.

The numerical main inlet has been scaled down from 20 mm to 7 mm and the annular air injection is also adjusted. To prevent the impact of the boundary conditions on the flow observed in figure 6.7, the upper and lower boundaries of the domain are merged with the inlet. Finally, the domain is discretized with508973 triangular cells with 0.05 edges.

The ignition process used in this simulation is the same as the one used in the previous 2D simulation that was detailed in part 6.1.2.

6.2.2 Key characteristics of the flame at $\Phi = 1.6$

The general shape of the obtained numerical flame can be compared to the experimental one obtained by Goroshin et al. [52]. This comparison is available in figure 6.11.

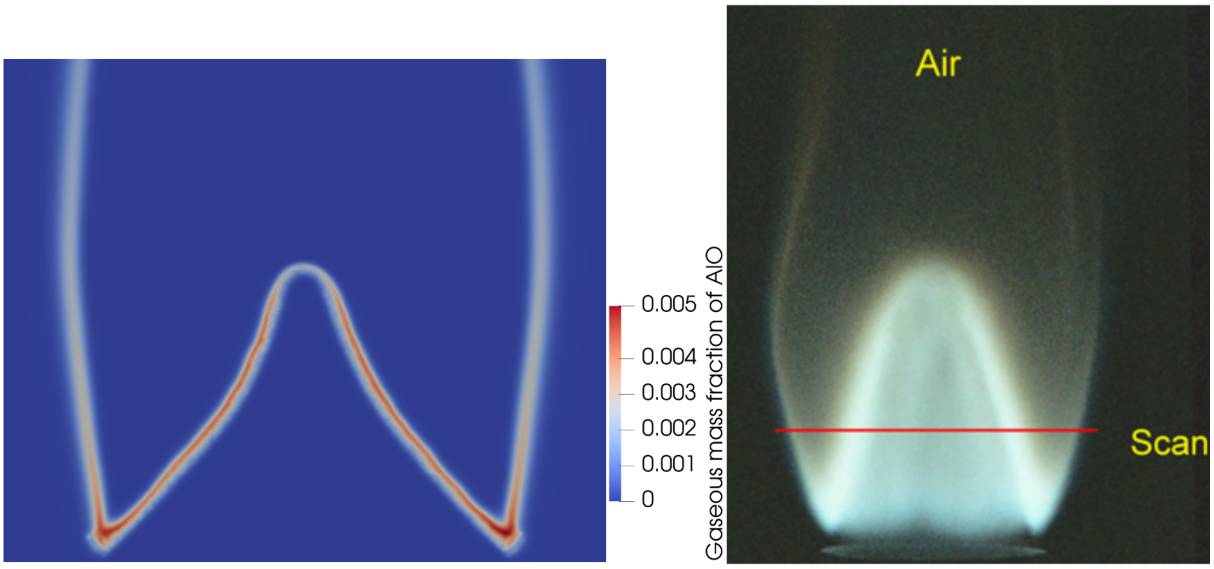

(a) (b)

Figure 6.11 – (a) Mass fraction field of AlO in the numerical domain. (b) Photograph of an experimental aluminum-air flame. Figure extracted from [52].

AlO is a key intermediate species present in aluminum-air flames which is a great indicator of the flame position. In figure 6.11, the gaseous mass fraction field of this intermediate obtained in the current work is compared to a photograph of the flame from Goroshin et al. [52].

While the numerically obtained flame stabilizes into a valid shape, it differs from the experimental flame by being proportionally smaller in height. However, the "W" shape of the flame created by the double flame front is well reproduced by the simulation. The causes and characteristics of this shape are discussed in more details in part 6.2.3.

Another key characteristic that can be compared with the experimental flame from Goroshin et al. [52] is the flame temperature. The computed temperature field is available in figure 6.12.

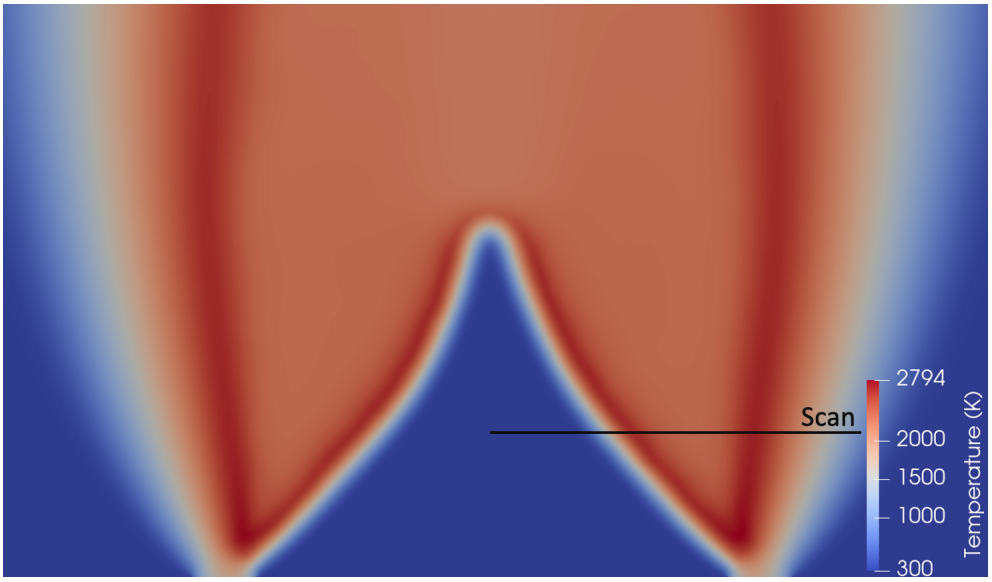

Figure 6.12 – Temperature field in the numerical domain. The black line labeled "Scan" corresponds to the line along which the temperature is plotted in figure 6.13.

As expected, the temperature field presents a similar "W" shape as the gaseous AlO field. The flame temperature never rises above 2800 K which is lower than the experimental flame temperature from Goroshin et al. [52] which can rise above 3300 K in some areas. This lower flame temperature is consistent with the results obtained in part 5.6 on 1D flames, which demonstrated that the implemented model tends to under-predict flame temperature for equivalence ratios different than 1.

It is interesting to compare the gas temperature along the line labeled "Scan" in figure 6.12 with the similarly named line present in figure 6.11b. Because the numerical burner is scaled down from a diameter of 20 mm to 7 mm, the experimental line length, as well as the position of the experimental results, are scaled down by a factor of $20/7 = 2.86$ for consistency. Both the scaling down of the injector diameter and the numerical model are responsible for a shorter numerical flame than the experimental one. Thus, the positional height of the "Scan" line needs to be scaled down too. The experimental flame has a height of 29.3 mm while the numerical flame has a height of 5.3 mm. Therefore, the "scan" line in the numerical flame is at a height of 2.17 mm. The temperature obtained in the current case along this line is compared with the scaled experimental results for flame temperature in figure 6.13.

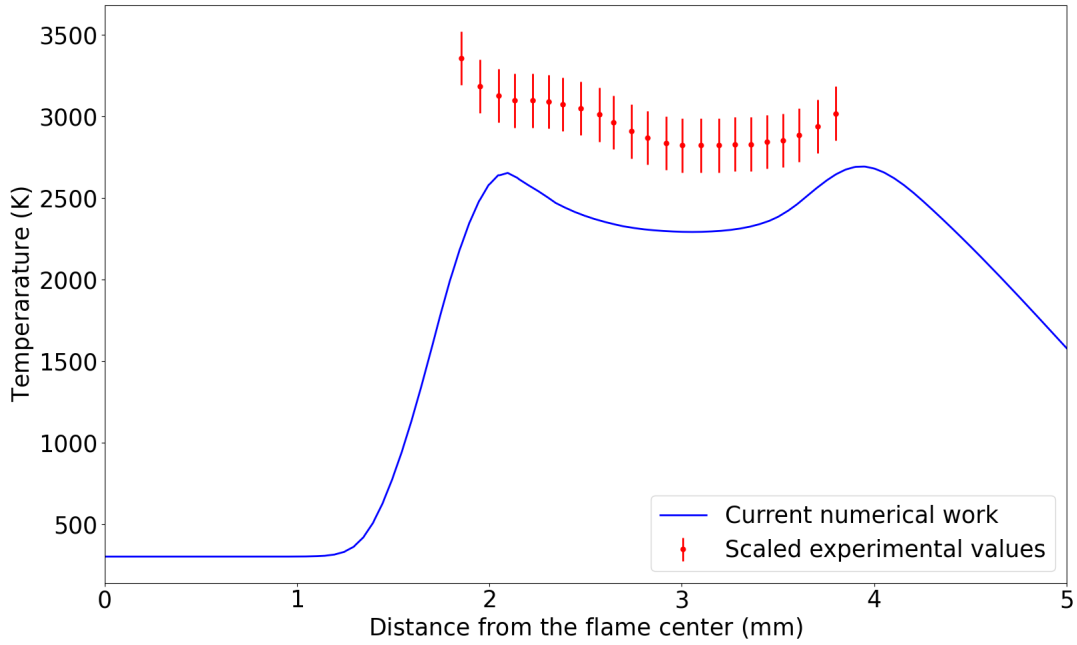

Figure 6.13 – Temperature distribution across the flame along the "Scan" line from figure 6.12. This numerical temperature distribution is compared with the experimental values obtained along the "Scan" line from figure 6.11b by Goroshin et al. [52].

The temperature distribution across the flame along the "Scan" line from figure 6.12 obtained in the 2D simulation differs from the experimental data by 357 to 650 K. This difference constitutes an error ranging from 12.1 to 21.3 % relatively to the experimental temperature.

Because the numerical simulation presents variations that are similar to the experimental data, this error is not attributable to the scaling of the "Scan" line. This error is purely due to the implemented model which incorrectly predicts a lower flame temperature than physically accurate for non stoichiometric flames, as already demonstrated on 1D flames in part 5.6.

6.2.3 Aluminum particle field and combustion regimes

Despite the shortcomings of the implemented model presented in the previous section, the "W" shape of the flame created by the double flame front is reproduced by the simulation. Indeed, the internal flame is the results of the combustion of the premixed injection of aluminum particles and air. This combustion does not consume all the aluminum which is in excess after this first flame front. As this excess aluminum encounters the oxygen from the air co-flow, a second flame front is created. Because the mass fraction of AlO is much higher in the first flame front, the combustion reactions are more important in this zone than in the second flame front.

It is interesting to note that part of the excess aluminum particles from the first flame front is consumed in the second flame front while some escape the domain through the outlet. This is visible in figure 6.14.

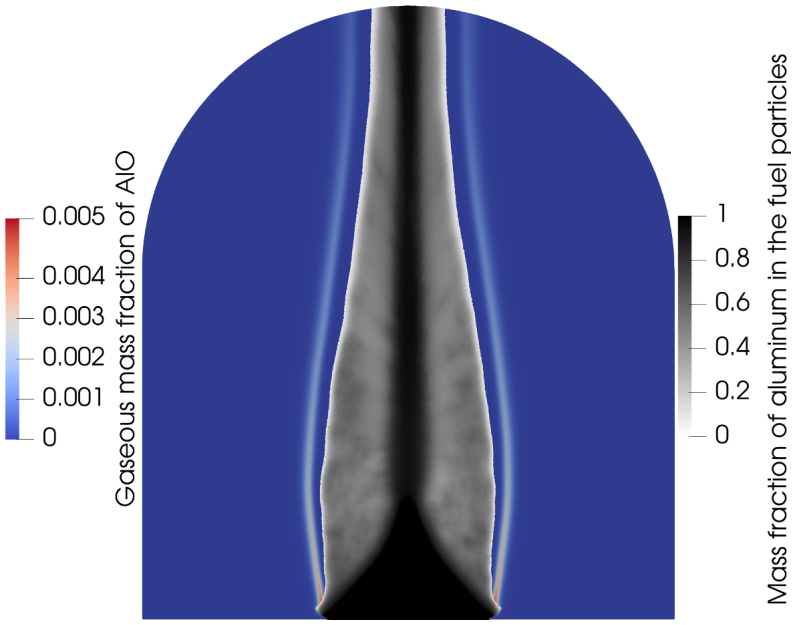

Figure 6.14 – Superposition of the mass fraction of aluminum in the fuel particles over the gaseous mass fraction of AlO visible in figure 6.11a.

In figure 6.14, the mass fraction of aluminum in the fuel particles is superposed over the gaseous mass fraction of AlO already presented in figure 6.11a. In the previous 2D simulation, the particles do not evaporate before the flame front and burn while crossing it, as visible in figure 6.5.

In the current 2D case, the particles also burn while crossing the first flame front, with a part of the population still remaining after it due to the excess aluminum in the main injector. However, before the second flame front, all the aluminum particles have evaporated and therefore only gaseous aluminum encounters the oxidizer. This is visible in figure 6.14 as there is a gap between the particle field and the second flame front located where there is gaseous AlO. If hydrocarbon particles were considered, this would already represent a major difference between the combustion regimes of the first and second flame front. However, for aluminum combustion, this observation is even more important. Indeed, if the particles burn in the flame front, both gaseous and surface reactions play a role. But because they evaporate before the second flame front, only gaseous reactions are playing a role here. Thus, the current configuration could be used in future work to study the impact of the surface reactions by comparing the two flame fronts.

Furthermore, the evaporation of the particles is due to the heat from the first flame front. As demonstrated in part 5.6 on 1D flames, the implemented model tends to underpredict flame temperature for equivalence ratios different than 1. It is, as expected, also the case in the present 2D simulation and this lower temperature induces a lower evaporation rate from the aluminum particles. Thus, the phenomenon of aluminum particles evaporating after the first flame front, resulting in the combustion regime of the second flame front being purely gaseous, should be even more important in reality.

6.2.4 Morphology of the combustion products

The current model can track the liquid combustion products. However, due to the absence of radiation and coagulation sub-models, it can only predict the size of the spherules. This aspect was detailed in part 5.9.

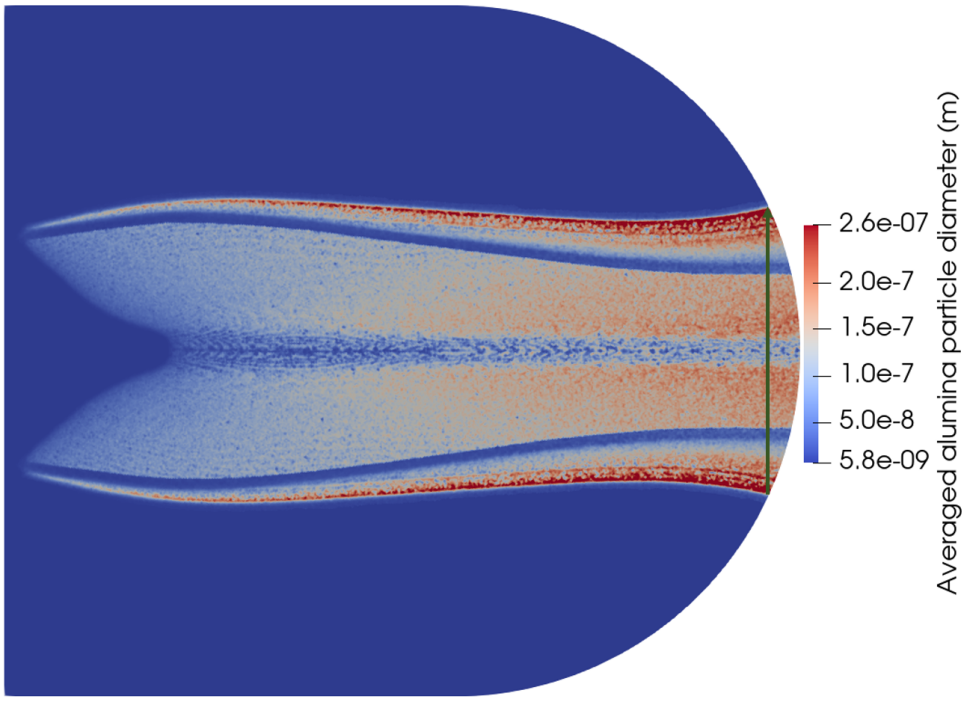

Figure 6.15 – Distribution of the averaged alumina particle diameter in the domain. The green arrow represents the plots over line available in figure 6.16.

Similarly to the results obtained in the previous 2D simulation that are available in figure 6.7, the particle diameter distribution is heterogeneous. In the previous 2D case, part of this heterogeneity is due to the boundary conditions of the domain and are therefore non physical. However, this has been corrected in the current 2D simulation by using inlets at the base of the domain and an outlet spreading from the exit to the sides of the numerical domain. These boundary conditions are illustrated in figure 6.10.

Therefore, in the current case, the variations of alumina particle diameter in the domain is integrally due to physical phenomena that are discussed hereafter.

First, in the wake of the flame from the main injector, the particle diameters progressively increase, except in the center of the domain. This is because the center line of the domain is the farthest from the reoxidizing air-coflow which means that the equivalence ratio is the highest. Thus, the combustion reactions, and therefore the alumina production, are at their lowest in this area. Indeed, this area can be superposed with the black central column visible in figure 6.14 which corresponds to the central excess aluminum particles that are not consumed due to the lack of oxidizer in this central zone.

Along the sides of the wake from the main injector, two blue curves can be observed in the wake of the 1mm separation between the main and secondary injectors present

at the inlet. As developed in part 6.2.3, there is a gap between the particles field and the second flame front where gaseous aluminum travels to the second flame front before burning when encountering the oxidizer from the air co-flow. Thus in this area, no alumina is produced and therefore the alumina particle diameter remains low. These smaller particles are visible as the blue lines that can be observed along the sides of the wake from the main injector.

Finally, as previously mentioned, when the gaseous aluminum traveling to the air co-flow encounters oxidizer it creates the secondary flame front. This secondary flame front is exclusively the result of gaseous reactions which generate an important quantity of gaseous alumina. This important quantity of gas condensates, creating more numerous and bigger alumina particles. These bigger particles form the thin red regions along the secondary flame front in figure 6.15.

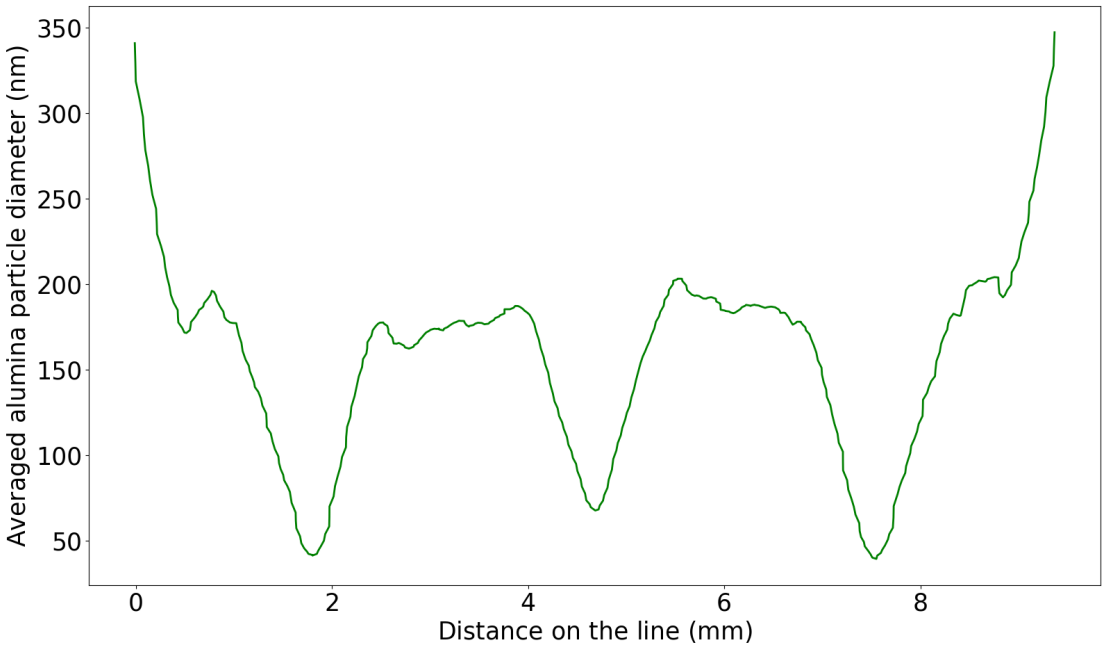

Figure 6.16 – Profile of averaged alumina particle diameter along the green arrow in figure 6.7.

The evolution of averaged alumina particle diameter close to the outlet is plotted in figure 6.16. The variations of the particle diameter can be explained by the observations developed in the previous paragraph. Indeed, the central minimum value of 67.1 nm corresponds to the middle of the flame where a lot of aluminum particles remain. The two other minimum values of 40.7 and 39.1 nm correspond to the zones along the edges of the particle field where only gaseous aluminum is present and has not yet encountered the second flame front. Finally, the maximum values, reaching up to 347 nm, observed on the sides of the profile correspond to regions along the secondary, purely gaseous, front flame.

It is impossible to quantitatively validate the averaged alumina diameter values obtained here. As explained in more details in part 5.9, this requires the implementation

of a thermal radiation model for the alumina particles. However, the order of magnitude obtained here is coherent with the order of magnitudes from previous simulations, as well as with the experimental values presented in 5.9. Furthermore, this section clearly demonstrates the potential of the current model to track and study the population of alumina particles in more details than ever before on such configurations.

In this chapter, the model was tested on two 2D configurations replicating scaled-down experimental burners from the literature. The model permitted the stabilization of aluminum-air flames in both configurations allowing for comparisons and discussions about the experimental results.
The model is in good agreement with the experimental values regarding flame shape and flame temperature at stoichiometry. Meanwhile, if a flame was stabilized at $Phi = 1.6$ with a coherent shape, both this shape and the flame temperature differ from the experimental values from the literature. This confirms the results obtained in chapter 5 on 1D flames.
Despite the lack of a thermal radiation model for the liquid combustion products, the obtained values for alumina particle diameters are in a similar order of magnitude with the experimental values available in the literature. More importantly, the potential of using Lagrangian particle tracking of the liquid products coupled with a state of the art condensation model was clearly demonstrated. This has never been performed before on such configurations.

In conclusion, the model can be used to correctly simulate aluminum dust flames and, with the future implementation of a radiation model, could be used to predict the morphology of the solid combustion products. Only few models in the literature are capable of stabilizing such flames and none can track and predict the morphology of the combustion products using an advanced sub-model such as the one from Finke et al. [36]. Thus, the current model abilities and future potential is quite unique and constitutes an important step towards the modeling of aluminum flames and the study on their solid combustion products.

Conclusion and perspectives

In the current work, a complete model for aluminum particle combustion accounting for the presence of the alumina cap, gas and surface reactions, as well as an advanced condensation model has been implemented in the code AVBP. This model combines a number of sub-models already available in the literature and mostly applied until now to simpler cases. A major originality is the creation and tracking of the liquid combustion products, allowing the prediction of their size which is critical for the use of aluminum as a fuel. Another progress made in this paper is the application of such complete model to realistic flame configurations.

The model has been tested in several test cases such as the combustion of an isolated aluminum particle, 1D aluminum flames and 2D aluminum dust flames. In the first case, the combustion time is in agreement with the literature and the roles of nucleation, condensation and agglomeration have been highlighted. In the 1D flame, the flame speed as well as the flame temperature are also in good agreement with experimental results from the literature. Finally, 2D aluminum-air flames have been successfully stabilized and compared with similar experimental configurations. At stoichiometry, the experimental flame shape is overall well retrieved and even if the model lacks a thermal radiation model for alumina liquid particles, the obtained spherule diameters are in the correct range. The 2D cases also demonstrated the capacity of the model to capture and therefore allow the study of complex physical behaviors. Interesting examples include a local change of equivalence ratio due to the particle inertia in the first simulation and the double flame front with different combustion regimes in each front in the second 2D simulation.

The abilities of the implemented model to correctly model stabilized stoichiometric flames while tracking the combustion products using a state of the art condensation sub-model is simply unique.

With the addition of a thermal radiation model and the correction of the non-physical results observed at non-stoichiometric equivalence ratios, this model could play a major role in pushing the understanding of aluminum combustion forward. Indeed, with these future corrections coupled with calculation cost optimizations, such a model could allow for the simulation of aluminum flames in complex configurations never studied before. Finally, with the future addition of a thermal radiation model, the unique capacity to predict the solid combustion products morphology would be a major leap towards a better understanding of how to collect and retrieve these products.

Appendix

CHEMKIN tables for the gaseous species

The properties of gaseous aluminum and its oxides have been implemented in AVBP by Suarez [105] during his PhD. Thus, the following tables are extracted from his PhD manuscript [105]. These tables are presented hereafter in the CHEMKIN format.

```
AL                  62987AL  1           2    G   0300.00   5000.00  0600.00    1
 0.02559589E+02-0.01063224E-02 0.072028 3 E-06-0.02121105E-09 0.02289429E-13  2
 0.03890214E+06 0.05234522E+02 0.027368 4 E+02-0.05912374E-02-0.04033938E-05  3
 0.02322343E-07-0.01705599E-10 0.03886795E+06 0.04363880E+02                  4
AL2O3           tpis96AL          2.O 3.  0.  0.G      200.000 6000.000 1000.      1
1.18224768E+01  1.72547969E-03   -6.77407352E-07   1.15824576E-10  -7.21083594E-15  2
-6.97100145E+04 -3.05568543E+01   5.63487396E+00   2.44276632E-02  -3.39723369E-05  3
2.31682578E-08  -6.27929522E-12  -6.82838850E+04   1.47501030E-02  -6.57754372E+04  4
ALO        tpis96  AL 1.O 1.  0.  0.G   200.000          6000.000          1000.          1
 2.87812691E+00   1.96920280E-03   -3.86303536E-07   7.31791832E-12   2.48454782E-15   2
 7.28872515E+03   9.56556843E+00   3.34913178E+00-   7.30811097E-05   7.10157373E-06   3
-1.06139198E-08   4.70712402E-12   7.05728468E+03   6.97458001E+00   8.09656925E+03   4

ALO2       tpis96  AL 1.O 2.  0.  0.G   200.000          6000.000          1000.          1
 6.82788443E+00   7.33105641E-04   -3.13759379E-07   5.96366292E-11   -3.91258986E-15  2
-6.86225611E+03   -7.06432998E+00   4.34294502E+00   8.65076281E-03   -8.91492593E-06  3
 3.12927133E-09    9.49015044E-14   -6.25626126E+03   5.43603439E+00   -4.64944681E+03  4

AL2O       tpis96  AL 2.O 1.  0.  0.G   200.000          6000.000          1000.          1
 6.83557723E+00   6.85036558E-04   -2.69320700E-07   4.60912632E-11   -2.87128689E-15  2
-2.00793927E+04   -9.02360368E+00   4.07405095E+00   1.12981458E-02   -1.66855499E-05  3
 1.20474407E-08   -3.43957451E-12   -1.94653414E+04   4.50607534E+00   -1.78737275E+04  4

AL2O2      tpis96  AL 2.O 2.  0.  0.G   200.000          6000.000          1000.          1
 9.14886135E+00   1.38425788E-03   -5.42174706E-07   9.25638703E-11   -5.75686436E-15  2
-5.15186949E+04   -1.84651707E+01   4.83765565E+00   1.67010188E-02   -2.23411191E-05  3
 1.48421603E-08   -3.96196410E-12   -5.04957125E+04   2.97081413E+00   -4.84809794E+04  4

O          g 8/97O 1.E -1.  0.  0.G   298.150          6000.000          1000.          1
 2.48542028E+00   2.56978695E-05   -1.28833378E-08   1.65525487E-12   1.09933344E-16   2
 1.87940874E+05   4.47425446E+00   2.50000000E+00   0.00000000E+00   0.00000000E+00   3
 0.00000000E+00   0.00000000E+00   1.87935284E+05   4.39337676E+00   1.88680659E+05   4
```

Figure 6.17 – Polynomials coefficients in the CHEMKIN format for aluminum and its oxides. Table extracted from [105].

Original kinetic scheme from Catoire et al. [24]

The original kinetic scheme from Catoire et al. [24] is detailed hereafter. This scheme was originally developed to be used in aluminum-sensitized Ram accelerator and therefore account for elements such as carbon or hydrogen. For the combustion of aluminum-air dust flames studied in the current work, these elements are not needed. Thus, the scheme used in the current work, which is available in table 3.1, is the one from Catoire et al. [24] without the reactions involving molecules containing non needed elements.

Reaction[b]	A	n	Θ
$Al + CO_2 = AlO + CO$	1.74×10^{14}	0	3221
$Al + O_2 = AlO + O$	9.72×10^{13}	0	80.5
$Al + O + M = AlO + M$	3×10^{17}	-1	0
$AlO + CO_2 = OAlO + CO$	1.5×10^{10}	0	-400
$AlO + O_2 = OAlO + O$	4.62×10^{14}	0	10008
$Al + H_2O = H + AlOH$	1.14×10^{12}	0	442.8
$Al + H_2O = AlO + H_2$	9.6×10^{13}	0	2868.6
$AlOH = Al + OH$	10^{15}	0	66431.8
$AlOH = AlO + H$	10^{15}	0	57725.2
$AlOAl = AlO + Al$	10^{15}	0	67035.7
$OAlO = AlO + O$	10^{15}	0	44564.6
$AlOAlO = AlOAl + O$	10^{15}	0	52466
$AlOAlO = Al + OAlO$	10^{15}	0	74937.1
$AlOAlO = AlO + AlO$	10^{15}	0	59335.7
$Al_2O_3 = AlOAlO + O$	3×10^{15}	0	49144.4
$Al_2O_3 = OAlO + AlO$	3×10^{15}	0	63915.4

Figure 6.18 – Al/C/O/H submechanism, $k = A \times T^n \exp(-\Theta/T)$ with $\Theta = E/R$ the activation temperature. The units used in this table are $\mathrm{cm}^3, \mathrm{mol}^{-1}, \mathrm{s}^{-1}, \mathrm{K}$. Table extracted from [24].

List of Figures

List of Tables

Bibliography

[1] The nasa 7-coefficient polynomial parameterization. https://cantera.org/science/species-thermo.html.

[2] Michel Armand and J.-M Tarascon. Building better batteries. Nature, 451:652–7, 03 2008.

[3] Marc J Assael, Konstantinos Kakosimos, R Michael Banish, Jürgen Brillo, Ivan Egry, Robert Brooks, Kenneth C Mills, Akira Nagashima, Yuzuru Sato, and William A Wakeham. Reference Data for the Density and Viscosity of Liquid Aluminum and Liquid Iron. J. Phys. Chem. Ref. Data, 35(1), 2015.

[4] Peter William Atkins, Julio De Paula, and James Keeler. Atkins' physical chemistry. Oxford university press, 2017.

[5] VA Babuk and VA Vasilyev. Model of aluminum agglomerate evolution in combustion products of solid rocket propellant. Journal of Propulsion and Power, 18(4):814–823, 2002.

[6] Darrel Baumgardner, R. C. Miake-Lye, M. R. Anderson, and R. C. Brown. An evaluation of the temperature, water vapor, and vertical velocity structure of aircraft contrails. Journal of Geophysical Research: Atmospheres, 103(D8):8727–8736, 1998.

[7] Richard Becker and Werner Döring. Kinetische behandlung der keimbildung in übersättigten dämpfen. Annalen der Physik, 416:719–752, 1935.

[8] M. W. Beckstead, Y. Liang, and K. V. Pudduppakkam. Numerical Simulation of Single Aluminum Particle Combustion (Review). Combustion, Explosion, and Shock Waves, 41(6):622–638, November 2005.

[9] Merrill Beckstead. A Summary of Aluminum Combustion. January 2002.

[10] Merrill Beckstead, Y. Liang, and K. Pudduppakkam. Numerical simulation of single aluminum particle combustion (review). Combust., Expl., Shock Waves, 41:622–638, 11 2005.

[11] Merrill W Beckstead. Correlating aluminum burning times. Combustion, Explosion and Shock Waves, 41:533–546, 2005.

[12] Jeffrey M. Bergthorson. Recyclable metal fuels for clean and compact zero-carbon power. Progress in Energy and Combustion Science, 68:169–196, September 2018.

[13] J.M. Bergthorson, S. Goroshin, M.J. Soo, P. Julien, J. Palecka, D.L. Frost, and D.J. Jarvis. Direct combustion of recyclable metal fuels for zero-carbon heat and power. Applied Energy, 160:368–382, December 2015.

[14] Graeme A Bird. Molecular gas dynamics and the direct simulation of gas flows. Oxford university press, 1994.

[15] Milton Blander and Joseph L Katz. The thermodynamics of cluster formation in nucleation theory. Journal of Statistical Physics, 4:55–59, 1972.

[16] Pablo Escot Bocanegra. Études expérimentales et modélisation de la combustion des nuages de particules micrométriques et nanométriques d'aluminium.

[17] LV Boichuk, Vladimir Gavrilovich Shevchuk, and Aleksey Igorevich Shvets. Flame propagation in two-component aluminum–boron gas suspensions. Combustion, Explosion and Shock Waves, 38:651–654, 2002.

[18] Alexandre Braconnier. Étude expérimentale de la combustion d'une particule d'aluminium isolée : influence de la pression et de la composition de l'atmosphère oxydante. These de doctorat, Orléans, October 2020.

[19] Alexandre Braconnier, Christian Chauveau, Fabien Halter, and Stany Gallier. DETAILED ANALYSIS OF COMBUSTION PROCESS OF A SINGLE ALUMINUM PARTICLE IN AIR USING AN IMPROVED EXPERIMENTAL APPROACH. International Journal of Energetic Materials and Chemical Propulsion, 17(2):111–124, 2018.

[20] Kriston Brooks and Merrill Beckstead. Dynamics of aluminum combustion. Journal of Propulsion and Power - J PROPUL POWER, 11:769–780, 07 1995.

[21] Alexander Burcat. Prof. burcat's thermodynamic data, 2014. http://garfield.chem.elte.hu/Burcat/burcat.html.

[22] Katie Camero. Aviation's dirty secret: Airplane contrails are a surprisingly potent cause of global warming, 2019. https://www.science.org/content/article/aviation-s-dirty-secret-airplane-contrails-are-surprisingly-potent\-cause-global-warming.

[23] Kenneth Cashdollar, Isaac Zlochower, Gregory Green, Richard Thomas, and Martin Hertzberg. Flammability of methane propane and hydrogen gases. Journal of Loss Prevention in the Process Industries, 13:327–340, 05 2000.

[24] Laurent Catoire, Jean-Francois Legendre, and Marc Giraud. Kinetic Model for Aluminum-Sensitized Ram Accelerator Combustion. Journal of Propulsion and Power, 19(2):196–202, March 2003.

[25] Quentin Cazères, Perrine Pepiot, Eleonore Riber, and Bénédicte Cuenot. A fully automatic procedure for the analytical reduction of chemical kinetics mechanisms for computational fluid dynamics applications. Fuel, 303:121247, 2021.

[26] Quentin Cazères, Perrine Pepiot, Eleonore Riber, and Bénédicte Cuenot. A fully automatic procedure for the analytical reduction of chemical kinetics mechanisms for computational fluid dynamics applications. Fuel, 303:121247, 2021.

[27] Cowling Chapman. The Mathematical Theory of Non-Uniform Gases. 1970.

[28] Malcolm W Chase. Nist-janaf thermochemical tables 4th ed. J. of Physical and Chemical Reffernce Data, pages 1529–1564, 1998.

[29] Martin Sommerfeld Yutaka Tsuji Clayton T. Crowe, John D. Schwarzkopf. Multiphase Flows with Droplets and Particles. 2011.

[30] Olivier Colin and Michael Rudgyard. Development of high-order taylor–galerkin schemes for les. Journal of Computational Physics, 162(2):338–371, 2000.

[31] F Collin-Bastiani. Modeling and large eddy simulation of two-phase ignition in gas turbines. 2019.

[32] Pablo G. Debenedetti. Metastable Liquids: Concepts and Principles. 1997.

[33] Christophe Devals. Contribution à l'étude de l'interaction ondes de choc - particules. PhD thesis, 2002. Thèse de doctorat dirigée par Estivalèzes, Jean-Luc Dynamique des fluides École nationale supérieure de l'aéronautique et de l'espace (Toulouse ; 1972-2007) 2002.

[34] Pablo Escot Bocanegra. Etudes expérimentales et modélisation de la combustion des nuages de particules micrométriques et nanométriques d'aluminium. PhD thesis, 2007. Thèse de doctorat dirigée par Gökalp, Iskender Mécanique des fluides, énergétique, thermique, combustion, acoustique Orléans 2007.

[35] Capcom espace. Ariane 5 caractéristiques, 2014. http://www.capcomespace.net/dossiers/espace_europeen/ariane/ ariane5/caracteristiques.htm.

[36] Jannis Finke and Fabian Sewerin. Combining a population balance approach with detailed chemistry to model the condensation of oxide smoke during aluminum combustion in spatially homogeneous reactors. Combustion and Flame, 248:112510, February 2023.

[37] Sheldon K Friedlander et al. Smoke, dust, and haze, volume 198. Oxford university press New York, 2000.

[38] Lucien Gallen. Prediction of soot particles in Gas Turbine Combustors using Large Eddy Simulation.

[39] Lucien Gallen, Anne Felden, Eleonore Riber, and Bénédicte Cuenot. Lagrangian tracking of soot particles in LES of gas turbines. Proceedings of the Combustion Institute, 37(4):5429–5436, 2019.

[40] Stany Gallier, Alexandre Braconnier, Franck Godfroy, Fabien Halter, and Christian Chauveau. The role of thermophoresis on aluminum oxide lobe formation. Combustion and Flame, 228:142–153, 2021.

[41] Stany Gallier, Alexandre Braconnier, Franck Godfroy, Fabien Halter, and Christian Chauveau. The role of thermophoresis on aluminum oxide lobe formation. Combustion and Flame, 228:142–153, June 2021.

[42] Alejandro L Garcia, Christian Van Den Broeck, Marc Aertsens, and Roger Serneels. A monte carlo simulation of coagulation. Physica A: Statistical Mechanics and its Applications, 143(3):535–546, 1987.

[43] R Garg, C Narayanan, and S Subramaniam. A numerically convergent lagrangian–eulerian simulation method for dispersed two-phase flows. International Journal of Multiphase Flow, 35(4):376–388, 2009.

[44] Steven L. Girshick and Chia-Pin Chiu. Kinetic nucleation theory: A new expression for the rate of homogeneous nucleation from an ideal supersaturated vapor. The Journal of Chemical Physics, 93(2):1273–1277, 07 1990.

[45] Julien Glorian. Cinétique hétérogène pour la combustion de l'aluminium.

[46] Julien Glorian. Cinétique hétérogène pour la combustion de l'aluminium. PhD thesis, 2015. Thèse de doctorat dirigée par Catoire, Laurent Chimie physique Palaiseau, École nationale supérieure de techniques avancées 2015.

[47] Julien Glorian, Stany Gallier, and Laurent Catoire. On the role of heterogeneous reactions in aluminum combustion. Combustion and Flame, 168:378–392, June 2016.

[48] B Glorieux, F Millot, and JC Rifflet. Surface tension of liquid alumina from contactless techniques. International Journal of Thermophysics, 23(5):1249–1257, 2002.

[49] O. G. Glotov, A. A. Onischuk, V. V. Karasev, V. E. Zarko, and A. M. Baklanov. Size and morphology of the nanooxide aerosol generated by combustion of an aluminum droplet. Doklady Physical Chemistry, 413(1):59–62, March 2007.

[50] Oleg G. Glotov and Vladimir E. Zarko. Formation of Nanosized Products in Combustion of Metal Particles. In Energetic Nanomaterials, pages 285–321. Elsevier, 2016.

[51] David Goodwin, Harry Moffat, and Raymond Speth. Cantera: An object-oriented software toolkit for chemical kinetics, thermodynamics, and transport processes. version 2.2.0. 01 2015.

[52] Samuel Goroshin, Jorin Mamen, Andrew Higgins, Tim Bazyn, Nick Glumac, and Herman Krier. Emission spectroscopy of flame fronts in aluminum suspensions. Proceedings of the Combustion Institute, 31(2):2011–2019, 2007.

[53] M. A. Gurevich, G. E. Ozerova, and A. M. Stepanov. Heterogeneous ignition of an aluminum particle in oxygen and water vapor. Combustion, Explosion, and Shock Waves, 6(3):291–297, July 1970.

[54] Doo-Hee Han and Hong-Gye Sung. A numerical study on heterogeneous aluminum dust combustion including particle surface and gas-phase reaction. Combustion and Flame, 206:112–122, August 2019.

[55] Xiaoming Hao, Haibo Zhao, Zuwei Xu, and Chuguang Zheng. Population balance-monte carlo simulation for gas-to-particle synthesis of nanoparticles. Aerosol science and technology, 47(10):1125–1133, 2013.

[56] Joseph O Hirschfelder, Charles F Curtiss, R Byron Bird, et al. Molecular theory of gases and liquids, volume 1964. Wiley New York, 1954.

[57] R.E. Honig and D.A. Kramer. Vapor Pressure Data for the Solid and Liquid Elements. RCA Laboratories, David Sarnoff Research Center, 1969.

[58] Ying Huang, Grant A Risha, Vigor Yang, and Richard A Yetter. Combustion of bimodal nano/micron-sized aluminum particle dust in air. Proceedings of the Combustion Institute, 31(2):2001–2009, 2007.

[59] Ying Huang, Grant A. Risha, Vigor Yang, and Richard A. Yetter. Effect of particle size on combustion of aluminum particle dust in air. Combustion and Flame, 156(1):5–13, January 2009.

[60] IEA. Growth in global oil demand is set to slow significantly by 2028, 2023. https://www.iea.org/news/growth-in-global-oil-demand-is-set-to-slow-significantly-by-2028.

[61] IEA. How many cars are there in the world in 2023?, 2023. https://hedgescompany.com/blog/2021/06/how-many-cars-are-there-in-the-world/#:~:text=If%20you%20want%20to%20know,stats%2C%20including%20cars%20per%20capita.).

[62] R.B. Bird J.O. Hirschfelder, C.F. Curtiss. 1969, title = Molecular theory of gases and liquids,.

[63] P. Julien, M. Soo, S. Goroshin, D. L. Frost, J. M. Bergthorson, N. Glumac, and F. Zhang. Combustion of Aluminum Suspensions in Hydrocarbon Flame Products. Journal of Propulsion and Power, 30(4):1047–1054, July 2014.

[64] Philippe Julien, James Vickery, Samuel Goroshin, David L Frost, and Jeffrey M Bergthorson. Freely-propagating flames in aluminum dust clouds. Combustion and Flame, 162(11):4241–4253, 2015.

[65] Philippe Julien, Sam Whiteley, Michael Soo, Samuel Goroshin, David L. Frost, and Jeffrey M. Bergthorson. Flame speed measurements in aluminum suspensions using a counterflow burner. Proceedings of the Combustion Institute, 36(2):2291–2298, 2017.

[66] V.I. Kalikmanov. Nucleation Theory, volume 860 of Lecture Notes in Physics. Springer Netherlands, Dordrecht, 2013.

[67] TR Kalra and PHT Uhlherr. Properties of bluff body wakes. In 4th Australasian conference on hydraulics and fluid mechanics, Melbourne, Australia. Citeseer, 1971.

[68] V.V. Karasev, A.A. Onischuk, O.G. Glotov, A.M. Baklanov, A.G. Maryasov, V.E. Zarko, V.N. Panfilov, A.I. Levykin, and K.K. Sabelfeld. Formation of charged aggregates of Al2O3 nanoparticles by combustion of aluminum droplets in air. Combustion and Flame, 138(1-2):40–54, July 2004.

[69] V.V. Karasev, A.A. Onischuk, O.G. Glotov, A.M. Baklanov, A.G. Maryasov, V.E. Zarko, V.N. Panfilov, A.I. Levykin, and K.K. Sabelfeld. Formation of charged aggregates of al2o3 nanoparticles by combustion of aluminum droplets in air. Combustion and Flame, 138(1):40–54, 2004.

[70] Merrill K King. Aluminum combustion in a solid rocket motor environment. Proceedings of the combustion institute, 32(2):2107–2114, 2009.

[71] Gregor Kotalczyk and F Einar Kruis. A monte carlo method for the simulation of coagulation and nucleation based on weighted particles and the concepts of stochastic resolution and merging. Journal of Computational Physics, 340:276–296, 2017.

[72] K. K. Kuo. 2005, title = Principles of combustion,.

[73] Kenneth K Kuo. Principles of combustion john wiley & sons. New York, 1986.

[74] Laura Lacassagne. Simulations et analyses de stabilité linéaire du détachement tourbillonnaire d'angle dans les moteurs à propergol solide.

[75] L.D. Landau, E.M. Lifshits, and E.M. Lifshits. Statistical Physics. Number ptie. 1 in A-W series in advanced physics. Pergamon Press, 1969.

[76] Peter Lax and Burton Wendroff. Systems of conservation laws. Communications on Pure and Applied Mathematics, 13(2):217–237, 1960.

[77] C. Le Quéré, R. M. Andrew, P. Friedlingstein, S. Sitch, J. Pongratz, A. C. Manning, J. I. Korsbakken, G. P. Peters, J. G. Canadell, R. B. Jackson, T. A. Boden, P. P. Tans, O. D. Andrews, V. K. Arora, D. C. E. Bakker, L. Barbero, M. Becker, R. A. Betts, L. Bopp, F. Chevallier, L. P. Chini, P. Ciais, C. E. Cosca, J. Cross, K. Currie, T. Gasser, I. Harris, J. Hauck, V. Haverd, R. A. Houghton, C. W. Hunt, G. Hurtt, T. Ilyina, A. K. Jain, E. Kato, M. Kautz, R. F. Keeling, K. Klein Goldewijk, A. Körtzinger, P. Landschützer, N. Lefèvre, A. Lenton, S. Lienert, I. Lima, D. Lombardozzi, N. Metzl, F. Millero, P. M. S. Monteiro, D. R. Munro, J. E. M. S. Nabel, S. Nakaoka, Y. Nojiri, X. A. Padin, A. Peregon, B. Pfeil, D. Pierrot, B. Poulter, G. Rehder, J. Reimer, C. Rödenbeck, J. Schwinger, R. Séférian, I. Skjelvan, B. D. Stocker, H. Tian, B. Tilbrook, F. N. Tubiello, I. T. van der Laan-Luijkx, G. R. van der Werf, S. van Heuven, N. Viovy, N. Vuichard, A. P. Walker, A. J. Watson, A. J. Wiltshire, S. Zaehle, and D. Zhu. Global carbon budget 2017. Earth System Science Data, 10(1):405–448, 2018.

[78] Hoesung Lee, Katherine Calvin, Dipak Dasgupta, Gerhard Krinner, Aditi Mukherji, Peter Thorne, Christopher Trisos, José Romero, Paulina Aldunce, Ko Barret, et al.

Ipcc, 2023: Climate change 2023: Synthesis report, summary for policymakers. contribution of working groups i, ii and iii to the sixth assessment report of the intergovernmental panel on climate change [core writing team, h. lee and j. romero (eds.)]. ipcc, geneva, switzerland. 2023.

[79] Matthias Leitner, Thomas Leitner, Alexander Schmon, Kirmanj Aziz, and Gernot Pottlacher. Thermophysical Properties of Liquid Aluminum. Metallurgical and Materials Transactions A, 48(6):3036–3045, June 2017.

[80] Yulan Lin, Kangtaek Lee, and Themis Matsoukas. Solution of the population balance equation using constant-number monte carlo. Chemical Engineering Science, 57(12):2241–2252, 2002.

[81] R. Lomba, P. Laboureur, C. Dumand, C. Chauveau, and F. Halter. Determination of aluminum-air burning velocities using PIV and Laser sheet tomography. Proceedings of the Combustion Institute, 37(3):3143–3150, 2019.

[82] Ricardo Lomba. Utilisation de la combustion métallique dans les machines thermiques. These de doctorat, Orléans, November 2016.

[83] Michaël Marion. Etudes sur la combustion des particules d'aluminium sous pression. PhD thesis, Université d'Orléans (UO), FRA., 1996.

[84] Bonnie J McBride. NASA Glenn coefficients for calculating thermodynamic properties of individual species. National Aeronautics and Space Administration, John H. Glenn Research Center . . . , 2002.

[85] William J Menz, Jethro Akroyd, and Markus Kraft. Stochastic solution of population balance equations for reactor networks. Journal of Computational Physics, 256:615–629, 2014.

[86] Aaron Meurer, Christopher P. Smith, Mateusz Paprocki, Ondřej Čertík, Sergey B. Kirpichev, Matthew Rocklin, AMiT Kumar, Sergiu Ivanov, Jason K. Moore, Sartaj Singh, Thilina Rathnayake, Sean Vig, Brian E. Granger, Richard P. Muller, Francesco Bonazzi, Harsh Gupta, Shivam Vats, Fredrik Johansson, Fabian Pedregosa, Matthew J. Curry, Andy R. Terrel, Štěpán Roučka, Ashutosh Saboo, Isuru Fernando, Sumith Kulal, Robert Cimrman, and Anthony Scopatz. Sympy: symbolic computing in python. PeerJ Computer Science, 3:e103, January 2017.

[87] R S Miller, K Harstad, and J Bellan. Evaluation of equilibrium and non-equilibrium evaporation models for many-droplet gas-liquid ¯ow simulations. International Journal of Multiphase Flow, 1998.

[88] SH Park, KW Lee, E Otto, and H Fissan. The log-normal size distribution theory of brownian aerosol coagulation for the entire particle size range: Part i—analytical solution using the harmonic mean coagulation kernel. Journal of Aerosol Science, 30(1):3–16, 1999.

[89] Damien Paulhiac. Modélisation de la combustion d'un spray dans un brûleur aéronautique.

[90] Perrine Pepiot. Automatic strategies to model transportation fuel surrogates. Stanford University, 2008.

[91] T.J Poinsot and S.K Lelef. Boundary conditions for direct simulations of compressible viscous flows. Journal of Computational Physics, 101(1):104–129, 1992.

[92] N. I. Poletaev, A. N. Zolotko, and Yu. A. Doroshenko. Degree of dispersion of metal combustion products in a laminar dust flame. Combustion, Explosion, and Shock Waves, 47(2):153–165, March 2011.

[93] Sotiris E Pratsinis. Simultaneous nucleation, condensation, and coagulation in aerosol reactors. Journal of colloid and interface science, 124(2):416–427, 1988.

[94] Grant Risha, Ying Huang, Richard Yetter, and Vigor Yang. Experimental investigation of aluminum particle dust cloud combustion. In 43rd AIAA aerospace sciences meeting and exhibit, page 739, 2005.

[95] Masatoshi Saba, Takafumi Kato, and Tatsuo Oguchi. Reaction modeling study on the combustion of aluminum in gas phase: The Al + O2 and related reactions. Combustion and Flame, 225:535–550, March 2021.

[96] Vincent Sarou-Kanian. Etude expérimentale de la combustion des gouttes d'aluminium en convection forcée. Influence de l'atmosphère gazeuse.

[97] A. M. Savel'ev and A. M. Starik. An improved model of homogeneous nucleation for high supersaturation conditions: aluminum vapor. Physical Chemistry Chemical Physics, 19(1):523–538, 2017.

[98] Alexander M. Savel'ev and Alexander M. Starik. The formation of (Al2O3)n clusters as a probable mechanism of aluminum oxide nucleation during the combustion of aluminized fuels: Numerical analysis. Combustion and Flame, 196:223–236, October 2018.

[99] Links Schiller. A drag coefficient correlation. Zeit. Ver. Deutsch. Ing., 77:318–320, 1933.

[100] Thilo Schonfeld and Michael Rudgyard. Steady and unsteady flow simulations using the hybrid flow solver avbp. AIAA Journal, 37(11):1378–1385, 1999.

[101] John H Seinfeld and Spyros N Pandis. Atmospheric chemistry and physics: from air pollution to climate change. John Wiley & Sons, 2016.

[102] William A Sirignano. Fluid dynamics and transport of droplets and sprays. Cambridge university press, 2010.

[103] Matthew Smith and Themis Matsoukas. Constant-number monte carlo simulation of population balances. Chemical Engineering Science, 53(9):1777–1786, 1998.

[104] Dudley Brian Spalding. Combustion of liquid fuels. Nature, 165(4187):160–160, 1950.

[105] Jimmy Suarez. Modélisation de la combustion diphasique de l'aluminium et application sur la post-combustion.

[106] HNV Temperley. Kinetic theory of liquids, 1947.

[107] Hesam Tofighian, E Amani, and M Saffar-Avval. Parcel-number-density control algorithms for the efficient simulation of particle-laden two-phase flows. Journal of Computational Physics, 387:569–588, 2019.

[108] K.A. Trowell, S. Goroshin, D.L. Frost, and J.M. Bergthorson. Aluminum and its role as a recyclable, sustainable carrier of renewable energy. Applied Energy, 275:115112, October 2020.

[109] Mikhaylo A. Trunov, Mirko Schoenitz, Xiaoying Zhu, and Edward L. Dreizin. Effect of polymorphic phase transformations in Al2O3 film on oxidation kinetics of aluminum powders. Combustion and Flame, 140(4):310–318, March 2005.

[110] Christian Vargel. Propriétés générales de l'aluminium et de ses alliages. Étude et propriétés des métaux, December 2005.

[111] Hanna Vehkamäki. Classical Nucleation Theory in Multicomponent System. 2006.

[112] Junlong Wang, Ningfei Wang, Xiangrui Zou, Wenhao Yu, and Baolu Shi. Modeling of micro aluminum particle combustion in multiple oxidizers. Acta Astronautica, 189:119–128, 2021.

[113] A. C. Zettlemoyer. Nucleation. Marcel Dekker Inc., New York, 1969.

[114] Jiarui Zhang, Oliver T. Stein, Tien D. Luu, Ali Shamooni, Zhixun Xia, Zhenbing Luo, Likun Ma, Yunchao Feng, and Andreas Kronenburg. Detailed modeling of aluminum particle combustion – From single particles to cloud combustion in Bunsen flames. Chinese Journal of Aeronautics, 35(5):319–332, May 2022.

RÉPUBLIQUE FRANÇAISE
Liberté
Égalité
Fraternité

Université de Toulouse

Titre : Simulation de la combustion des particules d'aluminium

Mots clés : Simulation, Aluminium, Combustion, Numérique

Résumé : Afin de limiter l'utilisation d'hydrocarbures, il est nécessaire de trouver un moyen propre de stocker et transporter l'énergie sur de grandes distances. Les combustibles métalliques constituent d'excellents candidats en tant que combustibles alternatifs, renouvelables et sans émissions de carbone. En effet, ils présentent une haute densité énergétique, sont disponibles à bas coût et sont faciles à stocker et transporter sous forme de poudre. De plus, les produits de combustion sont des oxydes métalliques solides qui pourraient être collectés et recyclés (J.M. Bergthorson et al., Applied Energy, 2015). L'aluminium est utilisé depuis de nombreuses années comme combustible, notamment en tant que carburant pour la propulsion spatiale et militaire. Cependant, la compréhension détaillée de la combustion des particules d'aluminium reste un enjeu majeur nécessitant de combiner résultats expérimentaux et simulations numériques avancées. La modélisation de ce type de combustion implique de prendre en compte tous les phénomènes impliqués. Ces phénomènes complexes sont nombreux, de la fusion et l'évaporation des particules d'aluminium à l'oxydation gazeuse et de surface, jusqu'à la condensation et la solidification en particules d'oxyde métallique des produits de combustion. Durant cette thèse, un modèle complet pour la combustion des particules d'aluminium a été implémenté dans le code massivement parallèle AVBP afin de stabiliser numériquement des flammes d'aluminium. Le modèle prend en compte la présence du lobe d'alumine sur les particules d'aluminium, les réactions hétérogènes de surface et la condensation détaillée des produits de combustion en utilisant le modèle proposé par Finke et al. (J. Finke., Combustion and Flame, 2023). Ce modèle permet de suivre les produits de combustion liquides de façon Lagrangienne contrairement aux travaux présents dans la littérature qui utilisent une formulation Eulérienne. Ce dernier point permet d'étudier l'évolution de la morphologie des particules d'alumine, ce qui constitue un enjeu clef dans le but de les collecter et de les recycler. Ce modèle a été utilisé pour simuler la combustion de particules d'aluminium isolées, des flammes 1D ainsi que des flammes 2D pouvant être comparées aux résultats expérimentaux présents dans la littérature.

Title: Numerical simulation of aluminum particle combustion

Key words: Simulation, Combustion, Aluminum, Numerical

Abstract: As society is moving away from hydrocarbons, there is a need for a clean way to store and transport energy over the globe. For this need, metal fuels are very attractive and excellent candidates as alternative carbon-free and renewable fuels. Due to their high energy density, availability, stability and low cost, metals and especially aluminum could replace hydrocarbons in many applications. In addition, metal oxides are solid and may be easily collected and recycled (J.M. Bergthorson et al., Applied Energy, 2015). Aluminum is already well known as a fuel, used for many years in space propulsion. However, the detailed understanding of the combustion of aluminum particles remains a challenge which requires to combine sophisticated experiments with numerical simulation. The modeling of aluminum combustion then must take into account all existing phenomena, from melting and evaporation of the metal particles to gaseous and heterogeneous oxidation and finally condensation and solidification into metal oxide particles. In this work, a complete model for burning aluminum particles has been developed and implemented in the massively parallel Navier-Stokes compressible solver AVBP in order to compute a stabilized laminar flame. The model includes the dual composition of the aluminum particles with an alumina cap, heterogeneous surface reactions and condensation of the combustion products, and nucleation of products into particles following Finke et al. (J. Finke., Combustion and flame, 2023). The Lagrangian tracking of these product particles is an original feature of the model, with regards to the literature where an Eulerian formulation is mostly reported. It offers the possibility to give more details about the formed metal oxide particles, in particular their size. Results and analysis of 1D and 2D stabilized aluminum laminar flames obtained with this model confirm the validity of the approach.